Construction of Transition Metal Composition via cost-effective Seawater Corrosive Technology for Efficient Electrochemical Water Splitting and Seawater Utilization

Zhaohui Zhang

Zhaohui Zhang. Construction of Transition Metal Composition via cost-effective Seawater Corrosive Technology for Efficient Electrochemical Water Splitting and Seawater Utilization. Micro and nanotechnologies/Microelectronics. Université de Lille, 2024. English. NNT : 2024ULILN010 . tel-04753943

HAL Id: tel-04753943
https://hal.science/tel-04753943v1

Submitted on 28 Oct 2024

THESE DE DOCTORAT

Présentée à

L'UNIVERSITE DE LILLE

L'école doctorale: ENGSYS Sciences de l'ingénierie et des systèmes

L'unité de recherche: CNRS-IEMN

Dans la spécialité: Micro-nanosystèmes et Capteurs

par

Zhaohui Zhang

Construction of Transition Metal Composition *via* cost-effective Seawater Corrosive Technology for Efficient Electrochemical Water Splitting and Seawater Utilization

Construction de la composition de métaux de transition via une technologie corrosive de l'eau de mer rentable pour une séparation électrochimique de l'eau et une utilisation de l'eau de mer efficaces

Soutenue le 21 Mai 2024 devant le composé de:

Prof. Alexandru VLAD	Rapporteur	Université Catholique de Louvain
Prof.Carmel BRESLIN	Rapporteur	Université de Maynooth
Associate Prof. Li HONG	Examinateur	Université Technologique de Nanyang
Prof.Henri HAPPY	Président du jury	Université de Lille, CNRS-IEMN
Dr. Rabah Boukherroub	Directeur de thèse	Université de Lille, CNRS-IEMN
Prof. Sabine Szunerits	Co-directeurs de thèse	Université de Lille, CNRS-IEMN

Abstract

Direct seawater electrolysis coupled with intermittent ocean current, wind, or solar energies is one of the potential and cleanest routes for high-purity hydrogen production. Seawater is abundant (>96% of the total reservoir), but its utilization and application are still poor till now, owing to the complex composition of seawater, such as high concentration of Cl^- leading to corrosion of catalyst materials. Therefore, exploring highly active and stable earth-abundant electrocatalysts for seawater splitting *via* a facile, cost-effective, and large-scale method is the main objective of the present PhD study.

Chapters I and II briefly introduce the fundamental mechanism of electrochemical water splitting, transition metal catalysts' advantages and their synthetic strategies, and direct seawater electrolysis opportunities and faced challenges. I analyzed and put forward several essential solutions. For example, by utilizing the potential of seawater, we developed three types of electrocatalysts via large-scale seawater corrosion engineering. In addition, water splitting assisted by small organic molecule oxidation strategy was proposed for highly efficient hydrogen production, effectively reducing anode overpotential, avoiding chlorine evolution reaction (CER) competition at the anode, and successfully converting waste into high-value-added products.

Chapter III describes a fundamental study of Cl^- accelerating oxygen corrosion strategy to construct iron-cobalt double layer hydroxide (Fe/Co LDH) nanoflower along with Pt loading to achieve high performance electrocatalyst for water splitting. The morphology, atom ratio, vacancy state and electrocatalyst performance of Pt-Co/Fe sample can be tailored through adjusting the corrosion solution "$NaCl$-$CoCl_2$" content. The coupling effects between Fe/Co-LDH and trace of noble metal, as well as the unique heterostructure of the flowers endowed the Pt-Co/Fe electrocatalyst with enhanced OER and HER performances, recording lower overpotential of 285 mV at100 mA cm^{-2} for OER and 36 mV at 10 mA cm^{-2} for HER in 1M KOH.

Chapter IV presents the preparation of effective catalysts for direct seawater electrolysis and seawater utilization. The nickel–iron layer double hydroxide and Ni_3S_2

heterostructure nanoflower bifunctional electrocatalysts (NiFe LDH-Ni_3S_2) were synthesized *via* seawater corrosion and ion exchange strategy, and exhibited HER/OER performance comparable to the state-of-the-art noble metal-based electrocatalysts. In addition, benefiting from the modulated electronic configuration and optimized free-energy of oxygen-containing intermediates adsorption and desorption, it featured outstanding urea oxidation reaction and overall seawater-urea splitting activities in 1 M KOH+0.33 M urea.

Chapter V mainly introduces the idea of OER/EGOR catalysts for high-performance seawater electrolysis and plastic PET electro-upcycling using amorphous CoFeNi catalyst. The synthesized A-CoFeNi catalyst displayed overpotential values as low as 1.55 and 1.39 V to deliver 100 mA cm^{-2} for OER and EGOR in alkaline natural seawater electrolyte, respectively. It effectively avoids CER reaction competition at the anode and successfully converts waste into high-value-added products. For example, the electrolyzer recorded high FE for the generation of H_2 (almost 100%) and high value-added formate (95.6%).

Résumé

L'électrolyse directe de l'eau de mer couplée aux courants marins intermittents, à l'énergie éolienne ou solaire est l'une des voies potentielles et les plus propres pour la production d'hydrogène de haute pureté. L'eau de mer est abondante (>96% des réserves d'eau présentes à la surface de la terre), mais son utilisation et son application sont encore limitées jusqu'à présent, en raison de la composition complexe de l'eau de mer, comme la concentration élevée de Cl^- qui entraîne la corrosion des matériaux catalytiques. Par conséquent, l'objectif principal de cette thèse de doctorat est d'explorer des électrocatalyseurs hautement actifs et stables pour la dissociation de l'eau de mer par le biais d'une méthode facile, rentable et à grande échelle.

Les chapitres I et II présentent brièvement le mécanisme fondamental de la dissociation électrochimique de l'eau, les avantages des catalyseurs à base de métaux de transition et leurs voies de synthèse, ainsi que les opportunités et les défis de l'électrolyse directe de l'eau de mer. J'ai analysé et proposé plusieurs solutions. Par exemple, en exploitant le potentiel de l'eau de mer, nous avons développé trois types d'électrocatalyseurs par le biais de l'ingénierie de la corrosion de l'eau de mer à grande échelle. En outre, nous avons proposé une stratégie de l'électrolyse de l'eau assistée par l'oxydation de petites molécules organiques pour une production d'hydrogène, réduisant efficacement la surtension de l'anode, évitant la concurrence de la réaction d'évolution du chlore (CER), et convertissant avec succès les déchets en produits à haute valeur ajoutée.

Le chapitre III décrit une étude fondamentale de la stratégie de corrosion de l'oxygène accélérée par le Cl^- pour préparer des nanofleurs d'hydroxyde à double couche de fer et de cobalt (Fe/Co LDH) dopées au Pt afin d'obtenir un électrocatalyseur à haute performance pour l'électrolyse de l'eau. La morphologie, le rapport atomique, l'état de valence et la performance électrocatalytique de l'échantillon Pt-Co/Fe peuvent être adaptés en ajustant la teneur de la solution de corrosion "$NaCl$-$CoCl_2$". Les effets de couplage entre Fe/Co-LDH et les traces de métal noble, ainsi que l'hétérostructure unique des fleurs ont permis d'améliorer les performances de l'électrocatalyseur Pt-

Co/Fe pour OER et HER, en enregistrant une surtension de 285 mV à 100 mA cm^{-2} pour l'OER et de 36 mV à 10 mA cm^{-2} pour l'HER dans une solution alcaline (1 M KOH).

Le chapitre IV décrit la préparation de catalyseurs efficaces pour l'électrolyse directe et l'utilisation de l'eau de mer. Les électrocatalyseurs bifonctionnels à double couche d'hydroxyde de nickel-fer et à nano-fleurs de Ni_3S_2 (NiFe LDH-Ni_3S_2) ont été synthétisés par corrosion de l'eau de mer et échange d'ions, et ont présenté des performances HER/OER comparables à celles des électrocatalyseurs à base de métaux nobles. En outre, grâce à la configuration électronique modulée et à l'optimisation de l'énergie libre de l'adsorption et de la désorption des intermédiaires contenant de l'oxygène, la réaction d'oxydation de l'urée et la génération d’hydrogène par électrolyse de l'eau de mer et de l'urée dans 1 M KOH+0.33 M d'urée ont été remarquables.

Le chapitre V concerne principalement les catalyseurs OER/EGOR pour l'électrolyse de l'eau de mer et l'électro-recyclage du plastique (PET) en utilisant le catalyseur CoFeNi amorphe. Le catalyseur A-CoFeNi a démontré des valeurs de surtension aussi basses que 1,55 et 1,39 V pour fournir 100 mA cm^{-2} pour l'OER et l'EGOR dans l'électrolyte d'eau de mer naturelle alcaline, respectivement. Il permet d'éviter efficacement la concurrence de la réaction d’évolution du chlore (CER) à l'anode et de convertir avec succès les déchets en produits à haute valeur ajoutée. Par exemple, l'électrolyseur a également enregistré une efficacité faradique élevée pour la production de H_2 (presque 100 %) et de formiate à haute valeur ajoutée (95.6 %).

Acknowledgments

My research was conducted within the Nano-Bio-Interfaces (NBl) group at the Institute of Electronics, Microelectronics, and Nanotechnology (IEMN). Though four years may seem short in the grand scheme of life, they have been profoundly memorable in my journey. During this time, my scientific research capabilities and innovative skills were honed, thanks to my teachers' and friends' support and guidance. Their selfless care and dedication have instilled in me a newfound confidence and enriched my life experiences.

From the beginning of the project to the successful completion of the dissertation, first and foremost, I would like to thank my supervisors, Dr. Rabah Boukherroub and Prof. Sabine Szunerits, for their patience and guidance over the past four years. With their enormous help and supervision, I have obtained much precious research experience, such as laboratory techniques and knowledge in chemistry and materials. It was indeed a great pleasure to study under their mentorships.

Also, I am grateful to my supervisor Dr. Long-cheng Tang in China, who introduced me to the field of scientific research. Without his guidance and support, I would not have been able to embark on this journey in research. I express my sincere appreciation to Dr. Alexandre Barras, Dr. Ahmed Addad, Dr. Pascal Roussel, Dr. Pardis Simon, Dr. Lydia Karmazin and Dr. Véronique Alaimo for their unwavering support and assistance in material characterization and analysis.

My heartfelt thanks go to all my colleagues for all the help, discussions and sharing. To Alex, working with you in the same lab for four years is a pleasure. Thanks for all your generous help and valuable advice. Also, many thanks go to Yi Zhang, Zhiran Yu, Yuanyuan Miao, Yisha Chen, Zhihao Wu, Yunchu Zeng, Michele, Tomasz Swebocki, Nasrin Shokouhfar, Kilaparthi Sravan Kumar, Shakila Behzadifar, Inès De Hoon, Teresa Rodrigues, Asmaa, Go Inoue… It is truly my honor to work with all of you.

I would also like to thank my friends, Jianlei Zhang, Yu Zhou, Hongzhuo Fan, Tao An, Haihong Li, Mingwei Tang, Yuzhe Zhu, and Zijing Li, Qingyu Tian, Hongyan Su… for their friendship and extensive support.

In particular, I would like to thank the China Scholarship Council (CSC), which offered

me the opportunity to pursue my PhD study in France.

Thanks to my family and my beloved parents. From childhood to now, they have given me unlimited support and encouragement for supporting me to pursue my dream. Their simplicity, hard work, strength, patience and humility will benefit me for life! Thanks to my girlfriend Qingyue Li for her many years of support and encouragement! Thanks to my other friends for their care and encouragement!

General introduction

Owing to the dual challenges of the energy crisis and climate change, researchers are dedicated to developing alternative energy sources to alleviate dependence on fossil fuels. Hydrogen is widely acknowledged as an effective driving force for the decarbonized transformation of global energy systems, owing to its high energy density, abundant availability, and environmental friendliness. Currently, hydrogen derived from sustainable technologies (i.e., green hydrogen) accounts for only 4% of hydrogen used in the global industry due to its higher cost factor. Energy efficiency improvement and cost reduction in water electrolysis technologies are imperative to facilitate a commercial scale comparable to that of gray hydrogen produced using fossil fuels. This goal can be achieved by developing innovative electrocatalytic materials that reduce the huge energy losses and costs of water electrolyzers. Water electrolysis involves two essential half-reactions of cathodic hydrogen evolution reaction (HER) and anodic oxygen evolution reaction (OER), which require high-performance electrocatalysts to overcome the sluggish kinetics and enhance reaction activity. Currently, the state-of-the-art performance belongs to Pt/C (HER), RuO_2 and IrO_2 (OER), exhibiting splendid electrocatalytic activity. However, the global reserve scarcity and the exorbitant price of these noble metals have largely hindered their large-scale and industrial applications. Developing cost-effective, active, and stable catalytic materials is imperative to overcome the above restrictions. Transition metal-based oxidation and layered double hydroxides have attracted widespread attention due to their appealing physicochemical properties and flexible structural composition, regarded as highly advanced electrocatalysts for water splitting. However, the traditional synthetic methodologies, e.g., hydrothermal and electrodeposition, require extra thermal and electrical energy, which necessitates the development of novel methods to decrease energy consumption.

In addition, considering the low availability of freshwater, seawater is a cost-free resource, accounting for about 97.5% of the earth's water. Seawater electrolysis (SWE) is endowed with financial, geographical, and technical merits, which is a perfect replacement electrolyte for scarce freshwater electrolysis. Conventional catalysts often prove ineffective for alkaline seawater electrolysis due to their inherent instability. Several factors contribute to the ineffectiveness of these catalysts, including the competition between the chlorine evolution reaction (CER) and the oxygen evolution reaction (OER) at the anode during direct alkaline seawater electrolysis. The thermodynamic potential of CER is only approximately 480 mV higher than that of OER. Additionally, the formation of corrosive hypochlorite can obstruct and damage the active sites of catalysts, leading to environmental hazards.

The work of this thesis concerns the preparation of catalysts with large surface areas and corrosion resistance ability to alleviate this issue. Furthermore, the replacement of slow OER by electrocatalytic oxidation of thermodynamically favorable small molecules offers a potential strategy for chlorine-free and energy-efficient hydrogen production.

Enlightened by the above discussion, the development of highly active and stable earth-abundant transition metal-based on Ni/Co/Fe composition with 3D porous architectures via natural corrosion engineering in combination with seawater and waste materials, is the main objective of my PhD thesis. Moreover, this dissertation provides a more in-depth analysis of their catalytic activities, microstructure evolution, and reaction mechanisms. Inspired by the process of developing more efficient catalysts for water splitting, the substitution of OER with faster and lower potential electro-oxidation reactions has been proposed. Various organic additives, including ethylene glycol and urea, have been introduced during seawater electrolysis to reduce OER overpotential. Overall, this work offers insights into the application of seawater corrosion engineering technique to modulate the electrocatalytic activity in energy conversion and seawater utilization systems, achieving efficient conversion of solar energy, electricity, and hydrogen.

This thesis is divided into six chapters, as follows:

Chapter I provides a brief introduction about fundamental mechanisms of electrochemical water splitting, hydrogen evolution reaction (HER) at cathode region, oxygen evolution reaction (OER) at anode region, and parameters for characterizing the electrochemical activity. Additionally, different types of transition metal catalysts and various synthetic strategies are also discussed. Direct seawater electrolysis holds opportunities but faces several challenges. Finally, the objectives of the thesis, the originality and novelty of my PhD thesis are presented.

Chapter II describes the experimental methods, the different techniques and electrochemical characterizations. Physical characterizations, including scanning electron microscopy (SEM), transmission electron microscopy (TEM), X-ray diffraction (XRD), X-ray photoelectron spectroscopy (XPS) and inductively coupled plasma mass spectrometry (ICP-MS), are performed to assess the morphologies, structures, element content and chemical valence of the fabricated catalysts. The electrochemical measurements, consisting of polarization curves and cyclic voltammetry (CV) curves, Tafel slopes, electrochemical active surface area (ECSA) and double-layer capacitance (C_{dl}), electrochemical impedance spectroscopy (EIS) and chronopotentiometry, were conducted to determine the performance of the developed electrocatalysts.

Chapter III is focused on the fundamental study of Cl^- accelerated oxygen corrosion strategy to construct iron-cobalt double layer hydroxide ((Fe/Co LDH) nanoflower along with Pt loading to achieve high performance electrocatalysts for water splitting. The morphology, atom ratio, vacancy state and electrocatalytic performance of the Pt-Co/Fe sample could be tailored through adjusting the corrosion solution “NaCl-$CoCl_2$” content. The coupling effects between Fe/Co-LDH and trace of noble metal, as well as the unique heterostructure of the flowers endowed the Pt-Co/Fe electrocatalyst with enhanced OER and HER performance, recording lower overpotential of 285 mV at 100 mA cm^{-2} for OER and 36 mV at 10 mA cm^{-2} for HER in 1 M KOH. The morphological, structural and chemical evolution of the catalyst before and after long time stability test are investigated to explain related mechanism by SEM, XRD and XPS, coupled with polarization curves. Clearly, the facile and scalable corrosion engineering to form metal hydroxides coupled with noble metals can be utilized to exploring other bifunctional electrocatalysts in the energy field.

Chapter IV mainly presents direct seawater electrolysis and seawater utilization. Nickel–iron layer double hydroxide and Ni_3S_2 heterostructured nanoflower bifunctional electrocatalysts (NiFe LDH-Ni_3S_2) were synthesized via seawater corrosion and ion exchange strategy. The desert rose shaped nanoflower morphology and unique heterostructure possessed highly intrinsic catalytic activity, large active surface area and facile charge/electrolyte/bubble migration, thus ensuring excellent HER/OER performance comparable to the state-of-the-art noble metal-based electrocatalysts. The as-prepared NiFe LDH-Ni_3S_2 electrodes recorded overpotentials as low as 257 and 280 mV to deliver 100 mA cm^{-2} for HER and OER in 1 M KOH seawater, respectively. In addition, benefiting from the modulated electronic configuration and optimized free-energy of oxygen-containing intermediates adsorption and desorption, NiFe LDH-Ni_3S_2 electrode featured outstanding urea oxidation reaction (UOR) and overall seawater-urea splitting activities in 1 M KOH + 0.33 M urea, which effectively reduced energy loss and avoided chlorine evolution reaction (CER) at anode region. This chapter introduces a novel process and catalyst mechanism via operando-EIS detection at various potentials. This work provides insights on the application of seawater corrosion engineering technique to modulate the electrocatalytic activity in energy conversion and seawater utilization systems, achieving efficient conversion of solar energy, electricity and hydrogen.

Chapter V gathers the results on electrochemical upcycling of plastic waste into valuable chemicals. Firstly, we applied the seawater corrosion engineering to construct CoFeNi amorphous material, which effectively converted ethylene glycol (from PET hydrolysate) into formate. The optimal CoFeNi only required 1.25 and 1.38 V *vs.* reversible hydrogen electrode (RHE) to achieve 10 and 100 mA cm^{-2}, respectively. In the co-electrolysis system, the A-CoFeNi@Pt-CoFeNi exhibited excellent Faradaic efficiencies for the simultaneous generation of formate (94.8%) and H_2 (100%). The high activity and stability of this system could be ascribed to CoFeNi trimetallic cooperation and strong electronic interactions. This work provides insights into the application of seawater corrosion technology to large-scale synthesis of catalysts, achieving efficient seawater utilization and electro-reforming PET plastic waste into valuable chemicals.

Chapter VI summarizes the conclusions of this research. Finally, the existing issues, perspectives and challenges are discussed for the future development of electrocatalysts that could operate at high current densities in the large-scale industrial electrolysis of water for the generation of hydrogen fuel; put forward new exploration directions for electrooxidation of small organic molecules. In conclusion, all the results obtained in this thesis work imply the promising potential application of transition metal-based hydroxide composites prepared *via* seawater corrosion strategy and provide valuable highlight to exploration of new composite materials for seawater utilization in future works.

Chapter I. Introduction

I.1 Development of hydrogen production (Background)

Fossil fuels, a long-standing cornerstone of the contemporary global economy, are undergoing re-evaluation as a primary energy source due to their significant contribution to environmental pollution and inherently limited availability [1]. The energy requirements of the world's growing population, coupled with industrial development in many developing countries, are forecast by some reports to surpass the existing reserves of crude oil within a few decades [2]. The remaining fossil fuel resources, including coal and natural gas, are similarly limited and associated with environmental pollution [3, 4]. Consequently, it is imperative to investigate alternative, renewable and environmental-friendly energy sources. As the global movement toward achieving Net Zero Emissions by 2050 gains momentum, green hydrogen, with a high energy density of 142 MJ kg^{-1}, is increasingly recognized as a critical player in both environmental and economic sustainability [5-7]. The application of hydrogen energy has gained achievements in various fields, such as transportation, synthetic fuels, upgrading oil, ammonia fertilizer, chemical processes and biorefinery applications. At present, the pathways for producing hydrogen energy are divided into: steam reforming of natural gas, coal gasification, partial oxidation of heavy oil, fossil with carbon capture, utilization and storage (CCUS), and water electrolysis. Governments worldwide have initiated efforts to advance the research, development, and commercialization of alternative hydrogen production pathways with minimal or no CO_2 emissions [8, 9]. Currently, over 90% of hydrogen is derived from fossil fuels, making a substantial contribution to CO_2 emissions [10]. Among the various methods for hydrogen production, electrochemical water splitting stands out as a promising green approach that can be seamlessly integrated with intermittent renewable energy sources such as wind, solar, and tidal power [11-13]. Hence, it is crucial to delineate and delve into the intricacies of fundamental electrochemical water splitting.

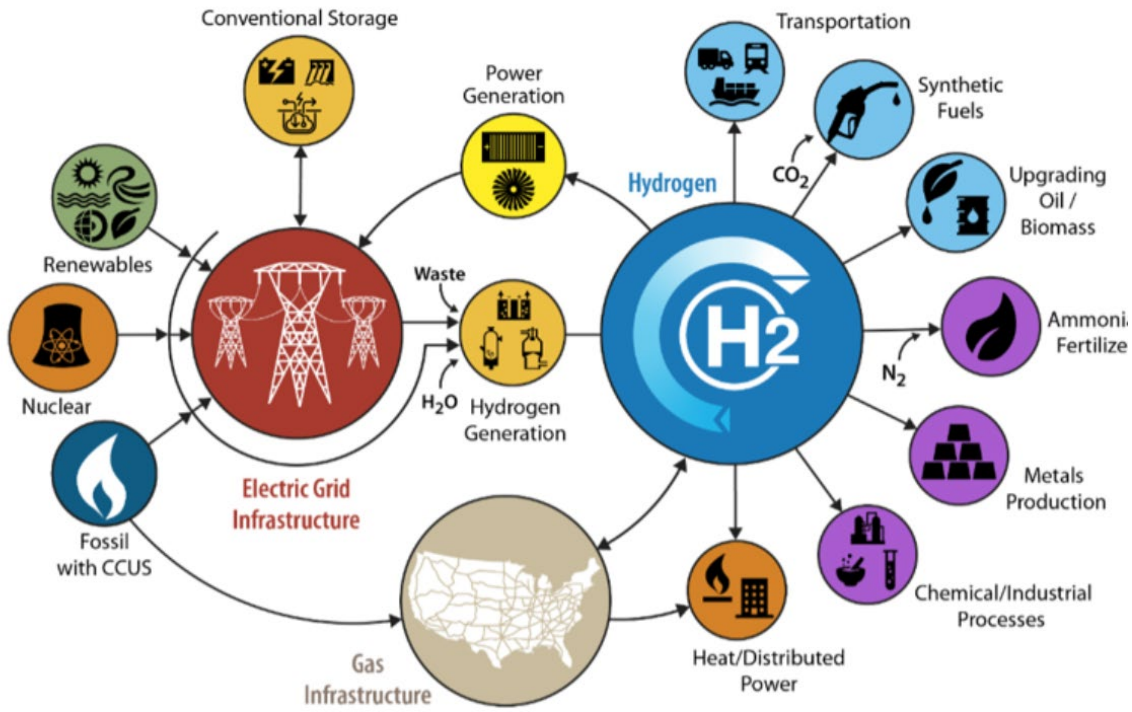

Figure 1. Schematic diagram of the production and application of hydrogen energy [14].

I.1.1 The principle of water electrolysis

In the absence of an electrochemical driving force, there exists an equilibrium among H_2O, hydrogen, and oxygen, with a pronounced preference for water [15, 16]. Upon the application of an electrochemical driving force, a thermodynamic minimum potential difference of 1.23 V at room temperature (298.15 K) is required to shift the equilibrium from H_2O towards hydrogen and oxygen [11, 17]. The water-splitting reaction, as expressed by equation (1), includes two half-reactions: the hydrogen evolution reaction (HER) occurring on the cathode and the oxygen evolution reaction (OER) at the anode. Following are the reactions that are proposed to be happening, depending on the reaction conditions.

$$H_2O \rightarrow H_2 + \frac{1}{2}O_2,\ E^0 = 1.23V \quad (Eq.1)$$

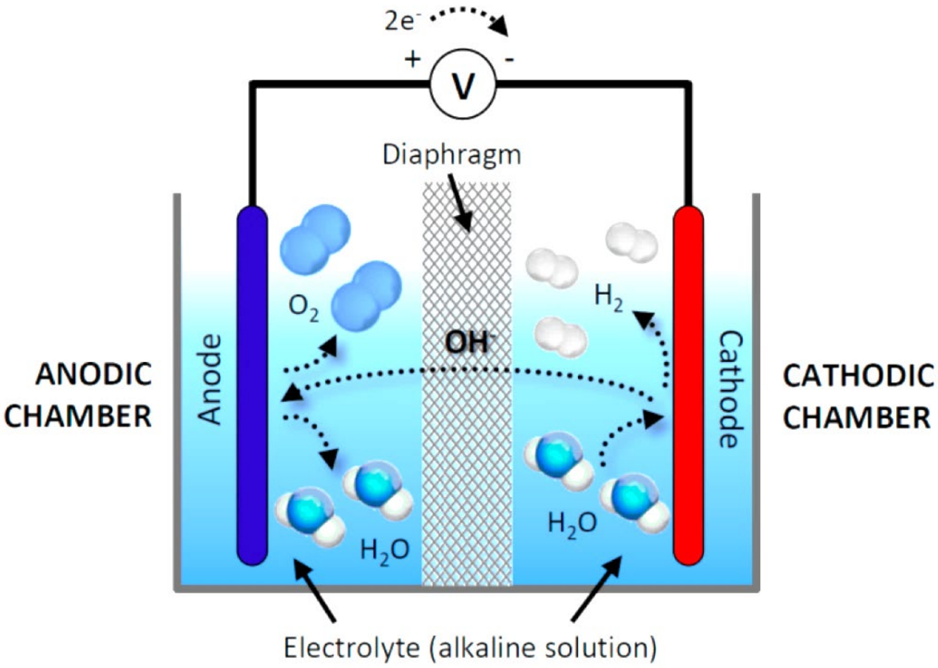

Figure 2. General scheme and operation of an alkaline electrolysis cell [18].

I.1.2 HER mechanism

One of the primary challenges impeding the advancement of hydrogen production via water electrolysis is the sluggish kinetics associated with the hydrogen evolution reaction (HER), which requires a large overpotential to activate. To minimize this overpotential (η) while preserving high energy conversion efficiencies, electrodes in a water electrolyzer undergo modification with active and stable electrocatalysts, enhancing the rates of electrochemical reactions.

The cathodic HER comprises a two-electron transfer process involving a central intermediate referred to as atomic H chemisorbed on the electrocatalyst surfaces (H*). The elemental steps of HER are elucidated through either the Volmer–Heyrovsky or the Volmer–Tafel mechanism, as depicted in equations (2) to (7):

In acidic condition:

$H^+ + e^- + M \rightarrow MH^*$ (Volmer step) (Eq.2)

$2MH_{ad} \rightarrow H_2 + 2M$ (Tafel step) (Eq.3)

$H^+ + MH^* + e^- \rightarrow H_2 + M$ (Heyrovsky step) (Eq.4)

In alkaline condition:

$H_2O + e^- + M \rightarrow MH^* + OH^-$ (Volmer step) (Eq.5)

$MH^* + H_2O + e^- \rightarrow H_2 + OH^- + M$ (Heyrovsky step) (Eq.6)

$2MH^* \rightarrow H_2 + 2M$ (Tafel step) (Eq.7)

The catalytic activity of the HER is predominantly governed by a volcano relation, correlating the high exchange current density with hydrogen adsorption-free energy close to zero [19, 20]. The reaction rate of the HER is intricately connected to the chemisorption of atomic hydrogen (H*). The chemisorption energy of H* varies across different electrocatalytic surfaces, showcasing the well-established volcano relationship concerning the reaction kinetics of the HER (**Figure 3**). This phenomenon is rationalized by the Sabatier principle: excessive binding strength between H* and the electrocatalyst stabilizes H*, hindering the subsequent elemental steps [21, 22]. On the contrary, overly weak binding limits the Volmer step rate, impeding effective electron transfer between the electrode and H*. As mentioned above, an outstanding alkaline HER electrocatalyst should meet several key parameters: appropriate H-binding energy, effective H_2O-adsorption, low H_2O-dissociation barrier and suitable OH-adsorption energy [23, 24]. As inferred from the volcano plots, platinum (Pt) demonstrates a moderate binding energy with H* (equivalent to a Gibbs' free energy, $\Delta GH^* \approx 0$) and serves as the reference point in HER investigations [25, 26]. However, being a precious metal, Pt faces constraints in terms of Earth's limited reserves. To advance the practical implementation of electrochemical H_2 generation, the ongoing exploration and refinement of efficient HER electrocatalysts composed of nonprecious metals assume paramount significance.

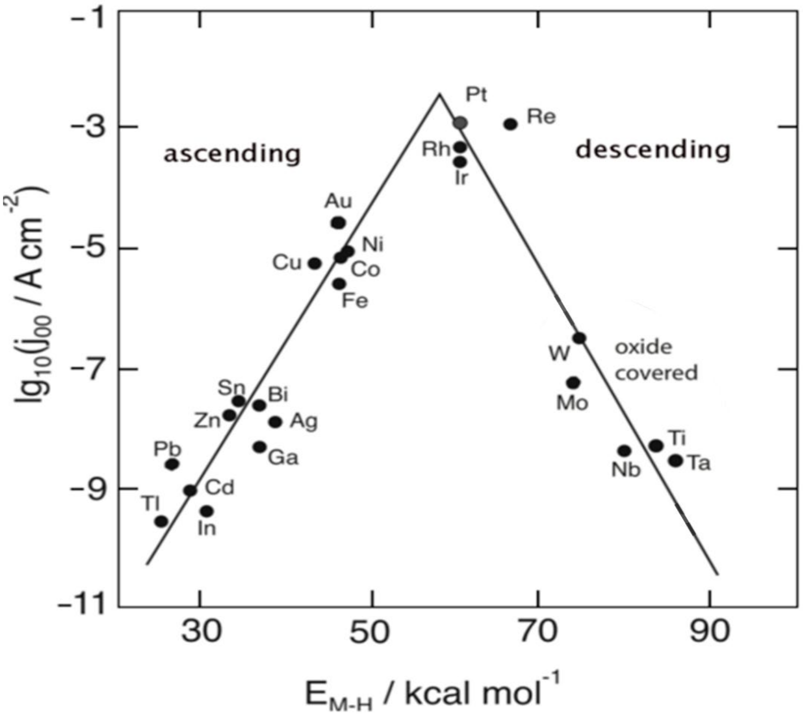

Figure 3. Catalyst activity for the HER presented as a volcano plot, depicting the connection between hydride formation energy ($E_{M–H}$) and current density [27].

I.1.3 OER mechanism

The OER is considered the bottleneck of water splitting because it requires a much larger overpotential than the HER to reach the same production rate [28]. The OER typically involves four proton/electron-coupled processes under alkaline conditions, with hydroxyl groups tending to combine to form oxygen and water molecules. There are different adsorption and desorption energies of reactants, products, and various reaction intermediates, such as O*, HO*, and HOO*, leading to complexity of OER mechanism (**Figure 4a**) [29]. As illustrated in **Figure 4b**, the OER elementary step, characterized by the largest free-energy change, is named the potential-determining step (PDS), also called as the thermodynamic bottleneck. The free energy span from the intermediate with the smallest free energy to the transition state with the highest free energy is the rate-determining step (RDS), recognized as the kinetic bottleneck [30-32]. It is noteworthy that the design of OER catalytic materials should be rooted in the thermodynamic consideration of binding energy, specifically related to the PDS. The OER steps involve the formation of oxygenated intermediates in most catalytic systems, such as O* or HOO* intermediates. Thus, the binding energy between oxygen-containing intermediates and the active sites is the key to determining the performance of the catalysts [33].

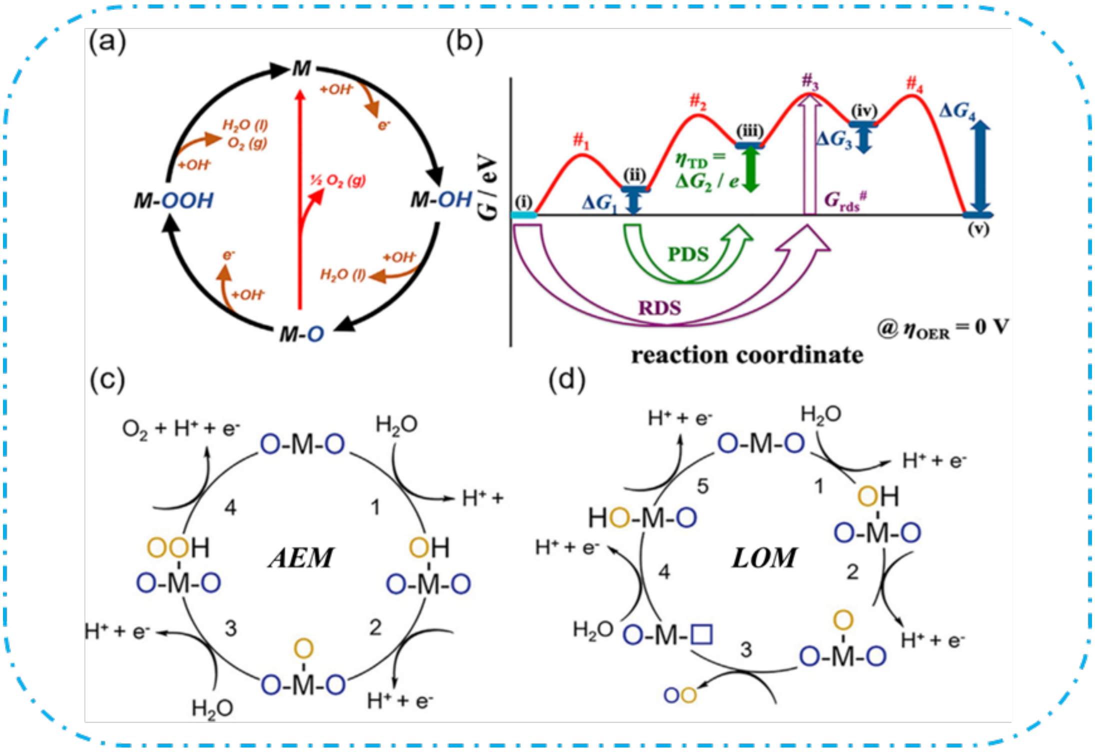

Figure 4. OER mechanism. (**a**) The OER mechanism for alkaline condition. (**b**) Concept of the thermodynamic overpotential. Two typical OER mechanisms. (**c**) AEM and (**d**) LOM mechanism [33].

Currently, several OER mechanisms have been reported and extensively discussed in the existing literature, which can be divided in two traditional types: adsorbate oxygen evolution mechanism (AEM) and lattice oxygen mechanism (LOM). The AEM is a general mechanism for OER catalysts, while LOM usually is adapted to highly covalent oxides [34]. In the AEM process, it is believed that the metal centre is the only active site for OER reaction. Thus, the strength of the adsorption energy between the OER intermediates and the active sites is the key to determining the catalytic activity, such as the current density, gTD, etc [35]. The AEM reaction process includes four consecutive proton–electron transfer steps as described in **(Eq. 8–11)**. Initially, a hydroxyl radical ($OH^{\bullet}$) is adsorbed onto the metal active site (M*) to form M*OH through one-electron oxidation. Subsequently, a coupled proton and electron are removed from M*OH to produce M*O. The succeeding O–O bond formation step is typically regarded as the rate-determining step for most catalysts. In this step, M*O reacts with another OH• to yield M*OOH. Finally, O_2 evolves through deprotonation with OH•, and the free active site is regenerated [20, 35-37]. The free energies associated with the above four steps are shown in $\Delta G_{1–4}$ and are calculated under standard conditions (pH = 0, T = 298.15 K) with zero applied potential (U = 0), which reflects the intrinsic feature of the electrocatalyst. The most excellent equilibrium free energy among ΔG°1–4 is denoted as ΔG_{OER} (**Eq. 12**), utilized to estimate the catalytic performance under the applied potential. The theoretical overpotential is calculated using **(Eq.13)**.

$$OH^- + M^* \rightarrow M^*OH + e^- \quad (\Delta G_1) \qquad (Eq.8)$$

$$M^*OH + OH^- \rightarrow M^*O + H_2O + e^- \quad (\Delta G_2) \qquad (Eq.9)$$

$$M^*O + OH^- \rightarrow M^*OOH + e^- \quad (\Delta G_3) \qquad (Eq.10)$$

$$M^*OOH + OH^- \rightarrow O_2 + * + H_2O + e^- \quad (\Delta G_4) \qquad (Eq.11)$$

$$G^{OER} = MAX\ [\Delta G_1, \Delta G_2, \Delta G_3, \Delta G_4,], (U = 0) \qquad (Eq.12)$$

$$\eta^{OER} = \frac{GOER}{e} - 1.23\ V \qquad (Eq.13)$$

In addition to AEM, the LOM (Lattice Oxygen Mechanism) has been widely recognized and established in recent years [38, 39], and the significant difference feature is that lattice oxygen instead of metals can also play a significant role in the OER process. As shown in **Figure 4d**, O_L and V_O represent lattice oxygen and surface oxygen vacancies, respectively. A crucial step in the LOM is the formation of oxygen vacancies, which triggers the degradation process (e.g., detachment of metal ions), ultimately resulting in the instability of the catalysts [40-47]. This aspect has been identified as the primary reason for the poor long-term stability of OER electrocatalysts [39]. Overall, the primary distinction between AEM and LOM depends on the O-O step couple method. The LOM process displays the faster reaction kinetics, because that lattice oxygen could effectively couple with the oxidation intermediates [48]. However, in the actual OER process, both mechanisms often coexist and compete. The covalent state of the metal–oxygen bond (M-O) has a particular influence on the catalytic reaction mechanism, with the LOM mechanism tending to prevail as the covalence of the metal–oxygen bond (M-O) increases [49]. Although the OER activity of LOM demonstrates better performance than that of AEM, it is often accompanied by metal dissolution and structural instability after a stability test [50]. Therefore, balancing their relationship is conducive to developing efficient and stable catalysts [51].

$$OH^- + * \rightarrow *OH + H_2O + e^- \qquad \text{(Eq.14)}$$

$$OH^- + *OH \rightarrow O* + H_2O + e^- \qquad \text{(Eq.15)}$$

$$O* + O_L \rightarrow O_2 + V_O \qquad \text{(Eq.16)}$$

$$OH^- + V_O \rightarrow *OH + e^- \qquad \text{(Eq.17)}$$

$$H* + OH^- \rightarrow * + H_2O + e^- \qquad \text{(Eq.18)}$$

I.2 Transition metal catalysts

To achieve the electrolysis of water at a large current density, the self-supported electrocatalyst should possess multiple features [52]: (i) The raw materials for electrocatalysts should be abundant on Earth and economically viable to meet the demands of industrial production; (ii) The preparation temperature of the electrode should not be excessively high, aiming to minimize energy consumption and cost; (iii) The electrocatalyst should exhibit excellent intrinsic activity; (iv) The morphology and microstructure should be tailored to facilitate effective contact with reactants, ensuring satisfactory wettability. This aids in accelerating the detachment of gas bubbles from the electrode surface while promoting charge and ion transfer in the external circuit; (v) Strong adhesion between the current collectors and electrocatalysts is crucial to prevent the peeling of the electrocatalytic active phase from the current collector, especially under high current density conditions; (vi) The electrocatalyst should demonstrate robust, long-term durability against corrosion at high current density, particularly in the presence of strong oxidizing processes. Notably, transition metal compounds have been widely used in electrochemical water splitting as one of the bifunctional catalysts, owing to their low cost, earth-abundance, suitable chemical properties and stable structure. In this section, we provide a detailed discussion on various types of transition metal compounds, primarily encompassing transition metal oxides (TMOs), transition metal sulfides (TMSs), transition metal carbides (TMCs), transition metal nitrides (TMNs) and transition metal phosphates (TMPs) [53, 54].

Figure 5. Self-supported transition metal-based electrocatalysts, including oxides, (oxy)hydroxides, sulfides, phosphides, nitrides, alloys and their composites in energy conversion applications [52].

I.2.1 Transition metal oxides (TMOs)

Transition metal-based oxides (TMOs) have garnered significant attention in electrocatalysis field due to their cost-effectiveness, strong reversibility, diversity of composition and structure, and high durability in alkaline solutions [29]. Efficient oxide-based OER electrocatalysts can be effectively fabricated by controlling the morphology and composition, tuning the electronic structure through external metal doping, and integrating hybrid structures into composites [55]. Notably, single metal oxides (mainly Co, Ni, and Mn oxides), spinel oxides (AB_2O_4), and perovskite oxides

(ABO_3) are the main types in TMOs, which have attracted extensive interest for the water electrolysis [56, 57].

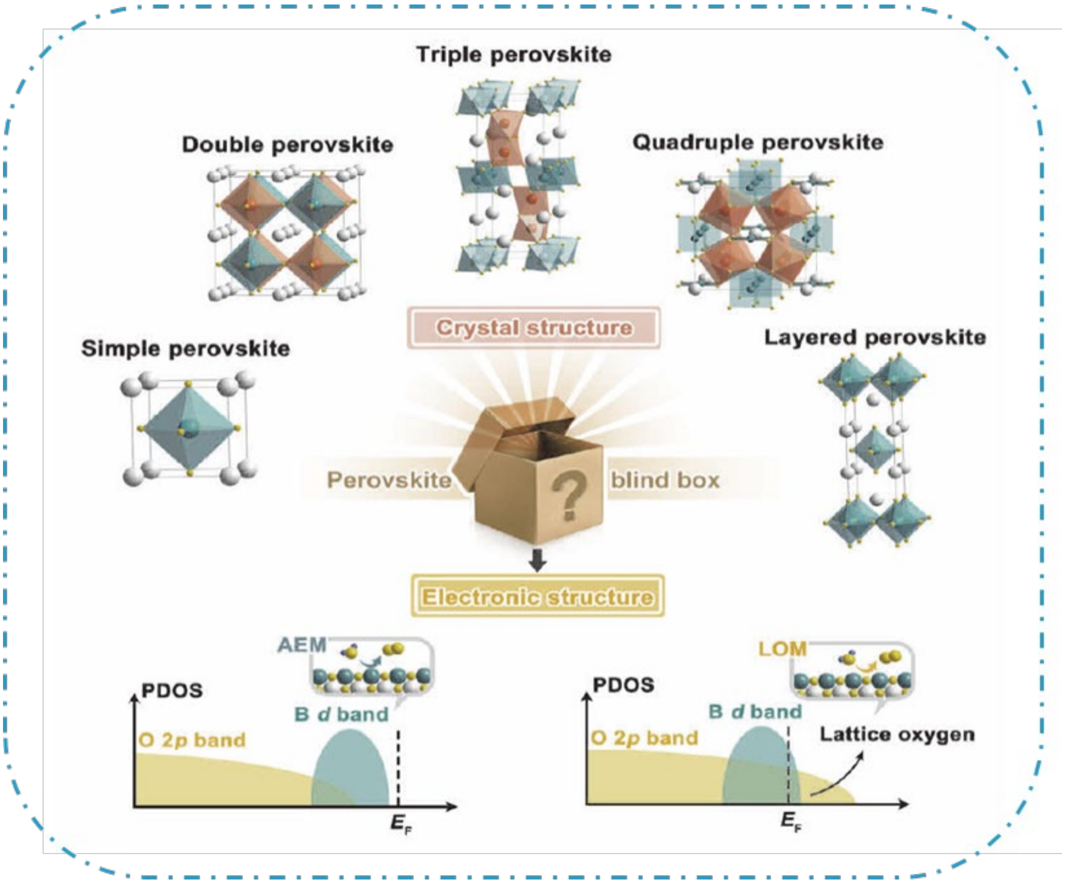

Figure 6. Schematic illustration of the significant regulation of perovskite oxide structural on OER process [58].

The OER activities of single transition-metal-based oxide electrocatalysts rely on the metal type, metal oxidation state, morphology, and substrate. Wen et al.[59] constructed nanosheet arrays of single-phase Co_3O_4/NiO nanocomposites on carbon cloth, which can be finely tuned via changing the Ni^{2+}/Co^{2+} ratio in the electrodeposition solution. As bimetallic oxides for the OER, the most studied spinel oxides, including MCo_2O_4 and MFe_2O_4 (M represents other transition metals), tend to exhibit better OER electrochemical performance than single metal oxide catalysts, owing to high charge transfer efficiency and high stability in harsh alkaline media. Representatively, Chen et al. reported a Co-Ni-Fe spinel oxide-carbonitride hybrid ($CoNiFeO_x$-NC) electrocatalyst with hierarchical structure through a unique ion-exchange based strategy, and displayed a low overpotential of 265 mV at 50 mA cm^{-2}

and a decent Tafel slope of 64.1 mV dec^{-1} [60]. Nakamura et al. found that spinel Co_2MnO_4 showed ultra-long lifetime over 2 months (1,500 hours) at 200 mA cm^{-2} even under acidic condition (pH=1) [61]. Perovskite oxides are characterized by the chemical formula ABO_3, where A represents a rare-earth or alkaline-earth metal, and B denotes a transition metal. In principle, perovskite oxides can manifest as $A^{2+}B^{4+}O_3$, $A^{3+}B^{3+}O_3$, or other variations [58]. Leveraging their highly adjustable metal combination and composition, distinctive 3d electronic structures, and exceptional stability, perovskite oxides demonstrate remarkable catalytic activities for the oxygen evolution reaction (OER). Huang et at.[62] proposed double perovskite $LaFe_xNi_{1-x}O_3$(LFNO) nanorods, exhibiting highly active and stable performance with a low overpotential of 302 mV at 10 mA cm^{-2}.

I.2.2 Transition metal hydroxides (TMHs)

Layered Double Hydroxides (LDHs) are typical 2D-layered materials belonging to the family of anionic clays or hydrotalcite-like compounds [60, 63-68]. They were initially characterized by Allmann and Taylor through the utilization of single-crystal X-ray diffraction technique. Generally, transition metal hydroxides (TMHs), composed of transition metal cations (such as M^{2+} and M^{3+}) and OH^-, have attracted great attention, owing to their abundance on the earth, special 2D-layered structure and abundant active sites. M^{2+} are divalent cations (e.g., Co^{2+}, Ni^{2+}, Zn^{2+}, Ca^{2+}, Mn^{2+}, Fe^{2+}, and Mg^{2+}) that are octahedrally coordinated to six OH hydroxyl groups and can be substituted by trivalent cations M^{3+} (e.g., Al^{3+}, Ga^{3+} Fe^{3+}, Ti^{3+}, Cr^{3+}, In^{3+}) in the brucite-like $M^{2+}(OH)_2$ layer [69, 70].

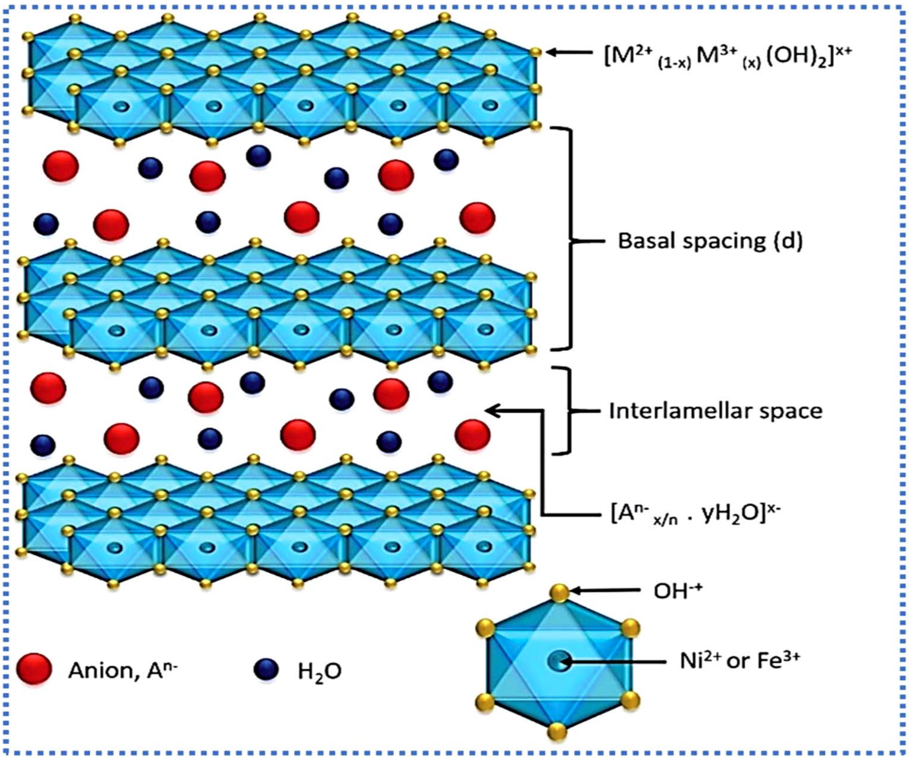

Figure 7. The structure of the NiFe-layered double hydroxide [71].

Although different LDH-based catalysts, such as carbon/LDHs, cobalt–manganese LDH, cobalt–iron LDH, iron/aluminum LDHs, and nickel/iron-based LDHs have shown good performance in energy storage and energy conversion applications, NiFe LDH-based materials have attracted the most significant attention of the researchers, owing to their excellent intrinsic activity as well as high catalytic durability. For example, Jia et al.[72] reported NiFe LDH@graphene material that exhibited high HER performance in an alkaline solution with an overpotential of 115 mV at a current density of 20 mA cm^{-2}, which can be attributed to the synergetic effects between highly exposed 3d transition metal atoms and carbon defects. Markovic et al. established the trends in the activity of different types of 3d transition metal (oxy)hydroxides, which OER activities were determined to be in the order Ni > Co > Fe > Mn [73]. Therefore, the LDH system with multiple metal atoms has been deeply explored. For example, Yang et al. prepared $Co_{1.98}$-NiFe LDH *via* the solvothermal method with controlled crystalline-amorphous interfacial site of the material. The material showed a low overpotential of 236 mV to achieve 20 mA cm^{-2} [74]. In addition, NiFeW LDH [75], MoNiFe LDH [76], CuO@CoNi LDH [67], Co_3O_4@NiCo LDH [77], NiFeZn LDH

[78] and NiMnCr LDH [79] systems have also been studied, further illustrating the variability and excellent performance of the LDH structure.

I.2.3 Transition metal sulfides (TMSs)

Transition metal sulfides (TMSs) are widely used in the field of electrocatalysis due to their special electronic structure and rich element composition. Among these compounds, MoS_2 has been the most extensively investigated material owing to its unique structural and electronic properties. Notably, both experimental and theoretical research studies have revealed that the electrocatalytic activity of bulk MoS_2 is inherently poor and highly dependent on the exposure of edge sites. Therefore, many research works focused on modification of MoS_2 to boost the HER electrocatalytic activity. For example, Tal et al.[80] fabricated an efficient and stable MoS_2-Ti_3C_2 MXene electrocatalyst *via* one-step hydrothermal method, in which the few-layers thick, edge-oriented, high-percentage 1T - phase (~ 85.0 %) MoS_2 nanosheets were well grown on the cation-modified Ti_3C_2 MXene. The as-synthesized MoS_2-Ti_3C_2 MXene exhibited remarkable electrocatalytic HER performance in acidic medium with a low overpotential of 98 mV at 10 mA cm^{-2}, a depressed Tafel slope of 45 mV dec^{-1} and a low electrochemical resistance. Meanwhile, it is well-known that the heterojunction structures combined with MoS_2 to improve the electrocatalytic activity is an effective method. In this line, Liu et al. applied an interface engineering strategy to construct efficient bifunctional electrocatalysts based on (Ni, Fe)S_2@MoS_2 heterostructures, which exhibited remarkable electrochemical activity and durability under alkaline condition, with a low overpotential of 130 mV for HER and 270 mV for OER to deliver a current density of 10 mA cm^{-2} [81].

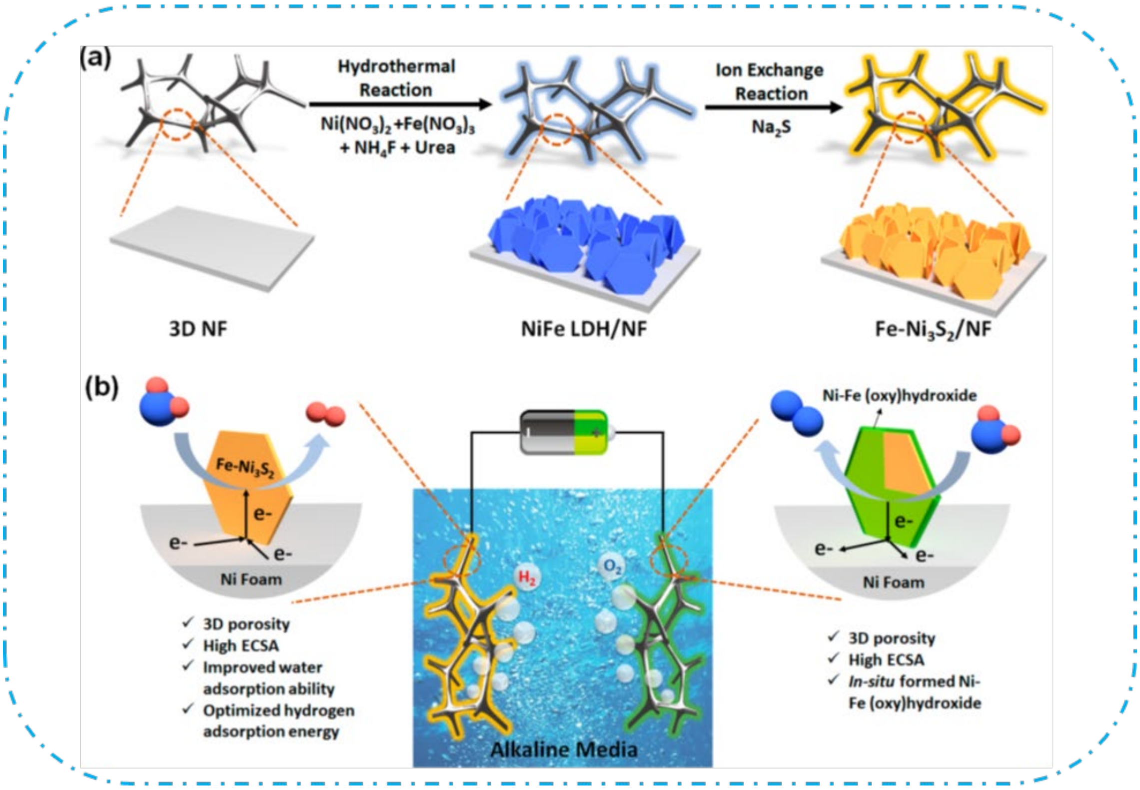

Figure 8. (**a**) Schematic illustration of the fabrication of Fe-Ni_3S_2/NF. (**b**) Two-electrode configuration of Fe-Ni_3S_2/NF for overall water splitting in alkaline media [82].

It is well-known that most TMSs especially MoS_2 display excellent HER performance, but poor OER activity. Therefore, in order to balance HER and OER performance for overall water splitting, a common approach involves the hybridization of 3d transition metal sulfides with oxides and hydroxides, which has been widely adopted to construct novel bifunctional transition metal phosphates (TMPs)-based electrocatalysts. In this regard, Cao's group developed a free-standing electrocatalyst in the form of vertically oriented Fe-doped Ni_3S_2 nanosheet array grown on three-dimensional (3D) Ni foam (Fe-Ni_3S_2/NF), and presented a high activity and durability for both HER and OER with a low cell voltage (1.54 V @ 10 mA cm^{-2}) for overall splitting water [82].

I.2.4 Transition metal phosphides (TMPs)

Transition metal phosphides (TMPs) have gained wide attention as water splitting catalysts especially for HER process in alkaline electrolyte, due to the phosphides doping active sites with a strong ability of attracting protons and outstanding conductivity. In addition, some reports demonstrated that the isotropic structures with more active harmoniously unsaturated surface atoms could be formed on TMPs, which could be applied at large current densities. Therefore, the conductive substrate not only could be favorable to grow plenty of active sites and enhance surface area, but also improve the charge transporting rates of the electrode.

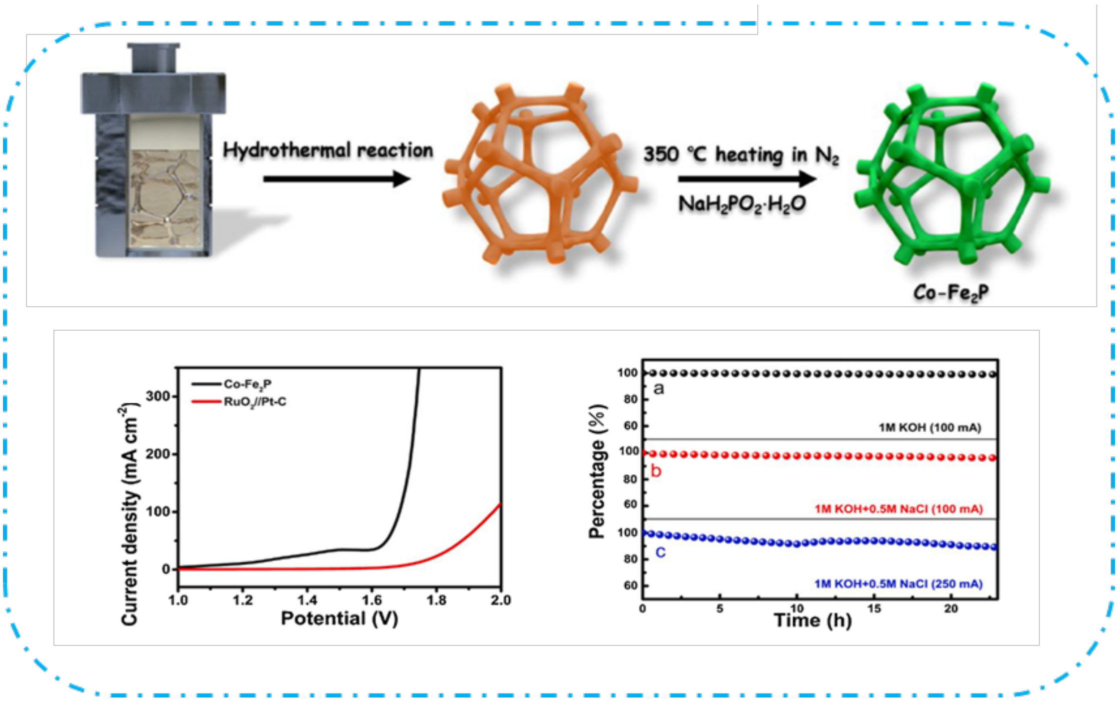

Figure 9. The synthesis process of Co-Fe_2P electrocatalyst [83].

For the preparation of the TMP-based catalysts, transition metal oxide/hydroxide-based precursors are normally first *in-situ* prepared on the 3D conductive substrate *via* electrodeposition or hydrothermal method. Subsequently, the precursors can undergo transformation into the corresponding transition metal phosphates (TMPs) through topological phosphorylation at a specific temperature, utilizing NaH_2PO_2 as the phosphorus source. In addition, direct phosphorization of the available metal substrate was also developed by sintering or solvothermal technique, which could avoid the complicated precursor synthesis. Representatively, Wang et al. fabricated three-dimensional structure metal phosphide electrocatalyst by depositing cobalt-doped Fe_2P (Co-Fe_2P) on Ni foam as an efficient bifunctional electrocatalyst achieving efficiently seawater electrolysis (1.69 V at 100 mA cm^{-2}). Density functional theory calculations further proved that its excellent hydrogen evolution reaction (HER) was ascribed to its suitable H* adsorption after phosphide doping [83]. Jiang et al. reported a phosphorus-doped carbon@MoP electrocatalyst *via* hydrothermal and electrochemical surface restructuring method, which endows the catalyst with excellent activity in terms of the HER in both acidic and alkaline environments (current density of 10 mA cm^{-2} at low overpotentials of 68 mV in 0.5 M H_2SO_4 and 67 mV in 1.0 M KOH) [84].

1.2.5 Transition metal nitrides (TMNs)

Transition metal nitrides (TMNs) exhibit diverse properties, which is conducive to regulating electronic structure, adsorption energy, and conducting capabilities. This versatility allows them to achieve effectively electrocatalytic activity and stability. The introduction of nitrogen (N) atoms serves a dual purpose, which not only modifies the d-band electron state density of the corresponding metal, but also mitigates the d-band occupation shortages. For example, Jiang et al.[85] proposed a unique nano-porous hierarchical structure of N-doped carbon (Fe_3C-Co/NC) *via* a facile template-removal method, which demonstrated prominent OER performance with an overpotential of 340 mV at 10 mA cm^{-2}. Fan et al. prepared 3D hierarchical porous nickel molybdenum nitride (NiMoN) on carbon cloth for HER electrocatalysis application, and exhibited outstanding HER performance with a small overpotential of around 109 mV to acquire a current density of 10 mA cm^{-2} with an outstanding durability [86]. Zhou et al. developed an inexpensive N-doped carbon-coated porous Ni_3Mo_3N microrods (NC/Ni_3Mo_3N/NF) electrocatalyst using a hydrothermal reaction and subsequent nitriding process. Ni_3Mo_3N electrocatalyst possessed various HER catalytic active sites with suitable ΔGH^* values (more than ten sites) due to the metallic semiconductor nature with special electronic structure, displaying efficient catalytic activity (136 mV at 100 mA cm^{-2}) for hydrogen evolution reaction [87].

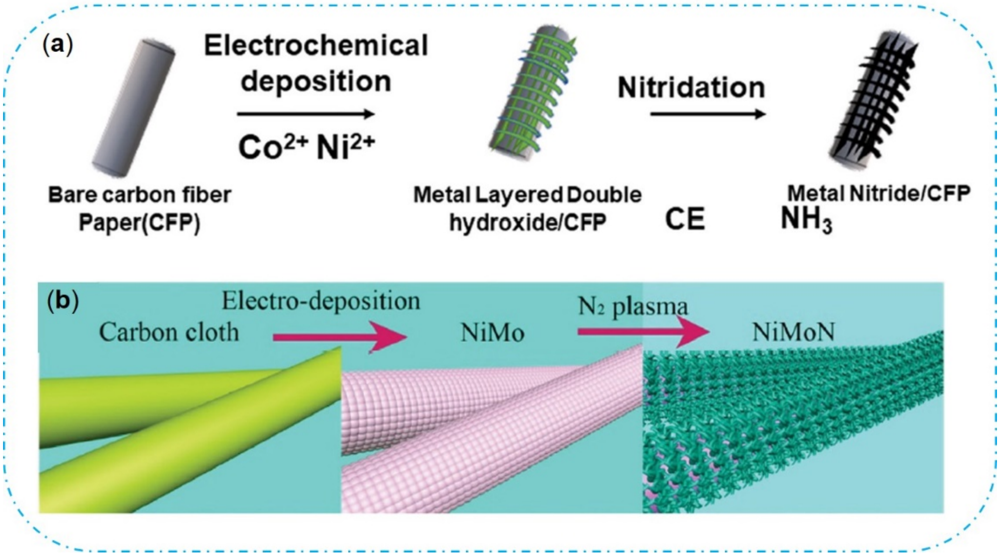

Figure10. Schematic representations of synthesis route of (**a**) $NiCo_2N$ [88] and (**b**) 3D hierarchical porous NiMoN [86].

I.2.6 Transition metal carbides (TMCs)

Transition metal carbides (TMCs) exhibit high catalytic activity and superior stability for the HER. However, their platinum-like HER catalytic performance is significantly impeded by their strong interaction with hydrogen. The d-orbitals of the metal hybridize with the s/p-orbitals of carbon, resulting in a broadened d-orbital of the metal in TMCs, imparting characteristics reminiscent of platinum. The electronic structure of the metal within TMCs requires optimization to further enhance the HER activity of TMCs. Additionally, DFT calculations have confirmed that the introduction of functional transition metal atoms (e.g., Ni, Co, Fe) significantly influences the enrichment of electrons on the metal sites. This results in a downshift of the center of the d-band and weakened H-binding, contributing to the activation of TMCs. For example, Li's group [89] introduced adsorbed nickel atoms on the TMC surface to construct Ni/TMC(M = V, Fe, Cr, and Mo), which recorded excellent HER performance with overpotentials of 128 and 93 mV at 10 mA cm^{-2} of the Ni/vanadium carbide (VC) and Ni/Fe_3C catalysts, respectively. In addition, W_2C and Mo_2C have gained extensive attention [90, 91]. Tang et al. developed a three-dimensional porous Ru/α-MoC, exhibiting excellent alkaline HER activity with a low overpotential of 25 mV at 10 mA cm^{-2}, outperforming commercial 20% Pt/C (45 mV), and robust electrocatalytic stability at an industrial-scale current density of 400 mA cm^{-2} [92]. Feng et al. prepared nitrogen-doped porous carbon nanosheets (Mo_2C@2D-NPCs) exhibiting a low overpotential of ~45 mV at a current density of 10 mA cm^{-2} and Tafel slope of 46 mV. The exceptional HER activity was ascribed to the abundant Mo_2C/NPC heterostructures, the synergistic contribution of nitrogen doping, the outstanding conductivity of graphene, and the abundance of active sites at the heterostructures [93]. Similarly, the purpose of promoting electron transfer and improving catalytic performance is achieved by atomic doping of the catalyst. Li et al.[94] doped Co element into Ni_3C/C material; compared with pure Ni_3C, the doped composite material showed more obvious electrochemical performance.

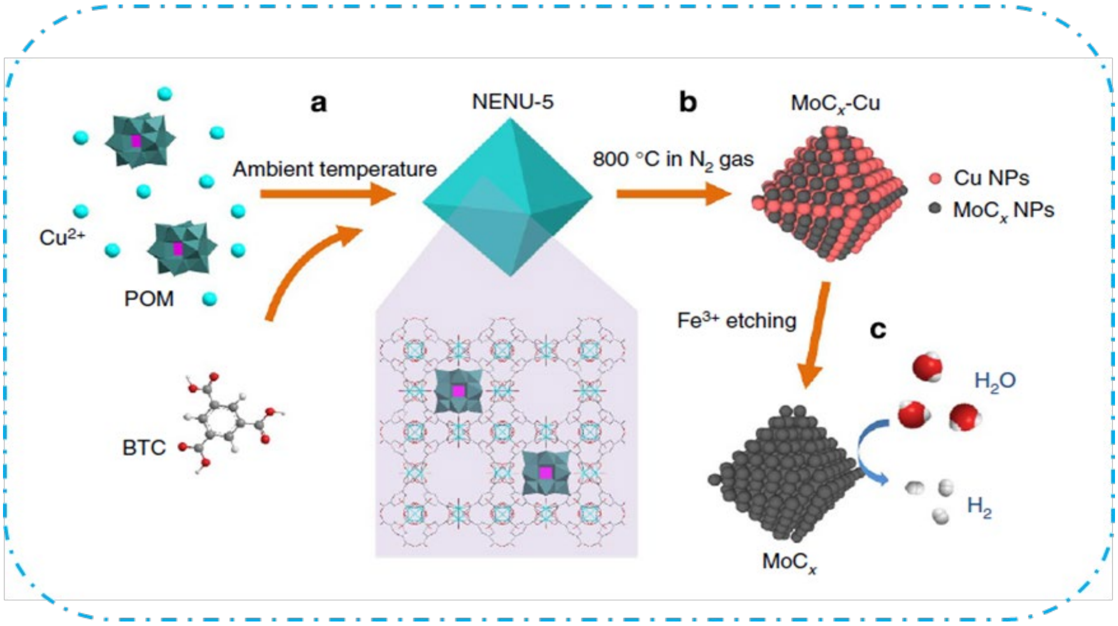

Figure 11. Schematic illustration of the synthesis procedure for porous MoC_x nano-octahedrons [91].

I.3 Synthetic methods of transition metal catalysts

I.3.1 Hydrothermal/solvothermal methods

Hydro/solvothermal methods represent typical synthetic strategies for preparing diverse inorganic catalytic materials, including metal oxides and hydroxides/oxides, under moderate temperatures and high-pressure conditions in a closed reaction vessel. In this approach, surface defects of the substrate material can serve as “reactors” for the formation and growth of nanostructured materials. Specifically, the two key-step nucleation and subsequent growth process of crystals was achieved by controlling parameters, such as temperature, pH, reactant concentration, and additives. Therefore, the catalysts obtained by this method generally possessed good crystallinity and controlled morphology (such as nanoparticles, nanosheets, nanowire array and nanoflower structures).

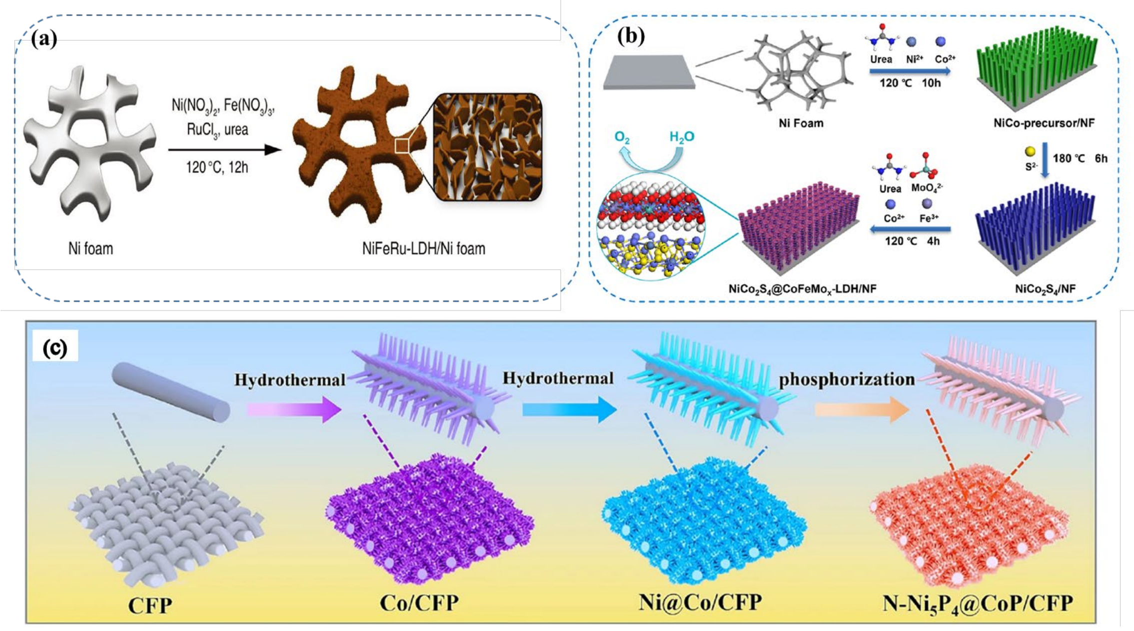

Figure 12. Schematic illustration of the synthesis process through hydrothermal method for (**a**) the NiFeRu-LDH on the Ni foam, (**b**) $NiCo_2S_4$@$CoFeMo_x$-LDH/NF and (**c**) N-Ni_5P_4@CoP [95-97].

Chen et al.[96] fabricated Ru-doped NiFe-LDH catalyst at 120 °C for 12 h *via* a one-pot hydrothermal reaction, which could tailor the water dissociation active sites on NiFe-LDH by partially substituting Fe centers with Ru dopants. Remarkably, the resultant NiFeRu-LDH exhibited excellent HER activity with an overpotential as low as 29 mV at a current density of 10 mA cm^{-2} and a substantially decreased Tafel slope of 31 mV dec^{-1} in a 1 M KOH aqueous solution. In addition, the strategy of combining hydrothermal and vulcanization methods has attracted more and more attention. Feng's group focused on self-supported hierarchical $NiCo_2S_4$ via a typical two step preparation process, in which Ni-Co carbonate hydroxide nanowires were firstly *in situ* grown on nickel foam at 120 °C through a hydrothermal method, and then applied anion-exchange reaction at 180 °C to obtain $NiCo_2S_4$ [97]. Ren's group reported the preparation of a novel FeS_2/Fe–Ni_3S_2 heterostructure material on Ni foam *via* a simple one-step *in situ* hydrothermal vulcanization using F− regulation engineering [98]. In addition, the method combining the hydrothermal method and phosphating approach is widely used by researchers to fabricate N-Ni_5P_4@CoP catalysts on the carbon fiber paper (CFP) *via* a coupling strategy involving the hydrothermal synthesis and subsequent phosphorization treatment [95]. Solvothermal methods offer more possibilities for reactions on complex substrates. Gao et al. developed a novel solvent-thermal strategy to prepare hierarchical nickel–iron–cobalt LDH nanosheets/carbon fibers (NiFeCoLDH/CF), by sacrificing ZIF-67 grown on carbon fiber (ZIF-67/CF) as the cobalt source and surfactant-like and *in situ* coprecipitating multimetal cations [99]. Ma's group synthesized CoS_2/CoS heterojunction nanoparticles *in situ* on graphite felt by a one-step solvothermal process, which can significantly boost electrocatalytic activities of I^-/I_3^- and S^{2-}/S_x^{2-} redox reactions by improving absorptivity of charged ions and promoting charge transfer [100].

I.3.2 Electrodeposition method

Electrodeposition presents another standard synthesis method for growing self-supported nanoarrays/nanosheets on different substrates. In this approach, nanostructured arrays can be deposited on conductive substrates quickly, owing to the applied electric field promoting the rapid diffusion of precursor ions for deposition. The morphology, element ratio, and thickness of thin films could be adequately regulated by controlling the current or voltage during the electrochemical deposition process. Unlike the challenging conditions involving high temperatures and pressures, electrochemical deposition occurs under close-to-equilibrium conditions, facilitating the formation of non-equilibrium material compositions. The typical electrochemical synthesis techniques include cyclic voltammetry (CV), potentiostatic/galvanostatic deposition, pulse deposition, and electrophoretic deposition (EPD) [54].

Cyclic voltametric electrodeposition:

In addition to the traditional electrochemical techniques used to detect electrochemical redox activity, CV, as a electrochemical synthetic method, possesses three main advantages [101]: (i) it allows the determination of the initial potential of the electrodeposition reaction, (ii) the potential linear scanning is beneficial to the growth of uniform active sites and conformal thin films, (iii) it is well-suited for the synthesis of multivalent materials, such as transition metal oxides.

Potentiostatic/Galvanostatic deposition:

According to the difference in the applied potential and thermodynamic equilibrium potential, potentiostatic deposition technology can be divided into underpotential deposition (UPD) and overpotential deposition (OPD) types via applying a constant voltage between the positive and the negative electrodes [102]. Galvanostatic deposition involves the electrodeposition at a constant current between the positive and negative electrodes of a two-electrode system. The recorded response is the time-dependent voltage of the electrolytic cell in the two-electrode system, i.e., the potential of the working electrode in the three-electrode system.

Pulse electrodeposition:

It involves rapidly alternating potential or current density between two different values. This is achieved through a series of pulses with equal amplitude, duration, and polarity, separated by periodic zero current or open-circuit potential, and each pulse consists of two "ON" and "OFF" times [103]. During the "OFF" period, ions in the electrolyte diffuse into the electric double layers along the surface of the deposited substrates, contributing to the uniform and fine-grained deposition during the "ON" period.

Electrophoretic deposition (EPD):

Electrophoretic deposition (EPD) differs from all the aforementioned techniques in several aspects. First, EPD utilizes suspended charged colloidal particles as charge carriers, not ions. Second, EPD involves electrostatic attraction between the particles and the substrate but does not entail charge transfer. Third, unlike electrodeposition, which relies on electrolytes to conduct ions, EPD can operate in a medium with poor conductivity, such as water [104]. The structure of the deposits can be adjusted by altering parameters, such as applied voltage, particle concentration, and deposition time. It is noteworthy that the stoichiometric ratio of electro-adsorbed particles directly determines the stoichiometric ratio of sediments.

Zhao et al. designed a facile two-step potentiostatic/galvanostatic deposition preparation route to fabricate nanoporous Ni/Cu/NF. Briefly, NiCu alloy particles are prepared by the galvanostatic electrodeposition by applying a current of 100 mA for 600 s in an electrolyte containing $NiSO_4$ and $CuSO_4$. After the deposition, selective dissolution of Cu from the Ni/Cu films was separately conducted at a constant potential of 1.0 V for 400 s with a stirring rate of 1000 rpm at room temperature [105]. Chou's group prepared NiM electrocatalysts by galvanostatic electrodeposition in a standard three-electrode system according to Pourbaix diagram; Ni^{2+} and $M^{\delta+}$ can be reduced to the corresponding metals when the electrode potential is lower than their reduction potential. In addition, the high negative potential electrodeposition process also promotes the construction of a porous structure due to the formation of hydrogen bubbles as soft templates [106]. Catalysts co-prepared through both hydrothermal and electrochemical synthesis methods exhibit morphological characteristics and good activity. Hou et al. applied a multistep process for the formation of a 3D hierarchical NiMoN/NiFe LDH electrocatalyst; firstly, $Ni_{0.2}Mo_{0.8}N$ nanorods arrays were prepared by hydrothermal and calcination process. Subsequently, amorphous NiFe LDH nanosheets were electrodeposited onto the NiMoN nanorods at −1.0V *vs.* Ag/AgCl for 200 s, and exhibited the industrially required current density of 1000 $mAcm^{-2}$ at a lower overpotential of 266 mV for OER [107].

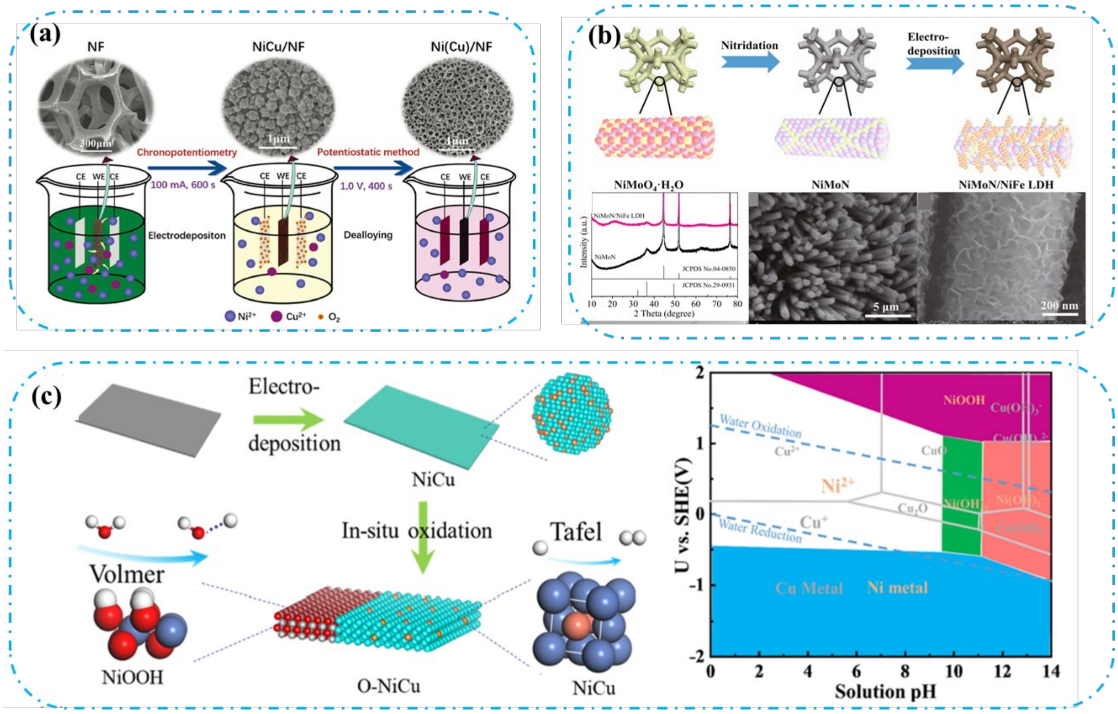

Figure 13. Schematic illustration of the synthesis procedure *via* electrodeposition method of (**a**) NiCu/NF [105], (**b**) NiMoN/NiFe LDH [107], (**c**) O-NiCu [106].

I.3.3 Chemical vapor deposition (CVD)

CVD is a well-established vacuum deposition method, which has emerged as a prominent technique for the preparation of electrocatalysts, offering precise control over the composition, structure, and morphology of the catalytic materials. In this method, a gaseous precursor undergoes chemical reactions at the substrate surface, leading to a thin film or nanostructured material deposition. CVD's versatility allows for the customization of electrocatalysts, enabling researchers to tailor their properties for specific energy conversion and storage applications [13, 108].

I.3.4 Template method

The template-directed synthesis method is a highly effective strategy for constructing highly ordered one-dimensional (1D) nanoarrays, including nanowires, nanotubes, and nanorods. There are many advantages to using template methods to synthesize catalyst materials, such as: (i) effectively controlling morphology and surface structure, (ii) regulating active sites and (iii) the electrochemical applications versatility via this method including batteries, supercapacitors, and electrocatalysts.

This approach can be categorized into two primary methods: hard template and soft template [109, 110]. One variant of the hard template method involves the use of sacrificial templates, often composed of materials that can be selectively removed after the synthesis process. For instance, a sacrificial template made of a polymeric material can be coated or filled with precursor materials. Subsequent removal of the template leaves behind a structured electrode material with a well-defined architecture, such as porous networks, nanowires, or hollow structures [111]. Generally, desired products must exhibit enough stability in HF or NaOH solutions to remove the hard template. For example, Yang et al. fabricated 3D mesoporous Ni_3FeN through KIT-6 as a hard templating and thermal nitridation. In the preparation process, the removal of the KIT-6 template was achieved by washing with a 2 M NaOH solution. Subsequently, nitridation was carried out under an NH_3 atmosphere to obtain the final products [112]. Soft templates lack fixed rigid structures and are formed *in situ* through intermolecular or intramolecular interactions during the reaction process. Small molecule surfactants or block copolymers (BCPs) serve as structure-directing agents (SDAs) and templates. The composite materials undergo transformation into mesoporous materials during the removal of the BCPs through calcination or solvent extraction [113, 114].

I.3.5 Corrosion engineering method

Corrosion engineering method is considered as a novel approach for the fabrication of catalysts. Metal corrosion, especially metals like Ni and Fe, is a common phenomenon in everyday life. Taking iron as an example, its corrosion can be categorized into two types based on reaction types: hydrogen evolution corrosion and oxygen corrosion. When iron substrates come into contact with water and air, they produce iron rust on the surface, posing harm to metal machinery and causing significant economic losses globally. In particular, exposure of metals like iron to seawater accelerates the corrosion rate due to the easy adsorption of chloride ions on the metal surface, damaging the passivation film [115]. Various efforts and research have been undertaken to develop different strategies to protect metals from chloride corrosion. However, in addition to damaging material properties, seawater corrosion technology can also impart useful functions to materials through corrosion engineering. Over the past five years, several studies have been dedicated to constructing 3D catalytic materials using cost-effective corrosion engineering, offering a novel approach to preparing electrode materials.

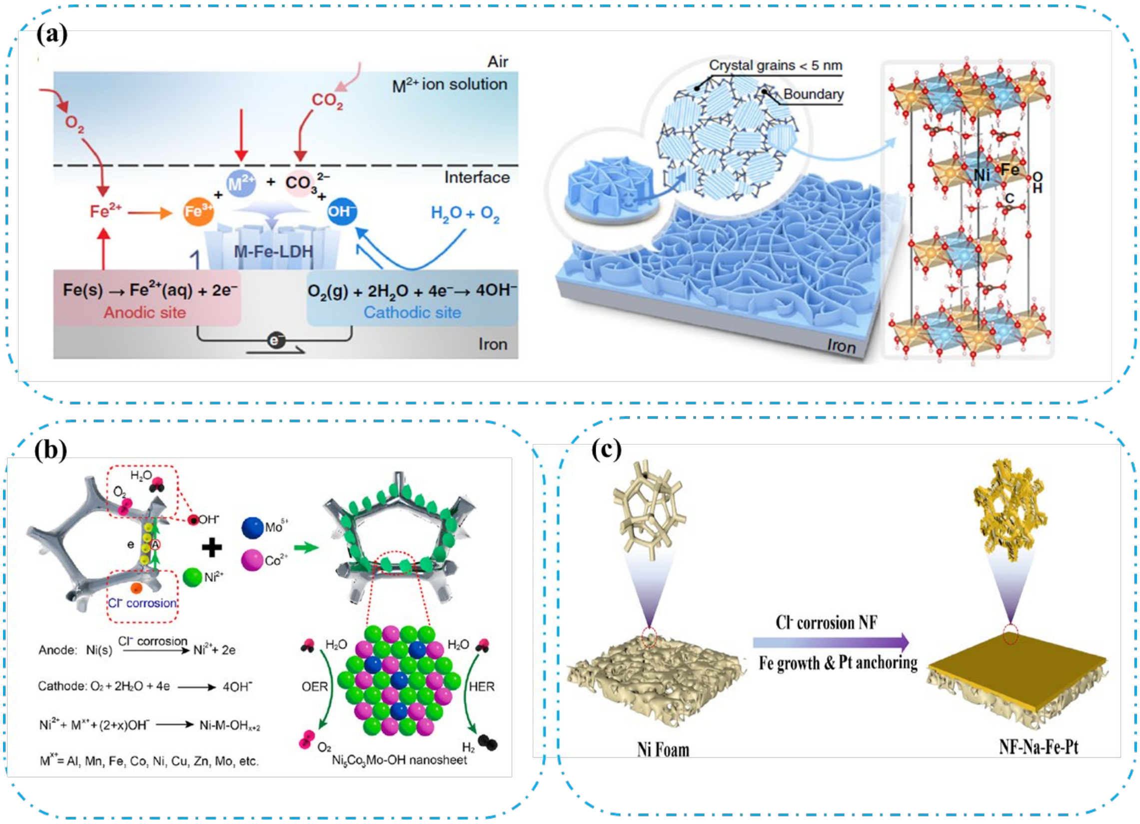

Figure 14. Schematic diagram of the corrosion method to prepare metallic hydroxide/oxides (**a**) M-Fe-LDH, (**b**) Ni_5Co_3Mo–OH, (**c**) NF-Na-Fe-Pt [115-117].

Liu et al. devised a scalable and energy-efficient corrosion engineering method for fabricating electrode materials on cost-effective iron substrates, such as iron plates and iron foam. The crucial aspect contributing to the success of this method is the introduction of suitable divalent cations into the corrosive environment, resulting in the formation of nanosheet array thin films of layered double hydroxides, which exhibited excellent catalytic activity and remarkable stability for the oxygen evolution reaction (OER), lasting for more than 6000 hours (over 8 months) even at high current densities [115]. Furthermore, Wang’s group synthesized NiFe LDH on Fe foams using oxygen corrosion engineering approach, exhibiting good OER performance. They employed a dual chloride aqueous system, labeled as "NaCl-$NiCl_2$," where Cl^- anions acted as accelerators for oxygen corrosion, and Ni^{2+} cations ensured the uniform growth of corrosion layers through chemical plating mechanisms [118]. Zhao et al. designed a corrosion engineering method to synthesize NF-Na-Fe-Pt electrocatalyst. The corrosion engineering approach allows to optimize the balance of hydroxyl ion and atomic hydrogen adsorption, demonstrating a synergistic effect between NiFe-LDH and trace amounts of noble metals. This nanomaterial displayed excellent electrocatalytic performance, requiring only 31 and 261 mV to drive 10 mA cm^{-2} for the HER and OER, respectively [117]. Furthermore, a series of catalysts, including NiCoMo, NiFe-N, and NiCo-Ru, prepared through the corrosion method, have been successively reported, thereby expanding the potential for their widespread industrial applications [116, 119].

I.4 Opportunities and Challenges

I.4.1 Seawater electrolysis

According to the International Energy Agency report, global hydrogen demand is expected to reach 115 million tons (Mt) by 2030, of which 24 Mt will come from water electrolysis [120]. Electrolyzed water technology requires continuous innovation and development to cope with the coming opportunities and challenges. In addition to developing cost-effective and high-performance catalysts, electrolytes are also an important factor to consider. Given freshwater resource shortage accounting for only 2.5 % of the earth's total water resources, it is imperative to substituting freshwater with seawater in future processes [121]. Seawater electrolysis has many advantages [122]. From a financial perspective, the abundance of natural seawater positions it as a nearly cost-neutral feedstock. From geographical perspective, it presents a golden opportunity for countries with extensive desert coastlines, especially those facing freshwater shortages. The integration potential with offshore renewables, such as wind and tidal energy, further broadens its feasibility. However, the complex composition of seawater poses significant challenges (**Figure 15**). Seawater comprises dissolved inorganic salts (Na^+, K^+, Mg^{2+}, Ca^{2+}, Cl^-, SO_4^{2-}, etc.), small organic molecules, microplastics, living organisms, and dissolved gases, all of which have the potential to deactivate catalysts, electrolyzers, or membranes [123, 124].

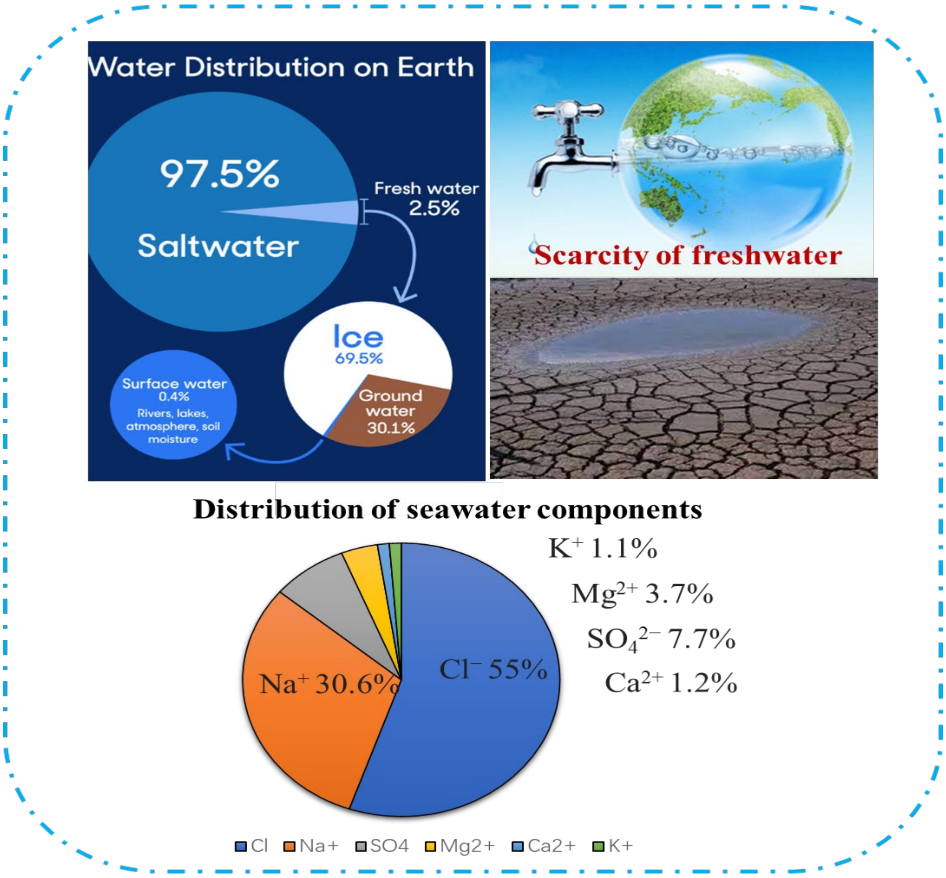

Figure 15. Distribution of water resources on earth.

The presence of these ions initiates multiple undesired reactions and production, as elucidated in **Figure 16**. In the cathode region of seawater electrolysis, with an increase in electrolytic current density, the local pH near the cathode significantly rises compared to that in an unbuffered or slightly buffered medium. When the pH value surpasses 9.5, insoluble and inactive $Ca(OH)_2$ and $Mg(OH)_2$ precipitate, blocking the active sites of electrocatalysts [124, 125]. This phenomenon reduces catalytic activity for the HER. A buffer solution or supporting electrolyte is typically required for the seawater electrolysis system to stabilize the pH value [121, 126, 127]. This involves using suitable electrolysis cells and membranes to separate the precipitate from the cathode.

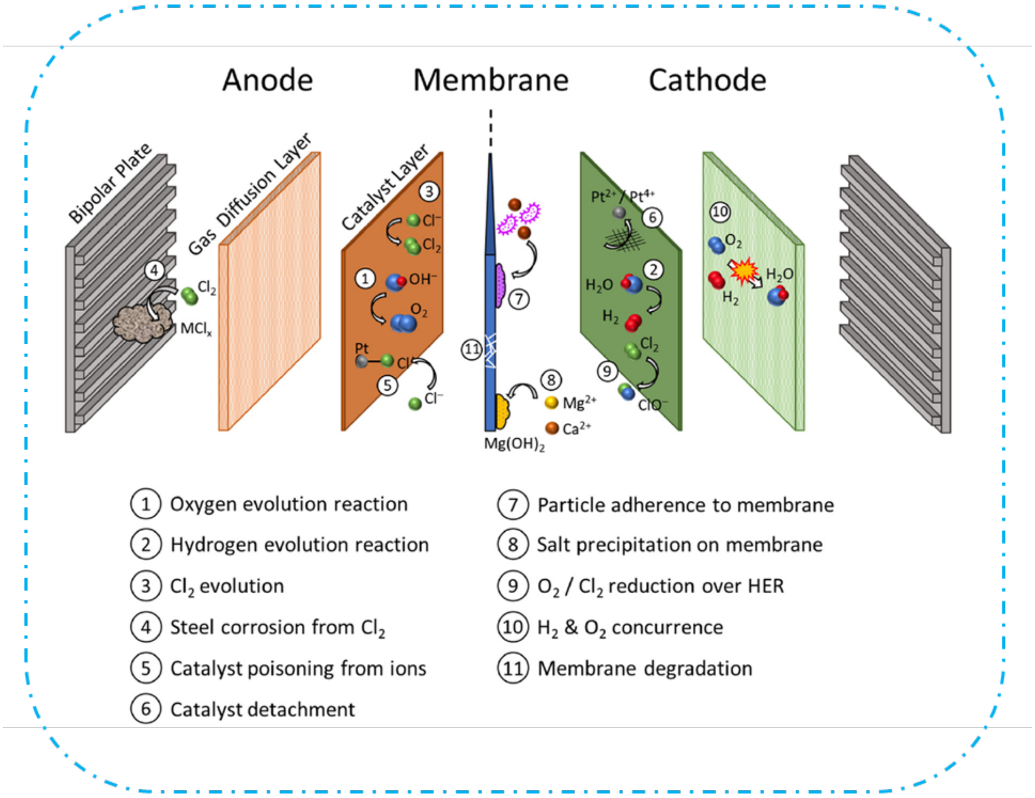

Figure 16. Schematic diagram illustrating H_2 production through direct seawater electrolysis (DSE) in an alkaline electrolyte, emphasizing potential side effects arising from the presence of common ions and substances [123].

For the anode region, the biggest challenge for seawater electrolysis is the presence of high concentration of Cl^- ions, which introduce a competitive dynamic between the OER (E = 1.23 V *vs.* RHE) and the chlorine evolution reaction (CER) [128, 129]. As described in Pourbaix diagram **Figure 17,** it is possible to generate corrosive by-products like Cl_2, HClO, or ClO^- under different pH values, which inevitably cause catalyst poisoning. When the pH exceeds 7.5, the dominant reaction is the formation of hypochlorite, and the standard redox potential of Cl^-/ClO^- is also pH-dependent, exhibiting a similar trend with OER in the Pourbaix diagram [130]. In alkaline conditions, the potential difference between OER and CER reaches a maximum of ≈ 480 mV. In principle, this allows the OER applied potential below 1.71 V (*vs.* RHE), which regarded as seawater "Alkaline Design Standard" [131, 132]. However, to achieve higher current densities required for industrial production, it is inevitable to apply a larger potential, leading to CER side reactions and decreasing production efficiency. In this regard, intensive studies have been undertaken to improve the selectivity toward OER and protect the anode catalysts against corrosion. In this section, we aim to discuss three typical strategies to overcome this challenge.

In acidic medium: $2Cl^- \rightarrow Cl_2 + 2e^-$

In alkaline medium: $Cl^- + 2OH^- \rightarrow ClO^- + H_2O + 2e^-$

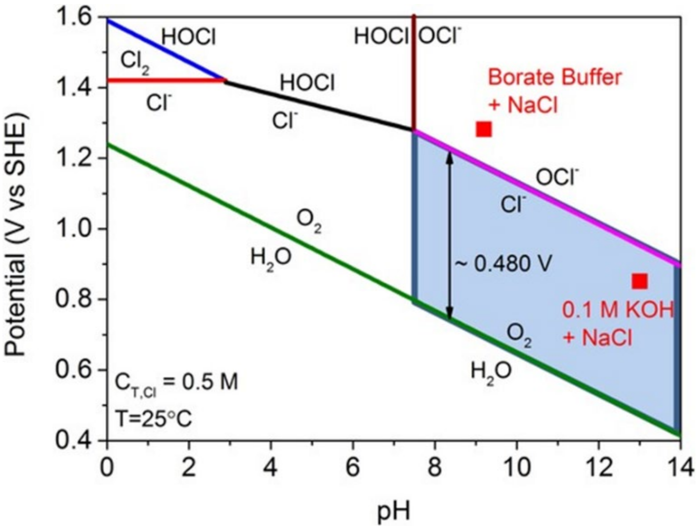

Figure 17. Pourbaix diagram for artificial seawater model [132].

I.4.2 Designing high performance electrocatalysts

To enhance hydrogen production efficient through seawater electrolysis, various approaches have been adopted to overcome the technical barriers associated with the aforementioned challenges. Developing high-performance electrocatalysts and electrodes is an effective strategy to achieve seawater electrolysis at lower overpotentials to obtain higher current densities and avoid unfavorable CER. On the other hand, building a protective layer on the catalyst surface, without affecting its activity, to prevent Cl^- corrosion of active sites or substrate materials has proven to be highly effective [133]. Furthermore, the standards and principles guiding the design of cathodes and anodes may differ due to distinct catalytic challenges. It is crucial to establish design principles for various seawater electrolysis systems, including acidic, alkaline, and neutral seawater. Recently, some research focused on modulating of electronic structure to optimize the adsorption of the intermediates and enhance the ability to anti-poison associated with Mg^{2+}, Ca^{2+}, or Cl^{-} [134, 135]. Other strategies have been developed including corrosion-resistant coatings, localized environment regulation, anionic charge repulsion, and charge repulsion additives [136, 137]. For example, Zhan's group reported NiFe-LDH@$FeNi_2S_4$ heterostructure exhibiting high catalyst performance and stability in seawater, which can be attributed to the presence of S^- species. The sulfate anions can evolve to repel chloride, and the doping of sulfur (S) can enhance the OER catalytic activity by increasing catalytic sites and optimizing the absorption energy [138].

1.4.3 Anode oxidation reaction strategy

Furthermore, large-scale industrial seawater electrolysis is a significant challenge, even using the most advanced OER electrocatalysts. Electrolyzers must meet industrial requirements and operate at high current densities exceeding 500 mA cm^{-2} under low voltage conditions to alleviate CER, while maintaining satisfactory long-term stability [139, 140]. To this end, hybrid SWE offers a promising replacement for the OER strategy with small molecules' anode oxidation reaction (AOR), which could effectively avoid interfering with CER even at high current densities while maintaining energy efficiency and cost-effective H_2 production [141]. The small molecules employed in the AOR can generally be classified into two categories: (1) sacrificial agents generating products of limited economic value, and (2) feedstocks that can be converted into chemicals or fuels of high-added value (**Figure18**) [142]. Specifically, the sacrificial molecules encompass various compounds (urea, hydrazine, sulfions etc.), prevalent environmental pollutants in industrial and domestic wastewater/flue gas [143-145]. Therefore, integrating the AOR of these molecules with the cathode reduction reaction facilitates energy-efficient and highly effective H_2 production and concurrently supports waste treatment efforts, contributing to the mitigation of environmental pollution. In addition, the feedstock-type SMs, including alcohols, aldehydes, and biomass derivatives (furfural, 5-hydroxymethylfurfural (HMF), glucose, etc.), and other substances can be upgraded to highly value-added chemical commodities [146, 147]. Meanwhile, its effectively decreases the potential risk of explosion from the

H_2/O_2 mixture.

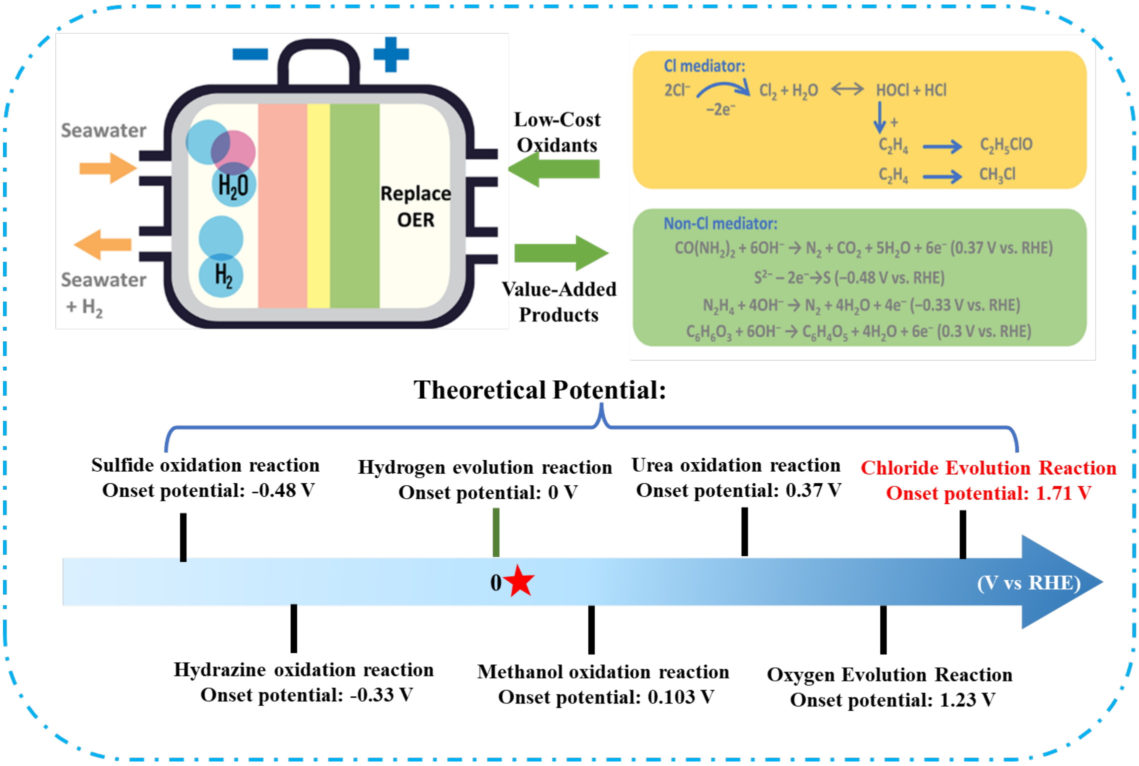

Figure18. Theoretical thermodynamic oxidation potentials of several representative small molecular on seawater electrolysis process [142].

(1) Urea Oxidation Reaction Assisted SWE

Urea is abundant globally, primarily in human/animal urine, agricultural wastewater. Approximately 80% of industrial and domestic wastewater containing urea directly pull into the environment annually, leading to pollution and eutrophication of groundwater, as the decomposition of urea under mild conditions produces ammonia (NH_3) and nitrate with high nitrogen content [148]. Hence, effective management of urea-rich wastewater is crucial for environmental remediation and resource reuse. Electro-oxidation of urea coupled with the HER represents a promising greener approach, which allows to realize wastewater treatment meanwhile generating H_2 in an energy-saving manner, considering that the UOR has a much lower theoretical thermodynamic oxidation potential ($CO(NH_2)_2 + 6OH^- \rightarrow N_2 + 5H_2O + CO_2 + 6e^-$, 0.37 V *versus* RHE) relative to that of the OER and the CER [149, 150]. Yu et al. fabricated a self-supported nickel-iron phosphosulfide (NiFeSP) electrode through a two-step sulfurization/phosphorization approach, which demonstrated good catalytic performance for the UOR. By coupling UOR with HER, the bifunctional NiFeSP electrode pair can efficiently catalyze the overall urea-mediated alkaline-saline water electrolysis at 500 mA cm^{-2} under 1.938 V for 1000 h without notable performance degradation [16]. In addition, Guo et al. fabricated multichannel nanorods of Ru, P dual-doped $NiMoO_4$ *in-situ* grown on nickel foam (Ru/P-$NiMoO_4$@NF), enabling chlorine-free hydrogen production through the coupling of seawater splitting with thermodynamically favorable urea oxidation. The two-electrode electrolyzer, constituting the overall urea splitting system, required a low voltage of 1.73 V to drive 500 mA cm^{-2} and exhibited remarkable durability, maintaining above 100 mA cm^{-2} for 145 h [151].

(2) HzOR Assisted SWE

Hydrazine (N_2H_4), as an abundant industrial raw material, has been widely utilized in the feedwater of power plants, high-energy fuel, synthesis chemistry, and pharmaceutics [152]. As an added agent on seawater electrolysis process, hydrazine oxidation reaction (HzOR, $N_2H_4 + 4OH^- \rightarrow N_2 + 4H_2O + 4e^-$) owns huge advantages, such as lower thermodynamic oxidation potential (−0.33 V *versus* RHE) and faster kinetics (a four-electron-transfer process) (**Figure19**) [153-155]. Significantly, the oxidation of hydrazine is a carbon-free process, devoid of carbon emissions and CO-related catalyst poisoning [156]. Anodic hydrazine oxidation not only facilitates hydrogen production, but also aids in the treatment of hydrazine-containing wastewater, especially from the pharmaceutical industry. Given that the potential of HzOR is far lower than the onset of the CER (1.71 V *versus* RHE), interference from the CER can be effectively suppressed, allowing for the unimpeded current density in H_2 production [131]. Due to these advantages, HzOR has garnered significant attention and has been extensively studied for its potential in co-electrolysis with the HER, leading to the design and synthesis of various electrocatalysts with suitable d-band structures. These include both precious metals (e.g., Pt, Pd, and Rh) and non-precious metals (e.g., Fe, Co, and Ni) and their corresponding nitrides, oxides, phosphides, and chalcogenides. Wang et al. exploited FeCoNiP@NC electrode on Ni foam as a highly efficient and durable bifunctional catalyst for both HzOR and HER. For the overall hydrazine splitting (OHzS) in alkaline seawater, FeCoNiP@NC revealed a low cell voltage of 0.56 V at 1000 mA cm^{-2}, stable operation for 100 h to keep ~500 mA cm^{-2}, which effectively avoided CER competition and achieved nearly 100% Faraday efficiency [157].

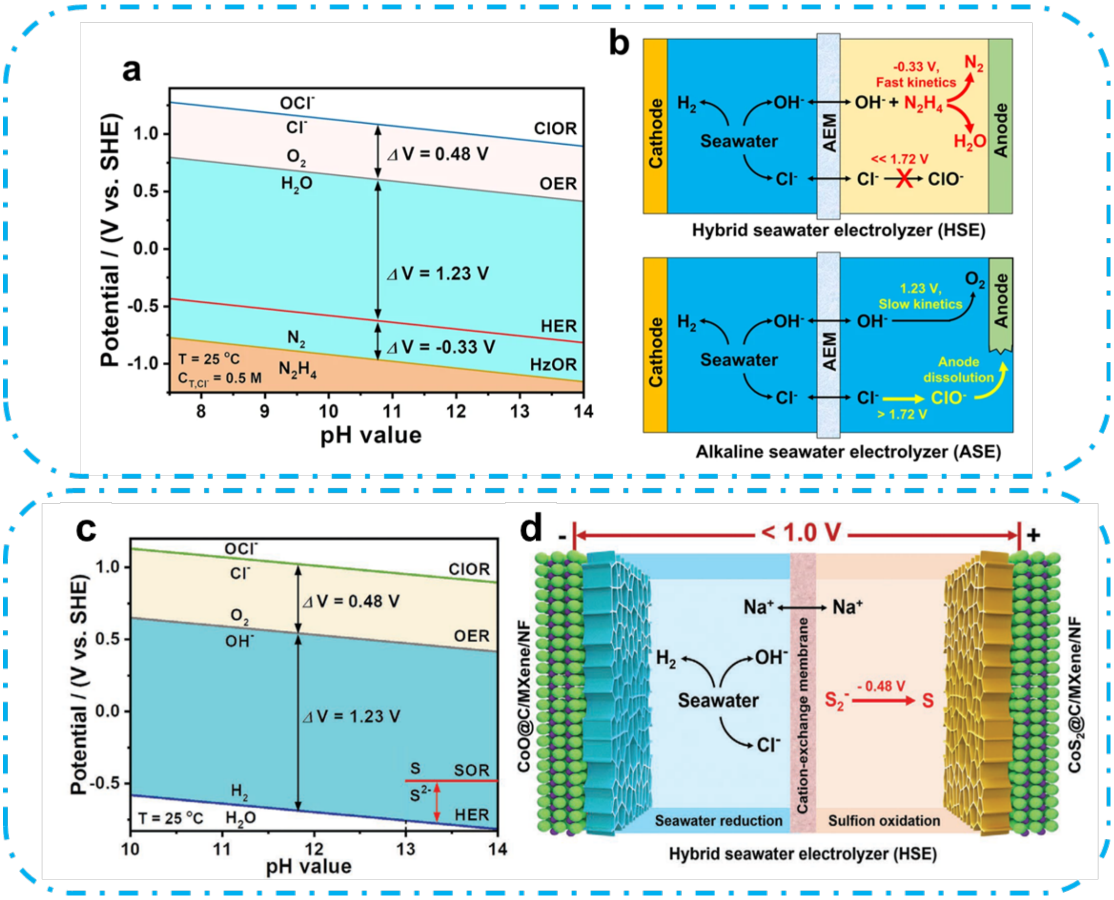

Figure 19. Pourbaix diagram of HER, OER, ClOR, (**a-b**) HzOR and (**c-d**) SOR under alkaline conditions [158].

(3) SOR Assisted SWE

Sulfion oxidation reaction (SOR) is also an anodic half-reaction, which demonstrates considerable thermodynamics theoretical potential (−0.48 V *versus* RHE) and rapid two electrons charge transfer kinetics for substituting the OER, enabling energy-saving hybrid SWE without the interfering CER [159]. Various sulfides/sulfions, as a class of pollutants in wastewater and atmosphere, represent major side products of the chemical industry and fossil fuel combustion in power plants, which will cause serious environmental issues, such as haze, PM 2.5 pollution, and acid rain [160]. Sulfion can be oxidized into elemental sulfur via the following reaction ($S^{2-} \rightarrow S + 2e^{-}$).

During the SOR process, the electrode surface may passivate, forming insulating sulfur under a mildly alkaline solution, leading to the decay of catalyst activity. To ensure operational efficiency and stability, SOR-assisted seawater electrolysis is typically carried out in strongly alkaline conditions, which prevent passivation, as sulfur can be dissolved into polysulfides that can be further overoxidized to soluble sulfur oxyanions [161, 162]. As shown in **Figure 19(c-d)**, Wang's group designed CoS_2/MXene-based electrocatalytic electrodes to exploit the potential of this chemistry in a hybrid seawater electrolyzer for HER and SOR, which could produce hydrogen even at a low cell voltage of 0.97 V, reducing power consumption to 2.32 kWh per m^3 H_2 at 300 mA cm^{-2} [158].

(4) AlOR Assisted SWE

Unlike the aforementioned substitutional AOR (i.e., urea, hydrazine, and sulfation sacrificial agent), alcohol electro-oxidation reactions (AlOR) can help circumvent the energy-demanding OER and interfere with CER, while reducing energy consumption and enabling high-value production (**Figure 20**)[141]. Recently, electro-oxidative upgrading of chemicals and biomass reforming has garnered considerable interest as an alternative to OER for H_2 production [163]. These approaches offer the advantages above and facilitate the co-production of chemicals or fuels with high-added value at the anode. In particular, hybrid seawater electrolysis (SWE) enabled by the alcohol oxidation reaction coupled with the HER has been the subject of extensive investigation. Numerous alcohols generally exhibit a low theoretical oxidation potential. This characteristic endows alcohol oxidation reaction-assisted H_2 production highly promising for energy-saving electrolysis compared to conventional methods [164]. Furthermore, besides H_2, valuable chemicals such as formate, aldehydes, or carboxylic acids can be obtained simultaneously [84]. The alcohol oxidation reaction can be generally described as follows: methanol (MeOH) [165-167], ethylene glycol (EG), isopropanol (IPA) [168], etc., as the simplest aliphatic alcohols, which have been intensively investigated in recent years. Particularly, for EG molecules, the electrocatalyst can catalyze ethylene glycol (EG) derived from PET waste toward formate with high selectivity, exhibiting a lower onset potential for EG oxidation reaction compared to water oxidation reaction [169-172]. For example, Chen et al. developed a low-cost nickel sulfide catalyst to selectively convert ethylene glycol (from PET hydrolysate) into formate, with the co-production of hydrogen fuel. The optimal B and Co co-doped Ni_3S_2 only required 1.34 V at 100 mA cm^{-2} for EGOR, and achieved high faradaic efficiency (>93%) and selectivity (>92%) for EG-to-formate conversion over a wide potential range. This work provides an novel idea for plastic upcycling and paves the way for low-carbon plastic waste management [173].

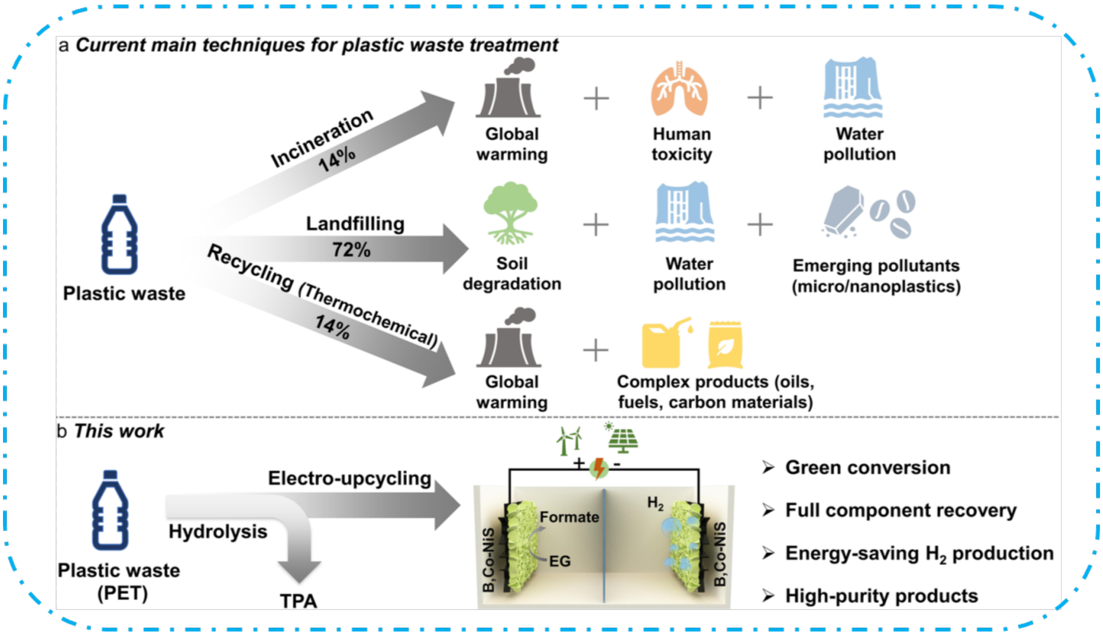

Figure 20. (**a**) Current techniques for plastic waste treatment and related environmental impacts. (**b**) Proposed electro-upcycling route for plastic waste (PET) valorization (TPA: terephthalic acid) [173].

I.5 Objectives

In order to obtain promising electrocatalysts that could withstand incredibly high current densities, which is required practically for industrial electrolyzers, the catalysts should fulfil multiple reequipments simultaneously: (i) high intrinsic activity for HER and OER; (ii) larger ESCA and rich active sites; (iii) facile charge/electrolyte/bubble transfer ability; (iv) excellent durability even in seawater corrosion condition, which prevent active sites peeling off and keep lower interfacial resistance during long-term electrocatalysis; (v) strong Cl^- repulsion ability, which avoids chloride oxidation, surface site blockage, catalyst poisoning and metal corrosion damage; (vi) good selectivity and high faradic efficiency, which could adapt to organic molecule (urea, EG) anode oxidation to decrease theoretical potential and produce high-added value molecules under the seawater electrolysis process. Meanwhile, in order to promote catalyst commercialization, it is necessary to find a manufacturing method that is easily scalable, has low energy consumption, and exhibits high production efficiency to prepare large-size electrodes. However, so far, it is still difficult to design a unique catalyst and preparation process that meets all the above criteria.

Therefore, hierarchical porous seawater electrolysis catalysts with cost effective, high catalytic reactivity and high structural stability *via* a simple and large-scale synthesis approach, were the targets of my PhD work and deserve to be strongly pursued, toward meeting our goal of making efficient catalysts that could operate at large current densities. In addition, we also considered applying different strategies to overcome multiple undesired reactions, owing to complexity of seawater condition (such as Ca^{2+}, Mg^{2+}, Cl^- e.g.) during seawater electrolysis process.

In details:

(1) From the perspective of catalyst preparation technology, there is an urgent need to design a process that is efficient, low-cost, and suitable for industrial systems. We applied facile seawater corrosion engineering on the typical commercial nickel (NF) foam and iron foam (FF) to obtain high-performance and robust HER/OER transition metal-based catalysts. The prepared transition metal oxide catalysts demonstrated high intrinsic activity and fast reaction kinetics for electrochemical water splitting. The catalyst morphology and structure could be tuned by seawater corrosion time, pH value, ion type and concentration, which not only allowed to achieve enhanced ECSA with redox reaction centers, but also facilitated mass diffusion, charge transport and maintained high electrocatalytic activity.

(2) From the catalyst durability perspective, the development of highly stable electrodes capable of withstanding the Cl_2 and hypochlorite environment has been a fundamental requirement for seawater splitting. This work proposed OER and HER

catalysts-based transition metals coupled with rare noble metals and S elements, focusing on optimizing the catalyst-electrolyte interface and local pH to enhance their activity and durability in seawater condition, which is one of the drastic requirements necessary for industrial applications. The *in situ* formed sulfate anions during alkaline seawater electrolysis generated a cation-selective polyatomic anion-rich environment on the anode surface which repulsed Cl^- ions.

(3) From the perspective of hydrogen production thermodynamics or kinetic efficiency, an appropriate anodic oxidation reaction was selected whose overpotential is lower than OER and ClER. Efficiency and long-term operation of the seawater electrolysis are primarily limited by CER, which can be controlled by maintaining an overpotential of less than 480 mV under alkaline electrolyte conditions. Using a faster, lower-potential organic molecules (Urea or EG molecules) electro-oxidation strategy to replace OER, which can effectively avoid CER interference in the seawater electrolysis process, leading to more efficient electrocatalytic processes. This work provides good idea for upgrading of plastic waste and energy-saving hydrogen evolution in seawater by the design of unique muti-transition metal oxide catalysts.

References

[1] N.S. Lewis, D.G. Nocera, Powering the planet: chemical challenges in solar energy utilization, Proceedings of the National Academy of Sciences 103(43) (2006) 15729-35. https://doi.org/10.1073/pnas.0603395103.

[2] S. Shafiee, E. Topal, When will fossil fuel reserves be diminished?, Energy Policy 37(1) (2009) 181-189. https://doi.org/10.1016/j.enpol.2008.08.016.

[3] M. Höök, X. Tang, Depletion of fossil fuels and anthropogenic climate change—A review, Energy Policy 52 (2013) 797-809. https://doi.org/https://doi.org/10.1016/j.enpol.2012.10.046.

[4] M. Grätzel, Photoelectrochemical cells, Nature 414 (2001) 338–344.

[5] C. Koroneos, T. Spachos, N. Moussiopoulos, Exergy analysis of renewable energy sources, Renewable Energy 28(2) (2003) 295-310. https://doi.org/https://doi.org/10.1016/S0960-1481(01)00125-2.

[6] Z.W. Seh, J. Kibsgaard, C.F. Dickens, I. Chorkendorff, J.K. Nørskov, T.F. Jaramillo, Combining theory and experiment in electrocatalysis: Insights into materials design, Science 355(6321) (2017) eaad4998. https://doi.org/10.1126/science.aad4998.

[7] Y. Jiao, Y. Zheng, M. Jaroniec, S.Z. Qiao, Design of electrocatalysts for oxygen-

and hydrogen-involving energy conversion reactions, Chem. Soc. Rev. 44(8) (2015) 2060-86. https://doi.org/10.1039/c4cs00470a.

[8] A. Majumdar, J.M. Deutch, R.S. Prasher, T.P. Griffin, A framework for a hydrogen economy, Joule 5(8) (2021) 1905-1908. https://doi.org/10.1016/j.joule.2021.07.007.

[9] L. Pingkuo, H. Xue, Comparative analysis on similarities and differences of hydrogen energy development in the World's top 4 largest economies: A novel framework, Int. J. Hydrogen Energy 47(16) (2022) 9485-9503. https://doi.org/10.1016/j.ijhydene.2022.01.038.

[10] G.W. Crabtree, M.S. Dresselhaus, M.V. Buchanan, The Hydrogen Economy, Phys. Today 57(12) (2004) 39-44. https://doi.org/10.1063/1.1878333.

[11] S.W. Boettcher, S.Z. Oener, M.C. Lonergan, Y. Surendranath, S. Ardo, C. Brozek, P.A. Kempler, Potentially Confusing: Potentials in Electrochemistry, ACS Energy Lett. 6(1) (2020) 261-266. https://doi.org/10.1021/acsenergylett.0c02443.

[12] W. Xu, F. Lyu, Y. Bai, A. Gao, J. Feng, Z. Cai, Y. Yin, Porous cobalt oxide nanoplates enriched with oxygen vacancies for oxygen evolution reaction, Nano Energy 43 (2018) 110-116. https://doi.org/10.1016/j.nanoen.2017.11.022.

[13] X. Ji, Y. Lin, J. Zeng, Z. Ren, Z. Lin, Y. Mu, Y. Qiu, J. Yu, Graphene/MoS_2/FeCoNi$(OH)_x$ and Graphene/MoS_2/FeCoNiP_x multilayer-stacked vertical nanosheets on carbon fibers for highly efficient overall water splitting, Nat. Commun. 12(1) (2021) 1380. https://doi.org/10.1038/s41467-021-21742-y.

[14] P.J. Mark F. Ruth, Nicholas Gilroy, Elizabeth Connelly, Richard Boardman, A.J. Simon,Amgad Elgowainy, and Jarett Zuboy, The Technical and Economic Potential of the H_2 Scale Concept within the United States, National Renewable Energy Laboratory, 2020.

[15] N. Wang, X. Li, M.-K. Hu, W. Wei, S.-H. Zhou, X.-T. Wu, Q.-L. Zhu, Ordered macroporous superstructure of bifunctional cobalt phosphide with heteroatomic modification for paired hydrogen production and polyethylene terephthalate plastic recycling, Appl. Catal., B 316 (2022) 121667. https://doi.org/10.1016/j.apcatb.2022.121667.

[16] Z. Yu, Y. Li, V. Martin-Diaconescu, L. Simonelli, J. Ruiz Esquius, I. Amorim, A. Araujo, L. Meng, J.L. Faria, L. Liu, Highly Efficient and Stable Saline Water Electrolysis Enabled by Self-Supported Nickel-Iron Phosphosulfide Nanotubes With Heterointerfaces and Under-Coordinated Metal Active Sites, Adv. Funct. Mater. 32(38) (2022) 2206138. https://doi.org/10.1002/adfm.202206138.

[17] J. Wang, H. Zhang, X. Wang, Recent Methods for the Synthesis of Noble-Metal-Free Hydrogen-Evolution Electrocatalysts: From Nanoscale to Sub-nanoscale, Small Methods 1(6) (2017) 1700118. https://doi.org/10.1002/smtd.201700118.

[18] J. Rodríguez, E. Amores, CFD Modeling and Experimental Validation of an Alkaline Water Electrolysis Cell for Hydrogen Production, Processes 8(12) (2020) 1634. https://doi.org/10.3390/pr8121634.

[19] A.J. Medford, A. Vojvodic, J.S. Hummelshøj, J. Voss, F. Abild-Pedersen, F. Studt, T. Bligaard, A. Nilsson, J.K. Nørskov, From the Sabatier principle to a predictive theory of transition-metal heterogeneous catalysis, J. Catal. 328 (2015) 36-42. https://doi.org/10.1016/j.jcat.2014.12.033.

[20] J.H. Montoya, L.C. Seitz, P. Chakthranont, A. Vojvodic, T.F. Jaramillo, J.K. Norskov, Materials for solar fuels and chemicals, Nat. Mater. 16(1) (2016) 70-81. https://doi.org/10.1038/nmat4778.

[21] W. Sheng, M. Myint, J.G. Chen, Y. Yan, Correlating the hydrogen evolution reaction activity in alkaline electrolytes with the hydrogen binding energy on monometallic surfaces, Energy Environ. Sci. 6(5) (2013) 1509. https://doi.org/10.1039/c3ee00045a.

[22] Z.-F. Huang, J. Song, S. Dou, X. Li, J. Wang, X. Wang, Strategies to Break the Scaling Relation toward Enhanced Oxygen Electrocatalysis, Matter 1(6) (2019) 1494-1518. https://doi.org/10.1016/j.matt.2019.09.011.

[23] R. Subbaraman, D. Tripkovic, D. Strmcnik, K.C. Chang, M. Uchimura, A.P. Paulikas, V. Stamenkovic, N.M. Markovic, Enhancing hydrogen evolution activity in water splitting by tailoring $Li(^{+})$-$Ni(OH)_2$-Pt interfaces, Science 334(6060) (2011) 1256-60. https://doi.org/10.1126/science.1211934.

[24] N. Mahmood, Y. Yao, J.W. Zhang, L. Pan, X. Zhang, J.J. Zou, Electrocatalysts for Hydrogen Evolution in Alkaline Electrolytes: Mechanisms, Challenges, and Prospective Solutions, Adv Sci (Weinh) 5(2) (2018) 1700464. https://doi.org/10.1002/advs.201700464.

[25] E. Skúlason, V. Tripkovic, M.E. Björketun, S. Gudmundsdóttir, G. Karlberg, J. Rossmeisl, T. Bligaard, H. Jónsson, J.K. Nørskov, Modeling the Electrochemical Hydrogen Oxidation and Evolution Reactions on the Basis of Density Functional Theory Calculations, The Journal of Physical Chemistry C 114(42) (2010) 18182-18197. https://doi.org/10.1021/jp1048887.

[26] G.J. B.E. Conway Relation of energies and coverages of underpotential and overpotential deposited H at Pt and other metals to the ‘volcano curve’ for cathodic H_2 evolution kinetics, Electrochim. Acta 45 (2000) 4075–4083.

[27] V. Muralidharan, S. Jayasubramaniyan, H.-W. Lee, Surpassing water-splitting potential in aqueous redox flow batteries: insights from kinetics and thermodynamics, EES Catalysis (2024). https://doi.org/10.1039/d3ey00231d.

[28] J. Song, C. Wei, Z.F. Huang, C. Liu, L. Zeng, X. Wang, Z.J. Xu, A review on fundamentals for designing oxygen evolution electrocatalysts, Chem. Soc. Rev. 49(7) (2020) 2196-2214. https://doi.org/10.1039/c9cs00607a.

[29] F. Song, L. Bai, A. Moysiadou, S. Lee, C. Hu, L. Liardet, X. Hu, Transition Metal Oxides as Electrocatalysts for the Oxygen Evolution Reaction in Alkaline Solutions: An Application-Inspired Renaissance, J. Am. Chem. Soc. 140(25) (2018) 7748-7759. https://doi.org/10.1021/jacs.8b04546.

[30] M.T.M. Koper, Analysis of electrocatalytic reaction schemes: distinction between rate-determining and potential-determining steps, J. Solid State Electrochem. 17(2) (2012) 339-344. https://doi.org/10.1007/s10008-012-1918-x.

[31] K.S. Exner, I. Sohrabnejad-Eskan, H. Over, A Universal Approach To Determine the Free Energy Diagram of an Electrocatalytic Reaction, ACS Catal. 8(3) (2018) 1864-1879. https://doi.org/10.1021/acscatal.7b03142.

[32] K.S. Exner, A Universal Descriptor for the Screening of Electrode Materials for Multiple-Electron Processes: Beyond the Thermodynamic Overpotential, ACS Catal.

10(21) (2020) 12607-12617. https://doi.org/10.1021/acscatal.0c03865.

[33] L. Li, X. Cao, J. Huo, J. Qu, W. Chen, C. Liu, Y. Zhao, H. Liu, G. Wang, High valence metals engineering strategies of Fe/Co/Ni-based catalysts for boosted OER electrocatalysis, J. Energy Chem. 76 (2023) 195-213. https://doi.org/10.1016/j.jechem.2022.09.022.

[34] A. Grimaud, W.T. Hong, Y. Shao-Horn, J.M. Tarascon, Anionic redox processes for electrochemical devices, Nat. Mater. 15(2) (2016) 121-6. https://doi.org/10.1038/nmat4551.

[35] I.C. Man, H.Y. Su, F. Calle-Vallejo, H.A. Hansen, J.I. Martínez, N.G. Inoglu, J. Kitchin, T.F. Jaramillo, J.K. Nørskov, J. Rossmeisl, Universality in Oxygen Evolution Electrocatalysis on Oxide Surfaces, ChemCatChem 3(7) (2011) 1159-1165. https://doi.org/10.1002/cctc.201000397.

[36] J. Rossmeisl, A. Logadottir, J.K. Nørskov, Electrolysis of water on (oxidized) metal surfaces, Chem. Phys. 319(1-3) (2005) 178-184. https://doi.org/10.1016/j.chemphys.2005.05.038.

[37] J. Rossmeisl, Z.W. Qu, H. Zhu, G.J. Kroes, J.K. Nørskov, Electrolysis of water on oxide surfaces, J. Electroanal. Chem. 607(1-2) (2007) 83-89. https://doi.org/10.1016/j.jelechem.2006.11.008.

[38] T. Binninger, R. Mohamed, K. Waltar, E. Fabbri, P. Levecque, R. Kotz, T.J. Schmidt, Thermodynamic explanation of the universal correlation between oxygen evolution activity and corrosion of oxide catalysts, Sci. Rep. 5 (2015) 12167. https://doi.org/10.1038/srep12167.

[39] K. Zhang, R. Zou, Advanced Transition Metal-Based OER Electrocatalysts: Current Status, Opportunities, and Challenges, Small 17(37) (2021) e2100129. https://doi.org/10.1002/smll.202100129.

[40] D. Gao, H. Zhou, F. Cai, J. Wang, G. Wang, X. Bao, Pd-Containing Nanostructures for Electrochemical CO_2 Reduction Reaction, ACS Catal. 8(2) (2018) 1510-1519. https://doi.org/10.1021/acscatal.7b03612.

[41] S. Deshpande, J.R. Kitchin, V. Viswanathan, Quantifying Uncertainty in Activity Volcano Relationships for Oxygen Reduction Reaction, ACS Catal. 6(8) (2016) 5251-5259. https://doi.org/10.1021/acscatal.6b00509.

[42] H.J. Lee, S. Back, J.H. Lee, S.H. Choi, Y. Jung, J.W. Choi, Mixed Transition Metal Oxide with Vacancy-Induced Lattice Distortion for Enhanced Catalytic Activity of Oxygen Evolution Reaction, ACS Catal. 9(8) (2019) 7099-7108. https://doi.org/10.1021/acscatal.9b01298.

[43] E. Tayyebi, Y. Abghoui, E. Skúlason, Elucidating the Mechanism of Electrochemical N_2 Reduction at the Ru(0001) Electrode, ACS Catal. 9(12) (2019) 11137-11145. https://doi.org/10.1021/acscatal.9b03903.

[44] V. Sumaria, D. Krishnamurthy, V. Viswanathan, Quantifying Confidence in DFT Predicted Surface Pourbaix Diagrams and Associated Reaction Pathways for Chlorine Evolution, ACS Catal. 8(10) (2018) 9034-9042. https://doi.org/10.1021/acscatal.8b01432.

[45] W. Luo, X. Nie, M.J. Janik, A. Asthagiri, Facet Dependence of CO_2 Reduction Paths on Cu Electrodes, ACS Catal. 6(1) (2016) 219-229.

https://doi.org/10.1021/acscatal.5b01967.

[46] Y. Basdogan, J.A. Keith, A paramedic treatment for modeling explicitly solvated chemical reaction mechanisms, Chem Sci 9(24) (2018) 5341-5346. https://doi.org/10.1039/c8sc01424h.

[47] S. Sakong, A. Groß, The Importance of the Electrochemical Environment in the Electro-Oxidation of Methanol on Pt(111), ACS Catal. 6(8) (2016) 5575-5586. https://doi.org/10.1021/acscatal.6b00931.

[48] Z.-F. Huang, J. Song, Y. Du, S. Xi, S. Dou, J.M.V. Nsanzimana, C. Wang, Z.J. Xu, X. Wang, Chemical and structural origin of lattice oxygen oxidation in Co–Zn oxyhydroxide oxygen evolution electrocatalysts, Nat. Energy 4(4) (2019) 329-338. https://doi.org/10.1038/s41560-019-0355-9.

[49] T. Guo, L. Li, Z. Wang, Recent Development and Future Perspectives of Amorphous Transition Metal-Based Electrocatalysts for Oxygen Evolution Reaction, Adv. Energy Mater. 12(24) (2022) 2200827. https://doi.org/10.1002/aenm.202200827.

[50] C. Yang, Z.-D. Yang, H. Dong, N. Sun, Y. Lu, F.-M. Zhang, G. Zhang, Theory-Driven Design and Targeting Synthesis of a Highly-Conjugated Basal-Plane 2D Covalent Organic Framework for Metal-Free Electrocatalytic OER, ACS Energy Lett. 4(9) (2019) 2251-2258. https://doi.org/10.1021/acsenergylett.9b01691.

[51] C. Spöri, P. Briois, H.N. Nong, T. Reier, A. Billard, S. Kühl, D. Teschner, P. Strasser, Experimental Activity Descriptors for Iridium-Based Catalysts for the Electrochemical Oxygen Evolution Reaction (OER), ACS Catal. 9(8) (2019) 6653-6663. https://doi.org/10.1021/acscatal.9b00648.

[52] S. Li, E. Li, X. An, X. Hao, Z. Jiang, G. Guan, Transition metal-based catalysts for electrochemical water splitting at high current density: current status and perspectives, Nanoscale 13(30) (2021) 12788-12817. https://doi.org/10.1039/d1nr02592a.

[53] M. Tahir, L. Pan, F. Idrees, X. Zhang, L. Wang, J.-J. Zou, Z.L. Wang, Electrocatalytic oxygen evolution reaction for energy conversion and storage: A comprehensive review, Nano Energy 37 (2017) 136-157. https://doi.org/10.1016/j.nanoen.2017.05.022.

[54] H. Li, X. Han, W. Zhao, A. Azhar, S. Jeong, D. Jeong, J. Na, S. Wang, J. Yu, Y. Yamauchi, Electrochemical preparation of nano/micron structure transition metal-based catalysts for the oxygen evolution reaction, Mater. Horiz. 9(7) (2022) 1788-1824. https://doi.org/10.1039/d2mh00075j.

[55] J.S. Kim, B. Kim, H. Kim, K. Kang, Recent Progress on Multimetal Oxide Catalysts for the Oxygen Evolution Reaction, Adv. Energy Mater. 8(11) (2018) 1702774. https://doi.org/10.1002/aenm.201702774.

[56] W.T. Hong, M. Risch, K.A. Stoerzinger, A. Grimaud, J. Suntivich, Y. Shao-Horn, Toward the rational design of non-precious transition metal oxides for oxygen electrocatalysis, Energy Environ. Sci. 8(5) (2015) 1404-1427. https://doi.org/10.1039/c4ee03869j.

[57] R. Rajendiran, D. Chinnadurai, K. Chen, A.R. Selvaraj, K. Prabakar, O.L. Li, Electrodeposited Trimetallic NiFeW Hydroxide Electrocatalysts for Efficient Water Oxidation, ChemSusChem 14(5) (2021) 1324-1335. https://doi.org/10.1002/cssc.202002544.

[58] Y. Wang, L. Wang, K. Zhang, J. Xu, Q. Wu, Z. Xie, W. An, X. Liang, X. Zou, Electrocatalytic water splitting over perovskite oxide catalysts, Chin. J. Catal. 50 (2023) 109-125. https://doi.org/10.1016/s1872-2067(23)64452-3.
[59] Y. Chen, Z. Sun, J.-M. Wu, R. Jiang, P. Yang, Y. Gu, W. Liu, J. Wu, W. Wen, Cobalt/nickel oxide nanosheet arrays for electrocatalytic water oxidation: Size modulation, composition/phase control, and surface decoration, Chem. Phys. Lett. 754 (2020) 137734. https://doi.org/10.1016/j.cplett.2020.137734.
[60] C. Chen, Y. Tuo, Q. Lu, H. Lu, S. Zhang, Y. Zhou, J. Zhang, Z. Liu, Z. Kang, X. Feng, D. Chen, Hierarchical trimetallic Co-Ni-Fe oxides derived from core-shell structured metal-organic frameworks for highly efficient oxygen evolution reaction, Appl. Catal., B 287 (2021) 119953. https://doi.org/10.1016/j.apcatb.2021.119953.
[61] A. Li, S. Kong, C. Guo, H. Ooka, K. Adachi, D. Hashizume, Q. Jiang, H. Han, J. Xiao, R. Nakamura, Enhancing the stability of cobalt spinel oxide towards sustainable oxygen evolution in acid, Nat. Catal. 5(2) (2022) 109-118. https://doi.org/10.1038/s41929-021-00732-9.
[62] H. Wang, J. Wang, Y. Pi, Q. Shao, Y. Tan, X. Huang, Double Perovskite $LaFe_xNi_{1-x}O_3$ Nanorods Enable Efficient Oxygen Evolution Electrocatalysis, Angew. Chem. Int. Ed. 58(8) (2019) 2316-2320. https://doi.org/10.1002/anie.201812545.
[63] W. Chen, B. Wu, Y. Wang, W. Zhou, Y. Li, T. Liu, C. Xie, L. Xu, S. Du, M. Song, D. Wang, Y. liu, Y. Li, J. Liu, Y. Zou, R. Chen, C. Chen, J. Zheng, Y. Li, J. Chen, S. Wang, Deciphering the alternating synergy between interlayer Pt single-atom and NiFe layered double hydroxide for overall water splitting, Energy Environ. Sci. 14(12) (2021) 6428-6440. https://doi.org/10.1039/d1ee01395e.
[64] L.-G. He, P.-Y. Cheng, C.-C. Cheng, C.-L. Huang, C.-T. Hsieh, S.-Y. Lu, $(Ni_xFe_yCo_{6-x-y})Mo_6C$ Cuboids as outstanding bifunctional electrocatalysts for overall water splitting, Appl. Catal., B 290 (2021) 120049. https://doi.org/10.1016/j.apcatb.2021.120049.
[65] Y. Chen, H. Yao, F. Kong, H. Tian, G. Meng, S. Wang, X. Mao, X. Cui, X. Hou, J. Shi, V_2C MXene synergistically coupling FeNi LDH nanosheets for boosting oxygen evolution reaction, Appl. Catal., B 297 (2021) 120474. https://doi.org/10.1016/j.apcatb.2021.120474.
[66] Y. Tang, Q. Liu, L. Dong, H.B. Wu, X.-Y. Yu, Activating The Hydrogen Evolution And Overall Water Splitting Performance Of NiFe LDH By Cation Doping And Plasma Reduction, Appl. Catal., B 266 (2020) 118627. https://doi.org/10.1016/j.apcatb.2020.118627.
[67] F. Chen, C. Chen, Q. Hu, B. Xiang, T. Song, X. Zou, W. Li, B. Xiong, M. Deng, Synthesis of CuO@CoNi LDH on Cu foam for high-performance supercapacitors, Chem. Eng. J. 401 (2020) 126145. https://doi.org/10.1016/j.cej.2020.126145.
[68] V.M. Nikolic, S.L. Maslovara, G.S. Tasic, T.P. Brdaric, P.Z. Lausevic, B.B. Radak, M.P. Marceta Kaninski, Kinetics of Hydrogen Evolution Reaction In Alkaline Electrolysis On a Ni Cathode In the Presence Of Ni–Co–Mo Based Ionic Activators, Appl. Catal., B 179 (2015) 88-94. https://doi.org/10.1016/j.apcatb.2015.05.012.
[69] A.I. Khan, D. O'Hare, Intercalation chemistry of layered double hydroxides: recent developments and applications, J. Mater. Chem. 12(11) (2002) 3191-3198.

https://doi.org/10.1039/b204076j.

[70] M. Shao, R. Zhang, Z. Li, M. Wei, D.G. Evans, X. Duan, Layered double hydroxides toward electrochemical energy storage and conversion: design, synthesis and applications, Chem. Commun. 51(88) (2015) 15880-93. https://doi.org/10.1039/c5cc07296d.

[71] P.M. Bodhankar, P.B. Sarawade, G. Singh, A. Vinu, D.S. Dhawale, Recent Advances In Highly Active Nanostructured NiFe LDH Catalyst For Electrochemical Water Splitting, J. Mater. Chem. A 9(6) (2021) 3180-3208. https://doi.org/10.1039/d0ta10712c.

[72] Y. Jia, L. Zhang, G. Gao, H. Chen, B. Wang, J. Zhou, M.T. Soo, M. Hong, X. Yan, G. Qian, J. Zou, A. Du, X. Yao, A Heterostructure Coupling of Exfoliated Ni-Fe Hydroxide Nanosheet and Defective Graphene as a Bifunctional Electrocatalyst for Overall Water Splitting, Adv. Mater. 29(17) (2017) 1700017. https://doi.org/10.1002/adma.201700017.

[73] R. Subbaraman, D. Tripkovic, K.-C. Chang, D. Strmcnik, A.P. Paulikas, P. Hirunsit, M. Chan, J. Greeley, V. Stamenkovic, N.M. Markovic, Trends in activity for the water electrolyser reactions on 3d M(Ni,Co,Fe,Mn) hydr(oxy)oxide catalysts, Nat. Mater. 11(6) (2012) 550-557. https://doi.org/10.1038/nmat3313.

[74] Y. Yang, S. Wei, Y. Li, D. Guo, H. Liu, L. Liu, Effect of cobalt doping-regulated crystallinity in nickel-iron layered double hydroxide catalyzing oxygen evolution, Appl. Catal., B 314 (2022) 121491. https://doi.org/10.1016/j.apcatb.2022.121491.

[75] P.-F. Guo, Y. Yang, W.-J. Wang, B. Zhu, W.-T. Wang, Z.-Y. Wang, J.-L. Wang, K. Wang, Z.-H. He, Z.-T. Liu, Stable and active NiFeW layered double hydroxide for enhanced electrocatalytic oxygen evolution reaction, Chem. Eng. J. 426 (2021) 130768. https://doi.org/10.1016/j.cej.2021.130768.

[76] Z. He, J. Zhang, Z. Gong, H. Lei, D. Zhou, N. Zhang, W. Mai, S. Zhao, Y. Chen, Activating lattice oxygen in NiFe-based (oxy)hydroxide for water electrolysis, Nat. Commun. 13(1) (2022) 2191. https://doi.org/10.1038/s41467-022-29875-4.

[77] R. Que, S. Liu, Y. Yang, Y. Pan, Core-shell structure Co_3O_4@NiCo LDH was used as a high efficiency catalyst for overall water splitting, Mater. Lett. 288 (2021) 129364. https://doi.org/10.1016/j.matlet.2021.129364.

[78] X. Zhang, H. Yi, M. Jin, Q. Lian, Y. Huang, Z. Ai, R. Huang, Z. Zuo, C. Tang, A. Amini, F. Jia, S. Song, C. Cheng, In Situ Reconstructed Zn doped Fex $Ni_{(1-x)}$ OOH Catalyst for Efficient and Ultrastable Oxygen Evolution Reaction at High Current Densities, Small (2022) e2203710. https://doi.org/10.1002/smll.202203710.

[79] M. Li, A. Addad, M. Dolci, P. Roussel, M. Naushad, S. Szunerits, R. Boukherroub, NiMnCr layered double hydroxide-carbon spheres modified Ni foam: An efficient positive electrode for hybrid supercapacitors, Chem. Eng. J. 396 (2020) 125370. https://doi.org/10.1016/j.cej.2020.125370.

[80] X. Li, X. Lv, X. Sun, C. Yang, Y.-Z. Zheng, L. Yang, S. Li, X. Tao, Edge-oriented, high-percentage 1T′-phase MoS_2 nanosheets stabilize Ti_3C_2 MXene for efficient electrocatalytic hydrogen evolution, Appl. Catal., B 284 (2021) 119708. https://doi.org/10.1016/j.apcatb.2020.119708.

[81] Y. Liu, S. Jiang, S. Li, L. Zhou, Z. Li, J. Li, M. Shao, Interface engineering of (Ni,

Fe)S_2@MoS_2 heterostructures for synergetic electrochemical water splitting, Appl. Catal., B 247 (2019) 107-114. https://doi.org/10.1016/j.apcatb.2019.01.094.

[82] G. Zhang, Y.-S. Feng, W.-T. Lu, D. He, C.-Y. Wang, Y.-K. Li, X.-Y. Wang, F.-F. Cao, Enhanced Catalysis of Electrochemical Overall Water Splitting in Alkaline Media by Fe Doping in Ni_3S_2 Nanosheet Arrays, ACS Catal. 8(6) (2018) 5431-5441. https://doi.org/10.1021/acscatal.8b00413.

[83] S. Wang, P. Yang, X. Sun, H. Xing, J. Hu, P. Chen, Z. Cui, W. Zhu, Z. Ma, Synthesis of 3D heterostructure Co-doped Fe_2P electrocatalyst for overall seawater electrolysis, Appl. Catal., B 297 (2021) 120386. https://doi.org/10.1016/j.apcatb.2021.120386.

[84] H. Jiang, L. Yan, S. Zhang, Y. Zhao, X. Yang, Y. Wang, J. Shen, X. Zhao, L. Wang, Electrochemical Surface Restructuring of Phosphorus-Doped Carbon@MoP Electrocatalysts for Hydrogen Evolution, Nano-Micro Lett. 13(1) (2021) 215. https://doi.org/10.1007/s40820-021-00737-w.

[85] C.C. Yang, S.F. Zai, Y.T. Zhou, L. Du, Q. Jiang, Fe_3C-Co Nanoparticles Encapsulated in a Hierarchical Structure of N-Doped Carbon as a Multifunctional Electrocatalyst for ORR, OER, and HER, Adv. Funct. Mater. (2019) 1901949. https://doi.org/10.1002/adfm.201901949.

[86] Y. Zhang, B. Ouyang, J. Xu, S. Chen, R.S. Rawat, H.J. Fan, 3D Porous Hierarchical Nickel-Molybdenum Nitrides Synthesized by RF Plasma as Highly Active and Stable Hydrogen-Evolution-Reaction Electrocatalysts, Adv. Energy Mater. 6(11) (2016) 1600221. https://doi.org/10.1002/aenm.201600221.

[87] Y. Chen, J. Yu, J. Jia, F. Liu, Y. Zhang, G. Xiong, R. Zhang, R. Yang, D. Sun, H. Liu, W. Zhou, Metallic Ni_3Mo_3N Porous Microrods with Abundant Catalytic Sites as Efficient Electrocatalyst for Large Current Density and Superstability of Hydrogen Evolution Reaction and Water Splitting, Appl. Catal., B 272 (2020) 118956. https://doi.org/10.1016/j.apcatb.2020.118956.

[88] S. He, Y. Chen, M. Wang, H. Nuomin, P. Novello, X. Li, S. Zhu, J. Liu, Metal nitride nanosheets enable highly efficient electrochemical oxidation of ammonia, Nano Energy 80 (2021) 105528. https://doi.org/10.1016/j.nanoen.2020.105528.

[89] C. Yang, R. Zhao, H. Xiang, J. Wu, W. Zhong, W. Li, Q. Zhang, N. Yang, X. Li, Ni-Activated Transition Metal Carbides for Efficient Hydrogen Evolution in Acidic and Alkaline Solutions, Adv. Energy Mater. 10(37) (2020) 2002260. https://doi.org/10.1002/aenm.202002260.

[90] Q. Gong, Y. Wang, Q. Hu, J. Zhou, R. Feng, P.N. Duchesne, P. Zhang, F. Chen, N. Han, Y. Li, C. Jin, Y. Li, S.T. Lee, Ultrasmall and phase-pure $W_{(2)}C$ nanoparticles for efficient electrocatalytic and photoelectrochemical hydrogen evolution, Nat Commun 7 (2016) 13216. https://doi.org/10.1038/ncomms13216.

[91] H.B. Wu, B.Y. Xia, L. Yu, X.Y. Yu, X.W. Lou, Porous molybdenum carbide nano-octahedrons synthesized via confined carburization in metal-organic frameworks for efficient hydrogen production, Nat. Commun. 6 (2015) 6512. https://doi.org/10.1038/ncomms7512.

[92] X. Fan, C. Liu, M. Wu, B. Gao, L. Zheng, Y. Zhang, H. Zhang, Q. Gao, X. Cao, Y. Tang, Synergistic effect of dual active sites over Ru/α-MoC for accelerating alkaline hydrogen evolution reaction, Appl. Catal., B 318 (2022) 121867.

https://doi.org/10.1016/j.apcatb.2022.121867.

[93] C. Lu, D. Tranca, J. Zhang, F.n. Rodríguez Hernández, Y. Su, X. Zhuang, F. Zhang, G. Seifert, X. Feng, Molybdenum Carbide-Embedded Nitrogen-Doped Porous Carbon Nanosheets as Electrocatalysts for Water Splitting in Alkaline Media, ACS Nano 11(4) (2017) 3933-3942. https://doi.org/10.1021/acsnano.7b00365.

[94] X. Jia, M. Wang, G. Liu, Y. Wang, J. Yang, J. Li, Mixed-metal MOF-derived Co-doped Ni_3C/Ni NPs embedded in carbon matrix as an efficient electrocatalyst for oxygen evolution reaction, Int. J. Hydrogen Energy 44(45) (2019) 24572-24579. https://doi.org/10.1016/j.ijhydene.2019.07.144.

[95] S. Zhang, C. Zhang, X. Zheng, G. Su, H. Wang, M. Huang, Integrating electrophilic and nucleophilic dual sites on heterogeneous bimetallic phosphide via enhancing interfacial electronic field to boost hydrazine oxidation and hydrogen evolution, Appl. Catal., B 324 (2023) 122207. https://doi.org/10.1016/j.apcatb.2022.122207.

[96] G. Chen, T. Wang, J. Zhang, P. Liu, H. Sun, X. Zhuang, M. Chen, X. Feng, Accelerated Hydrogen Evolution Kinetics on NiFe-Layered Double Hydroxide Electrocatalysts by Tailoring Water Dissociation Active Sites, Adv. Mater. 30(10) (2018) 1706279. https://doi.org/10.1002/adma.201706279.

[97] X. Shen, H. Li, Y. Zhang, T. Ma, Q. Li, Q. Jiao, Y. Zhao, H. Li, C. Feng, Construction dual-regulated $NiCo_2S_4$ @Mo-doped CoFe-LDH for oxygen evolution reaction at large current density, Appl. Catal., B 319 (2022) 121917. https://doi.org/10.1016/j.apcatb.2022.121917.

[98] D. Li, S. Wu, T. Jiang, S. Huang, Z. Wang, H. Wu, G. Cai, F. Ren, A highly efficient heterostructure nanorod bifunctional electrocatalyst for realizing enhanced overall water splitting at a large current density, J. Mater. Chem. A 11(34) (2023) 18158-18167. https://doi.org/10.1039/d3ta03113f.

[99] Y. Lin, H. Wang, C.K. Peng, L. Bu, C.L. Chiang, K. Tian, Y. Zhao, J. Zhao, Y.G. Lin, J.M. Lee, L. Gao, Co-Induced Electronic Optimization of Hierarchical NiFe LDH for Oxygen Evolution, Small 16(38) (2020) e2002426. https://doi.org/10.1002/smll.202002426.

[100] D. Ma, B. Hu, W. Wu, X. Liu, J. Zai, C. Shu, T. Tadesse Tsega, L. Chen, X. Qian, T.L. Liu, Highly active nanostructured CoS_2/CoS heterojunction electrocatalysts for aqueous polysulfide/iodide redox flow batteries, Nat. Commun. 10(1) (2019) 3367. https://doi.org/10.1038/s41467-019-11176-y.

[101] N. Elgrishi, K.J. Rountree, B.D. McCarthy, E.S. Rountree, T.T. Eisenhart, J.L. Dempsey, A Practical Beginner's Guide to Cyclic Voltammetry, J. Chem. Educ. 95(2) (2017) 197-206. https://doi.org/10.1021/acs.jchemed.7b00361.

[102] M. Palomar-Pardavé, I. González, N. Batina, New Insights into Evaluation of Kinetic Parameters for Potentiostatic Metal Deposition with Underpotential and Overpotential Deposition Processes, J. Phys. Chem. B 104(15) (2000) 3545-3555. https://doi.org/10.1021/jp9931861.

[103] L.B. M. Ghaemia, Effects of direct and pulse current on electrodeposition of manganese dioxide, J. Power Sources Adv. 111 (2002) 248–254.

[104] L. Besra, M. Liu, A review on fundamentals and applications of electrophoretic

deposition (EPD), Prog. Mater Sci. 52(1) (2007) 1-61. https://doi.org/10.1016/j.pmatsci.2006.07.001.

[105] Q. Sun, Y. Dong, Z. Wang, S. Yin, C. Zhao, Synergistic Nanotubular Copper-Doped Nickel Catalysts for Hydrogen Evolution Reactions, Small 14(14) (2018) e1704137. https://doi.org/10.1002/smll.201704137.

[106] J. Wang, S. Xin, Y. Xiao, Z. Zhang, Z. Li, W. Zhang, C. Li, R. Bao, J. Peng, J. Yi, S. Chou, Manipulating the Water Dissociation Electrocatalytic Sites of Bimetallic Nickel-Based Alloys for Highly Efficient Alkaline Hydrogen Evolution, Angew Chem Int Ed Engl 61(30) (2022) e202202518. https://doi.org/10.1002/anie.202202518.

[107] P. Zhai, C. Wang, Y. Zhao, Y. Zhang, J. Gao, L. Sun, J. Hou, Regulating electronic states of nitride/hydroxide to accelerate kinetics for oxygen evolution at large current density, Nat. Commun. 14(1) (2023) 1873. https://doi.org/10.1038/s41467-023-37091-x.

[108] J. Joyner, E.F. Oliveira, H. Yamaguchi, K. Kato, S. Vinod, D.S. Galvao, D. Salpekar, S. Roy, U. Martinez, C.S. Tiwary, S. Ozden, P.M. Ajayan, Graphene Supported MoS_2 Structures with High Defect Density for an Efficient HER Electrocatalysts, ACS Appl Mater Interfaces 12(11) (2020) 12629-12638. https://doi.org/10.1021/acsami.9b17713.

[109] L. Jiao, R. Zhang, G. Wan, W. Yang, X. Wan, H. Zhou, J. Shui, S.H. Yu, H.L. Jiang, Nanocasting $SiO_{(2)}$ into metal-organic frameworks imparts dual protection to high-loading Fe single-atom electrocatalysts, Nat. Commun. 11(1) (2020) 2831. https://doi.org/10.1038/s41467-020-16715-6.

[110] X. Zhang, Y. Zhao, X. Jia, Y. Zhao, L. Shang, Q. Wang, G.I.N. Waterhouse, L.-Z. Wu, C.-H. Tung, T. Zhang, Silica-Protected Ultrathin Ni_3FeN Nanocatalyst for the Efficient Hydrolytic Dehydrogenation of NH_3BH_3, Adv. Energy Mater. 8(12) (2018) 1702780. https://doi.org/10.1002/aenm.201702780.

[111] A. Saad, Z. Cheng, X. Zhang, S. Liu, H. Shen, T. Thomas, J. Wang, M. Yang, Ordered Mesoporous Cobalt–Nickel Nitride Prepared by Nanocasting for Oxygen Evolution Reaction Electrocatalysis, Adv. Mater. Interfaces 6(20) (2019) 1900960. https://doi.org/10.1002/admi.201900960.

[112] A. Saad, H. Shen, Z. Cheng, R. Arbi, B. Guo, L.S. Hui, K. Liang, S. Liu, J.P. Attfield, A. Turak, J. Wang, M. Yang, Mesoporous Ternary Nitrides of Earth-Abundant Metals as Oxygen Evolution Electrocatalyst, Nano-Micro Lett. 12(1) (2020) 79. https://doi.org/10.1007/s40820-020-0412-8.

[113] Y. Meng, D. Gu, F. Zhang, Y. Shi, H. Yang, Z. Li, C. Yu, B. Tu, D. Zhao, Ordered mesoporous polymers and homologous carbon frameworks: amphiphilic surfactant templating and direct transformation, Angew. Chem. Int. Ed. 44(43) (2005) 7053-9. https://doi.org/10.1002/anie.200501561.

[114] M.F. Sarac, W.-C. Wu, J.B. Tracy, Control of Branching in Ni_3C_{1-x} Nanoparticles and Their Conversion into $Ni_{12}P_5$ Nanoparticles, Chem. Mater. 26(10) (2014) 3057-3064. https://doi.org/10.1021/cm4034353.

[115] Y. Liu, X. Liang, L. Gu, Y. Zhang, G.D. Li, X. Zou, J.S. Chen, Corrosion engineering towards efficient oxygen evolution electrodes with stable catalytic activity for over 6000 hours, Nat. Commun. 9(1) (2018) 2609. https://doi.org/10.1038/s41467-

018-05019-5.

[116] S. Hao, L. Chen, C. Yu, B. Yang, Z. Li, Y. Hou, L. Lei, X. Zhang, NiCoMo Hydroxide Nanosheet Arrays Synthesized via Chloride Corrosion for Overall Water Splitting, ACS Energy Lett. 4(4) (2019) 952-959. https://doi.org/10.1021/acsenergylett.9b00333.

[117] Y. Zhao, Y. Gao, Z. Chen, Z. Li, T. Ma, Z. Wu, L. Wang, Trifle Pt coupled with NiFe hydroxide synthesized via corrosion engineering to boost the cleavage of water molecule for alkaline water-splitting, Appl. Catal., B 297 (2021) 120395. https://doi.org/10.1016/j.apcatb.2021.120395.

[118] X. Liu, M. Gong, D. Xiao, S. Deng, J. Liang, T. Zhao, Y. Lu, T. Shen, J. Zhang, D. Wang, Turning Waste into Treasure: Regulating the Oxygen Corrosion on Fe Foam for Efficient Electrocatalysis, Small 16(24) (2020) 2000663. https://doi.org/10.1002/smll.202000663.

[119] S. Hao, G. Zheng, S. Gao, L. Qiu, N. Xu, Y. He, L. Lei, X. Zhang, In Situ Synthesis of Ternary NiCoRu-Based Layered Double Hydroxide by Chlorine Corrosion toward Electrocatalytic Water Oxidation, ACS Sustainable Chem. Eng. 7(17) (2019) 14361-14367. https://doi.org/10.1021/acssuschemeng.9b03830.

[120] H. Jin, J. Xu, H. Liu, H. Shen, H. Yu, M. Jaroniec, Y. Zheng, S.Z. Qiao, Emerging materials and technologies for electrocatalytic seawater splitting, Sci. Adv. 9(42) (2023) eadi7755. https://doi.org/10.1126/sciadv.adi7755.

[121] S. Dresp, F. Dionigi, M. Klingenhof, P. Strasser, Direct Electrolytic Splitting of Seawater: Opportunities and Challenges, ACS Energy Lett. 4(4) (2019) 933-942. https://doi.org/10.1021/acsenergylett.9b00220.

[122] M.A. Khan, T. Al-Attas, S. Roy, M.M. Rahman, N. Ghaffour, V. Thangadurai, S. Larter, J. Hu, P.M. Ajayan, M.G. Kibria, Seawater electrolysis for hydrogen production: a solution looking for a problem?, Energy Environ. Sci. 14(9) (2021) 4831-4839. https://doi.org/10.1039/d1ee00870f.

[123] B. Lee, L. Wang, Z. Wang, N.J. Cooper, M. Elimelech, Directing the research agenda on water and energy technologies with process and economic analysis, Energy Environ. Sci. 16(3) (2023) 714-722. https://doi.org/10.1039/d2ee03271f.

[124] W. Zheng, L.Y.S. Lee, K.Y. Wong, Improving the performance stability of direct seawater electrolysis: from catalyst design to electrode engineering, Nanoscale 13(36) (2021) 15177-15187. https://doi.org/10.1039/d1nr03294a.

[125] I. Katsounaros, J.C. Meier, S.O. Klemm, A.A. Topalov, P.U. Biedermann, M. Auinger, K.J.J. Mayrhofer, The effective surface pH during reactions at the solid–liquid interface, Electrochem. Commun. 13(6) (2011) 634-637. https://doi.org/10.1016/j.elecom.2011.03.032.

[126] Z. Wang, C. Wang, L. Ye, X. Liu, L. Xin, Y. Yang, L. Wang, W. Hou, Y. Wen, T. Zhan, MnO(x) Film-Coated NiFe-LDH Nanosheets on Ni Foam as Selective Oxygen Evolution Electrocatalysts for Alkaline Seawater Oxidation, Inorg. Chem. 61(38) (2022) 15256-15265. https://doi.org/10.1021/acs.inorgchem.2c02579.

[127] A. Kumar, F. Du, J.H. Lienhard, Caustic Soda Production, Energy Efficiency, and Electrolyzers, ACS Energy Lett. 6(10) (2021) 3563-3566. https://doi.org/10.1021/acsenergylett.1c01827.

[128] D. Wu, D. Chen, J. Zhu, S. Mu, Ultralow Ru Incorporated Amorphous Cobalt-Based Oxides for High-Current-Density Overall Water Splitting in Alkaline and Seawater Media, Small 17(39) (2021) e2102777. https://doi.org/10.1002/smll.202102777.

[129] S. Gupta, M. Forster, A. Yadav, A.J. Cowan, N. Patel, M. Patel, Highly Efficient and Selective Metal Oxy-Boride Electrocatalysts for Oxygen Evolution from Alkali and Saline Solutions, ACS Appl. Energy Mater. 3(8) (2020) 7619-7628. https://doi.org/10.1021/acsaem.0c01040.

[130] W. Tong, M. Forster, F. Dionigi, S. Dresp, R. Sadeghi Erami, P. Strasser, A.J. Cowan, P. Farràs, Electrolysis of low-grade and saline surface water, Nat. Energy 5(5) (2020) 367-377. https://doi.org/10.1038/s41560-020-0550-8.

[131] F. Sun, J. Qin, Z. Wang, M. Yu, X. Wu, X. Sun, J. Qiu, Energy-saving hydrogen production by chlorine-free hybrid seawater splitting coupling hydrazine degradation, Nat. Commun. 12(1) (2021) 4182. https://doi.org/10.1038/s41467-021-24529-3.

[132] F. Dionigi, T. Reier, Z. Pawolek, M. Gliech, P. Strasser, Design Criteria, Operating Conditions, and Nickel-Iron Hydroxide Catalyst Materials for Selective Seawater Electrolysis, ChemSusChem 9(9) (2016) 962-72. https://doi.org/10.1002/cssc.201501581.

[133] Y. Zhang, Z. Zhang, Z. Yu, A. Addad, Q. Wang, P. Roussel, S. Szunerits, R. Boukherroub, Ruthenium Oxide Nanoparticles Immobilized on Ti_3C_2 MXene Nanosheets for Boosting Seawater Electrolysis, ACS Appl. Mater. Interfaces 15(50) (2023) 58345-58355. https://doi.org/10.1021/acsami.3c12254.

[134] L. Yu, Q. Zhu, S. Song, B. McElhenny, D. Wang, C. Wu, Z. Qin, J. Bao, Y. Yu, S. Chen, Z. Ren, Non-noble metal-nitride based electrocatalysts for high-performance alkaline seawater electrolysis, Nat. Commun. 10(1) (2019) 5106. https://doi.org/10.1038/s41467-019-13092-7.

[135] H. Jin, X. Liu, A. Vasileff, Y. Jiao, Y. Zhao, Y. Zheng, S.Z. Qiao, Single-Crystal Nitrogen-Rich Two-Dimensional Mo_5N_6Nanosheets for Efficient and Stable Seawater Splitting, ACS Nano 12(12) (2018) 12761-12769. https://doi.org/10.1021/acsnano.8b07841.

[136] L. Yu, L. Wu, B. McElhenny, S. Song, D. Luo, F. Zhang, Y. Yu, S. Chen, Z. Ren, Ultrafast Room-Temperature Synthesis of Porous S-Doped Ni/Fe (Oxy)Hydroxide Electrodes For Oxygen Evolution Catalysis in Seawater Splitting, Energy Environ. Sci. 13(10) (2020) 3439-3446. https://doi.org/10.1039/d0ee00921k.

[137] M. Yue, X. He, S. Sun, Y. Sun, M.S. Hamdy, M. Benaissa, A.A.M. Salih, J. Liu, X. Sun, Co-doped Ni_3S_2 nanosheet array: A high-efficiency electrocatalyst for alkaline seawater oxidation, Nano Res. (2023) 1998-0124 https://doi.org/10.1007/s12274-023-6002-6.

[138] L. Tan, J. Yu, C. Wang, H. Wang, X. Liu, H. Gao, L. Xin, D. Liu, W. Hou, T. Zhan, Partial Sulfidation Strategy to NiFe-LDH@$FeNi_2S_4$ Heterostructure Enable High-Performance Water/Seawater Oxidation, Adv. Funct. Mater. 32(29) (2022) 2200951. https://doi.org/10.1002/adfm.202200951.

[139] D. Yan, C. Mebrahtu, S. Wang, R. Palkovits, Innovative Electrochemical Strategies for Hydrogen Production: From Electricity Input to Electricity Output,

Angew. Chem. Int. Ed. 62(16) (2023) e202214333. https://doi.org/10.1002/anie.202214333.

[140] J.N. Hausmann, R. Schlögl, P.W. Menezes, M. Driess, Is direct seawater splitting economically meaningful?, Energy Environ. Sci. 14(7) (2021) 3679-3685. https://doi.org/10.1039/d0ee03659e.

[141] T. Wang, X. Cao, L. Jiao, Progress in Hydrogen Production Coupled with Electrochemical Oxidation of Small Molecules, Angew. Chem. Int. Ed. 61(51) (2022) e202213328. https://doi.org/10.1002/anie.202213328.

[142] Z. Yu, L. Liu, Recent Advances in Hybrid Seawater Electrolysis for Hydrogen Production, Adv. Mater. (2023) e2308647. https://doi.org/10.1002/adma.202308647.

[143] Y. Zhang, Z. Zhang, A. Addad, Q. Wang, P. Roussel, M.A. Amin, S. Szunerits, R. Boukherroub, 0D/2D Co_3O_4/Ti_3C_2 MXene Composite: A Dual-Functional Electrocatalyst for Energy-Saving Hydrogen Production and Urea Oxidation, ACS Appl. Energy Mater. 5(12) (2022) 15471-15482. https://doi.org/10.1021/acsaem.2c03052.

[144] Y. Wang, Z. Chen, H. Wu, F. Xiao, E. Cao, S. Du, Y. Wu, Self-assembly-induced mosslike Fe_2O_3 and FeP on electro-oxidized carbon paper for low-voltage-driven hydrogen production plus hydrazine degradation, ACS Sustainable Chem. Eng. 6(11) (2018) 15727-15736.

[145] C. Tang, R. Zhang, W. Lu, Z. Wang, D. Liu, S. Hao, G. Du, A.M. Asiri, Energy-saving electrolytic hydrogen generation: Ni_2P nanoarray as a high-performance non-noble-metal Electrocatalyst, Angewandte Chemie International Edition 56(3) (2017) 842-846.

[146] W. Yang, M. Peng, Y. Lv, M. Sun, J. Zhang, W. Li, Y. Fu, Selective electrooxidation of 2-hydroxybenzyl alcohol coupled with H_2 production promoted by surface reconstruction of β-$Ni(OH)_2$ nanosheets, Chem. Eng. J. 475 (2023) 146138. https://doi.org/10.1016/j.cej.2023.146138.

[147] Y. Song, X. Wan, Y. Miao, J. Li, Z. Ren, B. Jin, H. Zhou, Z. Li, M. Shao, Blocking oxygen evolution reaction for efficient organic electrooxidation coupling hydrogen production by using layered double hydroxide rich in active oxygen, Appl. Catal., B 333 (2023) 122808. https://doi.org/10.1016/j.apcatb.2023.122808.

[148] R.K. Singh, K. Rajavelu, M. Montag, A. Schechter, Advances in Catalytic Electrooxidation of Urea: A Review, Energy Technol. 9(8) (2021) 2100017. https://doi.org/10.1002/ente.202100017.

[149] B. Zhu, Z. Liang, R. Zou, Designing Advanced Catalysts for Energy Conversion Based on Urea Oxidation Reaction, Small 16(7) (2020) e1906133. https://doi.org/10.1002/smll.201906133.

[150] S. Huang, Q. Zhang, P. Xin, J. Zhang, Q. Chen, J. Fu, Z. Jin, Q. Wang, Z. Hu, Construction of Fe-doped NiS-NiS_2 Heterostructured Microspheres Via Etching Prussian Blue Analogues for Efficient Water-Urea Splitting, Small 18(14) (2022) 2106841. https://doi.org/10.1002/smll.202106841.

[151] L. Guo, J. Chi, J. Zhu, T. Cui, J. Lai, L. Wang, Dual-Doping $NiMoO_4$ With Multi-Channel Structure Enable Urea-Assisted Energy-Saving H_2 Production at Large Current Density In Alkaline Seawater, Appl. Catal., B 320 (2023) 121977.

https://doi.org/10.1016/j.apcatb.2022.121977.

[152] J.Y. Zhang, H. Wang, Y. Tian, Y. Yan, Q. Xue, T. He, H. Liu, C. Wang, Y. Chen, B.Y. Xia, Anodic Hydrazine Oxidation Assists Energy-Efficient Hydrogen Evolution over a Bifunctional Cobalt Perselenide Nanosheet Electrode, Angew. Chem. Int. Ed. 57(26) (2018) 7649-7653. https://doi.org/10.1002/anie.201803543.

[153] P. Tang, H. Wen, P. Wang, Hierarchically nanostructured Ni_2Fe_2N as an efficient electrocatalyst for hydrazine oxidation reaction, Chem. Eng. J. 431 (2022) 134123. https://doi.org/10.1016/j.cej.2021.134123.

[154] Y. Zhao, N. Jia, X.-R. Wu, F.-M. Li, P. Chen, P.-J. Jin, S. Yin, Y. Chen, Rhodium phosphide ultrathin nanosheets for hydrazine oxidation boosted electrochemical water splitting, Appl. Catal., B 270 (2020) 118880. https://doi.org/10.1016/j.apcatb.2020.118880.

[155] Y. Yu, S.J. Lee, J. Theerthagiri, Y. Lee, M.Y. Choi, Architecting the AuPt alloys for hydrazine oxidation as an anolyte in fuel cell: Comparative analysis of hydrazine splitting and water splitting for energy-saving H_2 generation, Appl. Catal., B 316 (2022) 121603. https://doi.org/10.1016/j.apcatb.2022.121603.

[156] T. Cui, J. Chi, J. Zhu, X. Sun, J. Lai, Z. Li, L. Wang, Tuning the size and chemisorption of FeP_4 by trace Ru doping for hydrazine-assisted hydrogen evolution in seawater at large-current-density, Appl. Catal., B 319 (2022) 121950. https://doi.org/10.1016/j.apcatb.2022.121950.

[157] X. Wang, W. Zhang, Q. Yu, X. Liu, Q. Liang, X. Meng, X. Wang, L. Wang, Fe-doped CoNiP@N-doped carbon nanosheet arrays for hydrazine oxidation assisting energy-saving seawater splitting, Chem. Eng. J. 446 (2022) 136987. https://doi.org/10.1016/j.cej.2022.136987.

[158] L. Zhang, Z. Wang, J. Qiu, Energy-Saving Hydrogen Production by Seawater Electrolysis Coupling Sulfion Degradation, Adv. Mater. 34(16) (2022) e2109321. https://doi.org/10.1002/adma.202109321.

[159] J. Du, D. Xiang, K. Zhou, L. Wang, J. Yu, H. Xia, L. Zhao, H. Liu, W. Zhou, Electrochemical hydrogen production coupled with oxygen evolution, organic synthesis, and waste reforming, Nano Energy 104 (2022) 107875. https://doi.org/10.1016/j.nanoen.2022.107875.

[160] L. Zhang, Y.Y. Qiu, Y. Zhou, G.H. Chen, M.C.M. van Loosdrecht, F. Jiang, Elemental sulfur as electron donor and/or acceptor: Mechanisms, applications and perspectives for biological water and wastewater treatment, Water Res. 202 (2021) 117373. https://doi.org/10.1016/j.watres.2021.117373.

[161] M. Zhang, J. Guan, Y. Tu, S. Chen, Y. Wang, S. Wang, L. Yu, C. Ma, D. Deng, X. Bao, Highly efficient H_2 production from H_2S via a robust graphene-encapsulated metal catalyst, Energy Environ. Sci. 13(1) (2020) 119-126. https://doi.org/10.1039/c9ee03231b.

[162] S. Zhang, Q. Zhou, Z. Shen, X. Jin, Y. Zhang, M. Shi, J. Zhou, J. Liu, Z. Lu, Y.N. Zhou, H. Zhang, Sulfophobic and Vacancy Design Enables Self-Cleaning Electrodes for Efficient Desulfurization and Concurrent Hydrogen Evolution with Low Energy Consumption, Adv. Funct. Mater. 31(31) (2021). https://doi.org/10.1002/adfm.202101922.

[163] C. Deng, C.Y. Toe, X. Li, J. Tan, H. Yang, Q. Hu, C. He, Earth-Abundant Metal-Based Electrocatalysts Promoted Anodic Reaction in Hybrid Water Electrolysis for Efficient Hydrogen Production: Recent Progress and Perspectives, Adv. Energy Mater. 12(25) (2022). https://doi.org/10.1002/aenm.202201047.

[164] Y. Li, X. Wei, L. Chen, J. Shi, Electrocatalytic Hydrogen Production Trilogy, Angew. Chem. Int. Ed. 60(36) (2021) 19550-19571. https://doi.org/10.1002/anie.202009854.

[165] Y. Guo, X. Yang, X. Liu, X. Tong, N. Yang, Coupling Methanol Oxidation with Hydrogen Evolution on Bifunctional Co-Doped Rh Electrocatalyst for Efficient Hydrogen Generation, Adv. Funct. Mater. (2022). https://doi.org/10.1002/adfm.202209134.

[166] K. Xiang, Z. Song, D. Wu, X. Deng, X. Wang, W. You, Z. Peng, L. Wang, J.-L. Luo, X.-Z. Fu, Bifunctional Pt–Co_3O_4 electrocatalysts for simultaneous generation of hydrogen and formate via energy-saving alkaline seawater/methanol co-electrolysis, J. Mater. Chem. A 9(10) (2021) 6316-6324. https://doi.org/10.1039/d0ta10501e.

[167] X. Du, M. Tan, T. Wei, H. Kobayashi, J. Song, Z. Peng, H. Zhu, Z. Jin, R. Li, W. Liu, Highly efficient and robust nickel-iron bifunctional catalyst coupling selective methanol oxidation and freshwater/seawater hydrogen evolution via CO-free pathway, Chem. Eng. J. 452 (2023). https://doi.org/10.1016/j.cej.2022.139404.

[168] S. Liu, H. Zhang, H. Yu, K. Deng, Z. Wang, Y. Xu, L. Wang, H. Wang, Defect-Rich PdIr Bimetallene Nanoribbons with Interatomic Charge Localization for Isopropanol-Assisted Seawater Splitting, Small 19(25) (2023) e2300388. https://doi.org/10.1002/smll.202300388.

[169] H. Zhang, Y. Wang, X. Li, K. Deng, H. Yu, Y. Xu, H. Wang, Z. Wang, L. Wang, Electrocatalytic upcycling of polyethylene terephthalate plastic to formic acid coupled with energy-saving hydrogen production over hierarchical Pd-doped NiTe nanoarrays, Appl. Catal., B 340 (2024) 123236. https://doi.org/10.1016/j.apcatb.2023.123236.

[170] X.-H. Wang, Z.-N. Zhang, Z. Wang, Y. Ding, Q.-G. Zhai, Y.-C. Jiang, S.-N. Li, Y. Chen, Ultra-thin $CoNi_{0.2}P$ nanosheets for plastics and biomass participated hybrid water electrolysis, Chem. Eng. J. 465 (2023) 142938. https://doi.org/10.1016/j.cej.2023.142938.

[171] X. Liu, Z. Fang, D. Xiong, S. Gong, Y. Niu, W. Chen, Z. Chen, Upcycling PET in parallel with energy-saving H_2 production via bifunctional nickel-cobalt nitride nanosheets, Nano Res. (2022). https://doi.org/10.1007/s12274-022-5085-9.

[172] R. Shi, K.S. Liu, F. Liu, X. Yang, C.C. Hou, Y. Chen, Electrocatalytic reforming of waste plastics into high value-added chemicals and hydrogen fuel, Chem. Commun. 57(94) (2021) 12595-12598. https://doi.org/10.1039/d1cc05032j.

[173] Z. Chen, W. Wei, Y. Shen, B.-J. Ni, Defective nickel sulfide hierarchical structures for efficient electrochemical conversion of plastic waste to value-added chemicals and hydrogen fuel, Green Chem. 25(15) (2023) 5979-5988. https://doi.org/10.1039/d3gc01499a.

Chapter II. Materials and Characterization Techniques.

II.1 Reagents and Material

Iron(III) nitrate nonahydrate ($Fe(NO_3)_3·9H_2O$), iron(III) chloride hexahydrate ($FeCl_3·6H_2O$), iron(II) chloride tetrahydrate ($FeCl_2·4H_2O$), ammonium iron(II) sulfate hexahydrate ($(NH_4)_2FeSO_4·6H_2O$), cobalt(II) chloride hexahydrate ($CoCl_2·6H_2O$), cobaltous nitrate hexahydrate ($Co(NO_3)_2·6H_2O$), chloroplatinic acid hydrate ($H_2PtCl_6×H_2O$, 99.9%), urea, sodium chloride (NaCl, 99.5%), hydrochloric acid (HCl, 38%), potassium hydroxide (KOH, 85%), chloroplatinic acid hydrate ($H_2PtCl_6×H_2O$, 99.9%), ethylene glycol (EG, 99.5%), poly(vinylidene fluoride) ($(CH_2CF_2)_n$, Mw ~534,000)), carbon black (99%), and 1-methyl-2-pyrrolidinone (C_5H_9NO, 99.5%) were purchased from Sigma-Aldrich (France) and used without further purification.

Acetone and ethanol were procured from Fisher Scientific SAS (Illkirch, France). Iron foam (FF) (100 × 100 mm^2, thickness=0.5 mm) and nickel foam (NF) (200 × 300 mm^2, thickness=1 mm) were obtained from Kunshan Lvchuang Electronic Technology Co., Ltd, China. Solar cell (50 × 50 mm^2, 2V) was purchased from Xu-Neng Trading Co., Ltd, China. The water used throughout the experiments was purified with an ultrapure water purification system Arium® comfort I from Sartorius (resistivity = 18.2 MΩ.cm). The H-type cell membrane (Dupont Proton Exchange Membrane N117) has the following characteristics: Thickness (183 μm), density (360 g/m^2), conductivity (0.083 S/cm), exchange capacity (0.89 meq/g). Pre-treatment method: the membrane was soaked in 5 wt.% of hydrogen peroxide (H_2O_2) for 1 h at 80ºC, then placed in deionized water for 0.5 h, and finally treated with 5 wt.% of sulfuric acid for 0.5 h at 80ºC.

II.2 Characterization

II.2.1 Scanning electron microscopy (SEM)

Scanning electron microscopy (SEM) is a widely employed technique for the observation of surface morphology. The fundamental principle involves capturing signals, particularly secondary electrons, generated when a high-energy electron beam irradiates the sample surface. These signals form distinct images, providing topographical information about the sample surface. Besides secondary electrons, the irradiated area can also generate characteristic X-rays. Utilizing an Energy Dispersive Spectrometer (EDS) allows for the analysis of element content and types based on the obtained X-ray information, enabling elemental scanning analysis [1].

SEM images of the synthesized samples in the thesis were acquired using the Hitachi-SU5000 electron microscope, featuring a thermal field emission emitter and three distinct detectors (EsB detector with filter grid, high-efficiency In-lens SE detector, and Everhart-Thornley secondary electron detector). Elemental mapping in Energy Dispersive Spectroscopy (EDS) utilized the k-line. Each image point underwent spectrum recording within the range of 0 to 20 KeV.

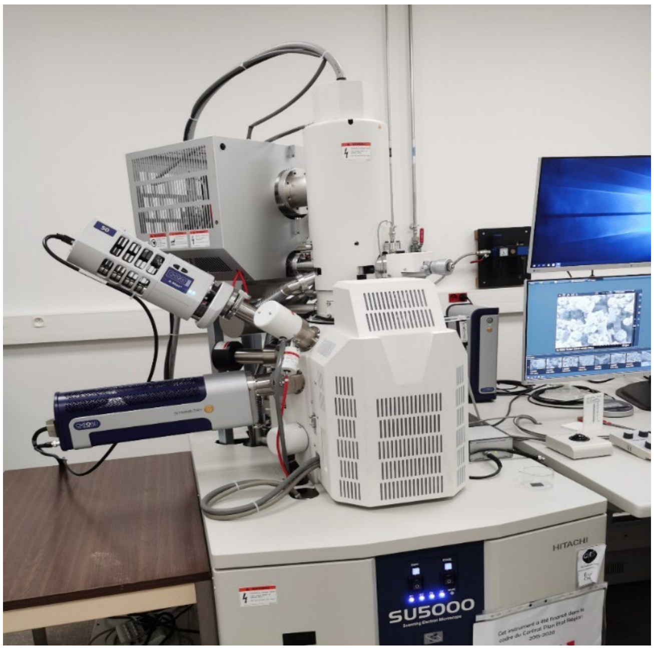

Figure 2.1. Hitachi SU5000 Schottky Field-Emission SEM

II.2.2 Transmission electron microscopy (TEM)

Transmission electron microscopy (TEM) facilitates detailed microscopic morphological observations of the prepared materials. By performing high-resolution inspection of specific selected areas, lattice fringes in the material can be observed. Additionally, surface elemental analysis (mapping) of the selected material provides a precise image of the element distribution on the sample surface [2]. In this thesis, TEM imaging was conducted using a TECNAI-G2 instrument equipped with an EDS spectrometer, operating at a working voltage of 200 kV. The samples grown on Ni foam or Fe foam were initially scratched off, dispersed on a thin carbon film of a 3 mm diameter copper grid, and then subjected to measurement.

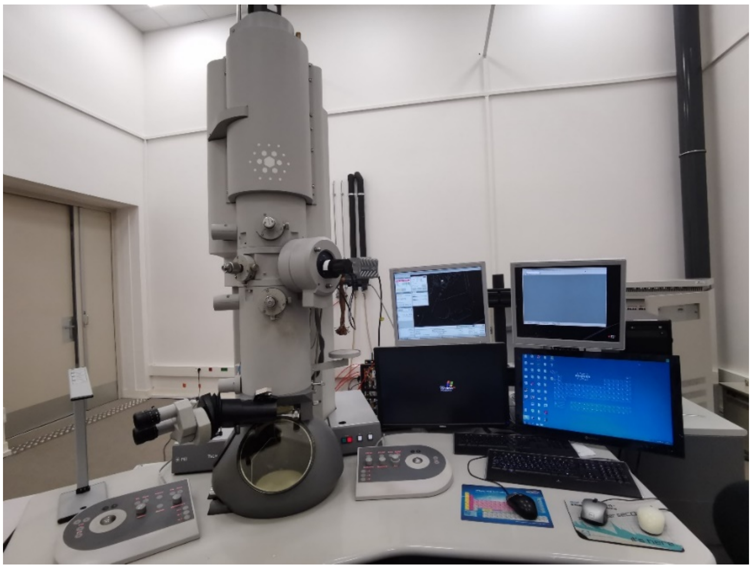

Figure 2.2 TECNAI-G2 FEI TEM instrument

II.2.3. X-ray diffraction (XRD)

X-ray diffraction (XRD) stands as a widely utilized technique for analyzing the phase and crystal structure of materials. The operational principle involves directing monochromatic X-rays onto the material's surface, leading to X-ray diffraction in various directions and intensities. Distinct diffraction patterns are obtained based on the diffraction direction and intensity, providing information about different phase components and crystal structures. When an X-ray beam intersects a sample, scattering occurs in all directions. The electric field of the X-ray wave interacts with electrons in an atom, leading to the emission of a wave with the same wavelength as the incident one. Consequently, the intensity of diffraction peaks in the diffractograms strongly correlates with the atomic number (Z) of the atoms involved in the diffraction phenomenon. Bragg's law describes the constructive interference between incident and emitted waves interacting with atoms in parallel planes((Eq.1). Therefore, the diffraction peaks exhibit varying relative intensities depending on crystal structure, aiding in the identification of phases [3, 4].

$$n \times \lambda = 2 \times d \times \sin(\theta) \text{ (Eq.1)}$$

where n corresponds to diffraction order; λ corresponds to X-ray wavelength; d is the interplanar distance; θ is the angle between the plane and incident X-ray wave, also known as Bragg angle.

Figure 2.3 D8 ADVANCE XRD instrument.

In this thesis, different foam samples were analyzed with XRD to obtain their crystal structure. XRD were recorded using a Bruker D8 ADVANCE Advance equipped with 1D LynxeEye detector at a scanning rate of 5° min^{-1} and 2θ value ranging from 5 to 80° using Cu Kα (α= 1.54056 Å) as the X-ray source and operates at a generator voltage of 45 kV and an anode current of 200 mA.

II.2.4 X-ray photoelectron spectroscopy (XPS)

X-ray photoelectron spectroscopy (XPS) is a technique rooted in the photoelectric effect, involving the emission of low-energy electrons, or photoelectrons, when a material is exposed to electromagnetic radiation [5-7]. In XPS analysis, the electromagnetic radiation originates from an X-ray source with a known energy, striking the material and prompting the emission of photoelectrons, whose kinetic energy is subsequently measured. During the analysis, the material's surface may become positively charged, particularly for non-conductive samples, causing a shift in kinetic energy. This can lead to miscalculations of binding energy. To address this issue, an internal standard is often employed, and low-energy electrons are injected with the assistance of a flood-gun device. The C 1s line from adventitious carbon is a common choice as an internal standard in many laboratories. Consequently, the C 1s spectrum is typically acquired at the beginning and end of analyses to verify its position (284.8 eV) [8]. In this thesis, X-ray photoelectron spectroscopy (XPS) analyses were carried out with a Kratos Axis Ultra DLD spectrometer using a monochromatic Al Kα source (1486.7 eV) operating at 225 W (15 kV). Data were treated with Casa XPS software and Avantage software applying Gaussian- Lorentzian profiles (Lorentzian 30%).

Figure 2.4. KRATOS AXIS UltraDLD used in this thesis.

II.2.5 Nuclear magnetic resonance (NMR)

Nuclear magnetic resonance (NMR) is a physical phenomenon whereby nuclei placed in a strong, constant magnetic field experience a perturbation from a weak, oscillating magnetic field (in the near field), resulting in the emission of an electromagnetic signal. This signal carries a frequency characteristic of the magnetic field at the nucleus. This phenomenon occurs in close proximity to resonance, where the oscillation frequency aligns with the intrinsic frequency of the nuclei, determined by factors such as the strength of the static magnetic field, the chemical environment, and the magnetic properties of the involved isotope. NMR spectroscopy exploits these magnetic properties to analyze the structure of organic molecules in solution and investigate molecular physics, crystals, and non-crystalline materials. The most commonly analyzed nuclei are ^{1}H and ^{13}C. In this thesis, ^{1}H and ^{13}C nuclear magnetic resonance (NMR) spectra were conducted on an NMR spectrometer (Bruker AVANCE 300 MHz), using 50 μL deuterium oxide + 550 μL sample water solution.

Figure 2.5 NMR spectrometer (Bruker AVANCE 300 MHz).

II.2.6 Inductively-coupled plasma optical emission spectrometry (ICP)

Inductively-coupled plasma optical emission spectrometry (ICP-OES) is a widely employed technique for the detection and quantification of various elements. However, when dealing with solid samples such as catalyst powders, a pretreatment is essential since samples can only be directly injected into the equipment in liquid or gas states. Acid digestion is a common method applied to release the analytes (elements of interest in the analyses) into the final solution. For liquid samples, a nebulizer device is used to convert them into an aerosol, which is then transported to the plasma. Plasma is generated through the collision of argon atoms, flowing through a torch, with ions and electrons produced in argon gas by a spark from a Tesla coil, which is radiofrequency (RF) powered. The continuous addition of energy provided by RF-induced collisions sustains the plasma, reaching temperatures of 10,000 K in its core, and this plasma-sustaining methodology is known as "inductive coupling" (hence the term "ICP") [9]. Upon contact with the plasma, the aerosol is rapidly dried, leading to the transition of particles into the gaseous state, and decomposition may occur. At this stage, atoms are generated and subsequently excited and ionized. The relaxation of excited electrons to ground states releases photons with characteristic energies. Optical instruments focus these photons onto the entrance aperture of a wavelength selection device. Since the number of photons is proportional to the quantity of the analyte, a calibration curve for an element can be constructed using a standard sample. This curve, presenting a linear profile, is then utilized for quantification analyses.

The catalyst on the iron foam is first pretreated with a mixed solution of HNO_3 and HCl solution for several days until the sample is completely dissolved in the solution. The element component analysis was characterized by inductively coupled plasma - optical emission spectrometry (ICP-OES) using ICPOES Agilent 5110 spectrometer.

II.2.7 Water contact (CA) angle measurements

The water contact angle (CA) measurements were performed with Ossila L2004A1 analyzer using a 10 μL water droplet at room temperature, which could detect the hydrophilic/hydrophobic properties of the sample, giving valuable information on the chemical properties of the sample. Test principle: Place the sample on the table, set the instrument probe to drop the volume of water droplets one by one each time, adjust the lighting, lens focus and within the visual range, the instrument automatically calculates the contact angle value based on the formula. Each sample was tested three times and averaged to obtain the final water contact angle. Different numerical ranges of contact angles indicate different hydrophobic characters of surface materials. A contact angle between 0°~90° means that the material surface is hydrophilic. A contact angle between 90~150° means that the material surface is hydrophobic and the liquid is repellent to the surface. When the contact angle is higher than 150°, the material exhibits superhydrophobic properties, and the liquid is highly repellent to the surface and can easily slide off the material surface.

Figure 2.6. Ossila L2004A1 instrument used for the determination of the water contact angles.

II.2.8 pH measurements

The pH values of the different reaction solutions were determined three times using a pH meter (Mettler Toledo-S210). Calibrate the pH meter with calibration solution before each use.

Figure 2.7. pH Mettler Toledo-S210.

II.2.9 Gas chromatography

Gas chromatography (GC) was performed with a pneumatically operated automatic gas sampling valve on an Agilent 7890A gas chromatograph to monitor the liberated gas. The electrolysis cell was linked to the GC setup by means of custom-made airtight glass-to-metal adapters and 1/8 in internal diameter copper tubing. The oven temperature was set at 45 ° C, and Ar with a flow rate of roughly 3 mL min^{-1} was the carrier gas.

II.3 Electrochemical performance parameters

To evaluate the catalytic activity of electrocatalysts for water electrolysis, the following common performance parameters are employed: onset potential (E_{onset}) and overpotential, electrochemical active surface area (ECSA), Tafel slope, exchange current density, electrochemical impedance spectrum (EIS), long-term stability, turnover frequency (TOF), mass/specific activity, and Faraday efficiency (FE).

II.3.1 Electrode and electrolyte

Electrochemical measurements were performed using an electrochemical workstation (Autolab PGSTAT204, Metrohm) at ambient temperature in a standard three-electrode system. The working electrode consisted of our prepared catalysts, the counter electrode was a carbon rod, and the reference electrode was Ag/AgCl (saturated KCl) or saturated calomel electrode (SCE). For the water electrolysis process, we have chosen 1M KOH freshwater as the electrolyte. For seawater electrolysis, 1M KOH+0.5M NaCl freshwater (simulated seawater) and 1M KOH seawater (nature seawater) were used as the electrolytes. For urea oxidation reaction, 1M KOH+0.33M urea was applied as the electrolyte. For ethylene glycol (EG) oxidation reaction, we used 1M KOH+0.3M EG as the electrolyte.

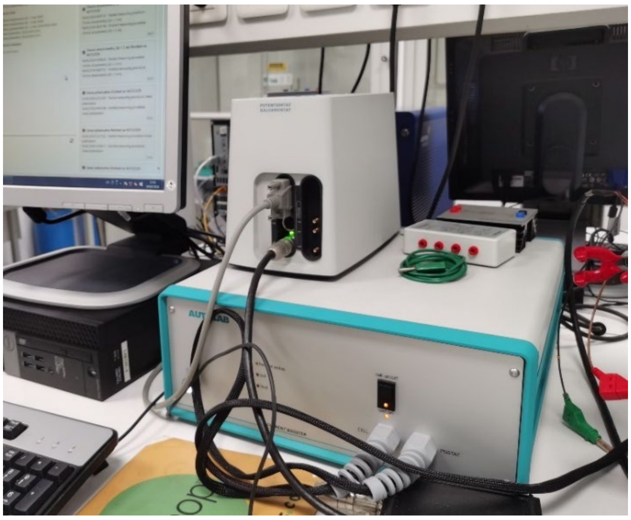

Figure 2.8. Electrochemical workstation (Autolab PGSTAT204, Metrohm) used for electrochemical studies.

II.3.2 Onset potential and overpotential

The onset potential (E_{onset}) is defined as the potential at which the Faraday reaction current initiates in linear sweep voltammetry (LSV) curves for the hydrogen evolution reaction (HER), oxygen evolution reaction (OER), and overall water splitting [10]. However, accurately determining E_{onset} poses challenges due to variations in material properties and instrument sensitivity. To address this issue, overpotential of electrode reaction is firstly introduced to assess electrocatalyst activity. For the electrocatalytic redox reaction, the applied potential can be expressed by the Nernst equation (Eq.2).

$$E = E^{\circ} + \frac{RT}{nF} \ln \frac{CO}{CR} \quad \text{(Eq.2)}$$

where E represents the applied electrode potential, E^0 is the standard potential, R is the gas constant, T is the thermodynamic temperature, F is the Faraday constant, and CO and CR are the concentrations of oxidized and reduced species, respectively.

In general, for better comparison of electrode reaction potentials, all applied potentials are expressed versus a reversible hydrogen electrode (RHE). However, potentials are often measured and reported with respect to reference electrodes other than the RHE, such as the saturated calomel electrode (SCE) or Ag/AgCl electrode. To standardize the evaluation criteria, the potential measurements were calibrated to a RHE based on the following equations (3-4) (pH=13.8, 1M KOH solution):

$$E_{RHE} = E_{Ag/AgCl} + 0.0591 \times pH + E_{0\ (Ag/AgCl,\ saturated\ KCl)} \quad (Eq.3)$$

$$E_{RHE} = E_{Ag/AgCl} + 1.014\ (E_0 = 0.197\ V)$$

$$E_{RHE} = E_{SCE} + 0.0591 \times pH + E_{0SCE} \quad (Eq.4)$$

$$E_{RHE} = E_{SCE} + 1.058 \quad (E_{0SCE} = 0.242\ V)$$

The water-splitting process through electrolysis requires a potential greater than the thermodynamic voltage of 1.23 V to overcome the resistance. This additional voltage is termed as overpotential (η) and represented in the following Eq.5, where E_{eq} denotes the equilibrium potential.

$$\eta = E - Eeq \quad (Eq.5)$$

In order to better evaluate catalyst performance, we need to eliminate additional resistance errors from the instrument, and between electrolytes and catalysts. iR compensation was the effective method to eliminate the impact of IR drop for electrocatalyst reaction process. For this system, we derived LSV polarization curves using 90% iR-correction. As shown in equation Eq.6, the common 90% iR-correction could effectively eliminate the errors caused by solution resistance and open circuit potential.

$$V = V_{measured} - I_{measured} * R_s * 90\% - V_{OCP} \quad (Eq.6)$$

R_s is the resistance of solution and V_{OCP} is the open-circuit potential.

II.3.3 Cyclic voltammetry (CV)

For the HER performance, linear sweep voltammetry (LSV) curves were recorded separately in 1 M KOH, 1M KOH+0.5M NaCl, 1M KOH seawater, 1M KOH+0.33M urea, and 1M KOH+0.3M EG at a scan rate of 5 mV s^{-1} over the potential range from -1 to -1.7 V (*vs.* RHE). It is important to note that the current density was normalized to the geometrical surface area. For the OER performance, cyclic voltammetry (CV) curves were recorded separately in 1M KOH, 1M KOH+0.5M NaCl, 1M KOH seawater, 1M KOH+0.33M urea, and 1M KOH+0.3M EG solutions in the potential range of 1.0 ~ 1.8 V (*vs.* RHE) at a scan rate of 5 mV s^{-1}.

II.3.4 Tafel slope and exchange current density

In electrochemical reaction systems, the reaction kinetics for HER/OER can be revealed by Tafel slopes, which represent the change rate relation of overpotential (η) with current density [11, 12]. The most common way of obtaining the Tafel slope value is by fitting the linear part of the Tafel curve (η *vs.* log|j|) derived from the LSV curve (j *vs.* E) [13]. Specifically, the Tafel plot portrays the relation between steady-state current densities and overpotentials, which is represented by the Butler–Volmer equation (7).

$$\mathrm{i} = \boldsymbol{i_0}[\boldsymbol{exp}\left(\alpha_a \boldsymbol{n}\frac{\boldsymbol{FE}}{\boldsymbol{RT}}\right) + \boldsymbol{exp}\ (\alpha_c \boldsymbol{n}\frac{\boldsymbol{F}}{\boldsymbol{RT}}] \text{ (Eq.7)}$$

where i_0 is the exchange current density, and α_a and α_c are the symmetrical coefficients for the anode and cathode, respectively.

The Tafel equation (8) is expressed as:

$$\eta = \boldsymbol{a} + \boldsymbol{b}\,\mathbf{log}(\boldsymbol{j}) \text{ (Eq.8)}$$

From the Tafel equation, we can derive two important parameters, namely, the Tafel slope (b) and exchange current density (j_0).

The small Tafel slope means that increasing the current density of the same magnitude requires a lower overpotential, which means the electrocatalyst has faster reaction kinetics. In addition, the Tafel slope plays a key role in revealing reaction mechanisms and identifying rate-determining steps. Exchange current density (j_0) is another critical parameter for evaluating the inherent kinetic properties of an electrocatalyst, which can be determined by extrapolating the Tafel curve in the x-axis direction. A higher j_0 in an electrode reaction implies that the required driving force (external current density) is lower, indicating that the electrochemical reaction proceeds more easily.

II.3.5 Electrochemical impedance spectroscopy (EIS)

EIS is an electrochemical measurement method that uses a small amplitude sinusoidal potential (or current) as the perturbation signal for the analysis of HER/OER kinetics and the electrode/electrolyte interface reactions [14-17]. The choice of the frequency range significantly influences the information derived from EIS spectra. For instance, the resistance values obtained in the high-frequency region (where no Faraday reaction occurs) can reflect the solution resistance of the catalytic material with the electrolyte, denoted as Rs. The low-frequency region contains much richer kinetic information, illustrating the speed of charge transfer from the electrocatalyst surface to the reactant, i.e., the charge transfer resistance (Rct). A smaller Rct indicates a fast-kinetic process, suggesting excellent catalytic activity of the electrocatalyst.

For HER process, EIS measurements were performed separately in the potential range of +0.114 ~ -0.386 V (*vs.* RHE) in the frequency range of 100 kHz to 0.01 Hz at an amplitude of 10 mV.

For OER/UOR/EGOR process, EIS measurements were acquired separately in the potential range of 1.0 ~ 1.5 V (*vs.* RHE) in the frequency range of 100 kHz to 0.01 Hz at an amplitude of 10 mV. R_s could be obtained from the resistance recorded at the frequency of 100 kHz.

II.3.6 Electrochemical active surface area (ECSA)

Accurate estimate of the electrochemical active surface area of catalysts is of considerable importance for an exact assessment of the number of active sites [18, 19]. The ECSA is determined using double layer capacitance (C_{dl}). The ECSA was explored by measuring the capacitive current associated with the double-layer charging from the scan-rate dependence of the CV plots. The CV potential window of 0.85-0.95 V (*vs.* RHE) was applied for the OER/EGOR/UOR process at various scan rates (20, 40, 60, 80, 100 and 120 mV s^{-1}), while the potential window of CV was 0.1-0.2 V *versus* RHE for HER process. The double-layer capacitance (C_{dl}) was calculated by plotting the ΔJ = ($Ja - J$c) at the middle of potential against the scan rate, while the linear slope is twice of the double-layer capacitance C_{dl}. High C_{dl} values mean larger exposed surface-active sites and higher current density.

II.3.7 Mass and specific activity

Mass activity is an accurate way to evaluate catalyst performance, which represents catalytic activity per electrocatalyst mass unit. In general, higher loading enhances activity resulting in lower η at the same current density, whereas reaction activity remains the same or decreasing as the load increases to the threshold. The reason could be that excessive loading impedes charge and mass transfer, causing a decline in activity. Specific activity, which evaluates intrinsic activity, is normalized by the electrode current to the ECSA or Brunauer–Emmett–Teller (BET) surface area. Specific activity eliminates the effects of active site number and mass loading, providing intrinsic activity per catalytic site [20].

II.3.8 Stability

The robustness of the catalyst is determined by long-term stability testing. Good structural and catalytic stabilities of a catalyst are of crucial importance especially for seawater electrolysis application. There are three typical strategies to obtain durability data for electrocatalysts: performing multiple CV cycles; chronopotentiometry and chronoamperometry [21-25]. During the CV process, the decay of the catalyst overpotential after hundreds to thousands of cycles is observed to determine the stability of the catalyst. Furthermore, stability data obtained with the chronopotentiometry and chronoamperometry methods are more convincing, and are adapted to real industry electrolytic water condition producing hydrogen at a constant high current density.

In this project, we used three different methods to verify the stability of the catalysts. For HER process, our prepared samples were evaluated by chronopotentiometry at a current density of ~10 and 100 mA cm^{-2} for long time separately in 1M KOH, 1M KOH+0.5M NaCl and 1M KOH seawater solutions. The chronoamperometry curves were acquired at a constant voltage of 1.5 V for 34 h to further evaluate the catalyst stability. In addition, 1000 CV cycles were recorded at a scan rate of 10 mV s^{-1} in the potential range from -1 to -1.7 V (*vs.* RHE). For OER process, the stability of A-CoFeNi sample was conducted by chronoamperometry at a voltage of 1.5 V for 105 h separately in 1M KOH, 1M KOH+0.5M NaCl and 1M KOH seawater solutions. The stability of NiFe LDH-Ni_2S_3 sample was conducted by chronopotentiometry at a current density of -10 mA cm^{-2} for 35 h separately in 1M KOH, 1M KOH+0.5M NaCl and 1M KOH seawater solutions. The multistep chronoamperometric measurements were acquired at various overpotentials. In addition, 1000 CV cycles were recorded at a scan rate of 10 mV s^{-1} in the potential range from 0.8 to 1.8 V (vs. RHE).

II.3.9 Turnover frequency (TOF)

For the same metal particles on carriers with different surface areas, specific activity varies but is not reflected in the specific activity [26]. In addition, different tests are always recorded using different electrocatalysts loading masses, which makes it difficult to judge the catalytic performance. To this end, turnover frequency (TOF) was developed by Boudart to more precisely describe the intrinsic activity of catalysts [27]. A high TOF value indicates an outstanding catalytic activity. The TOF is defined as the number of molecules that are catalytically generated per catalytic site per second and can be calculated by the following equation:

$$TOF = \frac{j \times A}{\alpha \times F \times n} \qquad \text{(Eq.9)}$$

where α represents the number of electrons transferred for conversion of reactants to one mole target product (O_2=4; H_2=2), F is the Faraday constant (96485 C mol^{-1}), n is the number of the moles of active sites, j is the current density, A is the working electrode geometric area.

II.3.10 Faradaic efficiency

Faradaic efficiency (FE) measures charge transfer efficiency in electrochemical reactions, essential for energy conversion efficiency assessment.

Cathode product analysis

The two common methods for calculating H_2 production FE are the water–gas displacement method and the gas chromatography (GC) method. Both methods require a sufficient volume of gas to minimize measurement errors.

Firstly, to achieve this, the volume of the gas liberated under the experimental conditions (designated here as V_{measured}) was first determined by gas chromatography (GC). The employed experimental conditions consisted on holding the catalyst at -1.0 V *vs.* RHE (for the HER) for 1 h in 1.0 M KOH solutions at 25 ºC during a controlled potentiostatic electrolysis (CPE). The FE value was then calculated using the ratio (Eq.10):

$$V_{\text{measured}}/V_{\text{calculated}} \quad \text{(Eq.10)}$$

where $V_{\text{calculated}}$ denotes the theoretical volume of the gas (the amount of the gas calculated from the charge passed through the WE during CA assuming 100% Faradaic efficiency). Measurements were conducted in a two-compartment bulk electrolysis cell with standard configuration. The cell consists of three electrodes: a working electrode, a counter electrode (a graphite rod, Sigma-Aldrich, 99.999%) and a reference electrode (Hg/HgO, NaOH (0.1 M). The formula shown below (Eq. 11) is used to calculate the Faradaic efficiency values for both the HER and OER:

$$\text{Faradaic efficiency (\%)} = [F \times n \times \text{mol gas (GC)} \times 100] / Q\text{(CPE)} \quad \text{(Eq.11)}$$

Where *F* is the Faraday's constant (*F* = 96485 C), mol gas (GC) refers to the amount of the gas (either H_2 or O_2) released during a controlled potential electrolysis (CPE) by GC, and *Q*(CPE) is the charge passed through the *WE* during the CPE.

For A-CoFeNi (chart 4) and NiFe LDH-Ni_3S_2 (chart 5) systems, hydrogen was gathered by the water displacement technique employed during the overall seawater splitting process. Subsequently, the volume of the resulting ideal gas was determined, taking into account a 100% theoretical Faradaic efficiency. In order to accomplish this, the Faradic efficiency was calculated using the equation 11. We assessed the electrochemical performance by comparing the theoretical gas volume with the gas quantity obtained experimentally in a two-electrode system for both overall water-splitting (Eq. 12).

$$\text{Faradaic efficiency} = [zF \times (n_{H2})] / Q \quad \text{(Eq.12)}$$

whereas z represents the number of electrons involved in the reaction (2 for H_2), n_{H2} stands for the number of H_2 moles estimated approximately from the Ideal Gas Law, F is the Faraday constant (96485 C mol^{-1}). Q is the charge consumed during the electrolysis process (Q = I × t, I is a given value of a constant applied current in the test and t is the reaction time (s) under the constant applied current). In this system, constant-current electrolysis was carried out at a current density of 50 mA cm^{-2} under standard conditions for 1000 s.

Anode product analysis: Formate production

The liquid products were analyzed by ^{1}H and ^{13}C nuclear magnetic resonance (NMR) spectrometry. NMR samples were prepared by adding 550 μL of PET hydrolysate electrolyte and 50 μL D_2O, and then analyzed via NMR spectrometry. We obtained calibration curves from a series of standard HCOOK solutions and quantified the concentration of the product from its NMR peak area. The faradaic efficiency (%) yield, and productivity of the product formation could be determined by the following equation 13-15:

$$\text{FE (\%)} = \frac{\text{N(formate yied)}}{\text{Total charge/(3*96485)}} *100\% \ \text{(Eq.13)}$$

$$\text{Yield(\%)} = \frac{\text{N（formate yield）}}{\text{2N（inital EG）}} *100\% \ \text{(Eq.14)}$$

$$\text{Formate productivity (mmol cm}^{-2}\text{ h}^{-1}) = \frac{\text{Amont of produced formate}}{\text{Anode area} \times \text{Reaction time}} *100\% \ \text{(Eq.15)}$$

Where 3 presents mole electrons per mole formate, 96485 is the Faraday constant (C mol^{-1}) (Eq.13)

In addition, for the anode region, there exist an undesired chlorine evolution reaction (CER) in sea water, which produces hypochlorite and hypochlorous, damaging and poisoning the electrode materials. To further verify whether hypochlorite is formed during overall seawater splitting electrocatalysis, we performed a 1-h chronoamperometry measurement. Following the stability tests, the seawater electrolyte used was subsequently examined using *N, N*-diethyl-p-phenylenediamine (DPD) and KI reagent to determine whether any hypochlorite was formed. The possible formation of CI oxidation products (ClO^-) in the electrolytes during the OER,UOR and EGOR stability tests, respectively, was examined using the DPD method, in which the hypochlorite oxidizes the iodide to iodine, and the iodine then oxidizes DPD to a pink colored species with an intensity in direct proportion to the hypochlorite concentration.

References

[1] R. Sharma, W.D. Yang, Perspective and Prospects of In Situ Transmission/Scanning Transmission Electron Microscopy, Microscopy (Oxf) (2023). https://doi.org/10.1093/jmicro/dfad057.

[2] J.M. Thomas, C. Ducati, Transmission Electron Microscopy, Characterization of Solid Materials and Heterogeneous Catalysts2012, pp. 655-701. https://doi.org/https://doi.org/10.1002/9783527645329.ch16.

[3] M. Behrens, R. Schlögl, X-Ray Diffraction and Small Angle X-Ray Scattering, Characterization of Solid Materials and Heterogeneous Catalysts2012, pp. 609-653. https://doi.org/https://doi.org/10.1002/9783527645329.ch15.

[4] H. Stanjek, W. Häusler, Basics of X-ray Diffraction, Hyperfine Interact. 154(1) (2004) 107-119. https://doi.org/10.1023/B:HYPE.0000032028.60546.38.

[5] J. Timoshenko, B. Roldan Cuenya, In Situ/Operando Electrocatalyst Characterization by X-ray Absorption Spectroscopy, Chem. Rev. 121(2) (2021) 882-961. https://doi.org/10.1021/acs.chemrev.0c00396.

[6] R. Mom, L. Frevel, J.J. Velasco-Velez, M. Plodinec, A. Knop-Gericke, R. Schlogl, The Oxidation of Platinum under Wet Conditions Observed by Electrochemical X-ray Photoelectron Spectroscopy, J. Am. Chem. Soc. 141(16) (2019) 6537-6544. https://doi.org/10.1021/jacs.8b12284.

[7] M. Favaro, W.S. Drisdell, M.A. Marcus, J.M. Gregoire, E.J. Crumlin, J.A. Haber, J. Yano, An Operando Investigation of (Ni–Fe–Co–Ce)Ox System as Highly Efficient Electrocatalyst for Oxygen Evolution Reaction, ACS Catal. 7(2) (2017) 1248-1258. https://doi.org/10.1021/acscatal.6b03126.

[8] G. Greczynski, L. Hultman, A step-by-step guide to perform x-ray photoelectron spectroscopy, J. Appl. Phys. 132(1) (2022). https://doi.org/10.1063/5.0086359.

[9] X. Hou, R.S. Amais, B.T. Jones, G.L. Donati, Inductively Coupled Plasma Optical Emission Spectrometry, Encyclopedia of Analytical Chemistry2021, pp. 1-29. https://doi.org/https://doi.org/10.1002/9780470027318.a5110.pub4.

[10] N.T. Suen, S.F. Hung, Q. Quan, N. Zhang, Y.J. Xu, H.M. Chen, Electrocatalysis for the oxygen evolution reaction: recent development and future perspectives, Chem. Soc. Rev. 46(2) (2017) 337-365. https://doi.org/10.1039/c6cs00328a.

[11] S. Parvin, A. Kumar, A. Ghosh, S. Bhattacharyya, An earth-abundant bimetallic catalyst coated metallic nanowire grown electrode with platinum-like pH-universal hydrogen evolution activity at high current density, Chem. Sci. 11(15) (2020) 3893-3902. https://doi.org/10.1039/d0sc00754d.

[12] Y. Liu, Y. Dou, S. Li, T. Xia, Y. Xie, Y. Wang, W. Zhang, J. Wang, L. Huo, H. Zhao, Synergistic Interaction of Double/Simple Perovskite Heterostructure for Efficient Hydrogen Evolution Reaction at High Current Density, Small Methods 5(2) (2021) e2000701. https://doi.org/10.1002/smtd.202000701.

[13] Y. Shi, B. Zhang, Recent advances in transition metal phosphide nanomaterials: synthesis and applications in hydrogen evolution reaction, Chem. Soc. Rev. 45(6) (2016) 1529-41. https://doi.org/10.1039/c5cs00434a.

[14] W. Chen, B. Wu, Y. Wang, W. Zhou, Y. Li, T. Liu, C. Xie, L. Xu, S. Du, M. Song,

D. Wang, Y. liu, Y. Li, J. Liu, Y. Zou, R. Chen, C. Chen, J. Zheng, Y. Li, J. Chen, S. Wang, Deciphering the alternating synergy between interlayer Pt single-atom and NiFe layered double hydroxide for overall water splitting, Energy Environ. Sci. 14(12) (2021) 6428-6440. https://doi.org/10.1039/d1ee01395e.

[15] K. Gu, D. Wang, C. Xie, T. Wang, G. Huang, Y. Liu, Y. Zou, L. Tao, S. Wang, Defect-Rich High-Entropy Oxide Nanosheets for Efficient 5-Hydroxymethylfurfural Electrooxidation, Angew Chem Int Ed Engl 60(37) (2021) 20253-20258. https://doi.org/10.1002/anie.202107390.

[16] C. Xie, W. Chen, S. Du, D. Yan, Y. Zhang, J. Chen, B. Liu, S. Wang, In-Situ Phase Transition Of WO_3 Boosting Electron And Hydrogen Transfer For Enhancing Hydrogen Evolution On Pt, Nano Energy 71 (2020) 104653. https://doi.org/10.1016/j.nanoen.2020.104653.

[17] P. Zhai, C. Wang, Y. Zhao, Y. Zhang, J. Gao, L. Sun, J. Hou, Regulating electronic states of nitride/hydroxide to accelerate kinetics for oxygen evolution at large current density, Nat. Commun. 14(1) (2023) 1873. https://doi.org/10.1038/s41467-023-37091-x.

[18] H.-S. Hu, Y. Li, Y.-R. Shao, K.-X. Li, G. Deng, C.-B. Wang, Y.-Y. Feng, NiCoP nanorod arrays as high-performance bifunctional electrocatalyst for overall water splitting at high current densities, J. Power Sources 484 (2021) 229269. https://doi.org/https://doi.org/10.1016/j.jpowsour.2020.229269.

[19] D. Voiry, M. Chhowalla, Y. Gogotsi, N.A. Kotov, Y. Li, R.M. Penner, R.E. Schaak, P.S. Weiss, Best Practices for Reporting Electrocatalytic Performance of Nanomaterials, ACS Nano 12(10) (2018) 9635-9638. https://doi.org/10.1021/acsnano.8b07700.

[20] Z.Y. Yu, Y. Duan, X.Y. Feng, X. Yu, M.R. Gao, S.H. Yu, Clean and Affordable Hydrogen Fuel from Alkaline Water Splitting: Past, Recent Progress, and Future Prospects, Adv. Mater. 33(31) (2021) e2007100. https://doi.org/10.1002/adma.202007100.

[21] J. Kang, F. Yang, C. Sheng, H. Xu, J. Wang, Y. Qing, Y. Wu, X. Lu, CoP Nanoparticle Confined in P, N Co-Doped Porous Carbon Anchored on P-Doped Carbonized Wood Fibers with Tailored Electronic Structure for Efficient Urea Electro-Oxidation, Small 18(24) (2022) e2200950. https://doi.org/10.1002/smll.202200950.

[22] D. Khalafallah, L. Xiaoyu, M. Zhi, Z. Hong, 3D Hierarchical NiCo Layered Double Hydroxide Nanosheet Arrays Decorated with Noble Metal Nanoparticles for Enhanced Urea Electrocatalysis, ChemElectroChem 7(1) (2019) 163-174. https://doi.org/10.1002/celc.201901423.

[23] D. Yang, Y. Gu, X. Yu, Z. Lin, H. Xue, L. Feng, Nanostructured Ni_2P-C as an Efficient Catalyst for Urea Electrooxidation, ChemElectroChem 5(4) (2018) 659-664. https://doi.org/10.1002/celc.201701304.

[24] C. Chen, S. He, K. Dastafkan, Z. Zou, Q. Wang, C. Zhao, Sea urchin-like $NiMoO_4$ nanorod arrays as highly efficient bifunctional catalysts for electrocatalytic/photovoltage-driven urea electrolysis, Chin. J. Catal. 43(5) (2022) 1267-1276. https://doi.org/10.1016/s1872-2067(21)63962-1.

[25] J. Xie, H. Qu, F. Lei, X. Peng, W. Liu, L. Gao, P. Hao, G. Cui, B. Tang, Partially Amorphous Nickel–Iron Layered Double Hydroxide Nanosheet Arrays For Robust

Bifunctional Electrocatalysis, J. Mater. Chem. A 6(33) (2018) 16121-16129. https://doi.org/10.1039/c8ta05054f.

[26] M. Boudart, A. Aldag, J.E. Benson, N.A. Dougharty, C. Girvin Harkins, On the specific activity of platinum catalysts, J. Catal. 6(1) (1966) 92-99. https://doi.org/https://doi.org/10.1016/0021-9517(66)90113-8.

[27] J. Yang, X. Du, B. Qiao, Comprehensive activity evaluation of single-atom catalysts, Chem Catal. 3(1) (2023) 100424. https://doi.org/https://doi.org/10.1016/j.checat.2022.09.049.

Chapter III: Preparation of Flower-shaped Co-Fe Layer Double Hydroxide Nanosheets Loaded with Pt Nanoparticles by Corrosion Engineering for Efficient Electrocatalytic Water Splitting

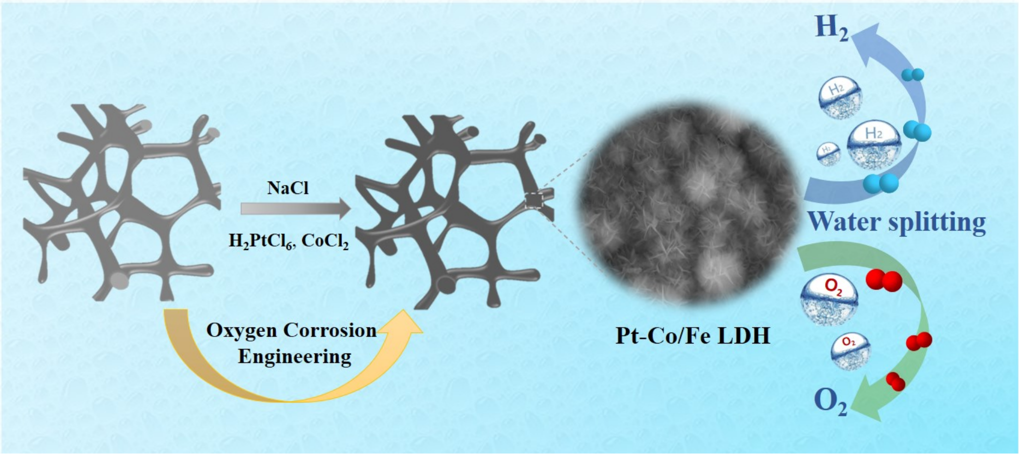

III.1. Abstract

Development of high-performance and cost-effective hydrogen evolution reaction (HER) and oxygen evolution reaction (OER) electrocatalysts is highly required for electrochemical water splitting. The sluggish reaction kinetics, poor stability as well as complicated processing restrict practical application of most electrocatalysts. Herein, we report a facile oxygen corrosion strategy for the fabrication of Pt nanoparticles loaded on cobalt-iron layer double hydroxide (Pt-Co/Fe LDH) on iron foam using oxygen corrosion method regulated by sodium chloride (NaCl). The as-prepared Pt-Co/Fe LDH electrodes featured overpotentials as low as 126 and 285 mV to deliver 100 mA cm^{-2} for HER and OER, respectively. Moreover, the Pt-Co/Fe LDH was applied as anode and cathode in an electrochemical electrolyzer and recorded a current density of 50 mA cm^{-2} at a small voltage of 1.66 V, which is superior to that of Pt/C-FF || RuO_2-FF system (1.89 V) and most of previously reported electrocatalysts. The excellent electrocatalytic activity of Pt-Co/Fe LDH could be assigned to its specific structure, consisting of 3D nanoflower-shaped nanosheets, favorable for promoting fast mass transport, ion diffusion and generation of more active sites for OER process. In addition, the synergistic effect between Pt and Co/Fe LDH heterojunction structure improves effectively the electronic

conductivity and H adsorption for HER performance. The oxygen corrosion method regulated by NaCl and interface engineering of the LDH structure is simple to implement and could be easily extended for the preparation of a plethora of other bifunctional and cost-effective electrocatalysts for various electrochemical processes.

III.2. Experimental section

Synthesis of Pt-Co/Fe LDH catalyst

Iron foam (FF) was pre-processed into 1×2 cm^2 and cleaned with acetone, hydrochloric acid (0.1 M), and ultrapure water *via* ultrasonic treatment (10 min each step) to remove the surface oxides and adsorbed organic molecules.

The Pt-Co/Fe LDH catalyst was synthesized *via* a one-step oxygen corrosion method at room temperature. Firstly, the cleaned FF was immersed in a mixture of 2 M NaCl, 50 mM $CoCl_2·6H_2O$ and 0.10 mM $H_2PtCl_6·\times H_2O$ and kept under shaking at room temperature for 15 h. The resulting brown-black product was washed copiously with deionized water and dried at 60 ºC for 8 h. Similarly, for further optimization of the electrocatalyst performance, various Co/Fe LDH samples were prepared by adjusting the $CoCl_2$ (0-100 mM) or NaCl content (0-4 M). In addition, NaCl-treated Fe foam, $CoCl_2$-Fe foam and Co/Fe LDH systems without Pt loading were also prepared for comparison and to gain some insights on the corrosion mechanism.

III.3. Results and discussion

III.3.1. Construction process of Pt-Co/Fe LDH catalysts

As a sustainable green-resource, high-purity hydrogen preparation *via* electrocatalytic water splitting method is widely used in energy research field, while methanol reforming and coal gasification approaches have been limited by the environmental pollution and low conversion rate, making them inefficient for future application [1]. In our strategy, in order to fabricate an efficient electrocatalyst, a 3D porous Fe foam (FF) with good electron transfer ability was considered as the prime substrate, and oxygen corrosion technology was applied to generate flower-shaped LDH structure with a large surface area and a myriad of exposed active sites. As illustrated in **Figure III.1**, hierarchical nanoarchitecture, Pt-Co/Fe double layer hydroxide (LDH), was prepared by introduction of a Pt salt during the oxygen corrosion process controlled by NaCl salt. More importantly, the entire preparation process was carried out at room temperature and could be easily adapted for large-scale production. Briefly, upon immersion of FF in $CoCl_2$, H_2PtCl_6 and NaCl mixed-solution, an *in-situ* growth process takes place at room temperature and continued for 15 h. The generated OH^- from the corrosion area reacts with metal ion to form metal hydroxide, while Pt nanoparticles were assembled on the nanoflowers' surface. Interestingly, the regulated oxygen corrosion was applied to construct Co/Fe LDH catalyst with the assistance of Cl^- anions to accelerate the corrosion process, which is a well-known chemical reaction pathway [2].

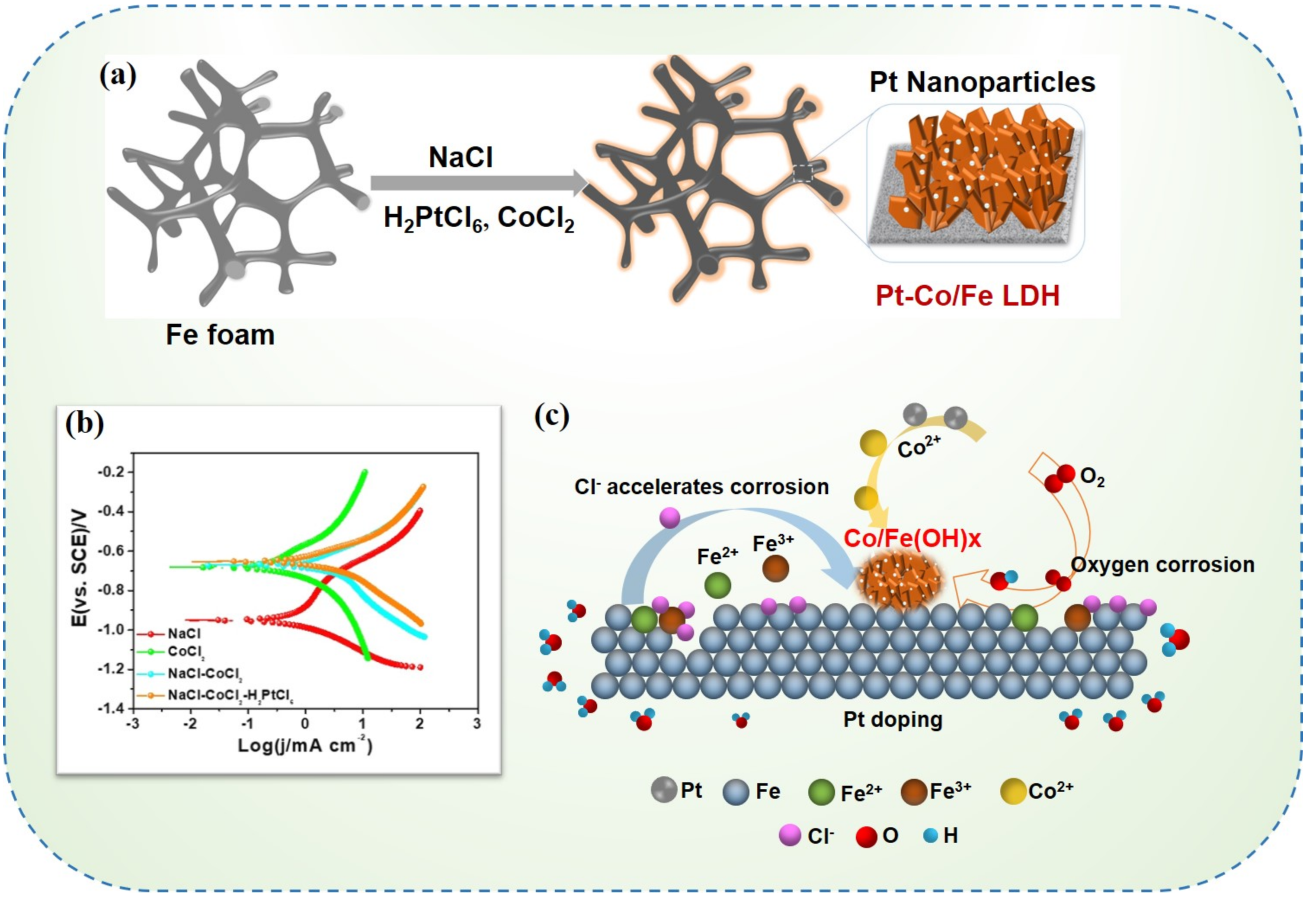

Figure III.1 (**a**) Schematic illustration of the one-step synthesis of Pt-Co/Fe LDH on Fe foam through oxygen corrosion method, (**b**) Corrosion polarization curves, and (**c**) *In-situ* growth mechanism of Pt-Co/Fe LDH.

To assess the corrosion displacement reaction mechanism, corrosion polarization curves were recorded for Fe foam (FF) immersed in 2 M NaCl, 5×10^{-2} M $CoCl_2$, 2 M NaCl + 5×10^{-2} M $CoCl_2$, 2 M NaCl + 5×10^{-2} M $CoCl_2$+ 0.10 mM H_2PtCl_6 aqueous solutions. FF, carbon rod and saturated calomel (SCE) electrodes were applied as working, counter and reference electrodes, respectively. Before recording the corrosion polarization curves, the pH values of the different reaction solutions were determined by a pH meter (Mettler Toledo-S210). Moreover, the open-circuit voltage (OCV) was firstly recorded and then the current-voltage curves were acquired in the potential window of OCV± 300 mV at a scan rate of 5 mV s^{-1}. To better analyze Fe/Co LDH corrosion growth mechanism, the corrosion polarization curves and solution pH values were determined and compared in **Figure III.2** and **Table 1**.

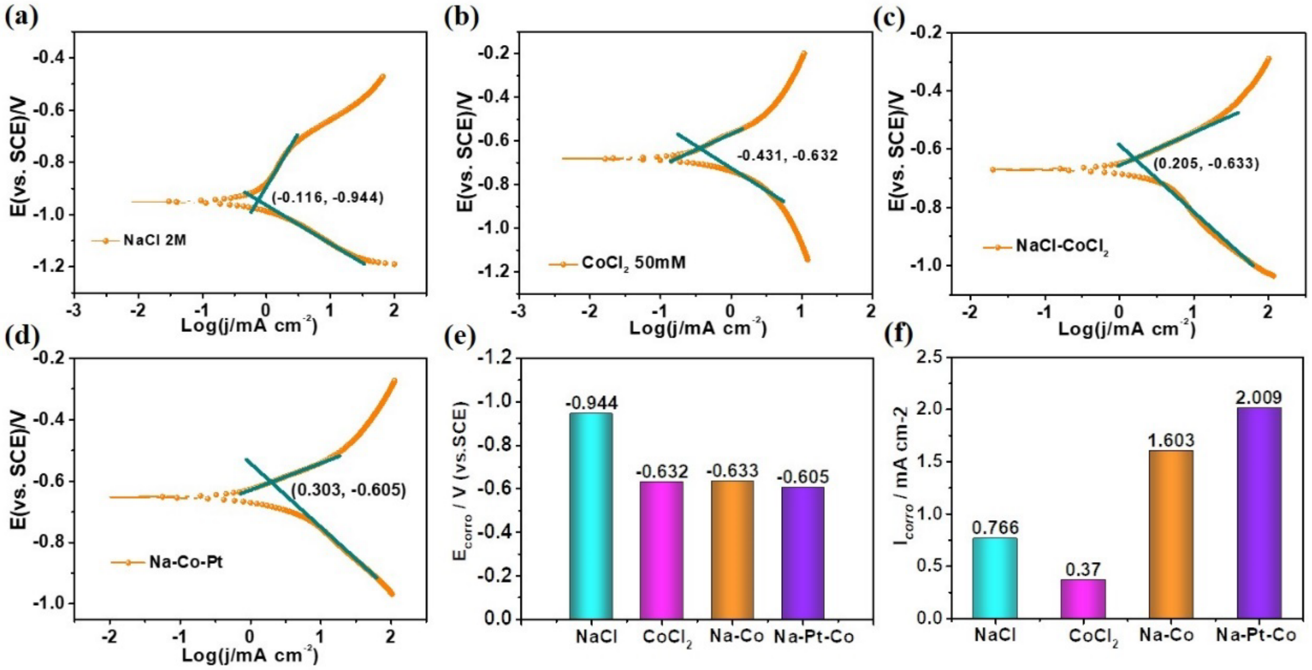

Figure III.2 Corrosion polarization curves of iron foam (FF) in (**a**) 2 M NaCl, (**b**) 50 mM $CoCl_2$, (**c**) 2 M NaCl+50 mM $CoCl_2$, and (**d**) 2 M NaCl+50 mM $CoCl_2$+$H_2PtCl_6\cdot(H_2O)_6$ aqueous solutions; (**e**) comparison of corrosion potentials (E_{corr}); (**f**) comparison of corrosion current densities (I_{corr}).

Solution	pH values tested for 3 times			Average pH value
NaCl	5.98	5.95	5.95	5.96
$CoCl_2$	5.42	5.47	5.48	5.46
NaCl-$CoCl_2$	5.53	5.54	5.55	5.54
NaCl-Pt-$CoCl_2$	4.50	4.49	4.49	4.49

Table 1. pH values of (**a**) 2 M NaCl, (**b**) 50 mM $CoCl_2$, (**c**) 2 M NaCl+50 mM $CoCl_2$ and (**d**) 2 M NaCl+50 mM $CoCl_2$ +0.10 mM $H_2PtCl_6\cdot(H_2O)_X$ aqueous solutions.

The corrosion polarization curves (**Figure III.1b** and **Figure III.2**) revealed that FF immersed in NaCl, $CoCl_2$ (in presence or absence of H_2PtCl_6) solutions exhibited different corrosion current densities (I_{corr}) and corrosion potentials (E_{corr}). Fe foam immersed in the NaCl-containing solutions, such as $CoCl_2$-NaCl and NaCl-$CoCl_2$-H_2PtCl_6 systems, displayed higher I_{corr} and E_{corr} compared with $CoCl_2$ system, inferring a stronger self-corrosion tendency. The values of the corrosion current density were 2.009 mA cm^{-2} (NaCl-$CoCl_2$-H_2PtCl_6) > 1.603 mA cm^{-2} (NaCl-$CoCl_2$) > 0.766 mA cm^{-2} (NaCl) > 0.370 mA cm^{-2} ($CoCl_2$). Benefiting from the natural power of corrosion, 3D Co/Fe LDH nanoflowers loaded with Pt nanoparticles were subtly constructed and designed, as shown in **Figure III.1c**. At the surface of FF, Fe atom was corroded and oxidized generating Fe^{2+}/Fe^{3+} ions and simultaneously releasing electrons, which combined with O_2 at the cathode to form OH^-. The sustained generation of metal hydroxide was ensured, owing to the chloride de-passivation ability which could destroy the metal oxide protective layer, while Pt particles were deposited on the layer surface [3, 4]. The weak acidic pH environment is favorable for the growth process of the Pt nanoparticles, Pt^{4+} ions can be easily reduced and form nanoparticle clusters [5]. So, Pt NPs formation is accompanied with $CoFe(OH)_x$ precipitation reaction, leading to Pt-Co/Fe LDH according to equations (1-3):

Anode reaction: $Fe \leftrightarrow Fe^{2+} + 2e^-$, $Fe^{2+} \leftrightarrow Fe^{3+} + e^-$ (1)

Cathode reaction: $O_2 + 2H_2O + 4e^- \leftrightarrow 4OH^-$ (2)

Precipitation reaction: $Fe^{3+} + Fe^{2+} + Co^{2+} + xOH^- \leftrightarrow CoFe(OH)_x$ (3)

III.3.2. Morphology and structural characterization

The morphology and nanofeatures of the samples were evaluated by scanning electron microscopy (SEM) and transmission electron microscopy (TEM) techniques. The SEM images of the FF support revealed its 3D microporous structure and smooth surface (**Figure III.3**). After exposure to 2 M NaCl solution for 15 h, the FF exhibited a rough surface and porous nodule phenomenon due to the corrosion reaction (**Figure III.4**).

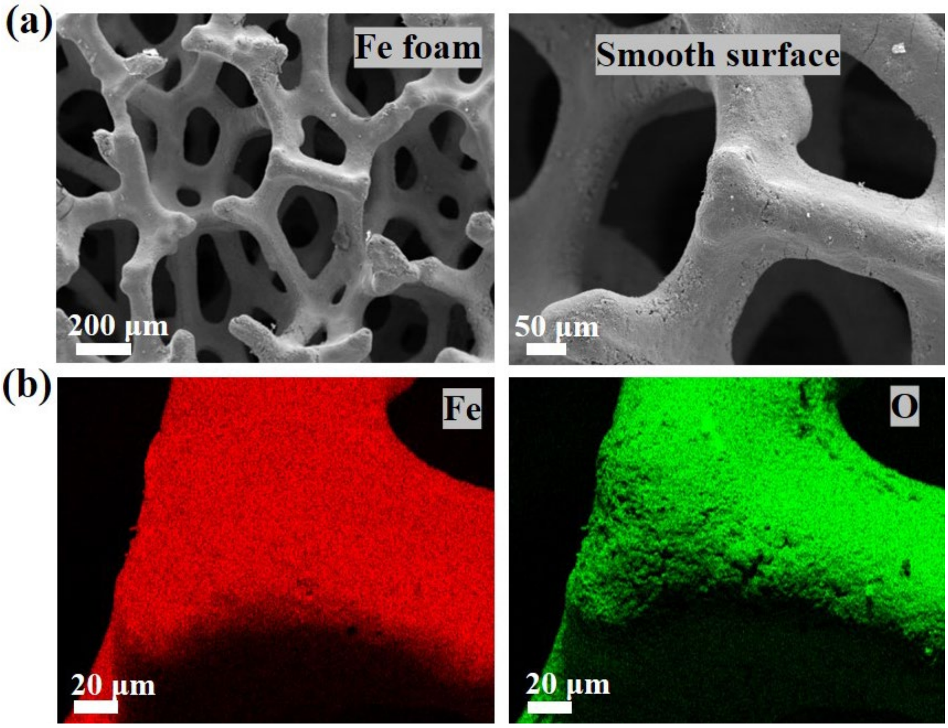

Figure III.3 (**a**) SEM images of Fe foam and (**b**) elemental mapping images of Fe and O.

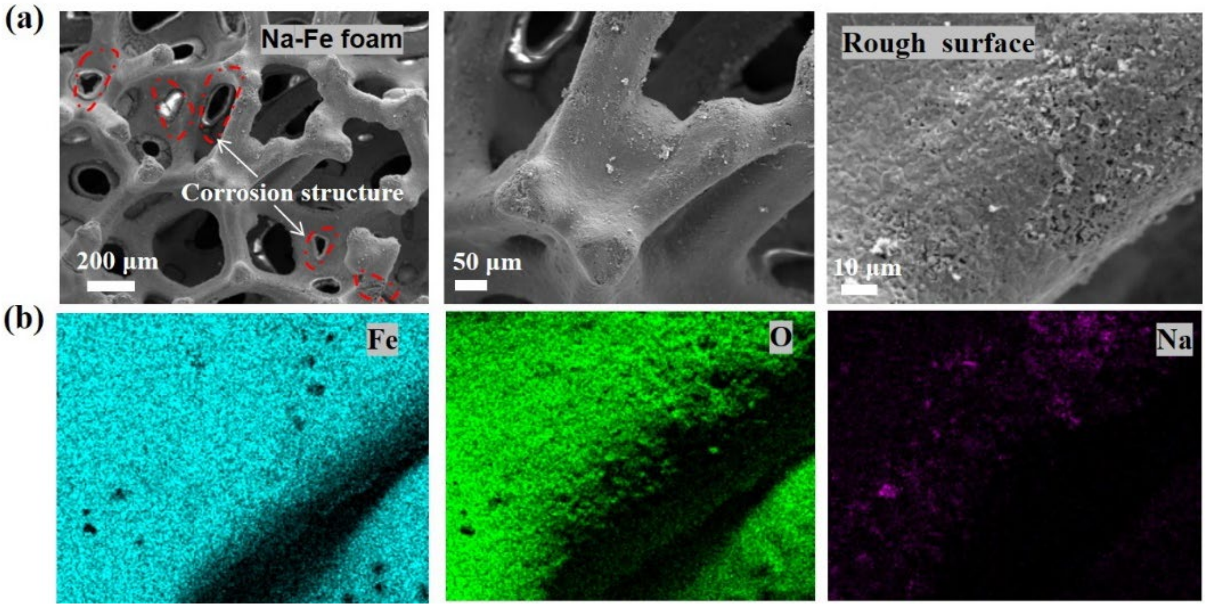

Figure III.4 (**a**) SEM images of Na-Fe foam corrosion region. It could be seen that oxygen corrosion occurred in some regions on the foam surface. (**b**) The corresponding EDS elemental mapping images of Fe, O and Na.

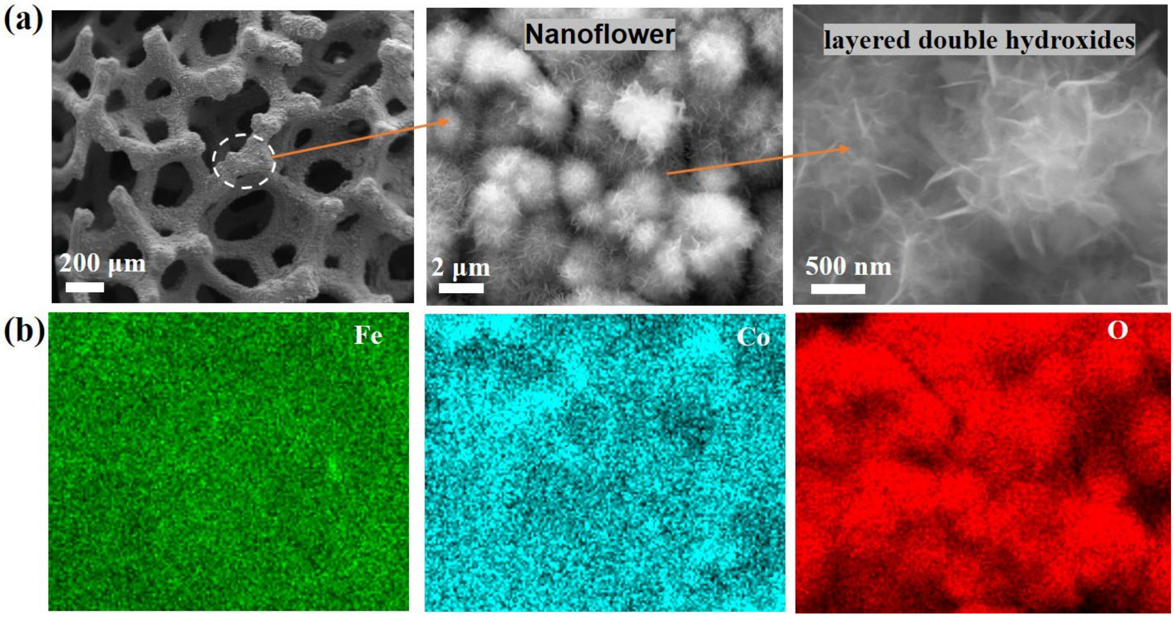

Figure III.5 (**a**) SEM images of the Co/Fe LDH, and (**b**) the corresponding EDS elemental mapping images of Fe, Co and O.

Notably, the SEM images of Pt-Co/Fe LDH catalyst showed a similar nanoflower morphology compared with that of Co/Fe LDH sample (**Figure III.5**), which was composed of numerous nanoflowers of 1~2 μm in size (**Figure III.6a-c**). In addition, it was evidenced that the Pt nanoparticles were uniformly distributed on the catalyst surface. The TEM image in **Figure III.6d** further confirmed a typical flower-like interconnected nanosheets on the Fe foam surface, forming a highly porous surface morphology with high amount of exposed active sites, which is expected to be beneficial for fast mass transport for effective electrocatalytic activity. The HR-TEM image revealed lattice fringe spacings of 0.25 and 0.33 nm corresponding to the (012) and (021) crystal planes of Co/Fe LDH (PDF-50-0235) and FeO(OH) (PDF-70-0714; PDF-34-1266), respectively, indicating a unique hierarchical heterojunction of Co/Fe LDH@FeO(OH) [6]. Furthermore, a distinctive lattice fringe of 0.221 nm was also identified in **Figure III.6f** and **Figure III.7**, which could be ascribed to the (110) plane of Pt. The selective area electron diffraction pattern comprised bright rings belonging to the (012), (015) and (110) planes of Co/Fe LDH. Energy dispersive X-ray spectroscopy (EDS) analysis **(Figure III.6h-i)** was employed to characterize the chemical composition and distribution of different elements. As expected, the presence of Fe (39.7 at. %), Co (16.6 at. %), O (42.6 at. %) and Pt (1.1 at. %) atoms is in full accordance with the chemical composition of the material. EDS mapping evidenced the homogeneous distribution of the different elements in Pt-Co/Fe LDH, which is favorable for electrocatalytic activity.

Furthermore, the Co element surface loading sites in Pt-Co/Fe LDH (surface loading ~ 9.57 at. % determined by XPS) was higher than the bulk loading ~1.18 at. % determined by ICP-OES **(Table 2)**; Pt element loading values followed a similar trend.

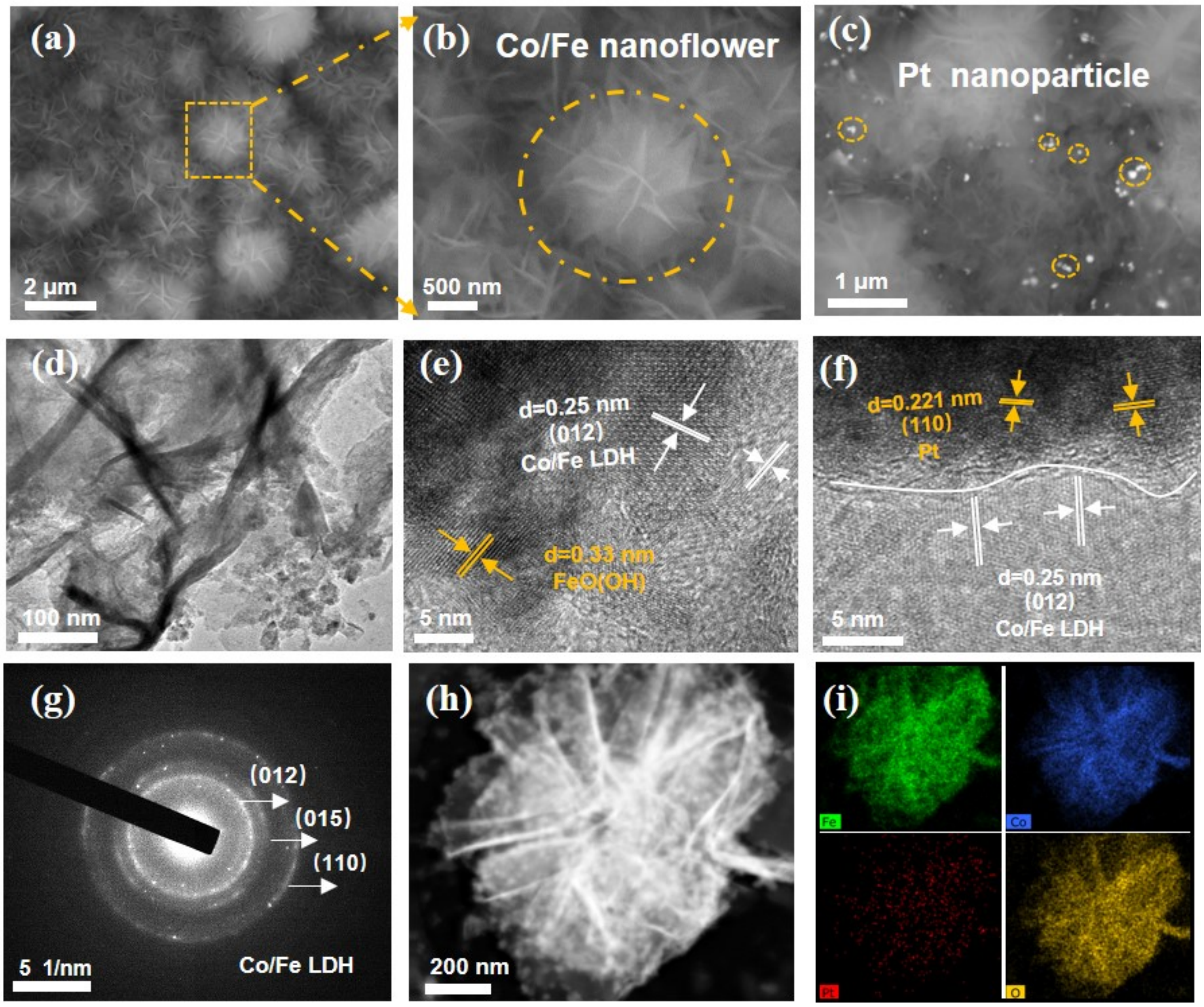

Figure III.6 (**a-c**) SEM micrographs, (**d**) TEM image, (**e-f**) HRTEM images, (**g**) SAED pattern of Pt-Co/Fe LDH, (**h**) TEM image of a Pt-Co/Fe LDH single nanoflower and (**i**) the corresponding Fe, Co, Pt, O elemental mappings.

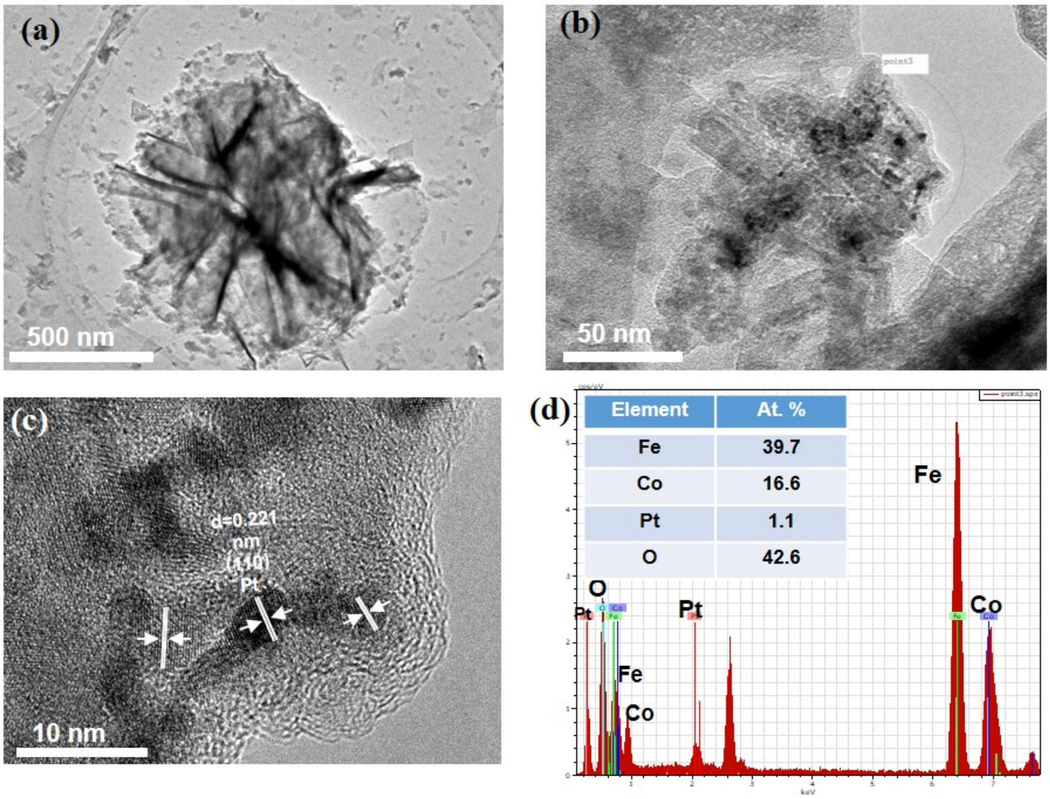

Element	At. %
Fe	39.7
Co	16.6
Pt	1.1
O	42.6

Figure III.7 Morphology and structural characterizations of Pt-Co/Fe LDH, further demonstrating nanoflower-like structure with trace Pt nanoparticles. (**a-b**) TEM images, (**c**) HRTEM images, (**d**) EDS profile and elemental composition determined from the EDS spectrum.

No	**Sample**	**Co (at. %)**	**Fe (at. %)**	**Pt (at. %)**
1	Surface composition of Pt-Co-Fe foam [a]	9.57	11.63	1.16
2	Nanoflower surface composition of Pt-Co-Fe foam [b]	16.6	39.7	1.1
3	Bulk composition of Pt-Co-Fe foam [c]	1.06	98.77	0.17

Table 2. Surface and bulk composition of Pt-Co/Fe LDH catalyst determined by [a] XPS, [b]TEM-EDX and [c]ICP-OES analysis.

The crystalline structure of the catalysts was assessed by X-ray diffraction (XRD). As shown in **Figure III.8**, the XRD plots of the initial FF before and after immersion in 2 M NaCl aqueous solution for 15 h at room temperature comprised two typical sharp peaks located at 44.3° and 64.5°

corresponding respectively to the (110) and (200) crystal planes of FF (PDF-85-1410). The peaks at 36.1° (111), 41.9° (200), 60.7° (220), 72.7° (311) and 76.5° (222) (PDF-77-2355) are indexed to the typical FeO structure (PDF-77-2355), confirming that the FF was easily oxidized to form an oxide layer on its surface. Importantly, the new weak peaks at 11.8° (110), 35.1° (211), and 55.9° (521) are indexed to FeO(OH) structure (PDF-34-1226) in the Fe foam immersed in 2 M NaCl aqueous solution, which further supports the successful fabrication of FeO(OH) on the Fe foam surface. Moreover, after oxygen corrosion engineering, the weak peaks at 11.1° (003), 22.6° (006), 33.6° (012), 41.9° (018), 59.0° (110) and 60.9° (113) (PDF-50-0235), observed in **Figure III.9a**, are indexed to the typical Co/Fe LDH structure; in addition, the FeO(OH) peaks, such as 27.1° (021), 36.2° (130), and 46.7 ° (150) (PDF-70-0714) are seen in both Co/Fe LDH and Pt-Co/Fe LDH samples, which is consistent with the results of SAED patterns and HRTEM analysis further confirming the successful fabrication of LDH.

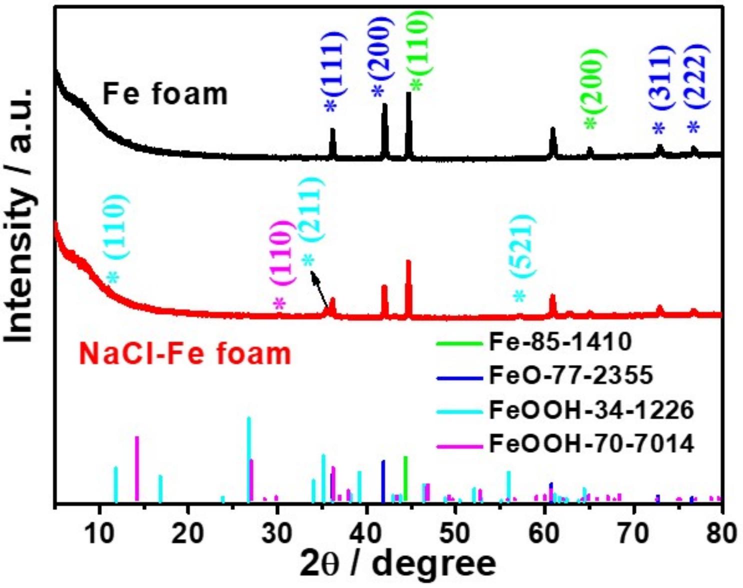

Figure 3.8 XRD patterns of Fe foam before (black) and after (red) immersion in 2 M NaCl aqueous solution for 15 h at room temperature.

X-ray photoelectron spectroscopy (XPS) was conducted to probe the surface composition and chemical valence states of the prepared catalysts. The full spectrum of Pt-Co/Fe catalyst further confirmed the presence of Co, Fe, O and Pt elements (**Figure III.9b**). The high resolution XPS plot of Pt 4f in **Figure III.9c** consists of two typical characteristic peaks at 74.1 and 70.7 eV assigned respectively to Pt $4f_{5/2}$ and Pt $4f_{5/2}$, demonstrating the effective intercalation of metallic Pt in the prepared Pt-Co/Fe LDH. As shown in **Figure III.9d**, the Co $2p_{1/2}$–$2p_{3/2}$ spin orbit level energy spacing of Co/Fe LDH (15.9 eV) and Pt-Co/Fe sample (15.9 eV) were about 16 eV, inferring the presence of Co in its +2-oxidation state [7]. Moreover, the major peaks at 781.9 and 797.3 eV could be attributed to Co (II), whereas the other weak peaks at 780.4 and 795.9 eV are assigned to Co (III), along with the satellite peaks at 786.6 and 803.0 eV.[8-10] The Fe 2p plots of the Co/Fe and Pt-Co/Fe LDH samples infer a similar valence distribution with two fitted peaks for Fe $2p_{3/2}$ due to Fe^{3+} (713.0 eV) and Fe^{2+} (710.7 eV), whereas the peaks located at binding energies of 724.5 eV (Fe^{3+}) and 726.9 eV (Fe^{2+}) correspond to Fe $2p_{1/2}$ deconvoluted regions, along with the satellite peaks at 719.3 and 733.5 eV (**Figure III.9e**) [11, 12]. The XPS analysis of Pt-Co/Fe LDH catalytic material not only indicates a similar valence state structure upon introducing trace of Pt nanoparticles compared with Co/Fe LDH, but also illustrates that Co, Fe and Pt are present in Co^{2+}, Fe^{3+}/Fe^{2+} and Pt^0 states. Furthermore, the O 1s spectrum could be deconvoluted into O1, O2 and O3 characteristic peaks;[13, 14] the O1 peak at 529.7 eV belongs to the metal-oxygen bond (M-O), O2 peak at 531.2 eV is associated with oxygen vacancy sites and O3 peak at 532.6 eV is ascribed to hydroxyl groups or surface-absorbed oxygen (**Figure III.9f**). Oxygen vacancies are representative of electron donors and their formation reduces the upper edge of the O 2p band. Pt-Co/Fe LDH possessed higher O2 and lower O1 contributions than Co/Fe LDH; the rich oxygen vacancies supply electrons which could be easily transferred to the metal conduction band, enhancing the catalyst's conductivity. These results further strengthen the evidence that there is a strong electronic interaction between Pt nanoparticles, Co/Fe LDH and FF substrate, and these tunable metal valence composition, sufficient oxygen vacancies, and hierarchical structure are advantageous for stable and efficient water splitting catalysts.

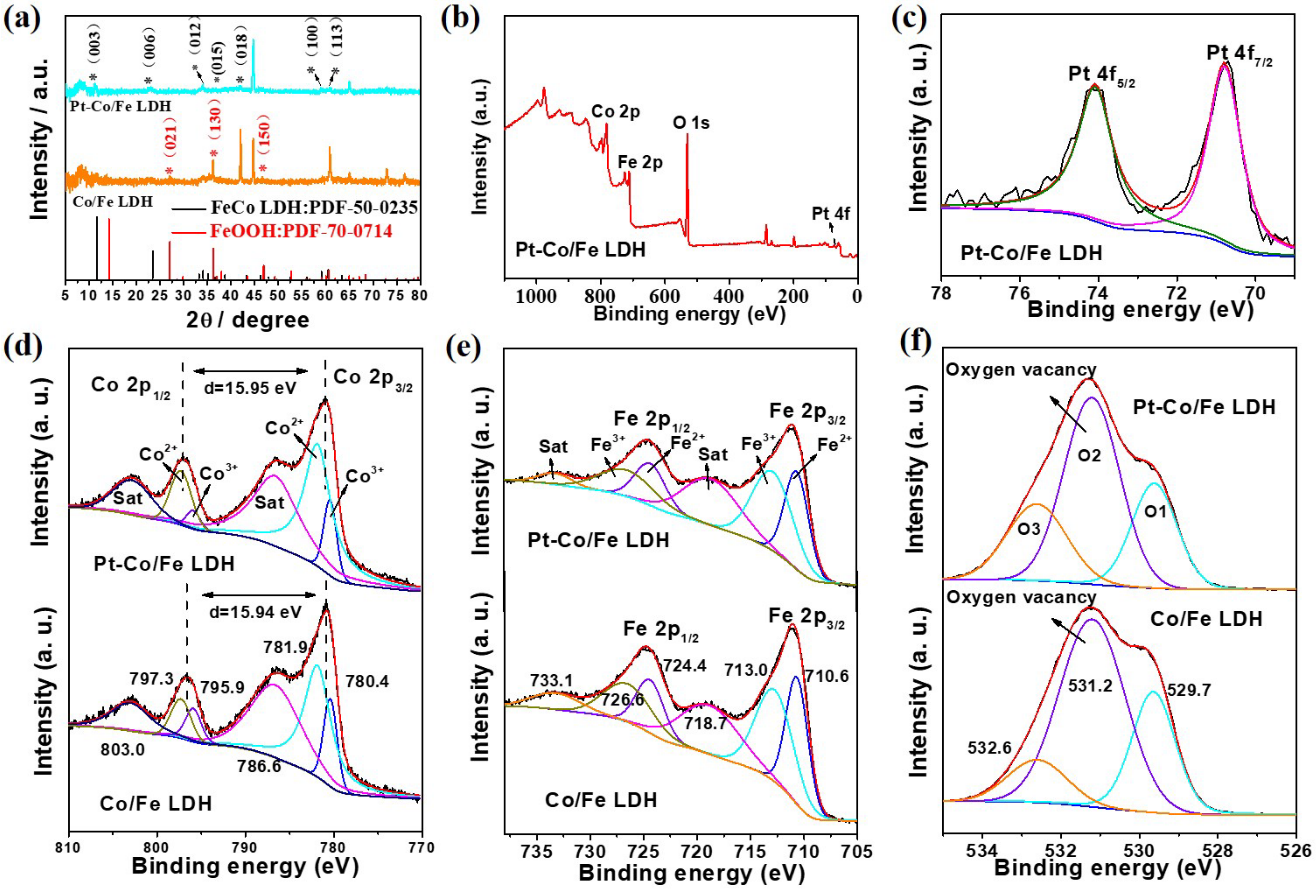

Figure III.9 (**a**) XRD patterns of Pt-Co/Fe and Co/Fe LDH. (**b**) XPS full scan and high-resolution XPS spectra of (**c**) Pt 4f, (**d**) Co 2p, (**e**) Fe 2p, and (**f**) O 1s.

III.3.3 Electrocatalytic performance

The electrocatalytic performance of the Pt-Co/Fe LDH was assessed in 1 M KOH electrolyte using a standard three-electrode system. Linear sweep polarization curves in **Figure III.10** and **Figure III.13a** revealed that Pt-Co/Fe LDH exhibited the lowest overpotential values of 36 and 87 mV to achieve a current density of respectively 10 and 50 mA cm^{-2} compared with FF (120, 371 mV), Pt/C-Fe foam (42, 114 mV) and Co/Fe LDH (63, 236 mV), indicating the coexistence of multi-metallic elements synergistic role for improving the electrocatalytic performance. Furthermore, the influence of different contents of $CoCl_2$ and NaCl in the corrosion solution was investigated to gain some insights on the catalytic mechanism (**Figures III.11-12**). Specifically, the HER performance of the prepared catalysts was enhanced upon increasing the $CoCl_2$ concentration up to 50 mM using a constant concentration of NaCl (2 M); an overpotential of 290 mV was recorded at a current density 100 mA cm^{-2}. Furthermore, the overpotential gradually decreases upon increasing the NaCl concentration at a constant concentration of $CoCl_2$ (50 mM), and the better performance was attained for NaCl (2 M)-$CoCl_2$ (50 mM) system. Therefore, the HER performance of Co/Fe LDH catalysts could be effectively tuned by controlling oxygen corrosion rate and the ratio of NaCl/$CoCl_2$ in the corrosion solution. Notably, the significant improvement of HER electrocatalyst activity was further achieved by loading a small amount of Pt; the presence of Pt atoms optimized the electronic structure and Pt-H_{ad} energy.

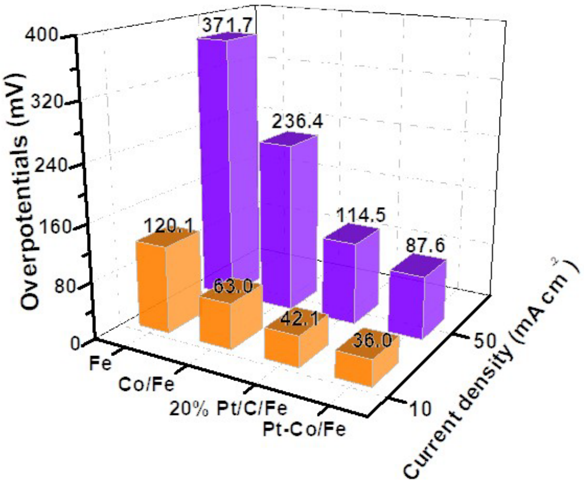

Figure III.10. Graphic comparison of the HER overpotentials of the different electrocatalysts prepared in this study to drive 10 and 50 mA cm^{-2}.

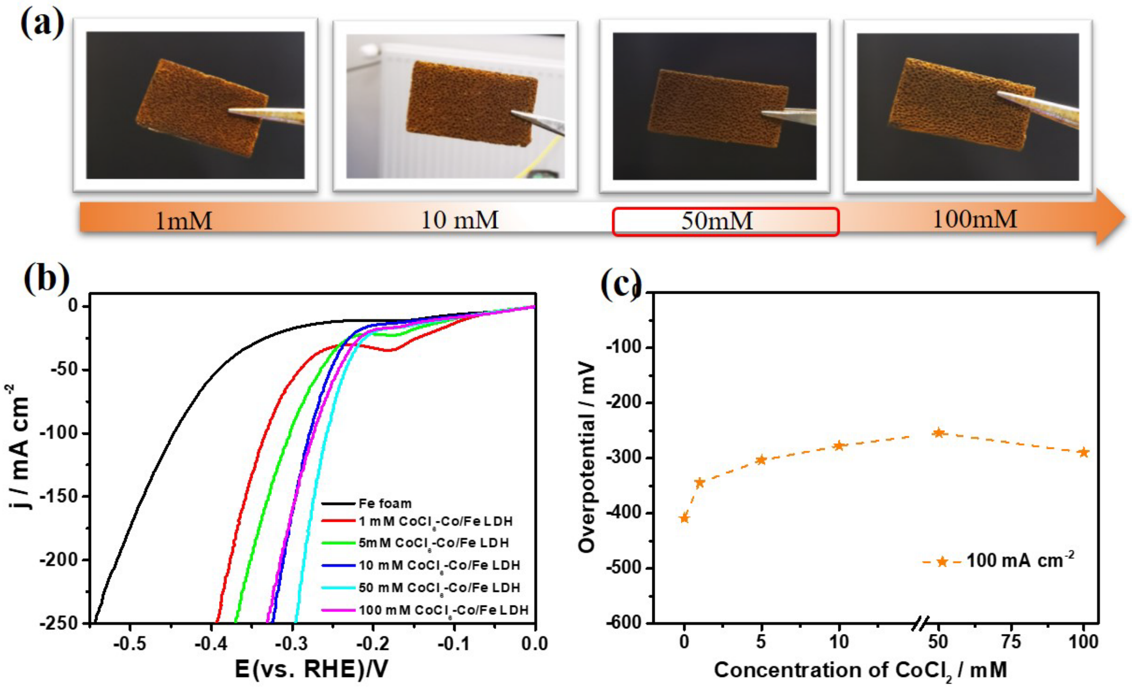

Figure III.11 (**a**) Photographs of Co/Fe LDH catalysts prepared using increasing concentrations of $CoCl_2$, (**b**) LSV polarization curves of Co/Fe LDH (2 M NaCl) prepared using various $CoCl_2$

concentrations for catalyzing HER in 1 M KOH at a scan rate of 5 mV s^{-1}, and (**c**) Comparison of their overpotential values at the current densities of 100 mA cm^{-2}.

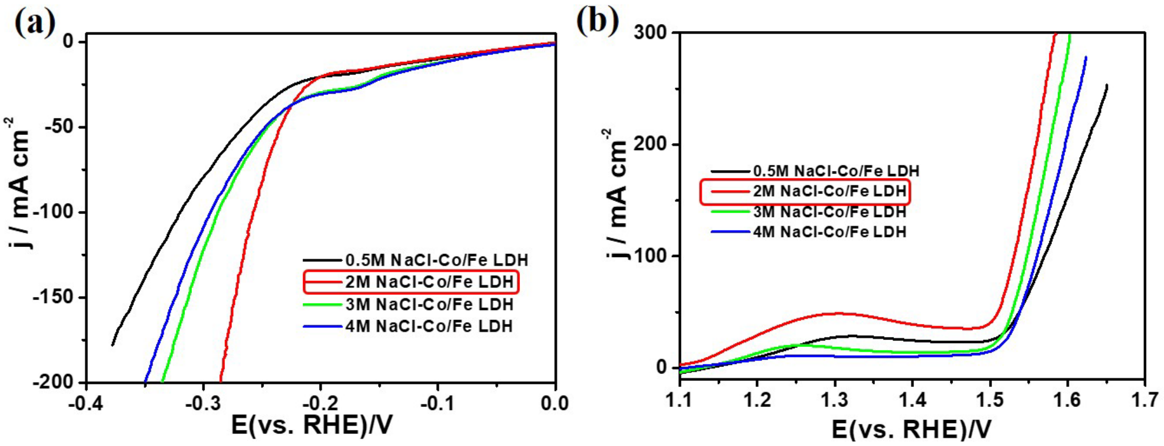

Figure III.12 LSV polarization curves of Co/Fe LDH (50 mM $CoCl_2$) prepared using different NaCl concentrations for catalyzing the (**a**) HER, and (**b**) OER in 1M KOH at a scan rate of 5 mV s^{-1}.

It is well-established that the free energy (ΔG_{H*}) of hydrogen adsorption on the catalyst surface is of paramount importance for HER [15]. In addition, the adsorption of OH* as another prerequisite could facilitate water dissociation in alkaline condition. Therefore, the optimal OH* adsorption represents an effective pathway for boosting the water dissociation reaction (Volmer reaction) [16]. In this system, the 3D flower-like morphology of Pt-Co/Fe LDH, exposing more active sites and strong OH* adsorption, effectively reduces the energy barrier of water dissociation in the Volmer step and accelerates the reaction kinetics during HER in alkaline media [17]. The Tafel slopes in **Figure III.13b** further proved the enhanced HER activity. The Pt-Co/Fe LDH electrode exhibited a small Tafel slope of 43.3 mV dec^{-1} compared to Fe foam (123.7 mV dec^{-1}), Pt/C-Fe foam (61.5 mV dec^{-1}), and Co/Fe LDH (97.1 mV dec^{-1}), inferring its favorable HER kinetics. In addition, the HER activity of Pt-Co/Fe LDH is also superior to that of most of recently-reported metal-based LDH electrocatalysts, as shown in **Figure III.13c** [18-33]. In addition to loading Pt element onto CoFe LDH sample, we have also used Pd, Ru, Au, Ir loading on the catalyst. The resulting catalysts exhibited poor HER activity and stability. Among them, Pt-Co/Fe LDH is the best sample for HER reaction. Remarkably, compared to the commercial Pt/C-Fe foam catalyst (with approximately 0.9 mg/cm² of Pt), the Pt-Co/Fe LDH (loading ≤ 0.032 mg/cm² of Pt) significantly reduces the catalyst cost and enhances the utilization rate of precious metals.

The Pt-Co/Fe LDH electrode was endowed with promising durability (**Figure III.13d-e**). Importantly, the overpotential to reach a current density of 10 mA cm^{-2} remained almost stable even after 36 h continuous operation. The current densities enhanced gradually by regulating the overpotential step-by-step, indicating the excellent stability even under high voltage condition, which is beneficial for large-scale commercial utilization.

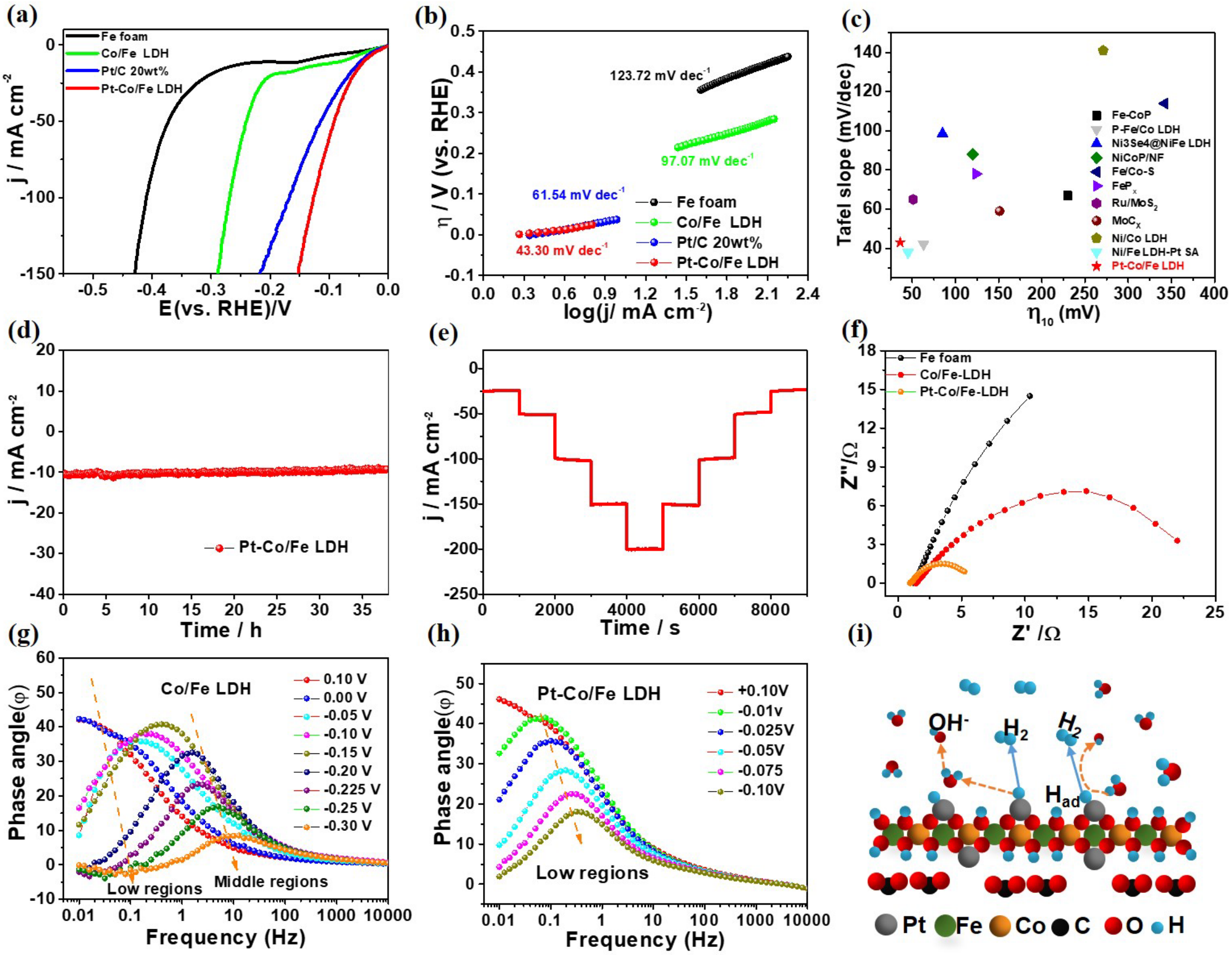

Figure III.13. The electrochemical HER behavior of FF, Pt/C-FF, Co/Fe LDH and Pt-Co/Fe LDH in 1 M KOH solution. (**a**) LSV polarization curves, (**b**) The corresponding Tafel plots, (**c**) Graphic of comparison of overpotential acquired at 10 mA cm^{-2} and a comparison of Tafel slopes with other recently-reported high performance electrocatalysts, (**d**) Long-term stability measurement of the Pt-Co/Fe LDH performed at a constant potential for 36 h, (**e**) Multistep chronoamperometric curve, (**f-h**) Nyquist and Bode plots at different overpotentials, and (**i**) Schematic representation of HER mechanism.

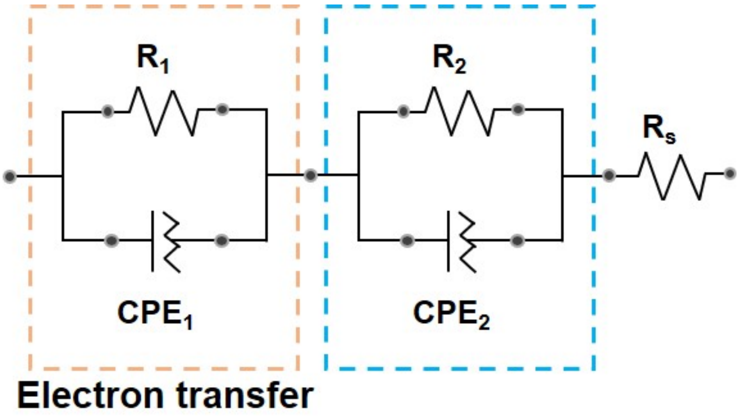

Figure III.14. The equivalent circuit diagram used for analysis of the EIS curves measured for the OER and the HER.

Electrochemical impedance spectroscopy (EIS) was utilized to analyze the reaction kinetics of the catalysts at the electrode/electrolyte interface [34]. All EIS data are fitted with the equivalent circuit depicted in **Figure III.14** consisting of an electrode solution resistance (R_s) in series with two parallel combinations of two resistors (R_1, R_2) and two constant phase elements (CP_1, CP_2), where R_2 corresponding to R_{ct} represents interfacial charge transfer resistance between electrode and electrolyte, whereas R_1 refers to the internal charge transfer resistance of the electrode. Fe foam exhibited the smallest R_1 at different potentials. However, the larger R_{ct} value and higher energy barrier limited its catalytic performance (**Figure III.15**). Therefore, the Co/Fe LDH catalyst was a successful construction with a smaller width of the semicircle than Fe foam at different HER potentials. The estimated R_{ct} and R_1 values displayed a similar variation trend, i.e., 44.38 Ω / 0.14 Ω for Co/Fe LDH, 68.68 Ω / 0.15 Ω for Fe foam at 0 V, which is attributed to the morphology of the fabricated of Co/Fe LDH as well as to the presence of hydrophilic oxygen functional species on the surface, as vividly revealed by XPS analysis. The Pt-Co/Fe LDH displayed the lowest R_{ct} (22.43 Ω) and R_1 (0.081 Ω) values at 0 V; its optimized structure and excellent electronic conductivity brought by the Pt nanoparticles are beneficial for electrochemical processes. For the Faradaic reaction region, the Pt-Co/Fe LDH recorded a much smaller charge transfer resistance (R_{ct}=4.57 Ω) compared with Co/Fe LDH (26.54 Ω) and Fe foam (80.81 Ω) in the HER process at an overpotential of 50 mV, suggesting improved charge transfer rate (**Figure III.13**).

For the HER process, the equivalent resistance of electrode solution and charge transfer resistance were evaluated at different overpotentials from the Bode plots (**Figure III.13g**, **Figure III.15**). The

Bode plots could be separated into three regions accounting for the HER mechanism: Volmer (low frequency), Heyrovsky (middle frequency) and Tafel presenting fast electron transfer ability (high frequency) steps [35, 36]. In general, the peak of the phase angle change at high frequencies is attributed to the electron conduction in the inner layer of the catalyst, while at low frequencies, it is ascribed to the charge transfer of the interfacial reaction. The Heyrovsky-Volmer mechanism is the major focus object in this system, where the electrochemical desorption of hydrogen (Heyrovsky step) dominates the whole reaction. As shown in **Figure III.13i**, the Volmer-Heyrovsky mechanism determined by Heyrovsky-step and two electrons transfer process is presented below (H_{ad} is an adsorbed H-species) [37, 38]:

$H_2O + M + e^- \leftrightarrow M\text{-}H_{ad} + OH^-$ (Volmer reaction; 118 $mV\cdot dec^{-1}$) (1)

$H_2O + M\text{-}H_{ad} + e^- \leftrightarrow M + H_2 + OH^-$ (Heyrovsky reaction; 40 $mV\cdot dec^{-1}$) (2)

$2M\text{-}H_{ad} \leftrightarrow 2\,M + H_2$ (Tafel reaction; 30 $mV\cdot dec^{-1}$) (3)

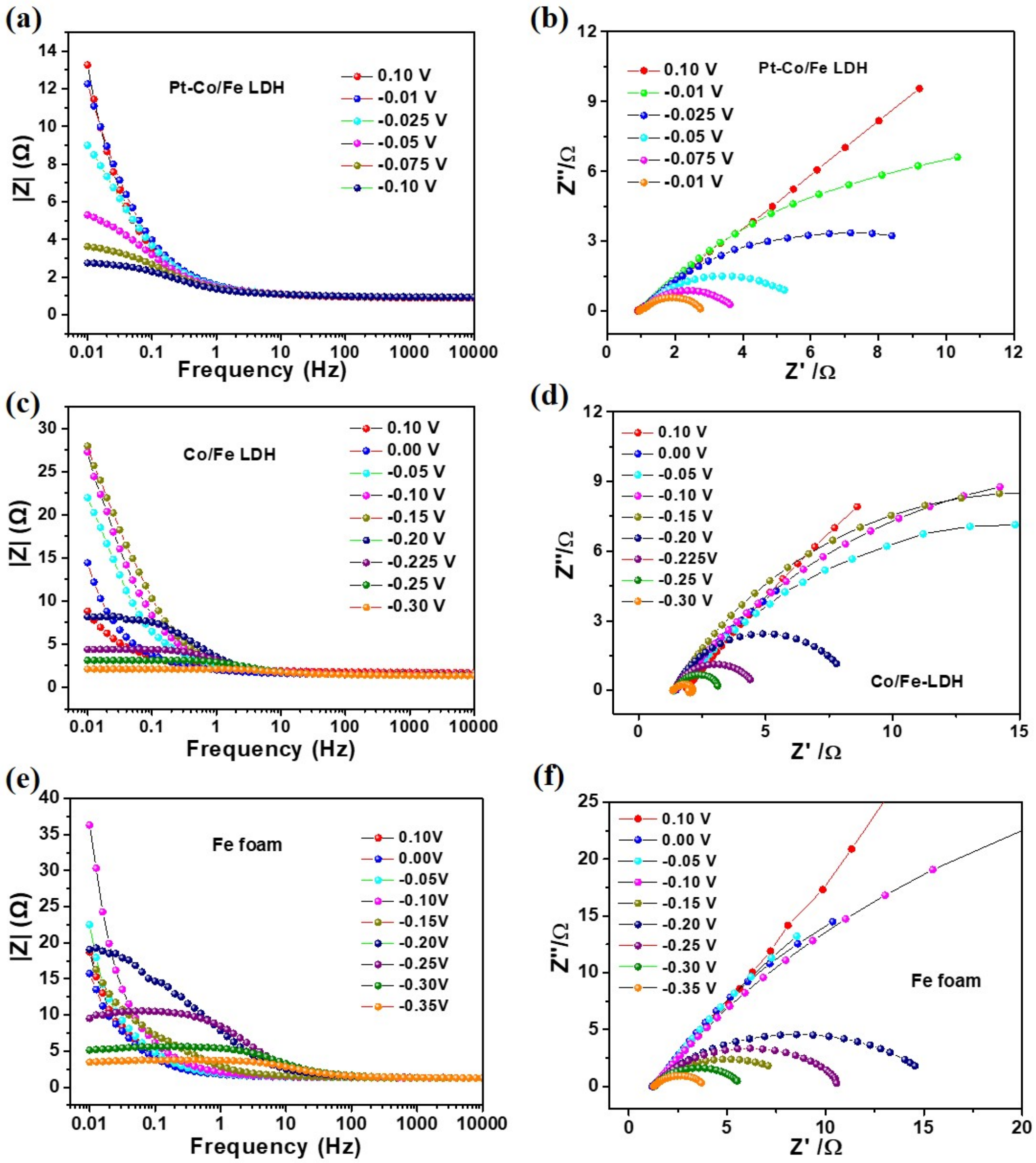

Figure III.15. Nyquist and Bode plots at various hydrogen potentials showing variation in impedance as a function of frequency of (**a, d**) Pt-Co/Fe LDH, (**b, e**) Co/Fe LDH, and (**c, f**) Fe foam.

In addition, **Figure III.15** represents the modulus of impedance *vs.* frequency on the a-axis with varied potential ranging from +0.10 to -0.35V to understand the mechanism of charge transfer resistance. As expected, the Bode plots depicted the same response trend for the three samples, featuring a maximum impedance at lower frequency. And the impedance was shifting and decreasing at the lower frequency region along with decreasing potential, whereas the impedance values were about minimum and remained constant even with increasing the frequency at -0.10 V for Pt-Co/Fe LDH, -0.25 V for Co/Fe LDH and -0.35 V for Fe foam. It could be seen that the Faradaic reaction of

Pt-Co/Fe LDH owns good electrochemical performance as electrode material.

Notably, the Bode spectra, presented in **Figure III 13h**, describe the expected behavior when increasing the cathodic overpotential, i.e., the phase angle values in the low frequency region gradually decreased upon increasing the HER overpotential (Volmer step) for the Co/Fe LDH, Fe foam and Pt-Co/Fe LDH. However, there is a clear difference of downward trend in the middle frequency region for different catalysts, i.e., the Fe foam and Co/Fe LDH displayed a slow decreasing process of phase angle, owing to the relatively sluggish Heyrovsky step. Notably, Pt-Co/Fe LDH showed the better ability for reducing the phase angle even in the lower overpotential. It is well-documented that the sluggish water dissociation is attributed to the limiting Heyrovsky-Volmer mechanism [39]. The beneficial feature of Pt-Co/Fe LDH, such as porous structure, high surface area and excellent electron transfer ability promoted water dissociation and significantly improved the confinement in the midrange region frequency, resulting in better HER activity than the commercial Pt/C [40].

In addition to the excellent HER performance, we also investigated the electrocatalytic OER activity of the Pt-Co/Fe LDH in the alkaline medium (**Figure III.17a**). As expected, the Pt-Co/Fe catalyst achieved the best performance by reaching a current density of 100 mA cm^{-2} at an overpotential of 285 mV, whereas the Co/Fe LDH required an overpotential of 297 mV, which is much better than RuO_2/Fe (460 mV), and Fe foam (495 mV), as shown in **Figure III.17c**. In order to deeply analyze the influencing factors of the OER activity and verify the synergistic mechanism between Co/Fe LDH and FeO(OH), the LSV curves were investigated by varying the $CoCl_2$ and NaCl concentrations, respectively (**Figure III.12**).

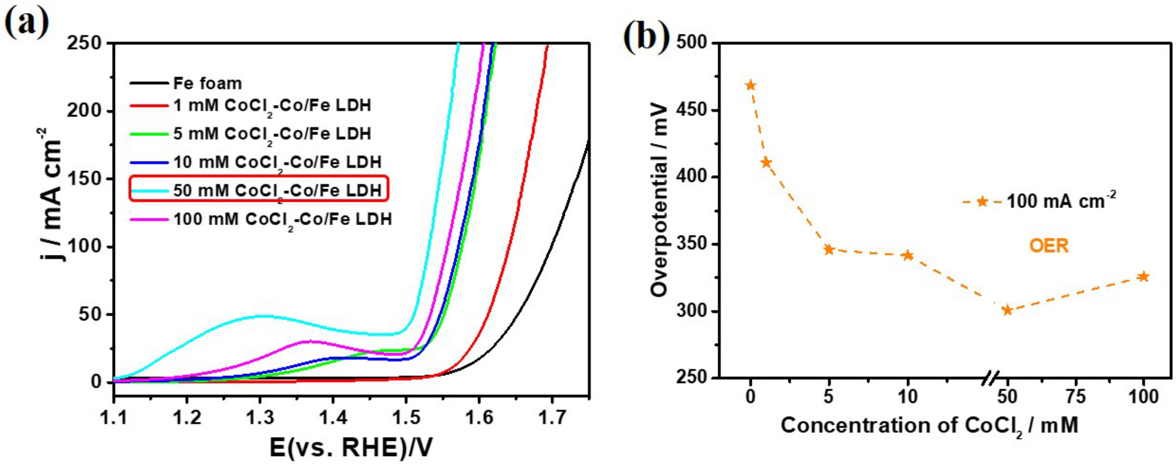

Figure III.16. (**a**) LSV polarization curves of Co/Fe LDH (2 M NaCl) prepared using various $CoCl_2$ concentrations for catalyzing OER in 1 M KOH at a scan rate of 5 mV s^{-1}, (**b**) Comparison of overpotential of Co/Fe LDH catalysts at a current density of 100 mA cm^{-2}.

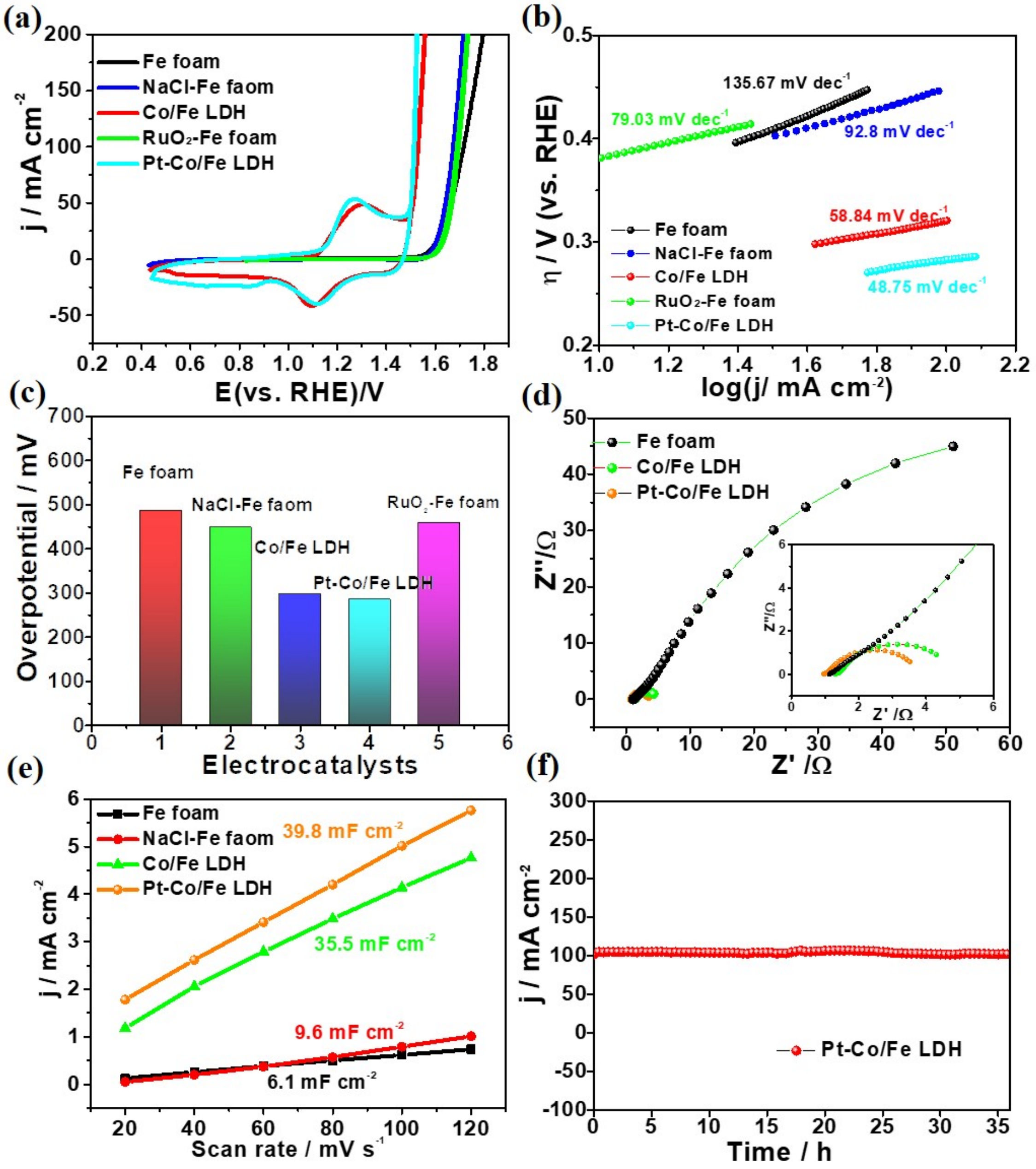

Figure III.17. A comparison of OER performance of the different catalysts in 1 M KOH solution at a scan rate of 5 mV s^{-1}. (**a**) CV curves, (**b**) Tafel plots, (**c**) Graphic comparison of overpotential at a current density of 100 mA cm^{-2}, (**d**) Electrochemical impedance spectra acquired at an overpotential of 300 mV, (**e**) Electrochemical double-layer capacitance as a function of scan rate, and (**f**) Long-term stability measurement of the Pt-Co/Fe LDH for OER over 36 h.

Firstly, the influence of NaCl concentration was studied. NaCl-treated FF demonstrated better OER activity than the non-treated FF, further indicating the enhanced activity, owing to the existence of

FeO(OH). Moreover, the CV curves of Co/Fe LDH samples revealed gradual enhancement of the OER performance with increasing NaCl concentration. Co/Fe LDH system, prepared using 2 M NaCl-50 mM $CoCl_2$ mixed solution, exhibited better catalytic performance, suggesting a synergistic effect between $Co(OH)_2$ and FeO(OH). Compared with NaCl concentration, the influence of $CoCl_2$ concentration was greater toward OER activity. As shown in **Figure III.16**, the Co/Fe LDH featuring the best performance belongs to 50 mM $CoCl_2$ system. Noteworthy, the peaks observed between 1.2 and 1.5 V *versus* reversible hydrogen electrode (RHE) could be ascribed to the oxidation of M^{2+} to M^{3+} (M=Co, Fe) in the Co/Fe LDH [40]. Additionally, the Pt-Co/Fe electrode featured the smallest Tafel slope of 48.76 mV dec^{-1} compared to Co/Fe (58.84 mV dec^{-1}), RuO_2/Fe foam (79.03 mV dec^{-1}), NaCl-Fe foam (92.80 mV dec^{-1}) and Fe foam (135.67 mV dec^{-1}), inferring that Pt-Co/Fe LDH acquired fast OER kinetics (**Figure III.17b**). The EIS results revealed that the Pt-Co/Fe achieved a much lower R_{ct} (2.47 Ω) among all the prepared samples at an overpotential of 300 mV, proving the fast charge transfer and favorable reaction kinetics of the hierarchical nanoarchitecture (**Figures III.17d**). In addition, EIS measurements in forms of Nyquist and Bode plots were recorded (**Figure III.18**). It was observed that Pt-Co/Fe LDH and Co/Fe LDH recorded comparable R_{ct} values and similar variation trend at different OER potentials, e.g., Pt-Co/Fe LDH (2.46 Ω *vs.* 1.5 V) and Co/Fe LDH (3.65 Ω *vs.* 1.5 V), which are much smaller than that of Fe foam (105.30 Ω *vs.* 1.5 V). This result could be attributed to Co/Fe LDH morphology exposing more active sites, which is adapted to interfacial charge transfer between electrolyte (1 M KOH) and catalyst. Noteworthy, the Pt-Co/Fe LDH displayed excellent OER catalytic performance and possessed the smallest R_{ct} values in the same potential, implying acceleration of the charge transfer and ion diffusion between electrolyte and electrode. The electrochemical double-layer capacitance (C_{dl}) was used to determine the electrochemical active surface area (ECSA), as a typical characteristic method for evaluating the OER activity. The Pt-Co/Fe displayed a C_{dl} value of 39.8 mF cm^{-2} higher than the other prepared catalysts, as revealed from the CV curves in **Figures III.17e** and **III.19,** indicating that the sample features more active sites. Long-time chronoamperometry and multistep chronoamperometry methods were carried out to assess the sample durability for the OER process (**Figures III.17f** and **III.20**). The results clearly showed the good stability of the Pt-Co/Fe electrode over 36 h continuous operation. By comprehensive analysis of structure and property, the excellent OER performance could be attributed to the appealing 3D configuration and flower-like nanosheets with abundant accessible active sites and faster ion diffusion, along with improved conductivity and high valence states of Co^{3+} and Fe^{3+} ions with more O vacancies of Pt-Co/Fe LDH heterostructure.

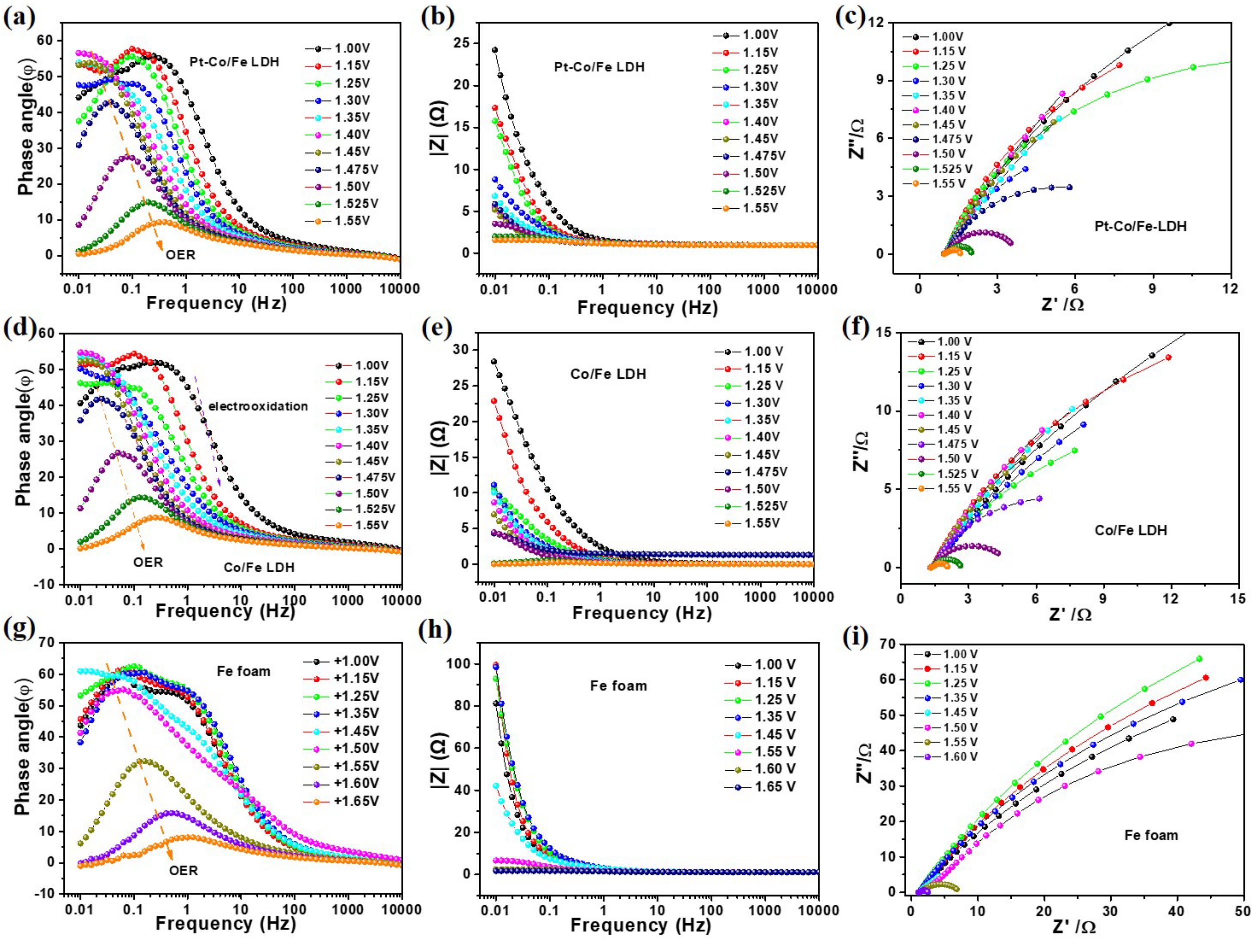

Figure III.18. Nyquist and Bode plots at various oxygen potentials of (**a-c**) Pt-Co/Fe LDH, (**d-f**) Co/Fe LDH, and (**g-i**) Fe foam.

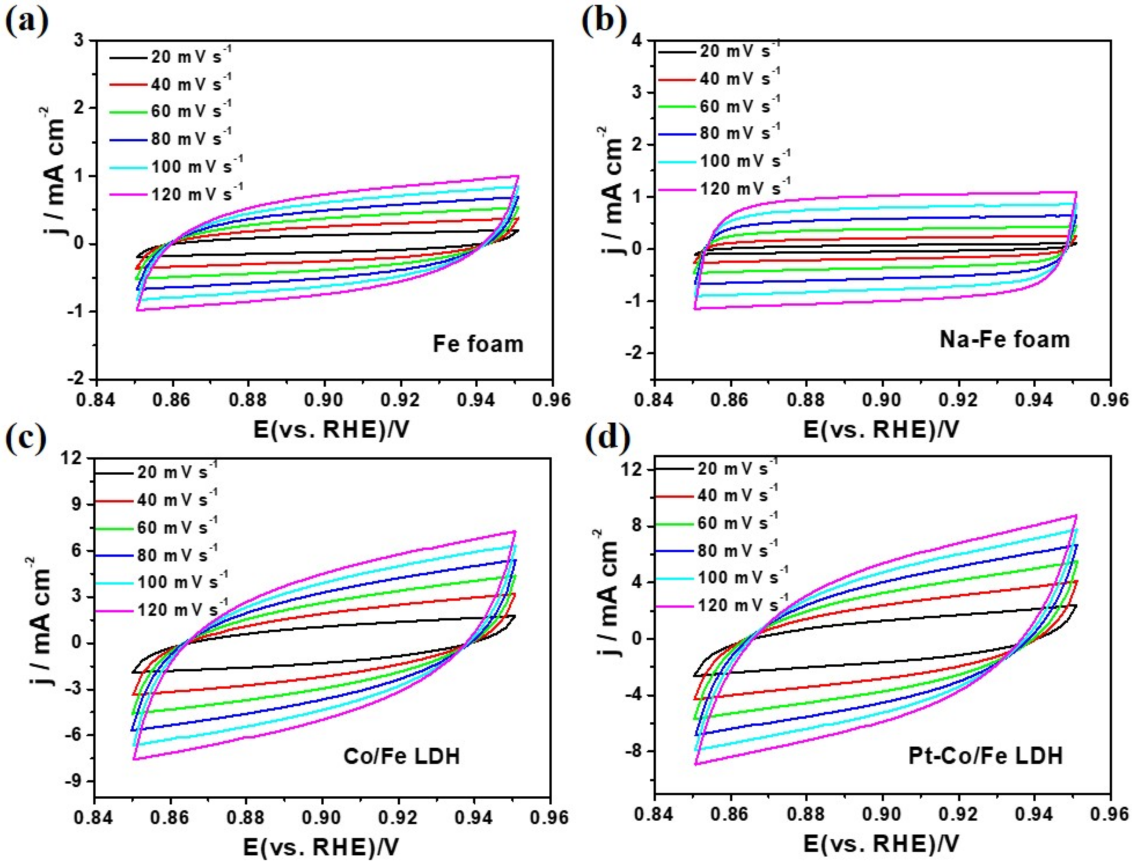

Figure III.19. CV curves in the potential range from 0.85 to 0.95 V at various scan rates in 1 M KOH solution of (**a**) Fe foam, (**b**) Na-Fe foam, (**c**) Co/Fe LDH, and (**d**) Pt-Co/Fe LDH.

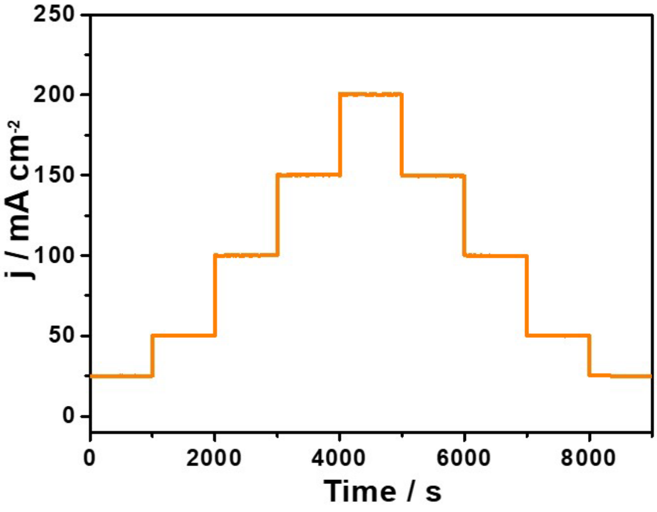

Figure III.20. Multistep chronoamperometric curve of Pt-Co/Fe LDH at various applied overpotentials for OER test.

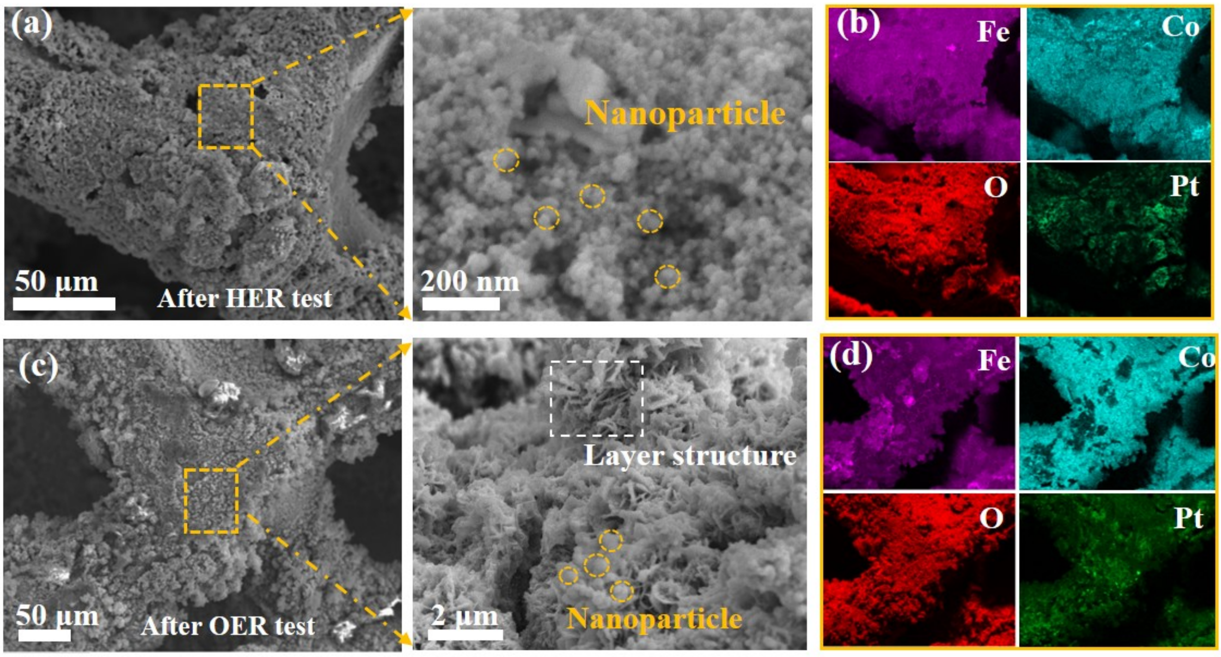

Figure III.21. SEM images at different magnifications of the Pt-Co/Fe LDH after 36 h of (**a**) HER and (**c**) OER stability tests, (**b**) and (**d**) are the corresponding EDS elemental mapping images, respectively.

Table 3. XPS analysis of Co, Fe, Pt, C and O elements before and after HER/OER stability tests.

No	Sample	Co (at.%)	Fe (at.%)	Pt (at.%)	C (at.%)	O (at.%)
1	Pt-Co/Fe sample	9.57	11.63	1.16	26.86	28.78
2	Sample after HER	9.04	15.98	1.15	28.32	45.51
3	Sample after OER	8.82	19.26	1.12	29.91	40.89

Table 4. ICP-OES analysis of the reaction solution of Co, Fe and Pt elements before and after HER/OER stability tests in 1M KOH.

No	Sample name	Co（ppm）	Fe（ppm）	Pt（ppm）
1	Solution immersed in 1M KOH 24h	0.06	0.26	0.02
2	Solution after HER reaction	0.07	0.20	0.01
3	Solution after OER reaction	0.08	0.31	<0.01

In order to further investigate the surface properties and reaction mechanism of the Pt-Co/Fe LDH catalyst before and after the stability tests, SEM and XPS methods were employed. **Figure III.21(a, c)** indicates that the Pt-Co/Fe LDH catalysts maintained their morphologies and structural integrities after HER or OER testing; no remarkable difference could be noticed compared to the prime electrode, owing to its 3D open porous structure possessing enough capacity to release the generated gas bubbles. Remarkably, there is a subtle change from high magnification observation that displayed the surface material transformation of Co phase from double layer sheets to nanoparticles, whose diameter varies from 50 to 100 nm. It could be assumed that cobalt nanoparticles were generated *via* electrochemical redox reactions. Interestingly, elemental mapping images of Pt-Co/Fe LDH after stability tests were recorded (**Figure III.21 b, d**). The Co, Fe, Pt and O elements were still homogeneously distributed on the catalyst surface after the long-time durability tests, implying a strong electronic interaction and bonding energy at the interface between metal-LDH nanostructure and Pt nanoparticles. The changes in the chemical composition of the Pt-Co/Fe foam and the reaction solution before and after the stability tests are summarized in **Tables 3-4**. The results revealed that the element content changes are relatively small in the reaction solution. An interesting phenomenon showed that the Co/Fe ratio decreased from 0.83 to 0.56 after the HER and 0.46 after the OER stability tests. The relative decrease of Co element content on the catalyst surface may be caused by the detachment of the generated H_2 or O_2 bubbles. However, after the catalytic reaction, the elemental distribution of each element is uniform, still confirming the stability during the catalytic process.

Moreover, XPS analysis of the Co $2p_{1/2}$–$2p_{3/2}$ spin-orbit level energy spacing of 15.5 eV of Pt-Co/Fe after HER stability test was detected compared to ~15.9 eV for the as-prepared sample, which could be assigned to the oxidation state of Co in the $CoO_x(OH)$ phase to be mostly Co(III) and a little amount of Co(II), as shown in **Figure III.22 a**.

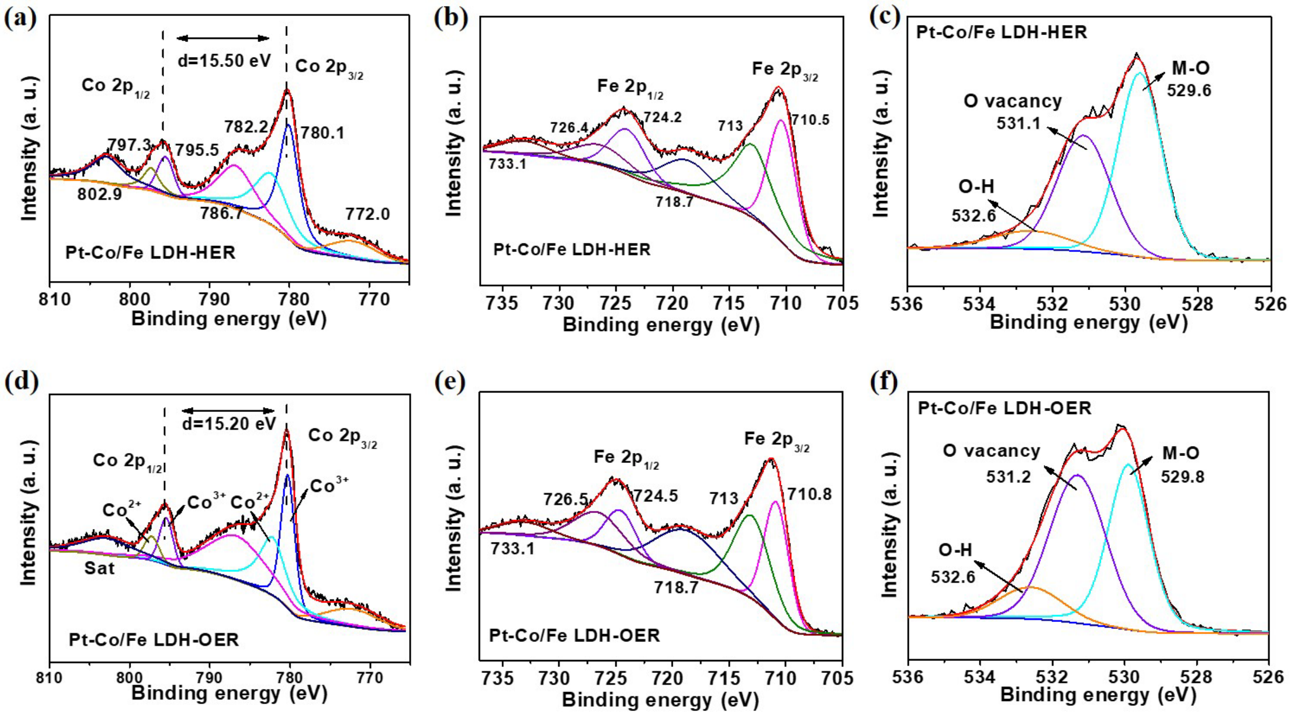

Figure III.22. High resolution XPS spectra of the (**a**) Co 2p, (**b**) Fe 2p and (**c**) O 1s after HER and (**d**) Co 2p, (**e**) Fe 2p and (**f**) O 1s after OER stability tests of Pt-CO/Fe LDH.

Similarly, after OER stability test, an energy spacing of 15.2 eV was recorded, indicating the oxidation state of Co was increased from Co(II) to Co(III) in the 1 M KOH alkaline solution (**Figure III.22 d)** [7, 14]. Furthermore, the Co $2p_{3/2}$ and Co $2p_{1/2}$ of Pt-Co/Fe after OER/HER measurements could be fitted with four peaks and two typical satellites peaks ascribed to Co^{3+} (780.1 eV) and Co^{2+} (782.2 eV) for Co $2p_{3/2}$ and Co^{3+} (795.5 eV) and Co^{2+} (797.3 eV) for Co $2p_{1/2}$ [41]. The Co^{3+}/Co^{2+} ratio increased significantly after the long-term stability testing, i.e., 1.22 for Pt-Co/Fe LDH-OER, 1.01 for Pt-Co/Fe LDH-HER as compared to 0.17 for Pt-Co/Fe LDH, indicating the phase transformation of metal oxide/oxyhydroxide and facilitating O vacancy formation [13, 42]. For the Fe 2p spectra, there are two spin-orbit peaks due to Fe $2p_{3/2}$ and Fe $2p_{1/2}$ and satellite peaks. The relatively constant ratio of Fe^{3+}/Fe^{2+} suggests that Fe oxidation state did not vary significantly after OER or HER stability tests (**Figure III.22b, e**). For the O 1s plots, the peak intensity located at the binding energy of 531.1 eV (O vacancy) slightly decreased but still maintained a high contribution after OER and HER stability measurements, further evidencing the existence of Co/Fe LDH structure and high density of active sites (**Figure III.22c, f**). Therefore, the excellent HER performance could be ascribed to the electronic structure tuning *via* optimizing valence state and M^{2+}/M^{3+} ratio along with Pt loading, which could effectively reduce the energy barrier of hydrogen atom adsorption process by promoting H−H bond formation [43]. For the outstanding OER process, the synergistic interface effect and large surface area between oxides and metal phase is beneficial to enhance the OH^- adsorption and then reduce the Gibbs free energy of the reaction intermediates. On the other hand, the high valence metal species are responsible for the enhanced OER activity, and the higher Co^{3+}/Fe^{3+} content could be considered as excellent active sites for OER [44, 45].

III.3.4 Water splitting application of Pt-Co/Fe LDH catalysts

On the basis of the promising performance of Pt-Co/Fe LDH electrode for HER and OER, it was applied as both anode and cathode for overall water splitting**.** The digital photograph of water splitting process is illustrated in **Figure III.23a,** showing the formation process of H_2 and O_2 bubbles at the cathode and anode at different overpotentials, respectively. The polarization curves for water splitting, conducted at a scan rate of 5 mV s^{-1}, are depicted in **Figure III.23b.** The Pt-Co/Fe LDH || Pt-Co/Fe LDH electrolyzer recorded a small voltage of 1.66 V at 50 mA^{-2}, which is superior to that of Pt/C-FF || RuO_2-FF system (1.89 V) and previously-reported electrocatalysts (**Table 5**). Apart from the catalytic activity, stability and durability are also crucial for evaluating the catalytic performance. Multistep chronoamperometric curves in **Figure III.23c** proved the catalyst stability at different voltages. Furthermore, the Pt-Co/Fe LDH || Pt-Co/Fe LDH system exhibited remarkable stability during the long-time overall water splitting process, characterized by a steady bubble generation (**Figure III.23d**).

In addition, the Faradaic efficiency (FE) measurements were also conducted on the best performing catalyst, namely Pt-Co/Fe LDH, to further evaluate its electrocatalytic performance towards HER and OER and confirm the electrochemical findings. As is shown in **Figure III.24**, the amounts of measured H_2 and O_2 match well with the calculated values, confirming the outstanding catalytic activity of the Pt-Co/Fe LDH catalyst. These FE values of the Pt-Co/Fe catalyst (99.5% and 99.7% for the HER and OER, respectively) exceeded those estimated for the commercial Pt/C (98.9% for the HER) and RuO_2 (99.2% for the OER) catalysts under the same experimental conditions. Benefiting from its excellent catalytic performance and simple and easy scale-up corrosion preparation process, the Pt-Co/Fe LDH catalyst holds great promise for application perspective.

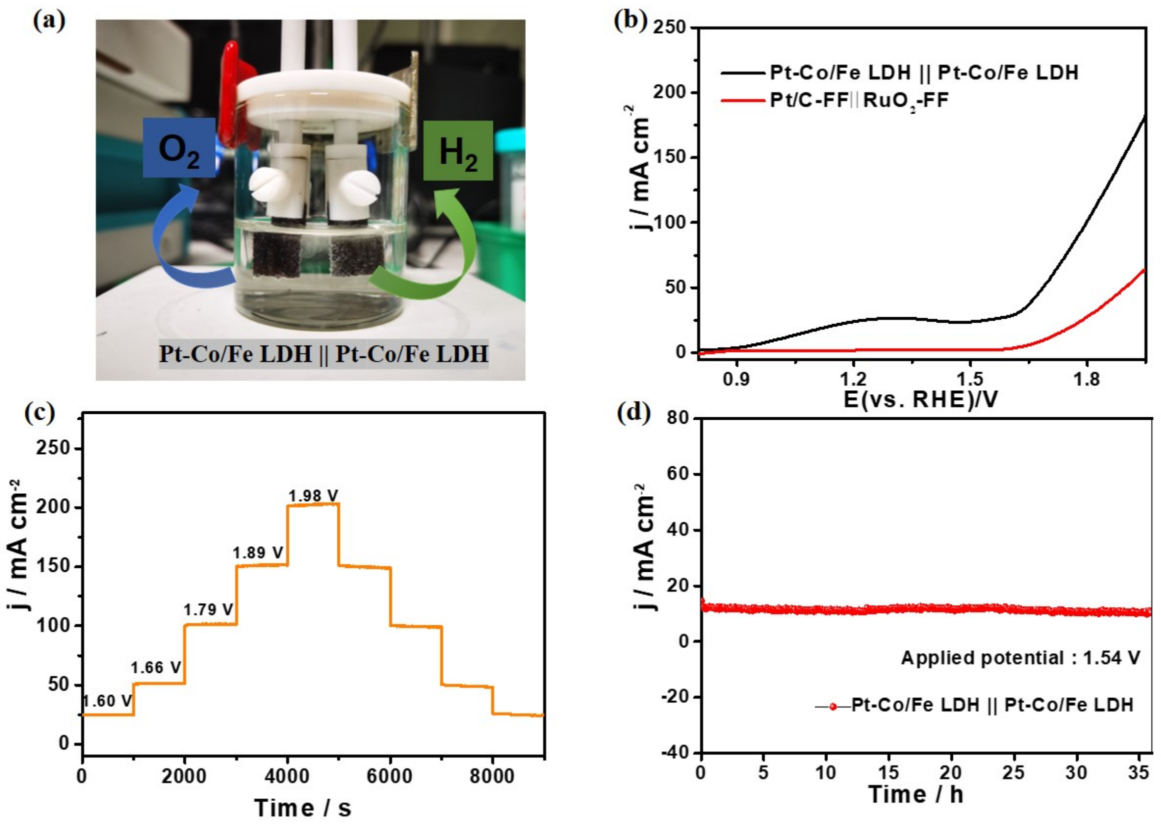

Figure III.23. (**a**) Catalyst driven by applied potential for overall water-splitting in 1 M KOH, (**b**) Polarization curves of Pt-Co/Fe LDH|| Pt-Co/Fe LDH, (**c**) Multistep chronoamperometric curves, and (**d**) Long-term stability measurement for 36 h.

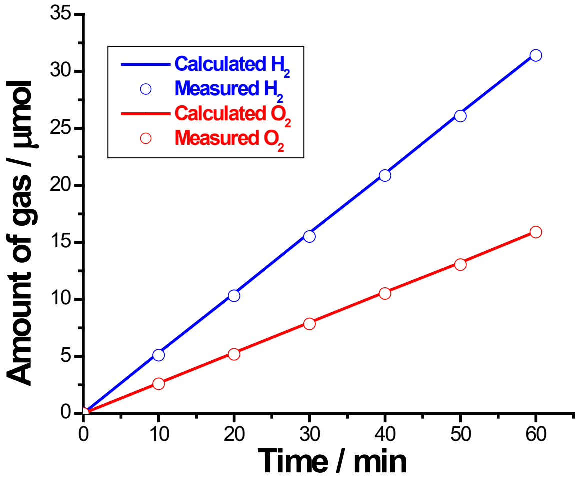

Figure III.24. Faradaic efficiency measurements for both HER and OER by the best performing catalyst (Pt-Co/Fe) in 1 M KOH. The electrode was held at -1.0 V *vs.* RHE (for the HER) and +1.0 V *vs.* RHE (for the OER) for 1 h in 1.0 M KOH solutions at 25 ºC. The amount of the gas liberated expected from the amount of charge passed (6.09 and 6.16 C for HER and OER, respectively) assuming 100% Faradaic efficiency is shown as a solid line. The amount of the released gas detected by the GC is shown as hollow spheres.

Table 5. Performance comparison of Pt-Co/Fe LDH for overall water splitting with other reported bifunctional catalysts in 1 M KOH. (IC: Ion corrosion technology; HT: Hydrothermal technology)

Electrode architecture (Electrocatalyst/ substrate)	Preparation Method	Current density (mA $^{\text{cm-2}}$)	Voltage (V)	Stability test (h)	Substrate	Reference
Pt-Co/Fe LDH	IC	**50**	**1.66**	**36**	**Fe foam**	**This work**
NiCo-LDH	HT	50	1.88	17	Ni foam	[46]
$NiCo_2S_4$	HT	50	1.87	12	Ni foam	[18]
Fe doped CoP	HT	50	1.67	/	Ni foam	[22]
Pt-Ni Fe LDH	IC	50	1.68	12	Ni foam	[47]
$Fe_{0.9}Co_{0.05}S_{1.05}$	HT	50	1.85	50	Ni foam	[43]
NiCoP/NF	HT	50	1.79	100	Ni foam	[40]
NiFe LDH	IC	50	1.61	168	Fe foam	[4]
Ni_2P-Fe	HT	50	1.69	12	Fe foam	[48]
FePx@Fe	HT	50	1.88	25	Fe foam	[49]
Ni_3Se_4@NiFe LDH/CFCs	HT	50	1.71	100	Ni foam	[50]
RhSA-S-Co_3O_4	HT	50	1.75	120	Ni foam	[51]
NiFe(II,III)-LDH	HT	50	1.72	45	Ni foam	[12]
NiFeRu-LDH	HT	50	1.64	10	Ni foam	[21]

III.4. Conclusion

In summary, a bifunctional electrode with flower-like heterostructure consisting of Fe/Co LDH loaded with small Pt nanoparticles was successfully synthesized through a facile oxygen corrosion method and applied for efficient overall water splitting. The effective OER performance benefited from the Co/Fe LDH and FeO(OH) heterostructure, which facilitated mass diffusion and enhanced reaction kinetics. In addition, loading trace of Pt element uniformly on the catalyst surface promoted faster charge transfer and decreased reaction barrier. Thus, the Pt-Co/Fe LDH electrode exhibited an outstanding HER, OER, and overall water splitting activities in an alkaline medium, which are superior to noble metal-based catalysts e.g., Pt/C and RuO_2. The Pt-Co/Fe LDH electrode recorded overpotential values as low as 126 and 285 mV to deliver 100 mA cm^{-2} for HER and OER, respectively. More importantly, an electrolyzer comprising Pt-Co/Fe LDH as both anode and cathode exhibited a small cell voltage of 1.66 V to reach 50 mA cm^{-2} with excellent stability. The facile and scalable strategy and nanoflower structure engineering of metal hydroxides coupled with noble metals can be utilized to exploring other bifunctional electrocatalysts in the energy field.

References

[1] G. Ji, J.G. Yao, P.T. Clough, J.C.D. da Costa, E.J. Anthony, P.S. Fennell, W. Wang, M. Zhao, Enhanced hydrogen production from thermochemical processes, Energy Environ. Sci. 11(10) (2018) 2647-2672. https://doi.org/10.1039/c8ee01393d.

[2] B. Zhang, J. Wang, B. Wu, X.W. Guo, Y.J. Wang, D. Chen, Y.C. Zhang, K. Du, E.E. Oguzie, X.L. Ma, Unmasking Chloride Attack on the Passive Film of Metals, Nat. Commun. 9(1) (2018) 2559. https://doi.org/10.1038/s41467-018-04942-x.

[3] S. Hao, L. Chen, C. Yu, B. Yang, Z. Li, Y. Hou, L. Lei, X. Zhang, NiCoMo Hydroxide Nanosheet Arrays Synthesized via Chloride Corrosion for Overall Water Splitting, ACS Energy Lett. 4(4) (2019) 952-959. https://doi.org/10.1021/acsenergylett.9b00333.

[4] X. Liu, M. Gong, D. Xiao, S. Deng, J. Liang, T. Zhao, Y. Lu, T. Shen, J. Zhang, D. Wang, Turning Waste into Treasure: Regulating the Oxygen Corrosion on Fe Foam for Efficient Electrocatalysis, Small 16(24) (2020) 2000663. https://doi.org/10.1002/smll.202000663.

[5] Y. Tan, R. Xie, S. Zhao, X. Lu, L. Liu, F. Zhao, C. Li, H. Jiang, G. Chai, D.J.L. Brett, P.R. Shearing, G. He, I.P. Parkin, Facile Fabrication of Robust Hydrogen Evolution Electrodes under High Current Densities via Pt@Cu Interactions, Adv. Funct. Mater. 31(45) (2021) 2105579. https://doi.org/10.1002/adfm.202105579.

[6] J.X. Feng, H. Xu, Y.T. Dong, S.H. Ye, Y.X. Tong, G.R. Li, FeOOH/Co/FeOOH Hybrid Nanotube Arrays as High-Performance Electrocatalysts for the Oxygen Evolution Reaction, Angew. Chem. Int. Ed. 55(11) (2016) 3694-8. https://doi.org/10.1002/anie.201511447.

[7] L. Pang, A. Barras, Y. Zhang, M.A. Amin, A. Addad, S. Szunerits, R. Boukherroub, CoO Promoted

the Catalytic Activity of Nitrogen-Doped MoS_2 Supported on Carbon Fibers for Overall Water Splitting, ACS Appl. Mater. Interfaces 11(35) (2019) 31889-31898. https://doi.org/10.1021/acsami.9b09112.

[8] H. Jia, Z. Wang, X. Zheng, J. Lin, H. Liang, Y. Cai, J. Qi, J. Cao, J. Feng, W. Fei, Interlaced Ni-Co LDH nanosheets wrapped Co_9S_8 nanotube with hierarchical structure toward high performance supercapacitors, Chem. Eng. J. 351 (2018) 348-355. https://doi.org/10.1016/j.cej.2018.06.113.

[9] H. Feng, J. Yu, L. Tang, J. Wang, H. Dong, T. Ni, J. Tang, W. Tang, X. Zhu, C. Liang, Improved hydrogen evolution activity of layered double hydroxide by optimizing the electronic structure, Appl. Catal., B 297 (2021) 120478. https://doi.org/10.1016/j.apcatb.2021.120478.

[10] X. Feng, Q. Jiao, W. Chen, Y. Dang, Z. Dai, S.L. Suib, J. Zhang, Y. Zhao, H. Li, C. Feng, Cactus-like $NiCo_2S_4$@NiFe LDH hollow spheres as an effective oxygen bifunctional electrocatalyst in alkaline solution, Appl. Catal., B 286 (2021) 119869. https://doi.org/10.1016/j.apcatb.2020.119869.

[11] C.-F. Li, J.-W. Zhao, L.-J. Xie, J.-Q. Wu, G.-R. Li, Fe doping and oxygen vacancy modulated Fe-Ni_5P_4/NiFeOH nanosheets as bifunctional electrocatalysts for efficient overall water splitting, Appl. Catal., B 291 (2021) 119987. https://doi.org/10.1016/j.apcatb.2021.119987.

[12] X. Meng, J. Han, L. Lu, G. Qiu, Z.L. Wang, C. Sun, Fe($^{2+}$) -Doped Layered Double (Ni, Fe) Hydroxides as Efficient Electrocatalysts for Water Splitting and Self-Powered Electrochemical Systems, Small 15(41) (2019) e1902551. https://doi.org/10.1002/smll.201902551.

[13] W. Xu, F. Lyu, Y. Bai, A. Gao, J. Feng, Z. Cai, Y. Yin, Porous cobalt oxide nanoplates enriched with oxygen vacancies for oxygen evolution reaction, Nano Energy 43 (2018) 110-116. https://doi.org/10.1016/j.nanoen.2017.11.022.

[14] P.W. Menezes, C. Panda, C. Walter, M. Schwarze, M. Driess, A Cobalt-Based Amorphous Bifunctional Electrocatalysts for Water-Splitting Evolved from a Single-Source Lazulite Cobalt Phosphate, Adv. Funct. Mater. 29(32) (2019) 1808632. https://doi.org/10.1002/adfm.201808632.

[15] Y. Jin, Z. Zhang, H. Yang, P. Wang, C. Shen, T. Cheng, X. Huang, Q. Shao, Boosting hydrogen production with ultralow working voltage by selenium vacancy-enhanced ultrafine platinum–nickel nanowires, SmartMat 3(1) (2022) 130-141. https://doi.org/10.1002/smm2.1083.

[16] J. Zheng, W. Sheng, Z. Zhuang, B. Xu, Y. Yan, Universal dependence of hydrogen oxidation and evolution reaction activity of platinum-group metals on pH and hydrogen binding energy, Sci Adv 2(3) (2016) e1501602. https://doi.org/10.1126/sciadv.1501602.

[17] C. Zhang, X. Liang, R. Xu, C. Dai, B. Wu, G. Yu, B. Chen, X. Wang, N. Liu, H_2 In Situ Inducing Strategy on Pt Surface Segregation Over Low Pt Doped $PtNi_5$ Nanoalloy with Superhigh Alkaline HER Activity, Adv. Funct. Mater. 31(14) (2021) 2008298. https://doi.org/10.1002/adfm.202008298.

[18] J. Liu, J. Wang, B. Zhang, Y. Ruan, L. Lv, X. Ji, K. Xu, L. Miao, J. Jiang, Hierarchical $NiCo_2S_4$@NiFe LDH Heterostructures Supported on Nickel Foam for Enhanced Overall-Water-Splitting Activity, ACS Appl. Mater. Interfaces 9(18) (2017) 15364-15372. https://doi.org/10.1021/acsami.7b00019.

[19] X. Nie, X. Kong, D. Selvakumaran, L. Lou, J. Shi, T. Zhu, S. Liang, G. Cao, A. Pan, Three-Dimensional Carbon-Coated Treelike Ni_3S_2 Superstructures on a Nickel Foam as Binder-Free Bifunctional Electrodes, ACS Appl. Mater. Interfaces 10(42) (2018) 36018-36027. https://doi.org/10.1021/acsami.8b13813.

[20] X. Wang, Y. Yang, L. Diao, Y. Tang, F. He, E. Liu, C. He, C. Shi, J. Li, J. Sha, S. Ji, P. Zhang, L. Ma, N. Zhao, CeO_x-Decorated NiFe-Layered Double Hydroxide for Efficient Alkaline Hydrogen Evolution by Oxygen Vacancy Engineering, ACS Appl. Mater. Interfaces 10(41) (2018) 35145-35153.

https://doi.org/10.1021/acsami.8b11688.

[21] G. Chen, T. Wang, J. Zhang, P. Liu, H. Sun, X. Zhuang, M. Chen, X. Feng, Accelerated Hydrogen Evolution Kinetics on NiFe-Layered Double Hydroxide Electrocatalysts by Tailoring Water Dissociation Active Sites, Adv. Mater. 30(10) (2018) 1706279. https://doi.org/10.1002/adma.201706279.

[22] Y. Jia, L. Zhang, G. Gao, H. Chen, B. Wang, J. Zhou, M.T. Soo, M. Hong, X. Yan, G. Qian, J. Zou, A. Du, X. Yao, A Heterostructure Coupling of Exfoliated Ni-Fe Hydroxide Nanosheet and Defective Graphene as a Bifunctional Electrocatalyst for Overall Water Splitting, Adv. Mater. 29(17) (2017) 1700017. https://doi.org/10.1002/adma.201700017.

[23] C. Tang, R. Zhang, W. Lu, L. He, X. Jiang, A.M. Asiri, X. Sun, Fe-Doped CoP Nanoarray: A Monolithic Multifunctional Catalyst for Highly Efficient Hydrogen Generation, Adv. Mater. 29(2) (2017) 1602441. https://doi.org/10.1002/adma.201602441.

[24] H. Yan, Y. Xie, A. Wu, Z. Cai, L. Wang, C. Tian, X. Zhang, H. Fu, Anion-Modulated HER and OER Activities of 3D Ni-V-Based Interstitial Compound Heterojunctions for High-Efficiency and Stable Overall Water Splitting, Adv. Mater. 31(23) (2019) e1901174. https://doi.org/10.1002/adma.201901174.

[25] L. Zhuang, L. Ge, Y. Yang, M. Li, Y. Jia, X. Yao, Z. Zhu, Ultrathin Iron-Cobalt Oxide Nanosheets with Abundant Oxygen Vacancies for the Oxygen Evolution Reaction, Adv. Mater. 29(17) (2017) 1606793. https://doi.org/10.1002/adma.201606793.

[26] T. Zhang, K. Yang, C. Wang, S. Li, Q. Zhang, X. Chang, J. Li, S. Li, S. Jia, J. Wang, L. Fu, Nanometric Ni_5P_4 Clusters Nested on $NiCo_2O_4$ for Efficient Hydrogen Production via Alkaline Water Electrolysis, Adv. Energy Mater. 8(29) (2018) 1801690. https://doi.org/10.1002/aenm.201801690.

[27] J. Hou, Y. Sun, Y. Wu, S. Cao, L. Sun, Promoting Active Sites in Core-Shell Nanowire Array as Mott-Schottky Electrocatalysts for Efficient and Stable Overall Water Splitting, Adv. Funct. Mater. 28(4) (2018) 1704447. https://doi.org/10.1002/adfm.201704447.

[28] Z. Qiu, C.-W. Tai, G.A. Niklasson, T. Edvinsson, Direct observation of active catalyst surface phases and the effect of dynamic self-optimization in NiFe-layered double hydroxides for alkaline water splitting, Energy Environ. Sci. 12(2) (2019) 572-581. https://doi.org/10.1039/c8ee03282c.

[29] L. Yu, H. Zhou, J. Sun, F. Qin, F. Yu, J. Bao, Y. Yu, S. Chen, Z. Ren, Cu nanowires shelled with NiFe layered double hydroxide nanosheets as bifunctional electrocatalysts for overall water splitting, Energy Environ. Sci. 10(8) (2017) 1820-1827. https://doi.org/10.1039/c7ee01571b.

[30] D. Li, H. Baydoun, C.N. Verani, S.L. Brock, Efficient Water Oxidation Using CoMnP Nanoparticles, J. Am. Chem. Soc. 138(12) (2016) 4006−4009. https://doi.org/10.1021/jacs.6b01543.

[31] X. Ji, Y. Lin, J. Zeng, Z. Ren, Z. Lin, Y. Mu, Y. Qiu, J. Yu, Graphene/MoS_2/$FeCoNi(OH)_x$ and Graphene/MoS_2/$FeCoNiP_x$ multilayer-stacked vertical nanosheets on carbon fibers for highly efficient overall water splitting, Nat. Commun. 12(1) (2021) 1380. https://doi.org/10.1038/s41467-021-21742-y.

[32] J. Luo, J.H. Im, M.T. Mayer, M. Schreier, M.K. Nazeeruddin, N.G. Park, S.D. Tilley, H.J. Fan, M. Grätzel, Water photolysis at 12.3% efficiency via perovskite photovoltaics and Earth-abundant catalysts, Science 345(6204) (2014) 1593-6. https://doi.org/10.1126/science.1258307.

[33] K.N. Dinh, P. Zheng, Z. Dai, Y. Zhang, R. Dangol, Y. Zheng, B. Li, Y. Zong, Q. Yan, Ultrathin Porous NiFeV Ternary Layer Hydroxide Nanosheets as a Highly Efficient Bifunctional Electrocatalyst for Overall Water Splitting, Small 14(8) (2018) 1703257. https://doi.org/10.1002/smll.201703257.

[34] V.M. Nikolic, S.L. Maslovara, G.S. Tasic, T.P. Brdaric, P.Z. Lausevic, B.B. Radak, M.P. Marceta

Kaninski, Kinetics of Hydrogen Evolution Reaction In Alkaline Electrolysis On a Ni Cathode In the Presence Of Ni–Co–Mo Based Ionic Activators, Appl. Catal., B 179 (2015) 88-94. https://doi.org/10.1016/j.apcatb.2015.05.012.

[35] Z. Ma, C. Chen, X. Cui, L. Zeng, L. Wang, W. Jiang, J. Shi, Hydrogen Evolution/Oxidation Electrocatalysts by the Self-Activation of Amorphous Platinum, ACS Appl. Mater. Interfaces 13(37) (2021) 44224-44233. https://doi.org/10.1021/acsami.1c10518.

[36] R.K. Shervedani, A.R. Madram, Kinetics of hydrogen evolution reaction on nanocrystalline electrodeposited $Ni_{62}Fe_{35}C_3$ cathode in alkaline solution by electrochemical impedance spectroscopy, Electrochim. Acta 53(2) (2007) 426-433. https://doi.org/10.1016/j.electacta.2007.06.006.

[37] R. Subbaraman, D. Tripkovic, D. Strmcnik, K.C. Chang, M. Uchimura, A.P. Paulikas, V. Stamenkovic, N.M. Markovic, Enhancing hydrogen evolution activity in water splitting by tailoring $Li(^+)$-$Ni(OH)_2$-Pt interfaces, Science 334(6060) (2011) 1256-60. https://doi.org/10.1126/science.1211934.

[38] Z.-Y. Pan, Z. Tang, Y.-Z. Zhan, D. Sun, Three-dimensional porous CoNiO2@reduced graphene oxide nanosheet arrays/nickel foam as a highly efficient bifunctional electrocatalyst for overall water splitting, Tungsten 2(4) (2020) 390-402. https://doi.org/10.1007/s42864-020-00065-3.

[39] N. Danilovic, R. Subbaraman, D. Strmcnik, K.C. Chang, A.P. Paulikas, V.R. Stamenkovic, N.M. Markovic, Enhancing the alkaline hydrogen evolution reaction activity through the bifunctionality of $Ni(OH)_2$/metal catalysts, Angew. Chem. Int. Ed. 51(50) (2012) 12495-8. https://doi.org/10.1002/anie.201204842.

[40] H. Zhang, X. Li, A. Hähnel, V. Naumann, C. Lin, S. Azimi, S.L. Schweizer, A.W. Maijenburg, R.B. Wehrspohn, Bifunctional Heterostructure Assembly of NiFe LDH Nanosheets on NiCoP Nanowires for Highly Efficient and Stable Overall Water Splitting, Adv. Funct. Mater. 28(14) (2018) 1706847. https://doi.org/10.1002/adfm.201706847.

[41] S. Lee, A. Moysiadou, Y.-C. Chu, H.M. Chen, X. Hu, Tracking high-valent surface iron species in the oxygen evolution reaction on cobalt iron (oxy)hydroxides, Energy Environ. Sci. 15(1) (2022) 206-214. https://doi.org/10.1039/d1ee02999a.

[42] Y. Tang, Q. Liu, L. Dong, H.B. Wu, X.-Y. Yu, Activating The Hydrogen Evolution And Overall Water Splitting Performance Of NiFe LDH By Cation Doping And Plasma Reduction, Appl. Catal., B 266 (2020) 118627. https://doi.org/10.1016/j.apcatb.2020.118627.

[43] D. Zheng, Z. Jing, Q. Zhao, Y. Kim, P. Li, H. Xu, Z. Li, J. Lin, Efficient Co-doped pyrrhotite $Fe_{0.95}S_{1.05}$ nanoplates for electrochemical water splitting, Chem. Eng. J. 402 (2020) 125069. https://doi.org/10.1016/j.cej.2020.125069.

[44] Y. Liang, H. Wang, J. Zhou, Y. Li, J. Wang, T. Regier, H. Dai, Covalent Hybrid of Spinel Manganese–Cobalt Oxide and Graphene as Advanced Oxygen Reduction Electrocatalysts, J. Am. Chem. Soc. 134(7) (2012) 3517-3523. https://doi.org/10.1021/ja210924t.

[45] H. Shin, H. Xiao, W.A. Goddard, In Silico Discovery of New Dopants for Fe-Doped Ni Oxyhydroxide ($Ni_{1-x}Fe_xOOH$) Catalysts for Oxygen Evolution Reaction, J. Am. Chem. Soc. 140(22) (2018) 6745-6748. https://doi.org/10.1021/jacs.8b02225.

[46] W. Liu, J. Bao, M. Guan, Y. Zhao, J. Lian, J. Qiu, L. Xu, Y. Huang, J. Qian, H. Li, Nickel-cobalt-layered double hydroxide nanosheet arrays on Ni foam as a bifunctional electrocatalyst for overall water splitting, Dalton Trans 46(26) (2017) 8372-8376. https://doi.org/10.1039/c7dt00906b.

[47] Y. Zhao, Y. Gao, Z. Chen, Z. Li, T. Ma, Z. Wu, L. Wang, Trifle Pt coupled with NiFe hydroxide synthesized via corrosion engineering to boost the cleavage of water molecule for alkaline water-

splitting, Appl. Catal., B 297 (2021) 120395. https://doi.org/10.1016/j.apcatb.2021.120395.

[48] M. Zhang, T. Wang, H. Cao, S. Cui, P. Du, Self-supported Ni_2P nanosheets on low-cost three-dimensional Fe foam as a novel electrocatalyst for efficient water oxidation, J. Energy Chem. 42 (2020) 71-76. https://doi.org/10.1016/j.jechem.2019.06.010.

[49] Y. Wang, B. Ma, Y. Chen, Iron phosphides supported on three-dimensional iron foam as an efficient electrocatalyst for water splitting reactions, J. Mater. Sci. 54(24) (2019) 14872-14883. https://doi.org/10.1007/s10853-019-03985-9.

[50] T. Zhang, L. Hang, Y. Sun, D. Men, X. Li, L. Wen, X. Lyu, Y. Li, Hierarchical hetero-Ni_3Se_4@NiFe LDH micro/nanosheets as efficient bifunctional electrocatalysts with superior stability for overall water splitting, Nanoscale Horiz. 4(5) (2019) 1132-1138. https://doi.org/10.1039/c9nh00177h.

[51] A. Kumar, X. Liu, J. Lee, B. Debnath, A.R. Jadhav, X. Shao, V.Q. Bui, Y. Hwang, Y. Liu, M.G. Kim, H. Lee, Discovering ultrahigh loading of single-metal-atoms via surface tensile-strain for unprecedented urea electrolysis, Energy Environ. Sci. 14(12) (2021) 6494-6505. https://doi.org/10.1039/d1ee02603h.

Chapter IV: Construction of Desert Rose Flower-Shaped NiFe LDH-Ni_3S_2 Heterostructure via Seawater Corrosion Engineering for Efficient Water-Urea Splitting and Seawater Utilization

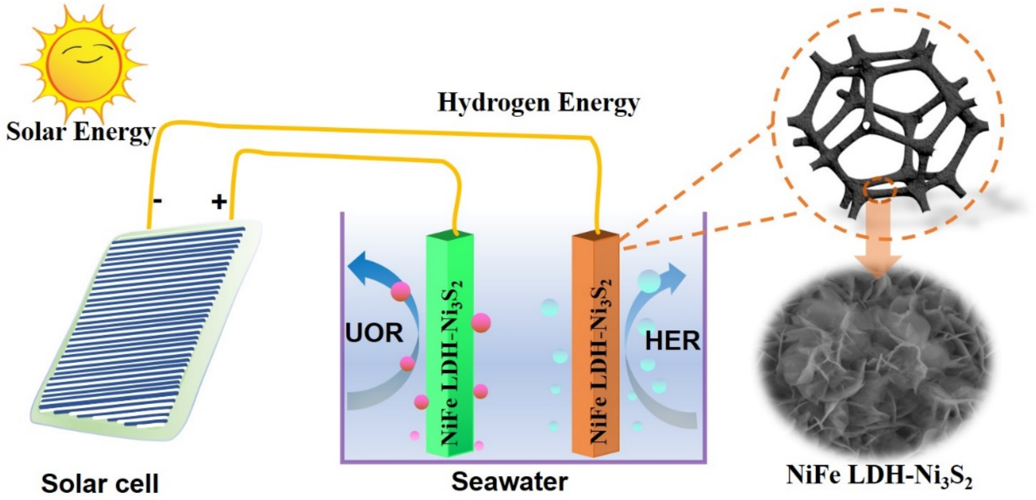

IV.1 Abstract

The development of high-performance and robust non-precious metal-based catalysts to accelerate electrocatalytic reaction kinetics is crucial for electrochemical seawater splitting. The common electrocatalysts for seawater electrolysis suffer from sluggish reaction kinetics and instability, restricting their practical application. Herein, nickel-iron layer double hydroxide and Ni_3S_2 heterostructured nanoflower bifunctional electrocatalysts (NiFe LDH-Ni_3S_2) were synthesized *via* seawater corrosion and ion exchange strategy. The desert rose shaped nanoflower structure of the catalyst was tuned by seawater corrosion time. The unique heterostructure not only possessed more redox reaction centers, but also enhanced anti-corrosion ability, which could effectively facilitate mass diffusion, charge transport and maintain high electrocatalytic activity in seawater. The as-prepared NiFe LDH-Ni_3S_2 electrodes recorded overpotentials as low as 257 and 280 mV to deliver 100 mA cm^{-2} for HER and OER in 1 M KOH seawater, respectively. In 1 M KOH seawater + 0.33 M urea, there was an obvious reduced urea oxidation reaction (UOR) potential of 1.37 V to reach 100 mA cm^{-2}, which is

about 140 mV lower than for OER. Noteworthy, Ni/Fe LDH-Ni_3S_2 as a bifunctional electrocatalyst featured an ultralow voltage of 1.63 V to reach a current density of 100 mA cm^{-2} and almost 100% Faradaic efficiency for overall water-urea splitting, which is superior to the most previously reported electrocatalysts. This work provides insights on the application of seawater corrosion engineering technique to modulate the electrocatalytic activity in energy conversion and seawater utilization systems, achieving efficient conversion of solar energy, electricity and hydrogen.

IV.2 Experimental section

Synthesis of NiFe LDH-Ni_3S_2 catalyst

Nickel foam (NF) was pre-processed into 2×4 cm^{-2} and wash-cleaned with acetone, hydrochloric acid (0.1 M), and ultrapure water *via* ultrasonic treatment (15 min each step) to remove the surface oxides and adsorbed organic molecules.

The NiFe LDH-Ni_3S_2 catalyst was synthesized *via* seawater corrosion and ion exchange two-step method. Firstly, NiFe LDH foam was prepared by seawater corrosion approach; NF was immersed in a mixture of 0.5 M NaCl, 30 mM $Fe(NO_3)_3 \cdot 9H_2O$ aqueous solution under orbital shaking for 12 h at room temperature. The resulting yellowish brown foam was rinsed several times with water to remove excess NaCl and dried at 60 °C for 2 h. For further optimization of electrocatalytic performance, a series of NiFe LDH catalysts was prepared by adjusting the Fe salt type and concentration, and corrosion time. Secondly, the NiFe LDH-Ni_3S_2 catalyst was constructed by ion exchange method; NiFe LDH on NF was transferred into 30 mL $Na_2S \cdot 9H_2O$ (0.5 M) aqueous solution and reacted for 6 h at 100 °C in autoclave. In this process, OH^- groups of NiFe LDH will be partially exchanged with S^{2-} by adjusting the reaction time. After natural cooling, the NiFe LDH-Ni_3S_2 supported on NF was taken out, thoroughly washed by water and dried at 60 °C in oven. The Ni, Fe, S and O atomic ratios in the final product were detected by energy dispersive spectroscopy (EDS) and X-ray photoelectron spectroscopy (XPS) analyses.

IV.3. Results and discussion

IV.3.1 Construction process of NiFe LDH-Ni_3S_2 catalysts

Seawater is one of the most abundant natural resources on our planet. It contains Na^+, Ca^{2+}, Mg^{2+}, and Cl^- ions and holds huge opportunities and challenges for development and utilization, particularly for freshwater production. Seawater corrosion is a double-edged sword which sometimes inevitably destroys industrial pipelines, whereas it contains huge potential for energy saving such as synthesis of catalysts *via* ion corrosion technology without additional thermal energy losses [1, 2]. In electrocatalysis field, three-dimension (3D) porous Ni foam (NF) was considered as efficient support, owing to its good electron transfer ability. Herein, seawater corrosion technology was applied to construct desert rose-shaped nanoflower structure with an average size of 500-900 nm. As illustrated in **Figure IV.1**, Ni/Fe double layer hydroxide (LDH) was firstly synthesized *via* introducing of NF in NaCl and Fe salt-containing simulated seawater environment.

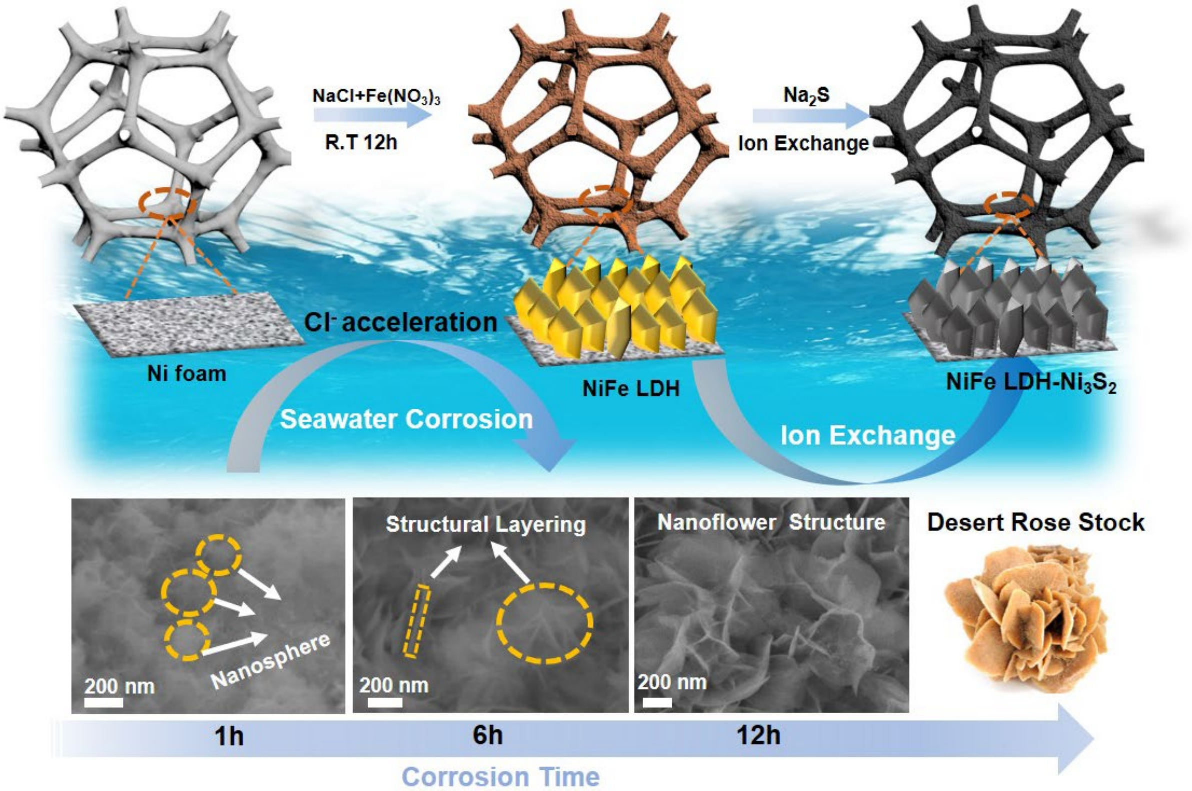

Figure IV.1. Schematic representation of the synthesis of 3D desert rose flower-shaped hierarchical NiFe LDH-Ni_3S_2 catalyst *via* seawater corrosion technology.

Scanning electron microscopy (SEM) images recorded the surface micromorphology variation accompanied with increasing the corrosion time. The morphology experienced notorious changes from nanoparticle/nanosphere to lamellar separation stage, while the generated OH^- from the corrosion area reacted with metal ion to form metal hydroxide (NiFe LDH). A replacement reaction between OH^- groups of NiFe LDH and Na_2S takes place to yield NiFe LDH-Ni_3S_2 heterostructure. Notably, the color change of the prepared catalyst featured three stages: silver (NF) - yellow (NiFe LDH) - black (NiFe LDH-Ni_3S_2).

To evaluate the corrosion displacement reaction behavior, the corrosion polarization curves were conducted as previously [3, 4], when NF was immersed in 0.5 M NaCl, 30 mM $Fe(NO_3)_3·9H_2O$ or 0.5 M NaCl+30 mM $Fe(NO_3)_3·9H_2O$ aqueous solutions, separately. In this system, NF, carbon rod and saturated calomel (SCE) electrodes acted respectively as working, counter and reference electrodes. For observing NiFe LDH corrosion-growth mechanism, the corrosion polarization (current-voltage) curves were acquired in the potential window of open circuit potential (OCP)±300 mV at a scan rate of 5 mV s^{-1}, as shown in **Figure IV.2**. The corrosion curent densities (I_{corr}) and corrosion potentials (E_{corr}) could be deduced from the above corrosion polarization curves. NF immmersed in NaCl-$Fe(NO_3)_3·9H_2O$ aqueous solution revealed higher I_{corr} and E_{corr} (6.48 mA cm^{-2}, -0.28 V *vs.* SCE, respectively) compared to NaCl (1.08 mA cm^{-2}, -0.38 V) or $Fe(NO_3)_3·9H_2O$ (3.06 mA cm^{-2}, -0.18 V) systems, indicating a stronger self-corrosion tendency. Taking advantage of the self-corrosion process, surface Ni atoms were oxidized assisted by Cl^- and generated Ni^{2+}/Ni^{3+} ions, while simultaneously released electrons (anode) and sustainable formation of OH^- at the cathode led to LDH formation, according to Eqs. (1-3) [5].

Anode reaction: $Ni \leftrightarrow Ni^{2+} + 2e^-, Ni^{2+} \leftrightarrow Ni^{3+} + e^-$ (1)

Cathode reaction: $O_2 + 2H_2O + 4e^- \leftrightarrow 4OH^-$ (2)

Precipitation reaction: $Fe^{3+} + Ni^{2+} + Ni^{3+} + xOH^- \leftrightarrow NiFe\ (OH^-)_x$ (3)

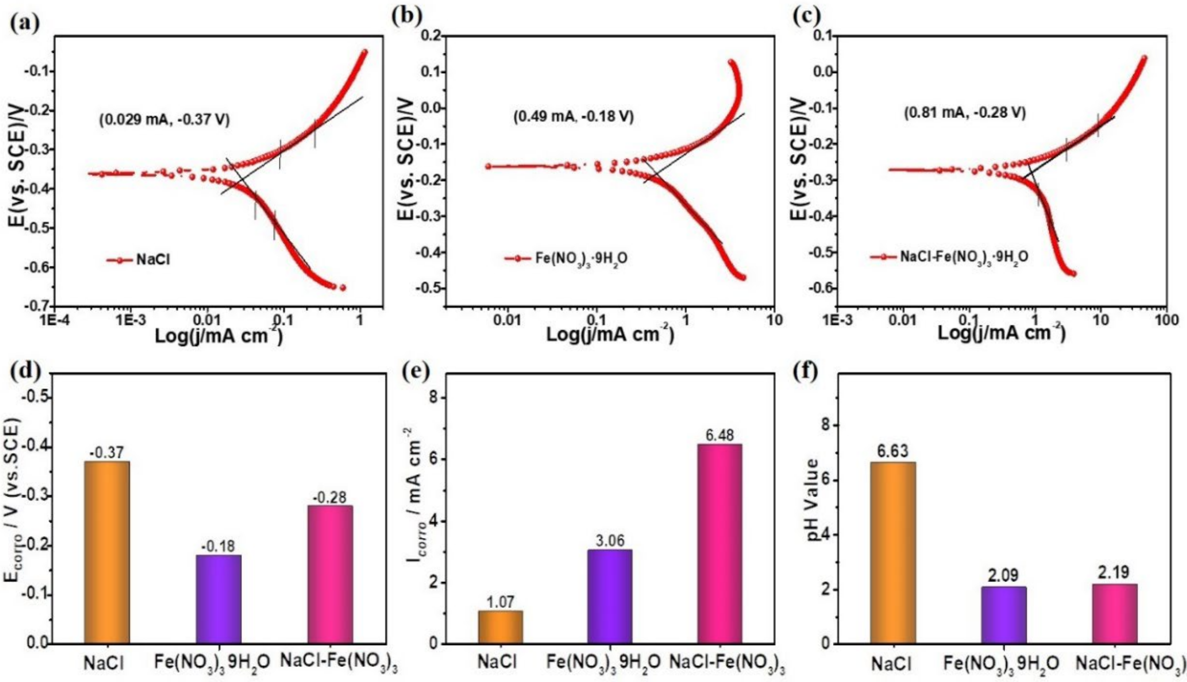

Figure IV.2. Corrosion polarization curves of nickel foam (NF) in (**a**) 0.5 M NaCl, (**b**) 30 mM $Fe(NO_3)_3 \cdot 9H_2O$, (**c**) 0.5 M NaCl+30 mM $Fe(NO_3)_3 \cdot 9H_2O$ aqueous solutions, (**d**) comparison of corrosion potentials (E_{corr}), (**e**) comparison of corrosion current densities (I_{corr}), (**f**) comparison of different solution pH values.

IV.3.2. Morphology and structural characterization

The morphology of the catalysts was firstly characterized by scanning electron microscopy (SEM). As illustrated in **Figure IV.3,** the pristine NF owned a 3D porous skeleton and smooth surface structure. This contrasts with the NF immersed in 0.5 M NaCl aqueous solution (NaCl-Ni foam) which exhibited a rough and wrinkled morphology, owing to the corrosion effect. Furthermore, the morphology of NiFe LDH-Ni foam, prepared at different corrosion times (1, 6, 12, 18 h), displayed numerous layered array structures and obvious nanoflowers after 12 h corrosion reaction (**Figure IV.4**).

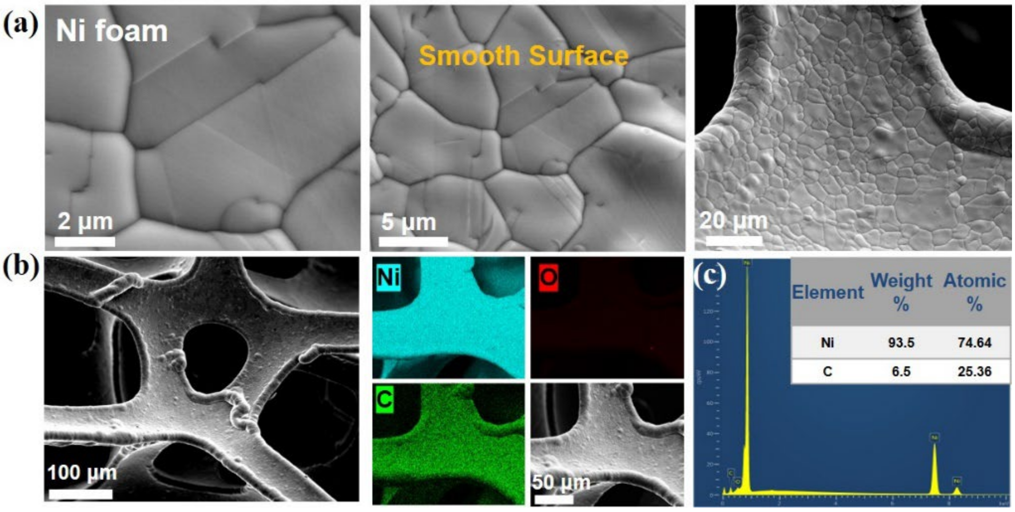

Element	Weight %	Atomic %
Ni	93.5	74.64
C	6.5	25.36

Figure IV.3. (**a**) SEM images at different magnifications, (**b**) elemental mapping images of Ni, C and O, and (**c**) EDX spectrum of the pristine Ni foam.

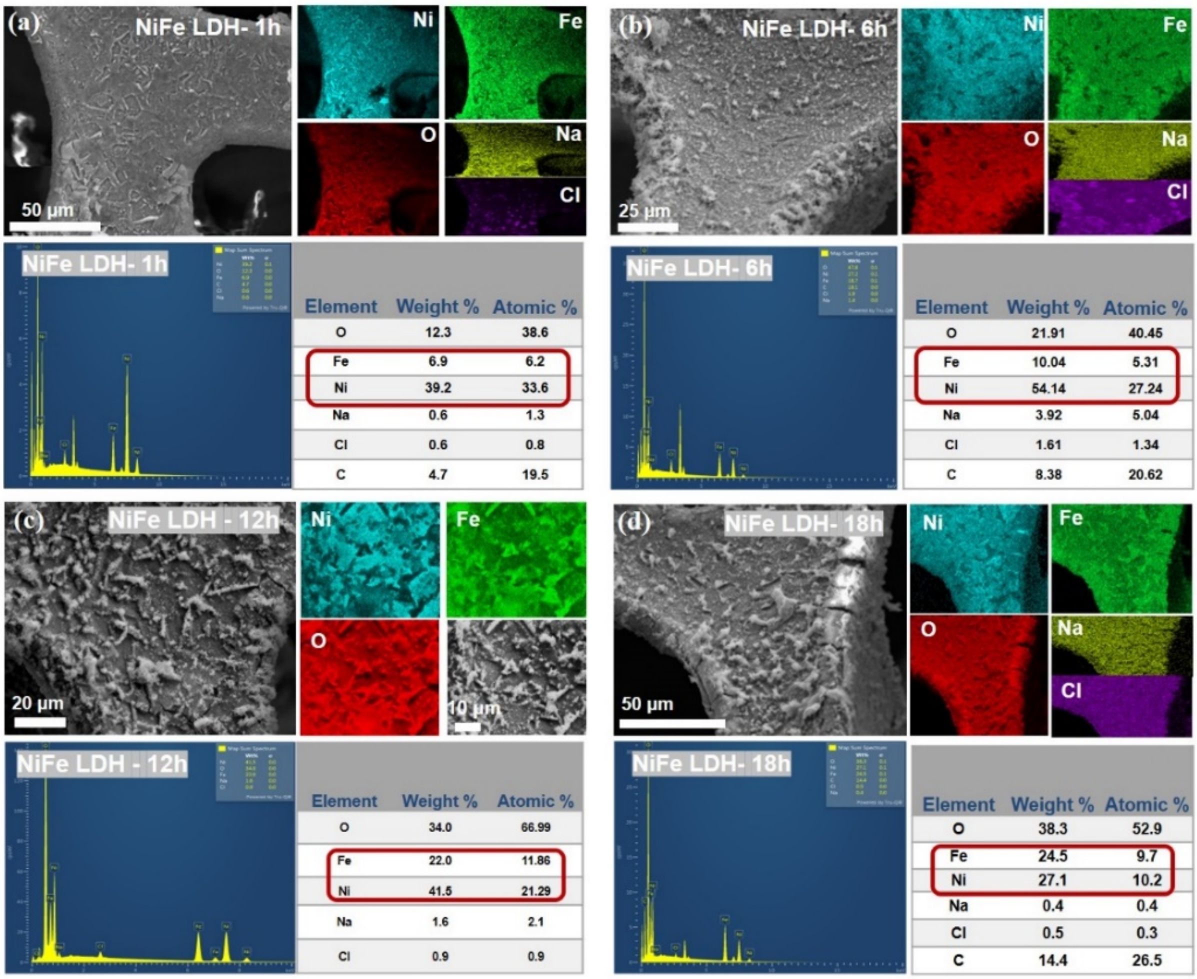

NiFe LDH- 1h

Element	Weight %	Atomic %
O	12.3	38.6
Fe	6.9	6.2
Ni	39.2	33.6
Na	0.6	1.3
Cl	0.6	0.8
C	4.7	19.5

NiFe LDH- 6h

Element	Weight %	Atomic %
O	21.91	40.45
Fe	10.04	5.31
Ni	54.14	27.24
Na	3.92	5.04
Cl	1.61	1.34
C	8.38	20.62

NiFe LDH - 12h

Element	Weight %	Atomic %
O	34.0	66.99
Fe	22.0	11.86
Ni	41.5	21.29
Na	1.6	2.1
Cl	0.9	0.9

NiFe LDH- 18h

Element	Weight %	Atomic %
O	38.3	52.9
Fe	24.5	9.7
Ni	27.1	10.2
Na	0.4	0.4
Cl	0.5	0.3
C	14.4	26.5

Figure IV.4. SEM and elemental mapping images of (**a**) NiFe LDH-1h, (**b**) NiFe LDH-6h, (**c**) NiFe LDH-12h and (**d**) NiFe LDH-18h. The corresponding EDX spectra and elemental composition of Ni, Fe, O, Na and Cl.

Sample	Ni (at. %)	Fe (at. %)	S (at. %)	O (at. %)
NiFe LDH-Ni_3S_2 foam [a]	11.35	4.93	6.24	40.87
NiFe LDH-Ni_3S_2 foam [b]	15.5	12.8	13.4	38.3

Table 1. Surface composition of NiFe LDH-Ni_2S_3 catalyst determined by [a] XPS and [b] TEM-EDX analysis.

After an incomplete sulfidation process, Ni/Fe LDH-Ni_3S_2 (**Figure IV.5a-b**) also featured similar desert rose shaped-flowers in the size of several micrometers (0.5~1 μm) and a thickness of dozens of nanometers (25~35 nm). Meanwhile, transmission electron microscopy (TEM) image in **Figure IV.5c** confirmed further the typical flower-like interconnected nanosheets of Ni/Fe LDH-Ni_3S_2 surface, forming a porous morphology with large surface size, which is expected to facilitate fast charge and mass transport for effective electrocatalytic activity. The lattice spacings of 0.250, 0.202 and 0.291 nm, in the high-resolution TEM (HRTEM) images in **Figure IV.5d-g**, were indexed to the (012), 202) and (110) crystal planes of NiFe LDH (51-0463) and Ni_3S_2 (44-1418), respectively, indicating a unique hierarchical heterojunction of NiFe LDH-Ni_3S_2. Energy-dispersive X-ray spectroscopy (EDS) analysis was conducted to acquire elemental chemical composition and distribution. As shown in **Figure IV.5h** and **Table 1**, the presence of Ni (15.5 at. %), Fe (12.8 at. %), S (13.4 at. %) and O (38.3 at. %) atoms is in full accordance with the chemical composition of the catalysts. EDS mapping disclosed the homogeneous distribution of the different elements in NiFe LDH-Ni_3S_2.

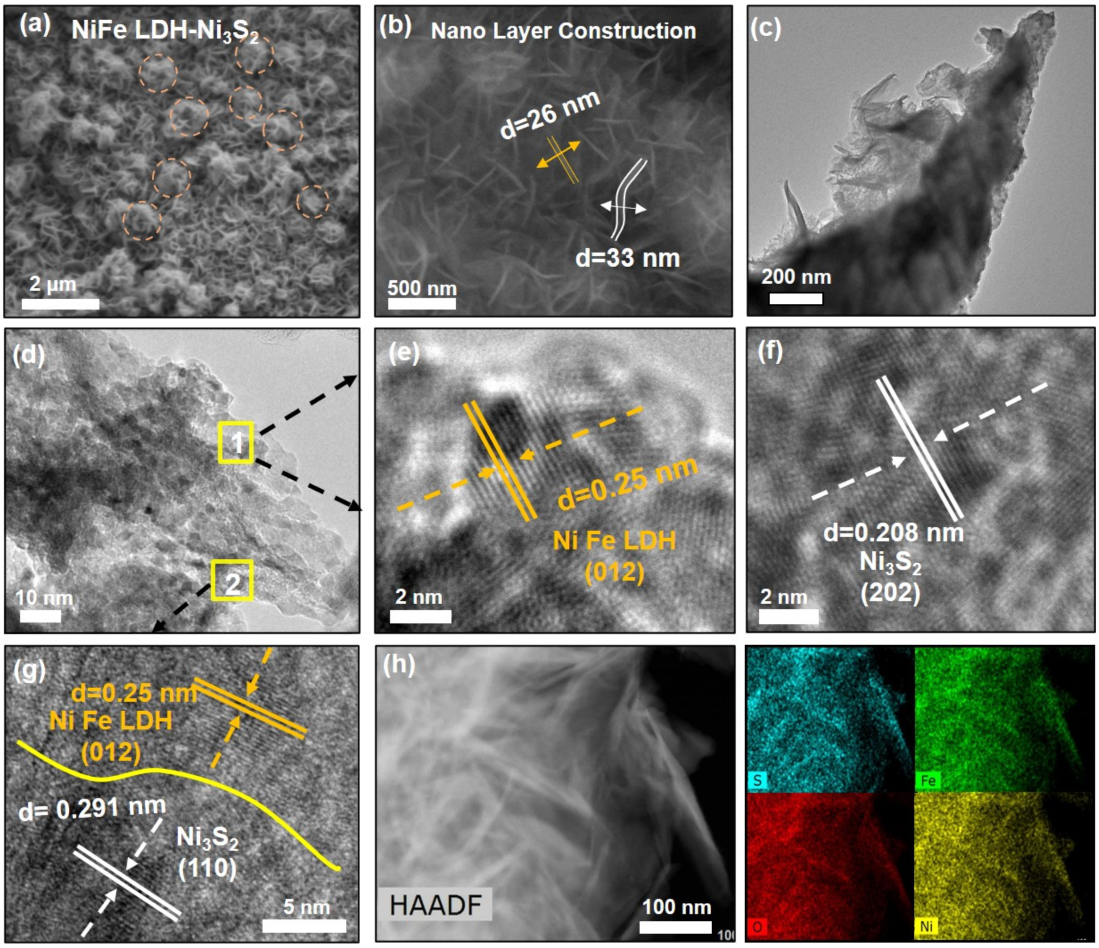

Figure IV.5. (**a, b**) SEM images, (**c**) TEM image (**d-g**) HRTEM images, and (**g**) TEM image and EDX elemental mapping (Fe, O, Ni, S) of the NiFe LDH-Ni_3S_2.

X-ray diffraction (XRD) analysis was employed to characterize the phase composition of the developed catalysts. As shown in **Figure IV.6** and **Figure IV.7**, there are three strong diffraction peaks at 44.5°, 51.8° and 76.4°, which are indexed to typical Ni peak (PDF 04-0850) for Ni foam, NaCl-Ni foam, NiFe LDH and NiFe LDH-Ni_3S_2, respectively. Importantly, the presence of new peaks at 11.5° (003), 23.3° (006), 34.5° (012), 39.2° (015), and 61.0° (113) are indexed to the typical NiFe LDH structure (PDF 51-0463) after NF immersion in NaCl and $Fe(NO_3)_3$ aqueous solution, indicating the successful fabrication of LDH structure on NF surface. Moreover, after sulfidation reaction with Na_2S, new peaks at 21.7° (101), 31.1° (110), 37.8° (003), 50.1° (211), and 55.1° (122) (PDF 44-1418) were observed in the XRD plot of NiFe LDH-Ni_3S_2, which is consistent with the HR-TEM analysis, further confirming the successful fabrication of the heterostructure. Ni_3S_2 is Hazelwoodite structured and crystallizes in the trigonal R32 space group. Ni+1.33+ is bonded to four equivalent S^{2-} atoms to form a mixture of distorted edge and introduce more defect sites.

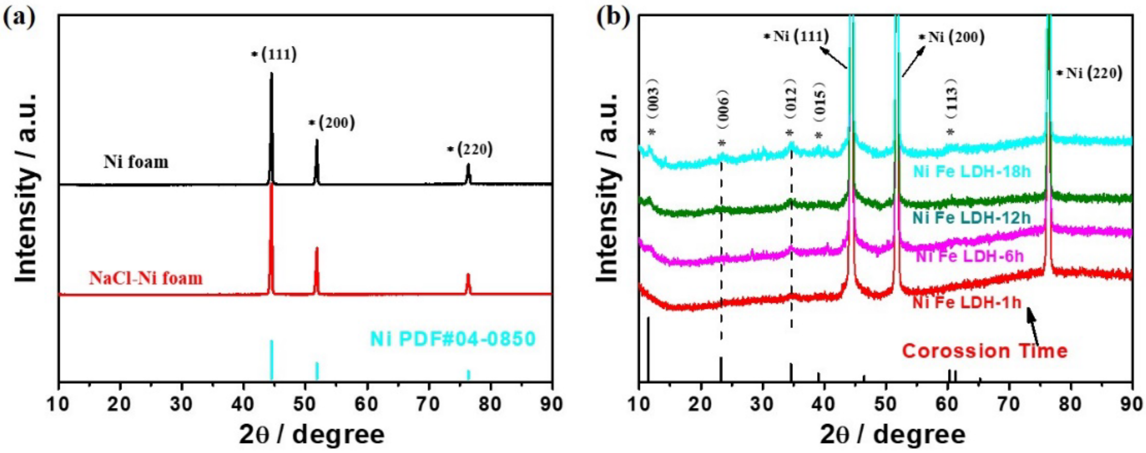

Figure IV.6. XRD patterns of (**a**) Ni foam before (black) and after (red) immersion in 0.5 M NaCl aqueous solution for 12 h at room temperature. (**b**) XRD patterns of NiFe LDH prepared using different corrosion times.

X-ray photoelectron spectroscopy was conducted to assess the surface chemical composition of samples. **Figure IV.7b** depicts the full spectrum of NiFe LDH, comprising Ni (13.09 at. %), Fe (6.11 at. %), O (45.51 at. %) and Cl (3.30 at. %). The low-resolution XPS plot of NiFe LDH-Ni$_3$S$_2$ consists of Ni (11.35 at. %), Fe (4.93 at. %), O (40.87 at. %), and S (6.24 at. %) which coincides with previous EDS mapping results, implying the successful sulfidation reaction.

The high-resolution plot of the S 2p could be fitted with several components at binding energies of 162.9 and 161.7 eV ascribed respectively to S 2p$_{1/2}$ and 2p$_{3/2}$ of S-M (metal) bond, whereas the peak of S-O (SO$_4^{2-}$), located at 168.5 eV, indicates the formation of oxidized sulfur atoms. Besides, the peaks of Ni 2p$_{1/2}$ (873.5 eV) and Ni 2p$_{3/2}$ (855.6 eV) of NiFe LDH-Ni$_3$S$_2$ heterostructure exhibited positive shifts of respectively 0.70 and 0.69 eV compared to those of NiFe LDH, further suggesting that electron transfer occurred at the heterojunction interfaces. In addition, Ni$_3$S$_2$ nanosheets also induced plenty of vacancies, resulting in a higher oxidation state of Ni atoms.

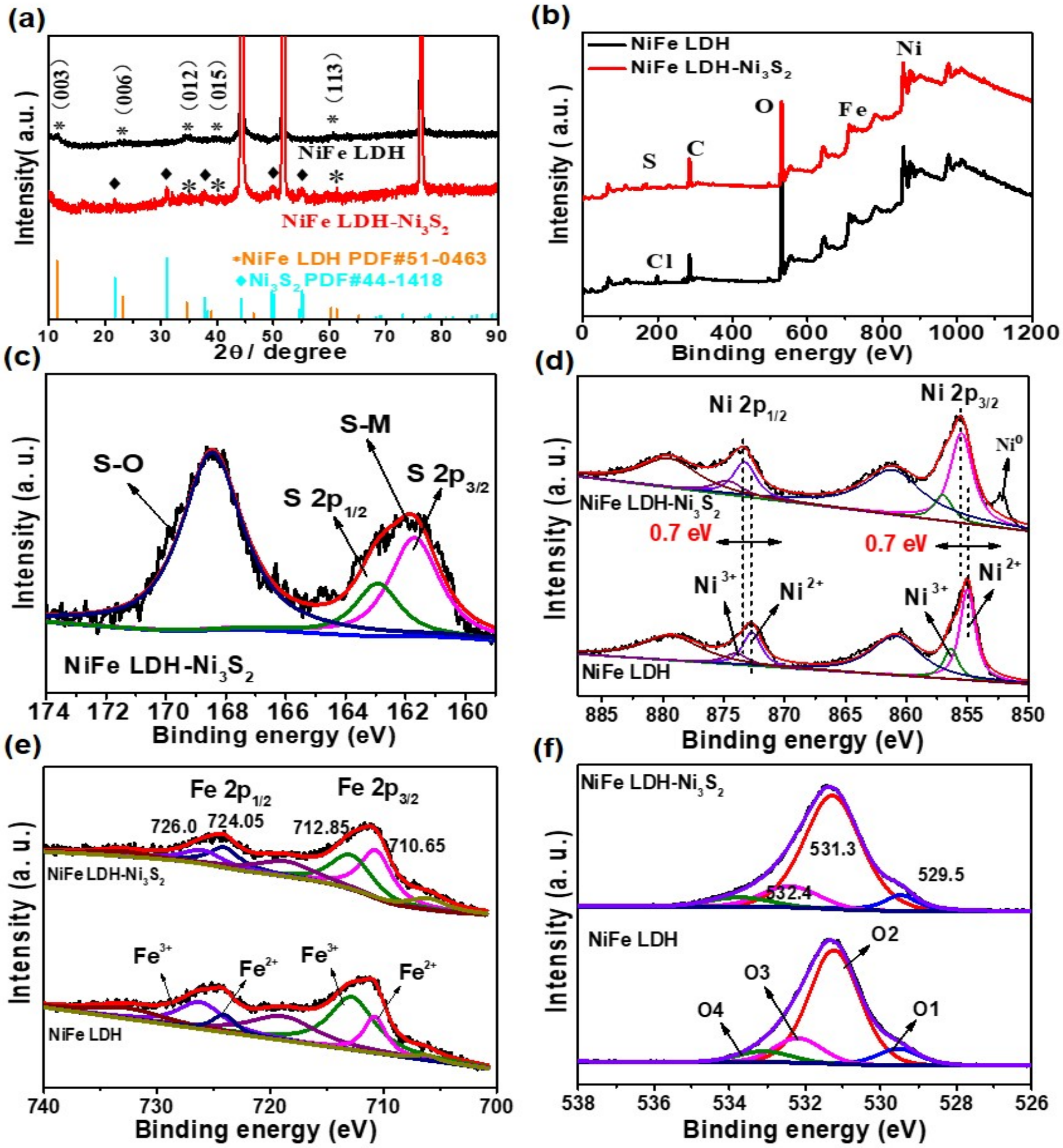

Figure IV.7. (**a**) XRD patterns, (**b**) XPS full scans and high-resolution XPS plots of (**c**) S 2p, (**d**) Ni 2p, (**e**) Fe 2p, (**f**) O 1s of Ni/Fe LDH and NiFe LDH-Ni_3S_2.

The Fe 2p spectrum of NiFe LDH before and after sulfidation infers a similar valence distribution with two fitted peaks for Fe $2p_{1/2}$ due to Fe^{3+} (726.3 eV) and Fe^{2+} (724.2 eV), whereas the peaks located at binding energies of 712.8 eV (Fe^{3+}) and 710.6 eV (Fe^{2+}) correspond to Fe $2p_{3/2}$ deconvoluted regions. In addition, the Fe^{2+}/Fe^{3+} ratio recorded obvious variation from 0.40 to 1.17 after sulfidation process, implying the presence of strong cation interactions in the NiFe LDH-Ni_3S_2 interface. Furthermore, the O 1s spectrum could be deconvoluted into four characteristic peaks; the O1 peak at 529.5 eV is associated with the metal−oxygen bond, the O2 peak at 531.3 eV belongs to defect sites with low oxygen coordination, and the components at 532.4 and 533.1 eV are ascribed to hydroxyl groups (O3) and adsorbed molecular water (O4), respectively. Both NiFe LDH and NiFe LDH-Ni_3S_2 samples possessed stronger O2 content, indicating the presence of abundant defect sites which could promote efficient catalytic reaction. The XPS data of as-prepared samples imply a strong interfacial interaction between NiFe LDH and Ni_3S_2 and presence of numerous defect sites, which are favorable attributes for effective electrocatalytic processes.

IV.3.3 Hydrogen evolution reaction (HER)

The electrocatalytic performance of prepared catalysts was firstly examined in 1M KOH freshwater solution using a standard three-electrode system. The linear sweep voltammetry (LSV) curves of all catalysts were calculated with 90% IR compensation **(Figure IV.9a)**. NiFe LDH-Ni_3S_2 exhibited a lower overpotential (101, 240 mV) to reach respectively a current density of 10 and 100 mA^{-2}, as compared to NF (237, 504 mV) and NiFe LDH (210, 342 mV). Even though its overpotential could not surpass that of Pt/C-Ni foam electrode at lower current densities, the HER performance of NiFe LDH-Ni_3S_2 gradually approached that of Pt/C electrode at higher current densities, owing to its unique heterostructure (**Figure IV.9b**). Furthermore, the influence of iron salt type and concentration, and corrosion reaction time were investigated by LSV (**Figures IV.8**). Firstly, the HER performance of Fe^{3+} salts ($Fe(NO_3)_3$, $FeCl_3$) disclosed much better activity compared to Fe^{2+} salts, owing to self-corrosion replacement reaction. Secondly, the LSV curves exhibited enhanced performance trend up to $Fe(NO_3)_3$ concentration of 30 mM at NaCl concentration of 0.5 M close to salt concentration in seawater. Furthermore, the overpotential gradually decreased upon increasing the corrosion reaction time due to the formation of three-dimensional desert rose flower-shaped architecture. The influence of the sulfidation time was further assessed. It could be seen that 6 h treatment achieved better electrocatalytic activity than other treatment times, which indicates that the proper proportion of sulfide phase in the NiFe LDH-Ni_3S_2 heterostructure is beneficial for HER and OER catalytic activities.

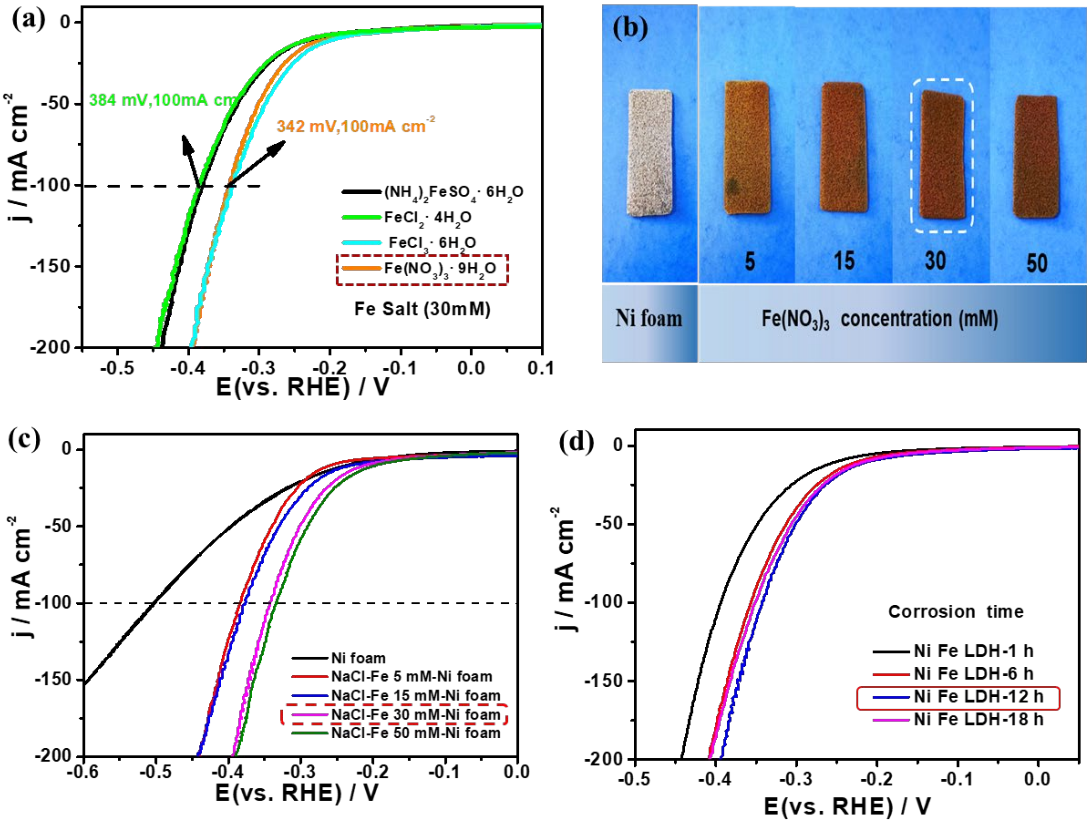

Figure IV.8. LSV polarization curves of NiFe LDH prepared using various types of Fe salts; (**b**) Photographs of NiFe LDH catalysts prepared via various $Fe(NO_3)_3$ concentrations and 0.5 M NaCl solution; (**c-d**) LSV polarization curves of NiFe LDH prepared using various $Fe(NO_3)_3$ concentrations and different corrosion time for catalyzing HER in 1M KOH at a scan rate of 5 mV s^{-1}.

The NiFe LDH-Ni_3S_2 was successfully prepared *via* ion exchange and displayed faster HER catalytic rate. As is shown in **Figure IV.9c,** the Tafel slope of NiFe LDH-Ni_3S_2 (95.3 mV dec^{-1}) is comparable to that of Pt/C electrode (93.2 mV dec^{-1}), suggesting the Volmer-Heyrovsky mechanism; this value is lower than those of NF (251.5 mV dec^{-1}) and NiFe LDH (124.5 mV dec^{-1}). Electrochemical impedance spectroscopy (EIS) is an effective analysis tool to characterize reaction kinetics of catalysts at the electrode/electrolyte interface [6, 7]. All EIS data are fitted with the typical Randle-model equivalent circuit (R_s represents electrode solution resistance and R_{ct} corresponds to charge transfer resistance between electrode and electrolyte), **Figure IV.9d**. The R_{ct} value of NiFe LDH-Ni_3S_2 is estimated to be 10.1 Ω, which is much smaller than those of NF (32.7 Ω) and NiFe LDH (27.8 Ω) from the Nyquist plot at -0.1 V *versus* RHE, indicating that the heterostructure promotes charge transfer and enhances HER kinetics.

Furthermore, EIS was investigated at different voltages to assess the electron transfer resistance and electrocatalytic kinetics during the HER process. As shown in **Figure IV.9e-f** and **Figure IV.10.**, the Nyquist plots displayed nearly vertical lines at low voltages (0.12 to -0.04 V *vs.* RHE) for NiFe LDH-Ni_3S_2, demonstrating larger R_{ct} values and hindered transfer processes. Interestingly, the semicircle of Nyquist plot appears at a lower applied voltage (-0.09 V) compared to Ni foam and NiFe LDH (-0.19 V), implying faster kinetics of the electrocatalytic HER process. In addition, the Bode plots, corresponding to the change of phase angle (θ) with frequency, could be divided into low and high frequency regions ascribed respectively to the electron conduction in the inner layer of the catalyst and interface reaction charge transfer [8, 9]. Herein, there is a clear difference of decreasing trend in the different frequency regions, i.e., the NiFe LDH-Ni_3S_2 displayed an ultra-low phase angle in the high frequency region regardless the applied potential, whereas NiFe LDH or Ni foam possessed large values, owing to the sluggish Tafel step. For the low frequency region (around 0.01-10 Hz), the sharp phase angle decreasing trend upon increasing the applied potential of NiFe LDH-Ni_3S_2 implies that the interface facilitated the charge transfer and promoted water dissociation due to the 3D porous structure and high surface area.

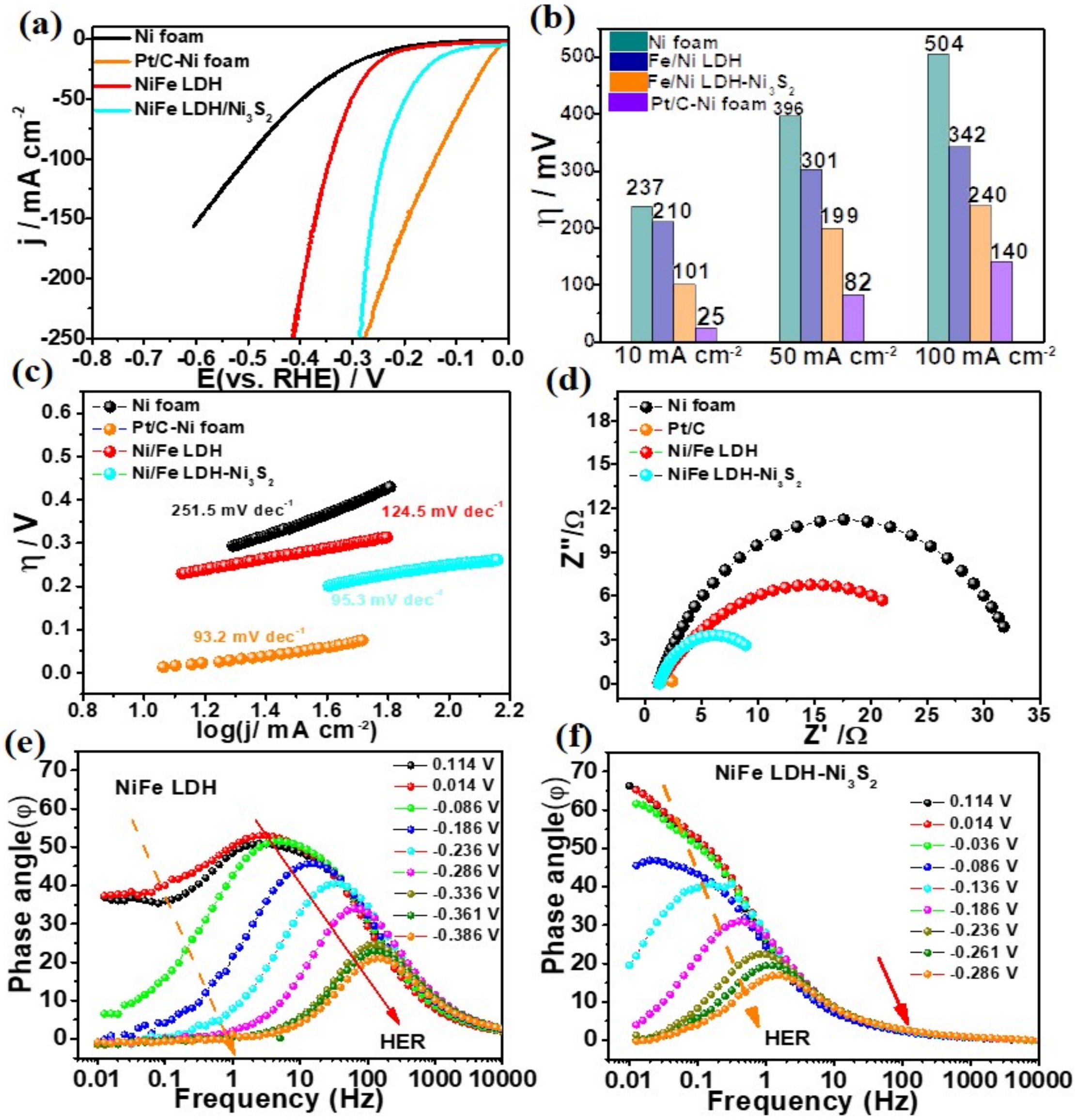

Figure IV.8. The electrochemical HER behavior of Ni foam, Pt/C-NF, NiFe LDH and NiFe LDH-Ni_3S_2 in 1M KOH aqueous solution. (**a**) LSV polarization curves, (**b**) Graphic of overpotential comparison acquired at 10, 50 and 100 mA cm^{-2}; (**c**) The corresponding Tafel plots, (**d**) Nyquist plots at -0.1 V *versus* RHE; (**e-f**) Bode plots of NiFe LDH and NiFe LDH-Ni_3S_2 at different potentials *versus* RHE.

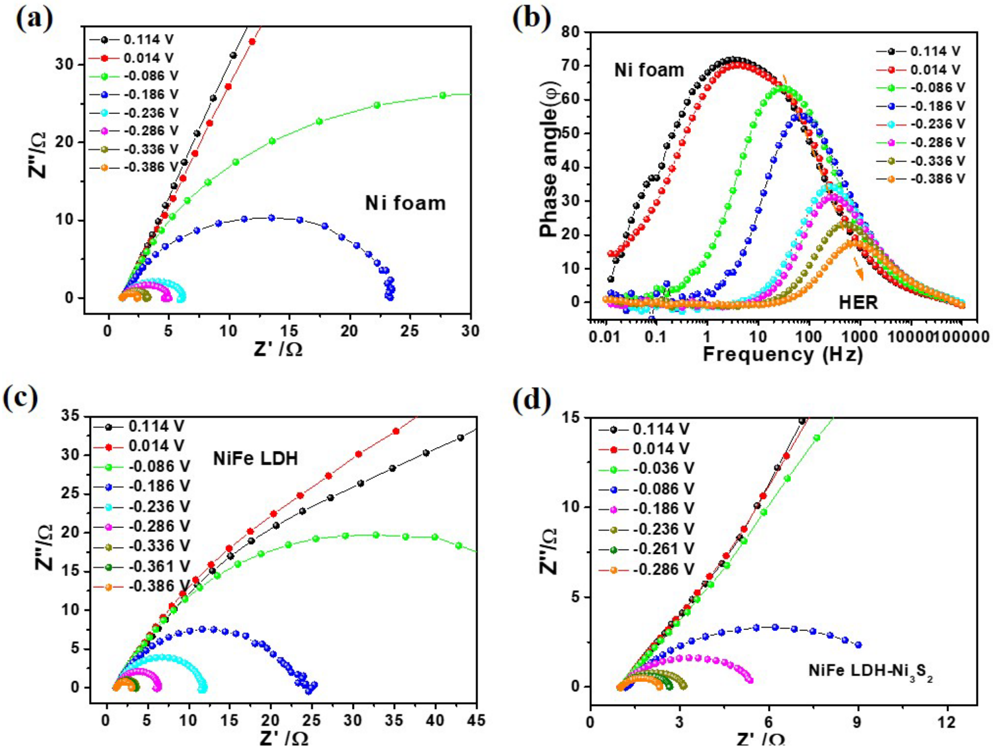

Figure IV.10. Nyquist and Bode plots at various potentials for HER process of (**a, b**) Ni foam, (**c**) NiFe LDH, and (**c**) NiFe LDH-Ni$_3$S$_2$ foam.

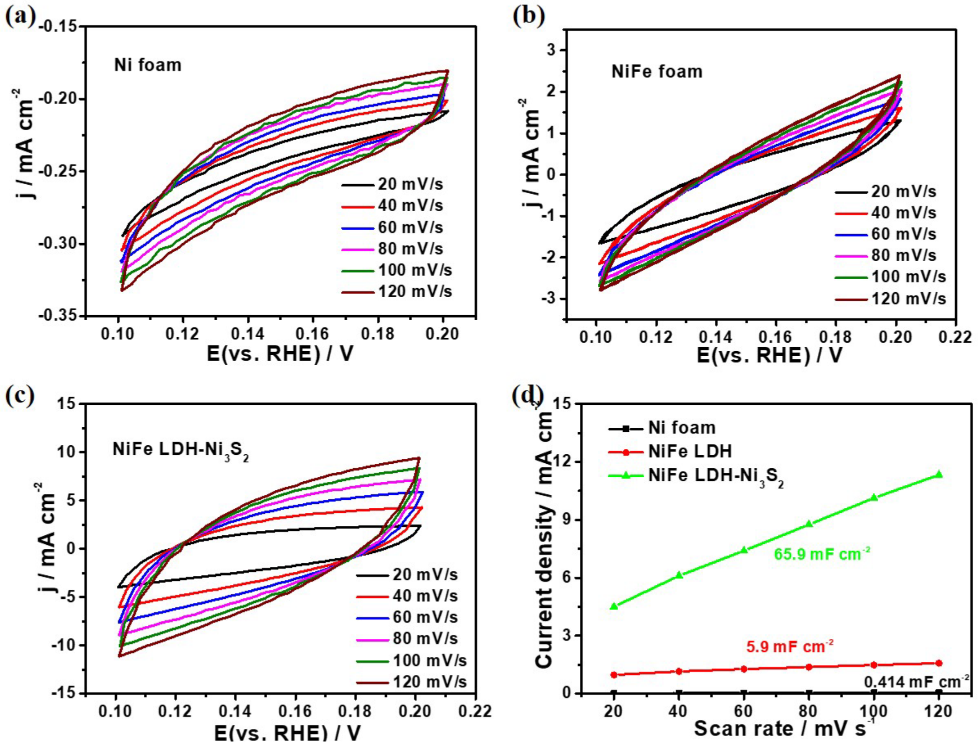

Figure IV.11. CV curves in the potential range from 0.10 to 0.20 V at various scan rates in 1 M KOH solution of (**a**) Ni foam, (**b**) NiFe LDH and (**c**) NiFe LDH-Ni$_3$S$_2$. (**d**) Electrochemical double-layer capacitance as a function of scan rate.

The electrochemical double-layer capacitance (C_{dl}), calculated from the CV curves, was used to determine electrochemical surface area (ECSA) of the catalysts (**Figure IV.11**). NiFe LDH-Ni_3S_2 recorded a higher C_{dl} value (65.9 mF cm^{-2}) than NiFe LDH (5.9 mF cm^{-2}) and NF (0.41 mF cm^{-2}), inferring that the sample possessed more available active sites. Based on above results, the electrocatalytic activities of NiFe LDH-Ni_3S_2 in 1 M KOH+0.5 M NaCl (simulated seawater) and 1 M KOH seawater electrolytes were deeply explored (**Figure IV.12a**). NiFe LDH-Ni_3S_2 required a slightly enlarged overpotential of 257 mV to reach a current density of 100 mA cm^{-2} in 1 M KOH seawater, as compared to 251 mV in 1 M KOH+0.5 M NaCl and 240 mV in KOH freshwater, indicating its potential for large-scale seawater splitting. Notably, the electrochemical activity of NiFe LDH-Ni_3S_2 showed no obvious decline in performance after 1000 CV cycles operation under chronopotentiometric mode for 35 h, or multi-step chronoamperometric operation by inreasing the current density from 25 to 200 mA cm^{-2} by varying the applied voltage (**Figure IV.12b-d**). Taken together, these results clearly evidenced the good durability and long-term catalyst stability. In addition, the SEM imaging (**Figure IV.13**) revealed that the 3D flower shaped nanosheets morphology of NiFe LDH-Ni_3S_2 after durability test is well-maintained with no apparent damage, implying its stable structure even at high current density or under cossorive seawater environment.

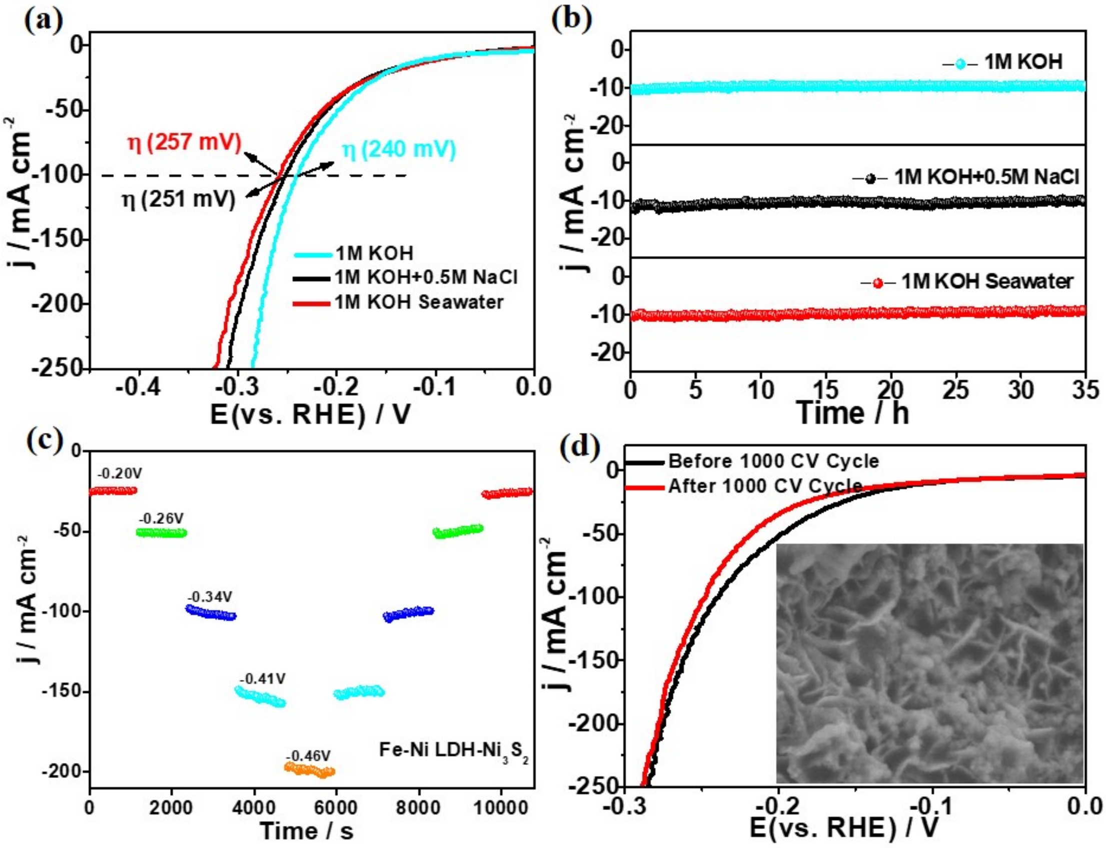

Figure IV.12. The electrochemical HER behavior in seawater. (**a**) Comparison of NiFe LDH-Ni_3S_2 LSV polarization curves in 1 M KOH, 1 M KOH+0.5 M NaCl, and 1 M KOH seawater solution, (**b**) Durability tests at a constant potential for 35 h in different electrolytes; (**c**) Long-term stability measurement via multistep chronoamperometric curves for HER process. (**d**) LSV curves of NiFe LDH-Ni_3S_2 before and after 1000 CV cycles in 1 M KOH solution (insets: SEM image of the post-HER sample).

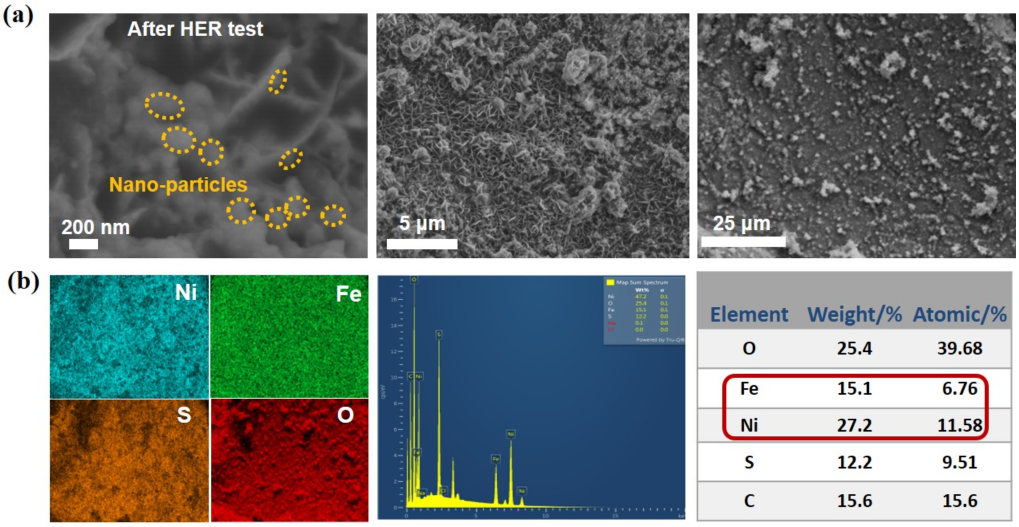

Element	Weight/%	Atomic/%
O	25.4	39.68
Fe	15.1	6.76
Ni	27.2	11.58
S	12.2	9.51
C	15.6	15.6

Figure IV.13. (**a**) SEM images at different magnifications of the NiFe-Ni_3S_2 after 1000 HER CV cycles, (**b**) the corresponding elemental mapping images, (**c**) EDX spectrum and element content analysis.

IV.3.4. Electrochemical OER performance evaluation

We utilized the prepared NiFe LDH-Ni_3S_2 sample with modulated electronic structure and abundant oxygen vacancies as OER electrocatalyst and systematically investigated its electrocatalytic performance in alkaline seawater solution. Firstly, the influence of type of iron salt was studied to obtain NiFe LDH assisted with 0.5 M NaCl. The LSV plots of the catalyst prepared using $Fe(NO_3)_3$ precursor displayed the lowest overpotential (268 mV) at a current density of 100 mA cm^{-2} compared with other iron salts, such as $FeCl_3$ (350 mV) and $FeCl_2$ (400 mV). In addition, the optimal amount of iron precursor and corrosion time are also key parameters in the preparation process of NiFe LDH. The best catalytic performance was achieved using 30 mM $Fe(NO_3)_3$ and 12 h corrosion time in 0.5 M NaCl water **(Figure IV.14)**.

Noteworthily, the peaks in the CV curves observed between 1.1 and 1.5 V *vs.* reversible hydrogen electrode (RHE) could be attributed to the oxidation of M^{2+} to M^{3+} (M=Ni, Fe) in the NiFe LDH. Furthermore, upon increasing reaction time during the exchange reaction (Na_2S) from 1 to 12 h, the OER performance was enhanced and reached the highest activity after 6 h in 0.5 M Na_2S. The OER electrocatalytic activities of all prepared catalysts and their overpotential at 10 and 100 mA cm^{-2} are summarized in **Figure IV.15.** The as-formed NiFe LDH-Ni_3S_2 recorded the lowest overpotential values of 198 mV at 10 mA cm^{-2} and 240 mV at

100 mA cm^{-2}, which are lower than those of NiFe LDH (268 mV) and RuO_2/Ni foam (414 mV) at 100 mA cm^{-2} (**Figure IV.15a,b**). Additionally, Tafel plots were calculated from their corresponding LVS curves (**Figure IV.15c**). The NiFe LDH-Ni_3S_2 electrode displayed the smallest Tafel slope of 43.5 mV dec^{-1} compared to NiFe LDH (45.6 mV dec^{-1}), RuO_2/Ni foam (77.7 mV dec^{-1}), and Ni foam (218.9 mV dec^{-1}), inferring that Ni/Fe LDH-Ni_3S_2 featured fast OER kinetics. Moreover, the OER activity of as-synthesized product is also superior to that of most recently-reported metal-based LDH electrocatalysts, as shown in **Figure IV.16** and **Table 2**. The electrochemical double-layer capacitance results revealed that NiFe LDH-Ni_3S_2 with 12.4 mF cm^{-2} owned the highest value than other prepared catalysts, indicating abundant active sites (**Figure IV.15d**). The above results demonstrated that the as-synthesized NiFe LDH-Ni_3S_2 catalyst exhibited the best OER activity, owing to its appealing 3D flower-like nanosheets and heterostructure, supplying abundant accessible active sites, faster ion diffusion, and excellent electron transfer.

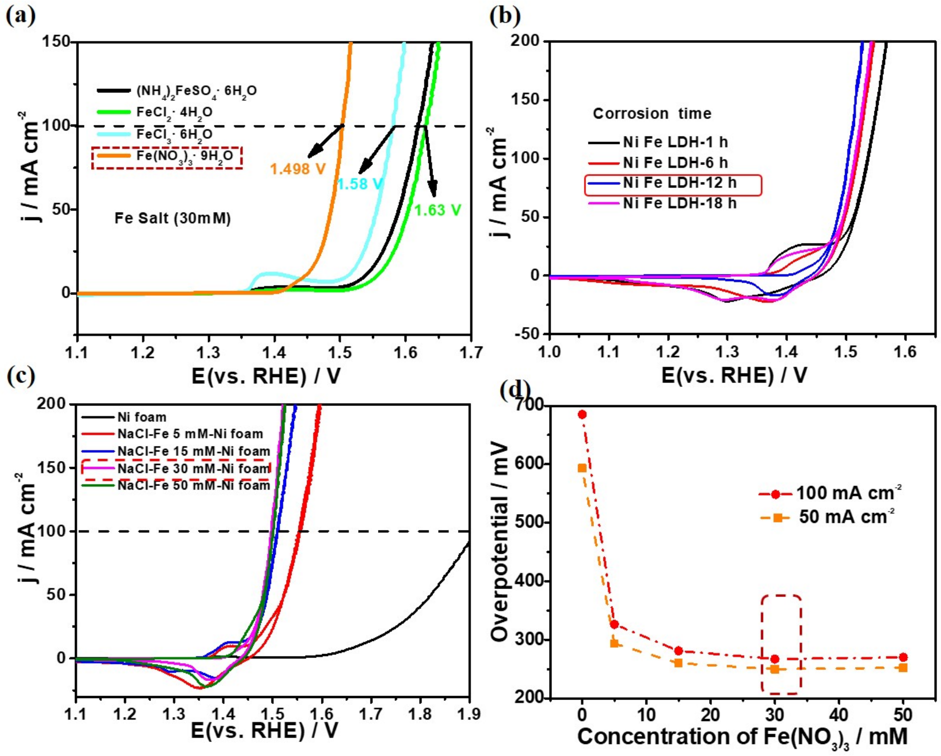

Figure IV.14. LSV and CV polarization curves of NiFe LDH prepared using (**a**) various types of Fe salts, (**b**) various corrosion times, (**c**) different $Fe(NO_3)_3$ concentrations for catalyzing HER. (**d**) Comparison of their overpotential values in 1 M KOH at a scan rate of 5 mV s^{-1}.

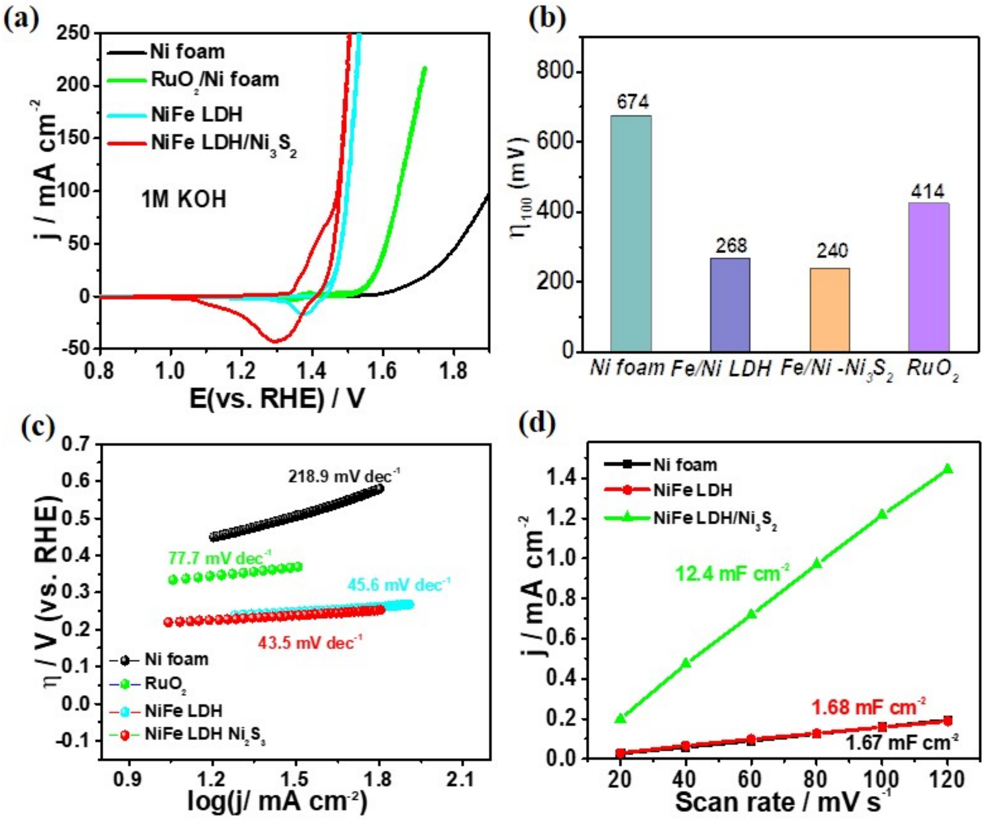

Figure IV.15. A comparison of OER performance of the different catalysts in 1 M KOH solution at a scan rate of 5 mV s^{-1}. (**a**) Polarization curves, (**b**) Graphic comparison of overpotential at 100 mA cm^{-2}, (**c**) Tafel plots, (**d**) Electrochemical double-layer capacitance as a function of scan rate.

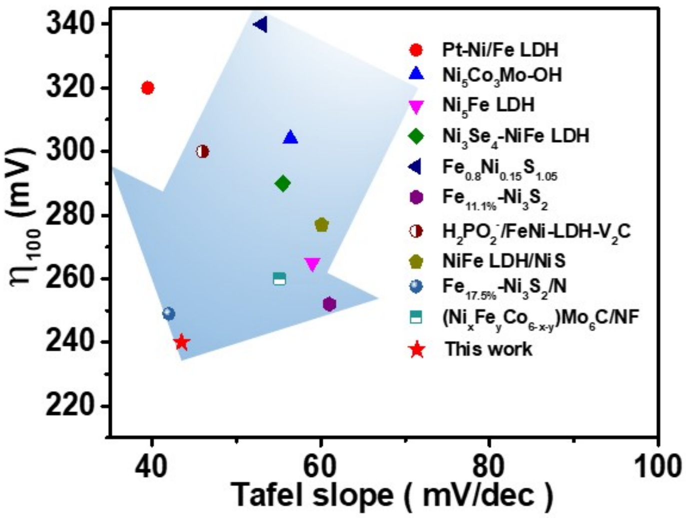

Figure IV.16. Graphic comparison of overpotential at 100 mA cm^{-2}.

Table 2. Comparison of the OER activity of NiFe LDH-Ni_3S_2 with other published metal-based OER electrocatalysts in 1 M KOH.

Catalytic	Preparation method	Current density (mA cm-2)	Overpotential (mV)	Tafel slope (mV dec^{-1})	Substrate	Reference
NiFe LDH-Ni_3S_2	**IC**	**10** **100**	**198** **240**	**43.5**	**Ni foam**	**This work**
NiFe LDH-Pt	IC	10 100	261 320	39.7	Ni foam	[10]
Ni_5Co_3Mo−OH	IC	100	304	56.4	Ni foam	[11]
Ni_5Fe LDH	HT	10 100	210 265	59	Ni foam	[12]
Ni_3Se_4@NiFe LDH	HT	10 100	223 290	55.5	CP	[13]
$Fe_{0.8}Ni_{0.15}S_{1.05}$	HT	100	340	53	RDE	[14]
pa-NiFe LDH NS	HT	100	326	157	Ni foam	[15]
Fe11.1%–Ni_3S_2	HT	100	252	61	Ni foam	[16]
H_2PO_2 /FeNi-LDH-V_2C	HT	100	300	46	RDG	[17]
(NixFeyCo$_6$-x-y) Mo_6C	HT	10 100	212 260	55.1	Ni foam	[18]
MoNiFe-27% (oxy)	HT	10 100	242 290	23	Ni foam	[19]
NiFe-LDH@$FeNi_2S_4$	HT	100	240	29.4	Ni foam	[20]
NIFE LDH/NIS	HT	100	277	60.1	Ni foam	[21]
Fe17.5%-Ni_3S_2/NF	HT	100	249	42	Ni foam	[22]

RDE: rotating disk electrode
CP: carbon paper
IC： ion corrosion method
HT: hydrothermal method

Based on above results, the OER test was carried out in seawater condition (**Figure IV.17a**). NiFe LDH-Ni_3S_2 displayed enlarged overpotential of 280 mV to acquire a current density of 100 mA cm^{-2} in 1 M KOH seawater compared to 269 mV in 1 M KOH+0.5 M NaCl, and 240 mV in KOH freshwater. However, this overpotential is still lower to that of many published electrocatalysts, such as $NiSe_2/Ni_3Se_4$/NF-1 (309 mV) [23] and S-(Ni, Fe)OOH (300 mV)[24] in alkaline seawater electrolyte. Notably, the overpotential is also lower than 490 mV (chloride oxidation potential), demonstrating the proper potential for large-scale seawater electrolysis [25]. In addition, the long-term and multistep chronoamperometry measurements were conducted to evaluate the OER stability performance (**Figure IV.17b-d**). The results clearly evidenced the good stability of NiFe LDH-Ni_3S_2 electrode over 35 h at 10 mA cm^{-2} in 1 M KOH, 1 M KOH+0.5 M NaCl or 1 M KOH seawater. The multistep chronoamperometry results confirmed the good operation of the catalyst at high current density, and LSV analysis after 1000 CV cycles showed no obvious decrease.

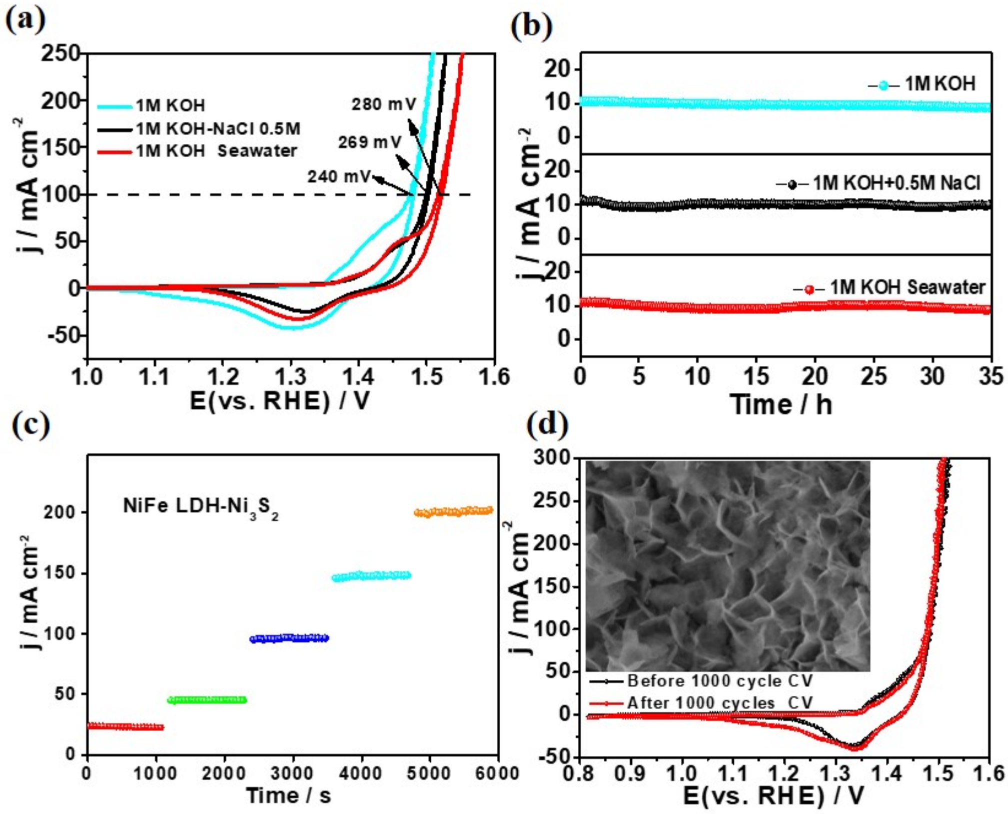

Figure IV.17. (**a**) LSV polarization curves of NiFe LDH-Ni_3S_2 sample in 1 M KOH, 1 M KOH+0.5 M NaCl, and 1 M KOH seawater electrolyte. (**b**) Durability tests at a constant potential for 35 h in different electrolytes; (**c**) Multistep chronoamperometric curves at various applied overpotentials. (**d**) LSV curves of NiFe LDH-Ni_3S_2 before and after 1000 CV cycles in 1 M KOH solution (insets: SEM image of the post-OER sample).

SEM imaging was applied to scrutinize the morphology variation after durability test; the catalyst still maintained its 3D nanostructure, as shown in **Figure IV.18**. XRD analysis illustrated no detectable diffraction peak change for NiFe LDH-Ni_3S_2 (**Figure IV.19**). The XPS study of NiFe LDH-Ni_3S_2 after the stability test (**Figure IV.20**) revealed a negative shift of Ni peak for $2p_{3/2}$ (0.47 eV) and for $2p_{1/2}$ (0.3 eV) due to a redox reaction. In addition, the position of Fe^{2+}/Fe^{3+} did not experience obvious variation, but the Fe^{2+}/Fe^{3+} ratio decreased from 1.17 to 0.61, suggesting the generation of more Fe^{3+} species (FeOOH) during the OER reaction [9, 26]. Above phenomenon demonstrated the electron rearrangement of the catalyst's surface due to anodic oxidation, which can accelerate the OER kinetics by modulating the adsorption energy for intermediate [27]. For the S 2p XPS spectrum after OER stability test, the two deconvoluted peaks ascribed to S $2p_{3/2}$ and S $2p_{1/2}$ were not affected, but the S element content declined to some extent. Interestingly, in the O 1s core level spectrum, the intensity of O2 peak (oxygen vacancies) decreased while O3 peak (hydroxyl groups) increased after OER durability test, which may derive from the filling of the oxygen vacancies with $OH^{-}_{(aq)}$ and the subsequent deprotonation of OH* in the electrochemical process, indicating that LOM mechanism may occur during the OER process [28].

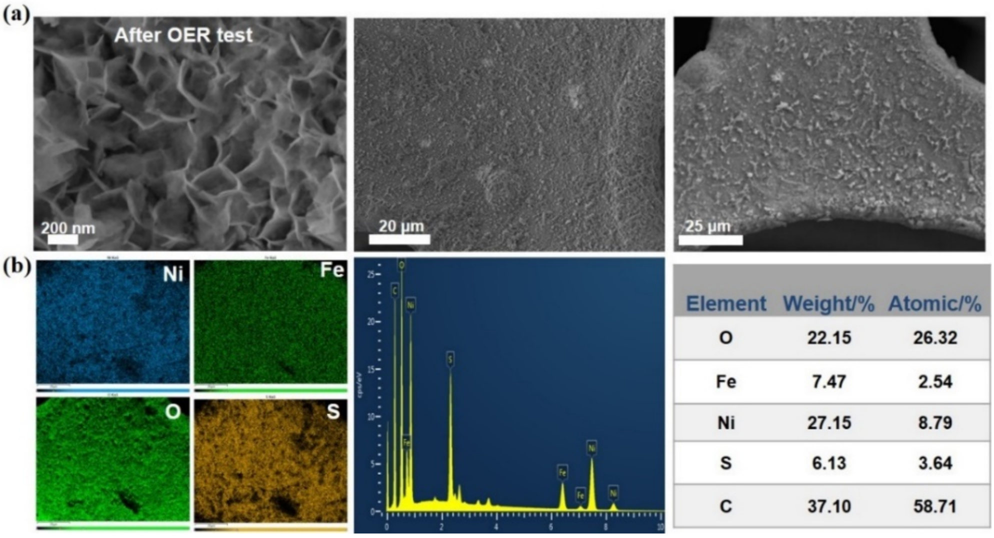

Element	Weight/%	Atomic/%
O	22.15	26.32
Fe	7.47	2.54
Ni	27.15	8.79
S	6.13	3.64
C	37.10	58.71

Figure IV.18. (**a**) SEM images at different magnifications of the NiFe-Ni_3S_2 after 1000 OER CV cycles, (**b**) the corresponding elemental mapping images, (**c**) EDX spectrum and element content analysis.

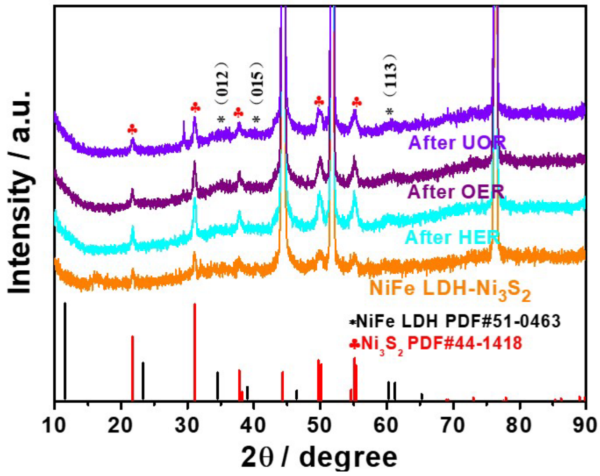

Figure IV.19. XRD spectra of NiFe LDH-Ni_3S_2 after HER, OER and UOR 1000 CV cycles.

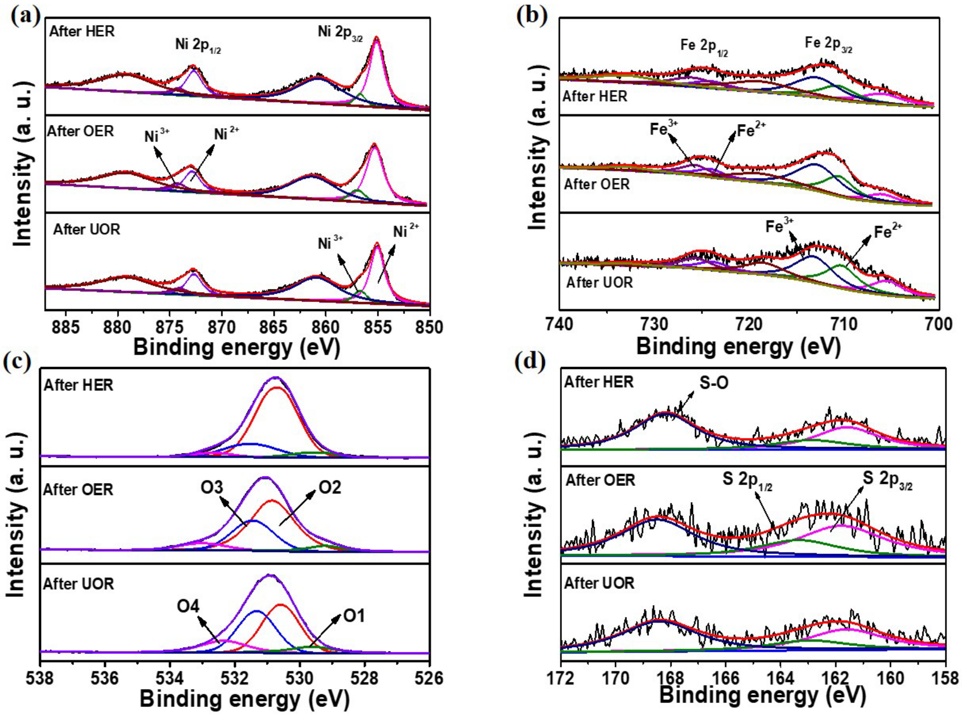

Figure IV.20. XPS high-resolution spectra of (**a**) Ni 2p, (**b**) Fe 2p, (**c**) O 1s and (**d**) S 2p of NiFe LDH-Ni_3S_2 after HER, OER and UOR 1000 CV cycles.

IV.3.4 OER reaction kinetics

In order to investigate the charge transfer kinetics, EIS measurements were carried out [29].

The NiFe LDH- Ni_3S_2 displayed the smallest charge transfer resistance (R_{ct}) of 0.28 Ω at 1.5 V *versus* RHE compared to NiFe LDH (0.32 Ω), RuO_2 (9.71 Ω) and Ni foam (12.11 Ω), suggesting its enhanced charge transfer rate (**Figure IV.21a**). In addition, the operando EIS of NiFe LDH-Ni_3S_2 in the OER potential window (1.0 ~ 1.514 V) is depicted in **Figure IV.21b-e**. In the 1.0 ~ 1.314 V region, the Nyquist spectra recorded vertical line, revealing larger R_{ct} values synonymous of low OER activity. Upon increasing the applied voltage to 1.364 V, an effective semicircle was obtained which possessed effective value of R_{ct} and gradually diminished with increasing the voltage, indicating the initial OER potential after 1.364 V [9]. Moreover, the Bode phase plots supplied more evidence and explanation in different frequency regions [30-32]. NiFe LDH-Ni_3S_2 consistently exhibited lower phase angle in the high frequency region (100–1000 Hz), suggesting the good electron conduction in catalyst inner-layer, whereas the phase angle of NiFe LDH and Ni foam decreased slowly upon gradual increase of the applied voltage, as indicated by the solid arrow in **Figure IV.21d-e.** In the low frequency (0.01-10 Hz), compared with other catalysts, NiFe LDH-Ni_3S_2 possessed much faster phase angle downtrend, indicating facile interface reaction charge transfer and faster OER kinetics.

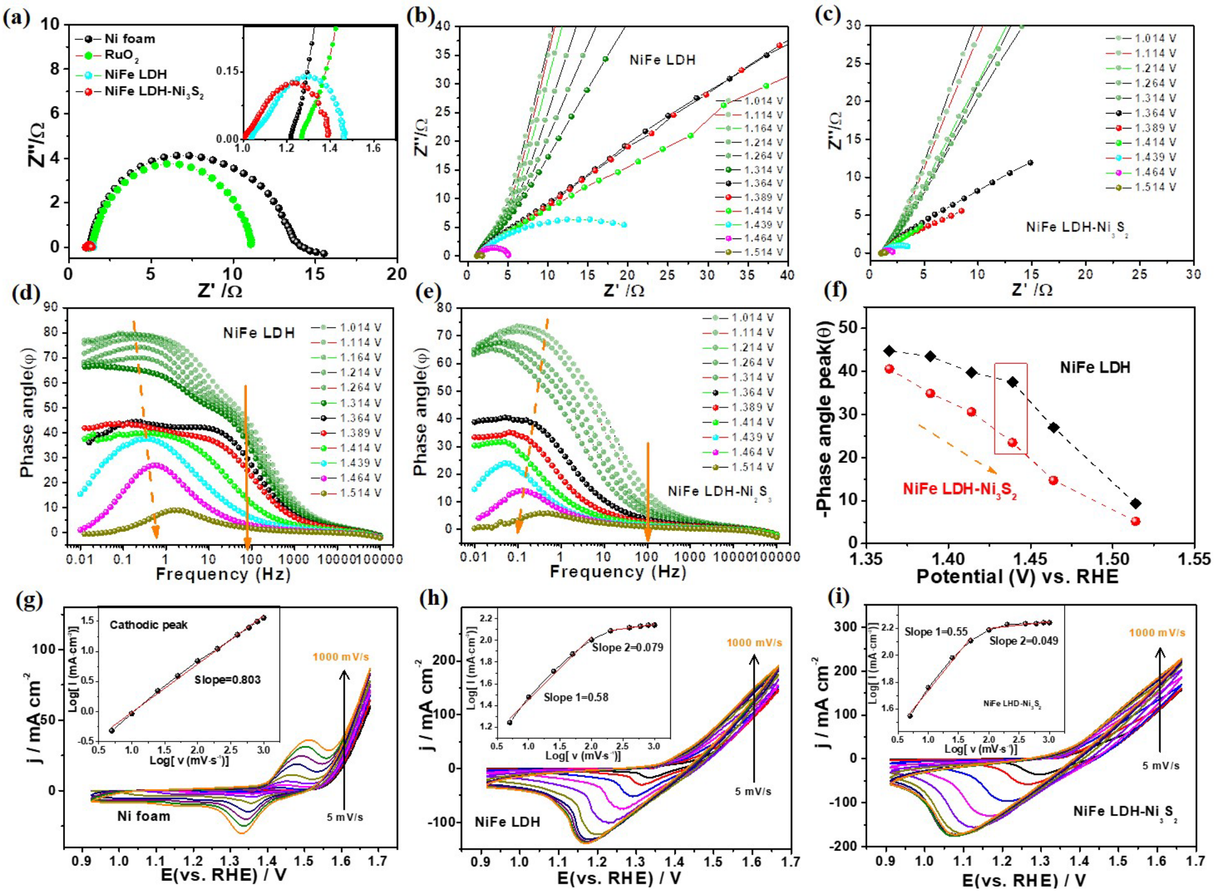

Figure IV.21. (**a**) Nyquist plots of Ni foam, RuO_2, NiFe LDH and NiFe LDH-Ni_3S_2 at 1.5 V *versus* RHE. (**b, c**) Nyquist and (**d, e**) Bode phase plots of NiFe LDH and NiFe LDH- Ni_3S_2 at different potentials *versus* RHE, respectively. (**f**) Phase peak angles of different prepared samples at 1.389–1.514 V *versus* RHE. CV curves recorded at scan rates of 5-1000 mV s^{-1} without IR compensation, and the insert plot of log (I_p, cathodic peak current) *versus* log (v, scan rate) of (**g**) Ni foam, (**h**) NiFe LDH and (**i**) NiFe LDH-Ni_3S_2.

To distinguish the interfering factors of OER process, we recorded CV curves between 0.9~1.7 V at various scan rates (5 ~1000 mV s^{-1}). For Ni foam, redox features corresponding to anodic and cathodic peaks attributed to Ni ($^{2+/3+}$) were observed. This contrasts with the CV plot of NiFe LDH for which the anodic redox peak (1.4 ~1.5V) was not obvious anymore and higher current density cathodic peaks were recorded (**Figure IV.21g-i**). A similar behavior was found for NiFe LDH-Ni_3S_2 along with enhanced current density as a function of the scan rate, further illustrating that redox reactivity could be effectively modulated and triggered. In order to analyze the reaction-controlled mechanism, we employed the typical equation (i_p=a * ν^b), where i_p and ν are respectively the cathodic peak current density and scan rate, and the value of b could be calculated from the slope of log i_p *vs.* log ν curve (Insets, **Figure IV.21g-i**) [8]. Ni foam with a higher b value (0.803) exhibited obvious capacitive behavior and weak diffusion-controlled process, whereas NiFe LDH (0.58) and NiFe LDH-Ni_3S_2 (0.55) close to 0.5, the diffusion dominates the electrochemical process; this could be ascribed to the concentration polarization effect of the electrolyte, which is beneficial to facilitate mass diffusion and improves the Faradaic efficiency [33]. Besides, the wettability of the electrode material in 1 M KOH electrolyte is another key player to analyze mass transfer ability (**Figure IV.22**). Obviously, NiFe LDH-Ni_3S_2 heterojunction nanosheet arrays featured the fastest complete infiltration time of < 0.5 s relative to Ni foam, inferring that the electrolyte could effectively be supplemented to resist rapid depletion even under high current catalysis. The good hydrophilicity performance may be brought by the rich porosity of the 3D nanoflower array. Therefore, the nanoflower configuration and coupling heterojunction interfaces act collaboratively to optimize charge and mass transfer, which contribute to the efficient catalytic performance at high current density.

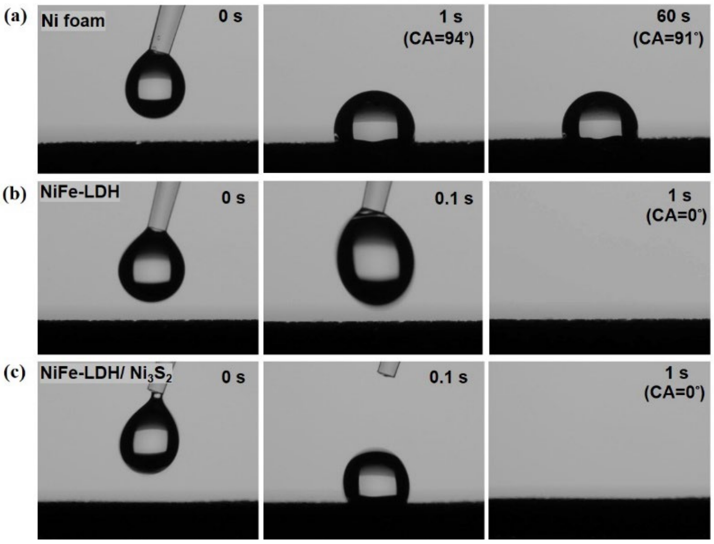

Figure IV.22. Contact angle (CA) measurements of (**a**) Ni foam, (**b**) NiFe-LDH and (**c**) NiFe LDH-Ni_3S_2 using 10 μL water droplet.

IV.3.5. Electrochemical UOR performance

To effectively inhibit chloride ion oxidation reaction in seawater under high power conditions, electrochemical UOR reaction was further investigated. Herein, we chose the typical 1 M KOH+0.33 M urea as electrolyte. From the LSV plots in **Figure IV.23a**, the NiFe LDH-Ni_3S_2 displayed driving potential values of 1.34 V (10 mA cm^{-2}) and 1.37 V (100 mA cm^{-2}), which are lower than other catalysts such as Ni foam (1.39 V, 10 mA cm^{-2}) and RuO_2 (1.38 V, 10 mA cm^{-2}). In addition, NiFe LDH-Ni_3S_2 also provided the lowest Tafel slope of 24.0 mV dec^{-1} relative to Ni foam (134.7 mV dec^{-1}), RuO_2/Ni foam (101.3 mV dec^{-1}) and Ni/Fe LDH (60.6 mV dec^{-1}), indicating fastest UOR catalytic kinetics (**Figure IV.23b**). Meanwhile, the maximum C_{dl} value of NiFe LDH-Ni_3S_2 (4.75 mF cm^{-2}) is a direct sign of the presence of plenty active sites, as compared with other catalysts (**Figure IV.23c**) for urea oxidation, in line with the above seawater results. The larger C_{dl} value of NiFe LDH-Ni_3S_2 could be attributed to the 3D hierarchical architecture with wrinkled surface that can provide a sizable surface area and numerous exposed active sites, thus leading to larger ECSA. The catalyst conductivity is another key factor for UOR reaction, and the charge transfer resistance (R_{ct}) was calculated by the typical equivalent circuit supplied in **Figure IV.23d**. The NiFe LDH-Ni_3S_2 displayed a small R_{ct} value of 0.65 Ω compared to Ni foam (3.7 Ω), RuO_2/Ni foam (4.86 Ω) and NiFe LDH (1.85 Ω), which could be at the origin of the promoted charge and mass transfer rates. Apart from the catalytic activity, durability is also crucial for evaluating the catalytic performance. Simultaneously, the in-situ EIS measurements were performed to explore the relationship between potential and interfacial reactions (**Figure IV.23e-f**). Firstly, the Bode phase plots provided additional evidence and clarification in various frequency ranges. NiFe LDH-Ni_3S_2 consistently displayed a lower phase angle in the high-frequency range during the progress of UOR in the 1.0-1.4 V detection range. This suggests good electron conduction within the catalyst's inner layer. Noteworthy, the UOR process exhibited a faster R_{ct} downtrend in the same potential compared to OER processes, indicating charge transfer and kinetics are more efficient. In addition, the catalytic reaction stability was further evaluated during the UOR process. As displayed in **Figure IV.23h**, the multistep chronoamperometric curve of NiFe LDH-Ni_3S_2 was acquired in 1 M KOH+0.33 M urea, confirming that the catalyst could operate continuously and stably work at different voltages. In addition, after 1000 cycles CV cycles, the post-sample performance experienced a slight decrease, but still maintained good stability and high catalytic activity (**Figure IV.23i**). From the SEM imaging, it was obvious that the sample maintained its nanoflower morphology after the long time UOR test.

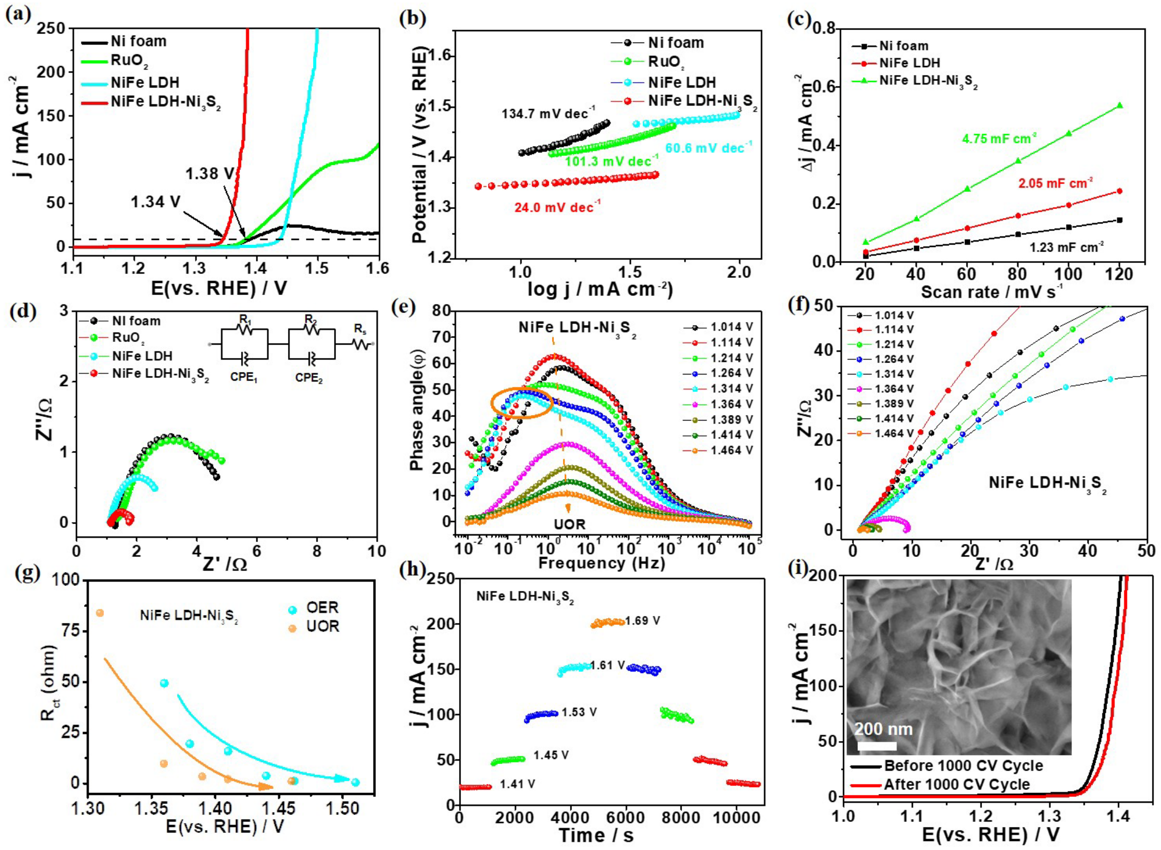

Figure IV23. UOR performance in 1M KOH+0.33M urea. (**a**) LSV curves of NiFe LDH-Ni$_3$S$_2$, NiFe LDH, RuO$_2$ and Ni foam, (**b**) the corresponding Tafel slopes, (**c**) the C$_{dl}$ values at different scan rates (20 - 120 mV s^{-1}). (**d**) Nyquist plots measured at 1.5 V *versus* RHE. (**e**) Nyquist and (**f**) Bode plots measured at various potential (1.01–1.46 V *versus* RHE). (**g**) The corresponding R$_{ct}$ values of prepared samples with and without urea molecular at various potential. (**h**) Multistep chronoamperometric curves at various applied overpotentials. (**i**) LSV curves of NiFe LDH-Ni$_3$S$_2$ before and after 1000 CV cycles (insets: SEM image of the post-UOR sample).

IV.3.6 Overall seawater-urea splitting performance

Benefitting from the splendid activity and durability of the NiFe LDH-Ni_3S_2 for both HER and UOR, the overall urea electrolysis was assessed using a two-electrode system in 1 M KOH+0.33 M urea seawater. The NiFe LDH-Ni_3S_2 // NiFe LDH-Ni_3S_2 system exhibited prominent overall urea electrolysis performance with a low cell voltage of 1.58 V to attain a current density of 50 mA cm^{-2} (**Figure IV.24a**). Besides, there is a larger potential difference of 180 mV at 100 mA cm^{-2} in 1 M KOH seawater with and without 0.33 M urea, suggesting that the urea molecule plays a positive role and enhances the efficiency of H_2 generation. Interestingly, NiFe LDH-Ni_3S_2 outperformed most of the previously reported bifunctional electrocatalysts for the overall urea splitting (**Figure IV.24b** and **Table 3**). Notably, the NiFe LDH-Ni_3S_2 with unique heterostructure inhibited considerably the Cl^- corrosion function in seawater, which maintained the original catalytic activity of product in seawater [34, 35].

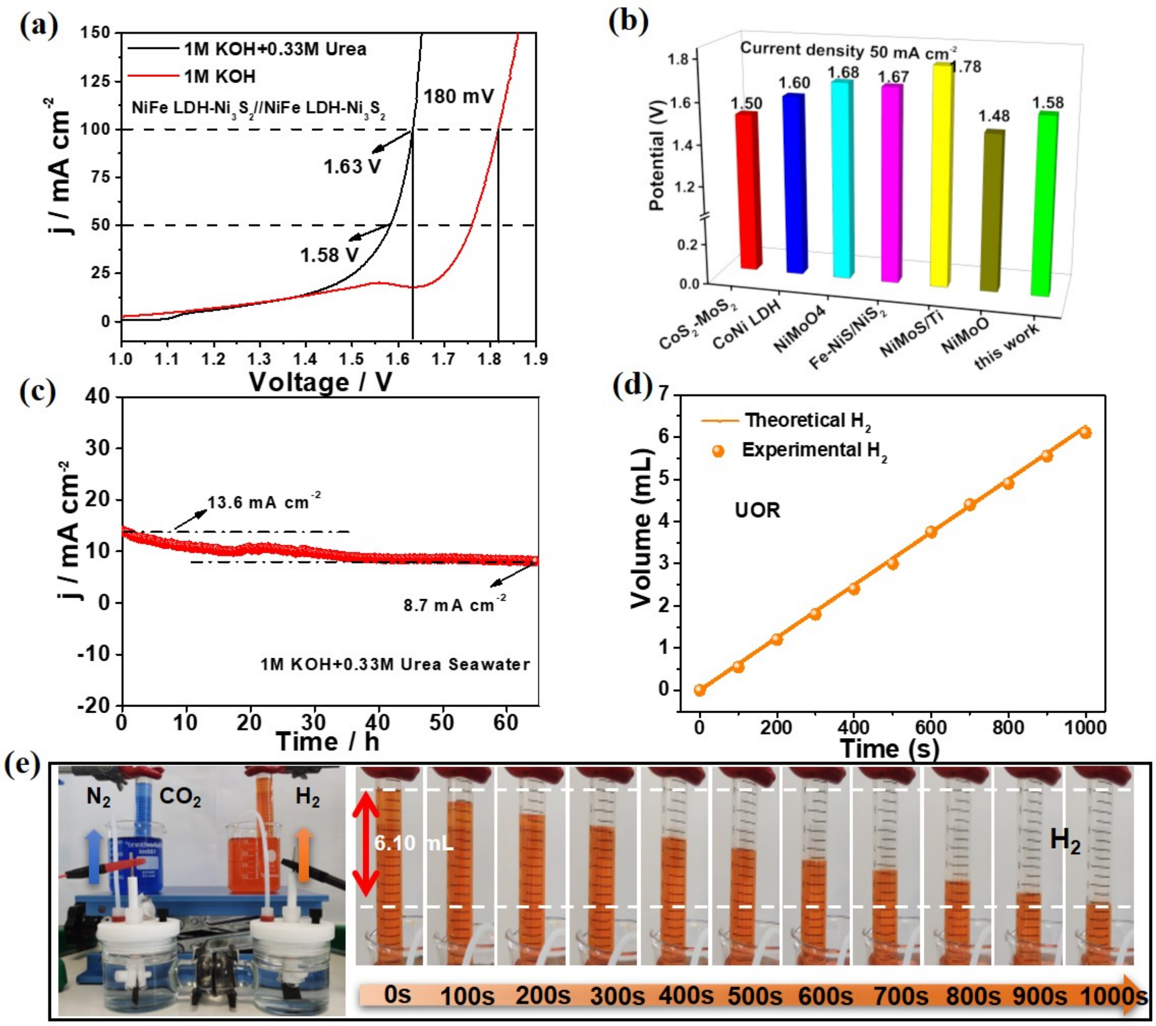

Figure IV.24. Overall water and urea splitting performance of NiFe LDH-Ni_3S_2. (**a**) the comparison of the polarization curves with or without 0.33 M urea for NiFe LDH-Ni_3S_2 // NiFe LDH-Ni_3S_2. (**b**) Comparison potential at 10 mA cm^{-2} between this work and other published works. (**c**) Long-term stability measurement for 65 h. (**d**) The volume of the gas changes with time. (**e**) Photo of the cell for the determination of the Faraday efficiency of device and gas collected at different times.

Table 3. Comparison of the two-electrode system potential of the developed catalyst and reported UOR catalysts.

Catalytic	Preparation method	Current density (mA cm^{-2})	potential (V)	Substrate	Reference
NiFe LDH-Ni$_2$S$_3$ // NiFe LDH-Ni$_2$S$_3$	**IC**	**50 100**	**1.58 1.63**	**Ni foam**	**This work**
FQD/CoNi-LDH@ FQD/CoNi-LDH	HT	50 100	1.6 1.70	Ni foam	[36]
NiMoO$_4$-300/NF@ NiMoO$_4$-300/NF	HT	50	1.68	Ni foam	[37]
Fe-doped NiS–NiS$_2$@ Fe-doped NiS–NiS$_2$	HT	50	1.67	Ni foam	[38]
NiCoP NS/CC@ NiCoP NS/CC	HT	50	1.50	carbon cloth	[39]
CoS$_2$-MoS$_2$@ CoS$_2$-MoS$_2$	HT	50	1.50	Ni foam	[40]
HC-NiMoS/Ti@ HC-NiMoS/Ti	HT	50	1.78	Ti mesh	[41]
NF/NiMoO-Ar@ NF/NiMoO-H$_2$	HT	50 100	1.48 1.55	Ni foam	[42]

The long-term durability test of two-electrode system (NiFe LDH-Ni$_3$S$_2$ // NiFe LDH-Ni$_3$S$_2$) for overall urea-seawater splitting was simultaneously employed by continuous electrolysis at 1.3 V constant potential to achieve a current density of 10 mA cm^{-2}. **Figure IV.24c** showed a gradual decrease trend from 13.6 to about 9 mA cm^{-2} at the beginning and maintained a steady current density over 65 h. As illustrated in **Figure IV.24d**, the faradaic efficiency of NiFe LDH-Ni$_3$S$_2$ electrocatalyst was determined in 1 M KOH+0.33 M urea by comparing the volume of gas collected experimentally and the theoretically calculated gas. H-type electrolyzer was used to collect the produced gas (H_2 at the cathode; CO_2 and N_2 at the anode). The volume of H_2 gas could be observed intuitively through the enlarged cylinder shown in **Figure IV.24e.** As expected, the collected V_{H2} value is in full agreement with the theoretically-calculated values, indicating that the NiFe LDH-Ni$_3$S$_2$ generated H_2 with almost 100% Faradaic efficiency in the

UOR process. In addition, The Faradaic efficiency of NiFe LDH-Ni_3S_2 in 1 M KOH + seawater was also employed and the obtained gas (H_2, O_2) was also almost close to the theoretical value, indicating excellent activity and stability.

Furthermore, the overall seawater-urea splitting process of NiFe LDH-Ni_3S_2, assisted by solar panels, represents an interesting approach for future potential application of the developed catalyst (**Figure IV.25**). In this strategy, the abundant natural seawater + 1M KOH electrolyte was used to keep the alkaline condition, while the Ca^{2+} and Mg^{2+} ions in the seawater will react with some ^{-}OH groups to form turbid solution. The turbid solution was allowed to stand overnight or subjected to centrifugation to separate the upper relatively clear solution and remove the lower sediment. After, the seawater resource and solar energy as a source of electricity generation could be directly utilized to produce H_2 *via* overall seawater splitting method assisted by molecular urea, enabling efficient conversion of solar energy, electricity and hydrogen. Benefiting from its excellent catalytic performance, low-cost and easy scale-up through the corrosion preparation process, the NiFe LDH-Ni_3S_2 catalyst holds great promise from an application perspective for energy-saving H_2 generation. In future work, we need to prepare better catalyst materials and electrolyzers that can be applied to any condition of natural seawater (acidic or alkaline). This is an important challenge for future electrolysis of seawater.

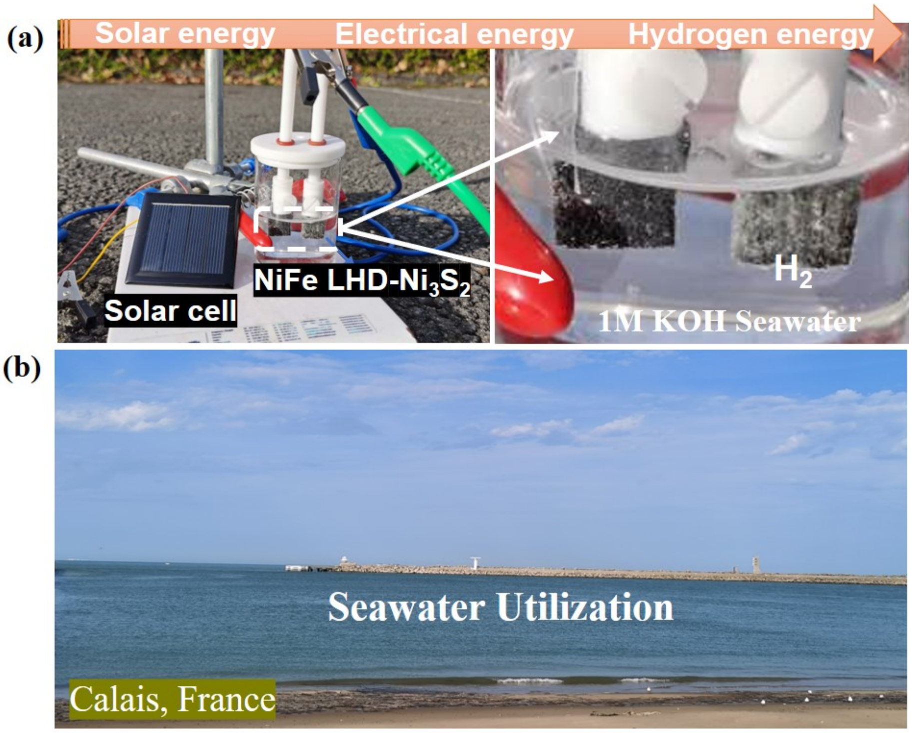

Figure IV.25. (**a**) Digital photograph of the solar-to-hydrogen energy conversion system through a commercial solar cell (2 V) and an NiFe LDH-Ni_3S_2 // NiFe LDH-Ni_3S_2 device in 1M KOH seawater. (**b**) Natural seawater collected from in Lighthouse Navigation, Calais, France.

IV.4. Conclusion

In summary, a NiFe LDH-Ni_3S_2 bifunctional electrode with a desert rose flower-shaped heterostructure was successfully synthesized *via* seawater corrosion and ion exchange, and successfully applied for efficient overall seawater splitting. The excellent HER/OER performance benefited from the NiFe LDH and Ni_3S_2 heterostructure, which facilitated mass diffusion and enhanced reaction kinetics. The NiFe LDH-Ni_3S_2 electrode displayed overpotential values as low as 257 and 280 mV to deliver 100 mA cm^{-2} for HER and OER in 1M KOH seawater, respectively. In addition, benefiting from the modulated electronic configuration and optimized free-energy of oxygen-containing intermediates adsorption and desorption, NiFe LDH-Ni_3S_2 electrode featured outstanding UOR and overall seawater-urea splitting activities in 1 M KOH+0.33 M urea, which are superior to commercial catalysts, e.g., Pt/C and RuO_2. Noteworthy, an electrolyzer comprising NiFe LDH-Ni_3S_2 as both anode and cathode exhibited a small cell voltage of 1.45 V to reach 10 mA cm^{-2} and almost 100% Faradaic efficiency for overall seawater-urea splitting process, demonstrating that urea plays an important role in reducing overpotential and energy consumption. The facile and scalable seawater corrosion synthesis strategy to prepare nanoflower heterostructure of metal hydroxides coupled with Ni_3S_2 can be utilized to explore other bifunctional electrocatalysts in the field of energy, achieving efficient conversion of solar energy, electricity and hydrogen. This study represents a significant step and new perspective to develop robust and active bifunctional catalysts for other electrocatalytic processes such as CO_2 and N_2 reduction by renewable energy sources.

References

[1] G. Li, F. Li, Y. Zhao, W. Li, Z. Zhao, Y. Li, H. Yang, K. Fan, P. Zhang, L. Sun, Selective Electrochemical Alkaline Seawater Oxidation Catalyzed by Cobalt Carbonate Hydroxide Nanorod Arrays with Sequential Proton-Electron Transfer Properties, ACS Sustainable Chem. Eng. 9(2) (2021) 905-913. https://doi.org/10.1021/acssuschemeng.0c07953.

[2] H.J. Song, H. Yoon, B. Ju, D.-Y. Lee, D.-W. Kim, Electrocatalytic Selective Oxygen Evolution of Carbon-Coated $Na_2Co_{1-x}Fe_xP_2O_7$ Nanoparticles for Alkaline Seawater Electrolysis, ACS Catal. 10(1) (2019) 702-709. https://doi.org/10.1021/acscatal.9b04231.

[3] X. Liu, M. Gong, D. Xiao, S. Deng, J. Liang, T. Zhao, Y. Lu, T. Shen, J. Zhang, D. Wang, Turning Waste into Treasure: Regulating the Oxygen Corrosion on Fe Foam for Efficient Electrocatalysis, Small 16(24) (2020) 2000663. https://doi.org/10.1002/smll.202000663.

[4] Z.-H. Zhang, Y. Zhang, A. Barras, A. Addad, P. Roussel, L.-C. Tang, M.A. Amin, S. Szunerits, R. Boukherroub, Preparation of Flower-Shaped Co-Fe Layer Double Hydroxide Nanosheets Loaded with Pt Nanoparticles by Corrosion Engineering for Efficient Electrocatalytic Water Splitting, ACS Appl. Energy Mater. 5(12) (2022) 15269-15281. https://doi.org/10.1021/acsaem.2c02905.

[5] B. Zhang, J. Wang, B. Wu, X.W. Guo, Y.J. Wang, D. Chen, Y.C. Zhang, K. Du, E.E. Oguzie, X.L. Ma, Unmasking Chloride Attack on the Passive Film of Metals, Nat. Commun. 9(1) (2018) 2559. https://doi.org/10.1038/s41467-018-04942-x.

[6] D. Merki, H. Vrubel, L. Rovelli, S. Fierro, X. Hu, Fe, Co, and Ni Ions Promote The Catalytic Activity of Amorphous Molybdenum Sulfide Films For Hydrogen Evolution, Chem. Sci. 3(8) (2012) 2515. https://doi.org/10.1039/c2sc20539d.

[7] V.M. Nikolic, S.L. Maslovara, G.S. Tasic, T.P. Brdaric, P.Z. Lausevic, B.B. Radak, M.P. Marceta Kaninski, Kinetics of Hydrogen Evolution Reaction In Alkaline Electrolysis On a Ni Cathode In the Presence Of Ni–Co–Mo Based Ionic Activators, Appl. Catal., B 179 (2015) 88-94. https://doi.org/10.1016/j.apcatb.2015.05.012.

[8] R. Chen, S.F. Hung, D. Zhou, J. Gao, C. Yang, H. Tao, H.B. Yang, L. Zhang, L. Zhang, Q. Xiong, H.M. Chen, B. Liu, Layered Structure Causes Bulk NiFe Layered Double Hydroxide

Unstable in Alkaline Oxygen Evolution Reaction, Adv. Mater. 31(41) (2019) e1903909. https://doi.org/10.1002/adma.201903909.

[9] X. Chen, Q. Wang, Y. Cheng, H. Xing, J. Li, X. Zhu, L. Ma, Y. Li, D. Liu, S-Doping Triggers Redox Reactivities of Both Iron and Lattice Oxygen in FeOOH for Low-Cost and High-Performance Water Oxidation, Adv. Funct. Mater. 32(26) (2022) 2112674. https://doi.org/10.1002/adfm.202112674.

[10] Y. Zhao, Y. Gao, Z. Chen, Z. Li, T. Ma, Z. Wu, L. Wang, Trifle Pt coupled with NiFe hydroxide synthesized via corrosion engineering to boost the cleavage of water molecule for alkaline water-splitting, Appl. Catal., B 297 (2021) 120395. https://doi.org/10.1016/j.apcatb.2021.120395.

[11] S. Hao, L. Chen, C. Yu, B. Yang, Z. Li, Y. Hou, L. Lei, X. Zhang, NiCoMo Hydroxide Nanosheet Arrays Synthesized via Chloride Corrosion for Overall Water Splitting, ACS Energy Lett. 4(4) (2019) 952-959. https://doi.org/10.1021/acsenergylett.9b00333.

[12] Y. Zhang, Q. Shao, Y. Pi, J. Guo, X. Huang, A Cost-Efficient Bifunctional Ultrathin Nanosheets Array for Electrochemical Overall Water Splitting, Small 13(27) (2017) 1700355. https://doi.org/10.1002/smll.201700355.

[13] T. Zhang, L. Hang, Y. Sun, D. Men, X. Li, L. Wen, X. Lyu, Y. Li, Hierarchical hetero-Ni_3Se_4@NiFe LDH micro/nanosheets as efficient bifunctional electrocatalysts with superior stability for overall water splitting, Nanoscale Horiz. 4(5) (2019) 1132-1138. https://doi.org/10.1039/c9nh00177h.

[14] Z. Jing, Q. Zhao, D. Zheng, L. Sun, J. Geng, Q. Zhou, J. Lin, Nickel-doped pyrrhotite iron sulfide nanosheets as a highly efficient electrocatalyst for water splitting, J. Mater. Chem. A 8(39) (2020) 20323-20330. https://doi.org/10.1039/d0ta07624d.

[15] J. Xie, H. Qu, F. Lei, X. Peng, W. Liu, L. Gao, P. Hao, G. Cui, B. Tang, Partially Amorphous Nickel–Iron Layered Double Hydroxide Nanosheet Arrays For Robust Bifunctional Electrocatalysis, J. Mater. Chem. A 6(33) (2018) 16121-16129. https://doi.org/10.1039/c8ta05054f.

[16] W. Zhu, Z. Yue, W. Zhang, N. Hu, Z. Luo, M. Ren, Z. Xu, Z. Wei, Y. Suo, J. Wang, Wet-chemistry topotactic synthesis of bimetallic iron–nickel sulfide nanoarrays: an advanced and versatile catalyst for energy efficient overall water and urea electrolysis, J. Mater. Chem. A 6(10) (2018) 4346-4353. https://doi.org/10.1039/c7ta10584c.

[17] Y. Chen, H. Yao, F. Kong, H. Tian, G. Meng, S. Wang, X. Mao, X. Cui, X. Hou, J. Shi, V_2C MXene synergistically coupling FeNi LDH nanosheets for boosting oxygen evolution reaction, Appl. Catal., B 297 (2021) 120474. https://doi.org/10.1016/j.apcatb.2021.120474.

[18] L.-G. He, P.-Y. Cheng, C.-C. Cheng, C.-L. Huang, C.-T. Hsieh, S.-Y. Lu, $(Ni_xFe_yCo_{6-x-y})Mo_6C$ Cuboids as outstanding bifunctional electrocatalysts for overall water splitting, Appl. Catal., B 290 (2021) 120049. https://doi.org/10.1016/j.apcatb.2021.120049.

[19] Z. He, J. Zhang, Z. Gong, H. Lei, D. Zhou, N. Zhang, W. Mai, S. Zhao, Y. Chen, Activating lattice oxygen in NiFe-based (oxy)hydroxide for water electrolysis, Nat. Commun. 13(1) (2022) 2191. https://doi.org/10.1038/s41467-022-29875-4.

[20] L. Tan, J. Yu, C. Wang, H. Wang, X. Liu, H. Gao, L. Xin, D. Liu, W. Hou, T. Zhan, Partial Sulfidation Strategy to NiFe-LDH@$FeNi_2S_4$ Heterostructure Enable High-Performance Water/Seawater Oxidation, Adv. Funct. Mater. 32(29) (2022) 2200951.

https://doi.org/10.1002/adfm.202200951.

[21] Q. Wen, K. Yang, D. Huang, G. Cheng, X. Ai, Y. Liu, J. Fang, H. Li, L. Yu, T. Zhai, Schottky Heterojunction Nanosheet Array Achieving High-Current-Density Oxygen Evolution for Industrial Water Splitting Electrolyzers, Adv. Energy Mater. 11(46) (2021) 2102353. https://doi.org/10.1002/aenm.202102353.

[22] G. Zhang, Y.-S. Feng, W.-T. Lu, D. He, C.-Y. Wang, Y.-K. Li, X.-Y. Wang, F.-F. Cao, Enhanced Catalysis of Electrochemical Overall Water Splitting in Alkaline Media by Fe Doping in Ni_3S_2 Nanosheet Arrays, ACS Catal. 8(6) (2018) 5431-5441. https://doi.org/10.1021/acscatal.8b00413.

[23] L. Tan, J. Yu, H. Wang, H. Gao, X. Liu, L. Wang, X. She, T. Zhan, Controllable Synthesis And Phase-Dependent Catalytic Performance Of Dual-Phase Nickel Selenides On Ni Foam For Overall Water Splitting, Appl. Catal., B 303 (2022) 120915. https://doi.org/https://doi.org/10.1016/j.apcatb.2021.120915.

[24] L. Yu, L. Wu, B. McElhenny, S. Song, D. Luo, F. Zhang, Y. Yu, S. Chen, Z. Ren, Ultrafast Room-Temperature Synthesis of Porous S-Doped Ni/Fe (Oxy)Hydroxide Electrodes For Oxygen Evolution Catalysis in Seawater Splitting, Energy Environ. Sci. 13(10) (2020) 3439-3446. https://doi.org/10.1039/d0ee00921k.

[25] Y. Kuang, M.J. Kenney, Y. Meng, W.H. Hung, Y. Liu, J.E. Huang, R. Prasanna, P. Li, Y. Li, L. Wang, M.C. Lin, M.D. McGehee, X. Sun, H. Dai, Solar-driven, highly sustained splitting of seawater into hydrogen and oxygen fuels, Proc Natl Acad Sci U S A 116(14) (2019) 6624-6629. https://doi.org/10.1073/pnas.1900556116.

[26] R.-Y. Fan, X.-Y. Zhang, N. Yu, F.-G. Wang, H.-Y. Zhao, X. Liu, Q.-X. Lv, D.-P. Liu, Y.-M. Chai, B. Dong, Rapid "Self-Healing" Behavior Induced By Chloride Anions to Renew The Fe–Ni(Oxy)Hydroxide Surface For Long-Term Alkaline Seawater Electrolysis, Inorg. Chem. Front. 9(16) (2022) 4216-4224. https://doi.org/10.1039/d2qi01078j.

[27] Y. Li, G. Chen, Y. Zhu, Z. Hu, T.S. Chan, S. She, J. Dai, W. Zhou, Z. Shao, Activating Both Basal Plane and Edge Sites of Layered Cobalt Oxides for Boosted Water Oxidation, Adv. Funct. Mater. 31(38) (2021) 2103569. https://doi.org/10.1002/adfm.202103569.

[28] Z.F. Huang, S. Xi, J. Song, S. Dou, X. Li, Y. Du, C. Diao, Z.J. Xu, X. Wang, Tuning of Lattice Oxygen Reactivity And Scaling Relation To Construct Better Oxygen Evolution Electrocatalyst, Nat Commun 12(1) (2021) 3992. https://doi.org/10.1038/s41467-021-24182-w.

[29] J.X. Feng, H. Xu, Y.T. Dong, S.H. Ye, Y.X. Tong, G.R. Li, FeOOH/Co/FeOOH Hybrid Nanotube Arrays as High-Performance Electrocatalysts for the Oxygen Evolution Reaction, Angew. Chem. Int. Ed. 55(11) (2016) 3694-8. https://doi.org/10.1002/anie.201511447.

[30] C. Xie, W. Chen, S. Du, D. Yan, Y. Zhang, J. Chen, B. Liu, S. Wang, In-Situ Phase Transition Of WO_3 Boosting Electron And Hydrogen Transfer For Enhancing Hydrogen Evolution On Pt, Nano Energy 71 (2020) 104653. https://doi.org/10.1016/j.nanoen.2020.104653.

[31] K. Gu, D. Wang, C. Xie, T. Wang, G. Huang, Y. Liu, Y. Zou, L. Tao, S. Wang, Defect-Rich High-Entropy Oxide Nanosheets for Efficient 5-Hydroxymethylfurfural Electrooxidation, Angew. Chem. Int. Ed. Engl. 60(37) (2021) 20253-20258. https://doi.org/10.1002/anie.202107390.

[32] R.L. Doyle, M.E.G. Lyons, Kinetics and Mechanistic Aspects of the Oxygen Evolution

Reaction at Hydrous Iron Oxide Films in Base, J. Electrochem. Soc. 160(2) (2013) H142-H154. https://doi.org/10.1149/2.015303jes.

[33] M.E. Lyons, M.P. Brandon, Redox Switching And Oxygen Evolution Electrocatalysis In Polymeric Iron Oxyhydroxide Films, Phys Chem Chem Phys 11(13) (2009) 2203-17. https://doi.org/10.1039/b815338h.

[34] D. Wu, D. Chen, J. Zhu, S. Mu, Ultralow Ru Incorporated Amorphous Cobalt-Based Oxides for High-Current-Density Overall Water Splitting in Alkaline and Seawater Media, Small 17(39) (2021) e2102777. https://doi.org/10.1002/smll.202102777.

[35] L. Wu, L. Yu, Q. Zhu, B. McElhenny, F. Zhang, C. Wu, X. Xing, J. Bao, S. Chen, Z. Ren, Boron-Modified Cobalt Iron Layered Double Hydroxides For High Efficiency Seawater Oxidation, Nano Energy 83 (2021) 105838. https://doi.org/10.1016/j.nanoen.2021.105838.

[36] Y. Feng, X. Wang, J. Huang, P. Dong, J. Ji, J. Li, L. Cao, L. Feng, P. Jin, C. Wang, Decorating CoNi layered double hydroxides nanosheet arrays with fullerene quantum dot anchored on Ni foam for efficient electrocatalytic water splitting and urea electrolysis, Chem. Eng. J. 390 (2020) 124525. https://doi.org/10.1016/j.cej.2020.124525.

[37] C. Chen, S. He, K. Dastafkan, Z. Zou, Q. Wang, C. Zhao, Sea urchin-like $NiMoO_4$ nanorod arrays as highly efficient bifunctional catalysts for electrocatalytic/photovoltage-driven urea electrolysis, Chin. J. Catal. 43(5) (2022) 1267-1276. https://doi.org/10.1016/s1872-2067(21)63962-1.

[38] S. Huang, Q. Zhang, P. Xin, J. Zhang, Q. Chen, J. Fu, Z. Jin, Q. Wang, Z. Hu, Construction of Fe-doped NiS-NiS_2 Heterostructured Microspheres Via Etching Prussian Blue Analogues for Efficient Water-Urea Splitting, Small 18(14) (2022) 2106841. https://doi.org/10.1002/smll.202106841.

[39] L. Xie, Q. Liu, Y. Luo, Z. Liu, Y. Xu, A.M. Asiri, X. Sun, F. Xie, Bimetallic NiCoP Nanosheets Array for High-Performance Urea Electro-Oxidation and Less Energy-Intensive Electrolytic Hydrogen Production, ChemistrySelect 2(31) (2017) 10285-10289. https://doi.org/10.1002/slct.201702071.

[40] C. Li, Y. Liu, Z. Zhuo, H. Ju, D. Li, Y. Guo, X. Wu, H. Li, T. Zhai, Local Charge Distribution Engineered by Schottky Heterojunctions toward Urea Electrolysis, Adv. Energy Mater. 8(27) (2018) 1801775. https://doi.org/10.1002/aenm.201801775.

[41] X. Wang, J. Wang, X. Sun, S. Wei, L. Cui, W. Yang, J. Liu, Hierarchical coral-like NiMoS nanohybrids as highly efficient bifunctional electrocatalysts for overall urea electrolysis, Nano Res. 11(2) (2017) 988-996. https://doi.org/10.1007/s12274-017-1711-3.

[42] Z.-Y. Yu, C.-C. Lang, M.-R. Gao, Y. Chen, Q.-Q. Fu, Y. Duan, S.-H. Yu, Ni–Mo–O nanorod-derived composite catalysts for efficient alkaline water-to-hydrogen conversion via urea electrolysis, Energy Environ. Sci. 11(7) (2018) 1890-1897. https://doi.org/10.1039/c8ee00521d.

Chapter V: Seawater Corrosive Engineering Assisted *in-situ* Room-Temperature Synthesis of Ni/Co/Fe Trimetallic Composition to Achieve Polyester Plastics Upgrading and Green Hydrogen Production

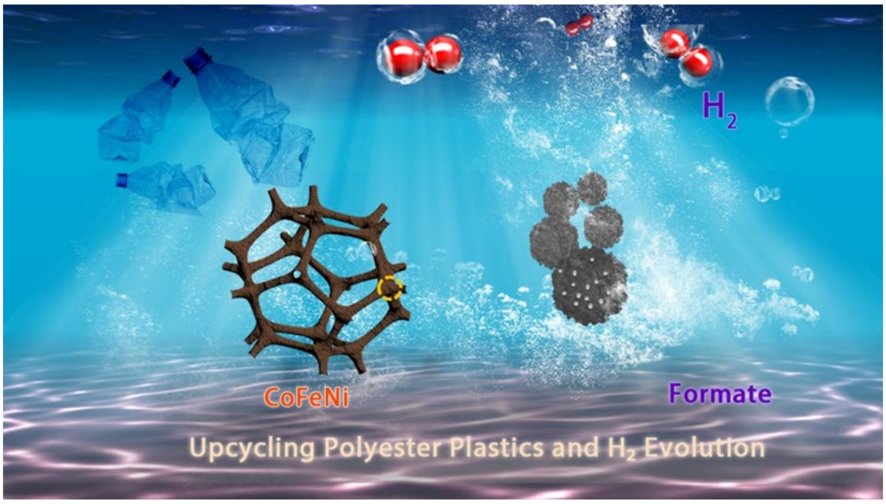

V.1 Abstract

Electrochemical upcycling of plastic waste into valuable chemicals is an optimal method for utilizing and extracting value from waste resources. Herein, we developed a low-cost and large-scale approach based on seawater corrosion engineering to construct amorphous CoFeNi material on nickel foam (A-CoFeNi), which effectively converts ethylene glycol (EG) from polyethylene terephthalate (PET) hydrolysate into formate. The optimized A-CoFeNi only necessitates 1.25 and 1.38 V *vs.* reversible hydrogen electrode (RHE) at 10 and 100 mA cm^{-2}, respectively. In addition, coating an ultra-low content of Pt on A-CoFeNi, to prepare Pt-CoFeNi cathode catalyst, recorded overpotentials as low as 44 and 122.1 mV to deliver respectively 10 and 100 mA cm^{-2} for HER in 1 M KOH seawater. In the co-electrolysis system, the Pt-CoFeNi//CoFeNi exhibited excellent Faradaic efficiencies for the simultaneous generation of formate (94.8%) and H_2 (~100%). The high activity and stability of this system could be ascribed to CoFeNi trimetallic cooperation and strong electronic interactions. This work provides insights into the application of seawater corrosion technology for large-scale synthesis

of catalysts, achieving efficient seawater utilization and electro-reforming PET plastic waste into valuable chemicals.

V.2. Experimental section

2.1 Synthesis of Pt/C-Ni foam and RuO_2-Ni foam

Nickel foam (NF) was initially cut into 2×4 cm^2 pieces and subsequently cleaned using a sequence of solvents, including acetone, hydrochloric acid (0.1 M), and ultrapure water. Each cleaning stage involved ultrasonic treatment for 15 min to eliminate any surface oxides and organic contamination.

First, weigh 4 mg of Pt/C sample and 14 mg of carbon black. Add a few milliliters of ethanol solution as a solvent, stir the mixture evenly. Evaporate the ethanol of product at room temperature and then dry it thoroughly in the oven at 120°C for 10 h. Secondly, weigh 2 mg of polyvinylidene fluoride (PVDF) and thoroughly mix it with the Pt/C and carbon black mixture, using N-methyl-2-pyrrolidone (NMP) as the solvent. Finally, apply the slurry onto the Ni foam surface and dry it in the oven for later use. The preparation process of RuO_2-Ni foam also adopts the same method.

V.2.2 Synthesis of A-CoFeNi catalyst

The amorphous A-CoFeNi catalyst was synthesized using a one-pot seawater corrosion technology [1-4]. The NF was immersed in a mixture solution comprising 0.5 M NaCl, 2.5 mM $Fe(NO_3)_3\cdot 9H_2O$, and 20 mM $Co(NO_3)_3\cdot 6H_2O$, followed by shaking for 12 h at ambient temperature. During this process, the NF surface underwent an exchange with Co and Fe elements, overcoming the passivation reaction assisted by seawater Cl^- element. For further optimization of electrocatalytic performance, a series of A-CoFeNi catalysts were prepared by adjusting the Co/Fe concentration and corrosion time. The resulting NF, characterized by a yellowish-brown color, underwent multiple washes with water to eliminate any excess of NaCl, followed by drying at 60 °C for 2 h. The atomic ratios of Co, Fe, Ni, and O in the final product were determined through energy dispersive spectroscopy (EDS) and X-ray photoelectron spectroscopy (XPS) investigations (**Tables 2-4**).

V.2.3 Synthesis of Pt-CoFeNi catalyst

The Pt-CoFeNi catalyst was synthesized using the same seawater corrosion method. In a typical procedure, NF was immersed in a mixture solution containing 0.5 M NaCl, 2.5 mM $Fe(NO_3)_3 \cdot 9H_2O$, 20 mM $Co(NO_3)_3 \cdot 6H_2O$, and 0.1 mM H_2PtCl_6. The process involved atomic rearrangement and construction at the foam surface for 12 h. Subsequently, the resulting dark brown Pt-CoFeNi was washed with deionized water and dried under vacuum at 60 °C 12 h for further use.

V.2.3 PET hydrolysate treatment

The PET hydrolysate used as the electrolyte was prepared by processing used plastic bottles. Initially, waste PET plastic bottles (4 g) were cut into pieces (1×2 cm) and added to 30 mL of 3 M KOH solution [5]. Subsequently, the mixed solution with PET pieces was heated at 120 °C for 10 h. The resulting PET hydrolysate was diluted with 1 M KOH. Finally, the ethylene glycol concentration in the PET hydrolysate was determined through ^1H NMR analysis, yielding an approximate concentration of 0.3 M determined by an internal standard normalization.

V.2.4 Corrosion behavior measurements

To assess the corrosion displacement reaction mechanism, the corrosion polarization curves were recorded for Ni foam (NF) immersed in 0.5 M NaCl, 20 mM $Co(NO_3)_2 \cdot 6H_2O$, 0.5 M NaCl + 20 mM $Co(NO_3)_2 \cdot 6H_2O$, 0.5 M NaCl + 20 mM $Co(NO_3)_2 \cdot 6H_2O$ + 2.5 mM $Fe(NO_3)_3 \cdot 9H_2O$, 0.5 M NaCl + 20 mM $Co(NO_3)2 \cdot 6H_2O$ + 2.5 mM $Fe(NO_3)_3 \cdot 9H_2O$ + 0.10 mM H_2PtCl_6 aqueous solutions. NF, carbon rod and saturated calomel (SCE) electrodes were applied as working, counter and reference electrodes, respectively. Before recording the corrosion polarization curves, a pH meter was used to determine the pH values of the different reaction solutions (Mettler Toledo-S210, **Table1**). Additionally, the open-circuit potential (OCP) was initially measured, and then the current-voltage curves within the OCP± 300 mV potential range at a scan rate of 5 mV s^{-1}.

V.3 Results and Discussion

V.3.1 Construction Process of A-CoFeNi Catalysts

Seawater, one of the most abundant natural resources, has enormous potential in various aspects. For example, this potential can be harnessed for the synthesis of materials through ion corrosion technology [2, 6, 7]. As shown in **Figure V.1,** 3D porous A-CoFeNi catalyst was prepared *via* low-cost and large-scale seawater corrosion technology. In order to exploit this process on the foam surface, we adopted the electrochemical corrosion polarization curve strategy, as shown in **Figure V.2**. The corrosion current densities (I_{corr}) and corrosion potentials (E_{corr}) could be derived from the above corrosion polarization curves. NF immersed in NaCl-$Fe(NO_3)_3$-$Co(NO_3)_2$ aqueous solution revealed higher I_{corr} and lower E_{corr} (1.88 mA cm^{-2}, -0.254 V *vs.* SCE, respectively) compared to NaCl (0.052 mA cm^{-2}, -0.262 V) or $Fe(NO_3)_3$-$Co(NO_3)_2$ (0.607 mA cm^{-2}, -0.114 V) systems, indicating a stronger self-corrosion tendency. The surface Ni atoms were oxidized to generate Ni^{3+}/Ni^{2+} ions in a high concentration of Cl^- solution occurring in the anode region, while simultaneously released electrons (anode) and sustainable formation of OH^- at the cathode. Ultimately, the Fe^{3+}/Co^{2+} cations and the diffusion of Ni^{2+} simultaneously react with OH^- to produce a precipitation and generate amorphous tri-metallic A-NiCoFe nanoflower catalyst supported on NF [1]. Utilizing this self-corrosion principle, we scaled up the sample preparation. As shown in **Figure V.3**, the A-CoFeNi catalyst can be successfully prepared by immersing a large piece of Ni foam (20×30 cm) in a seawater solution with $Fe(NO_3)_3$-$Co(NO_3)_2$, and shaking at room temperature for 24 h.

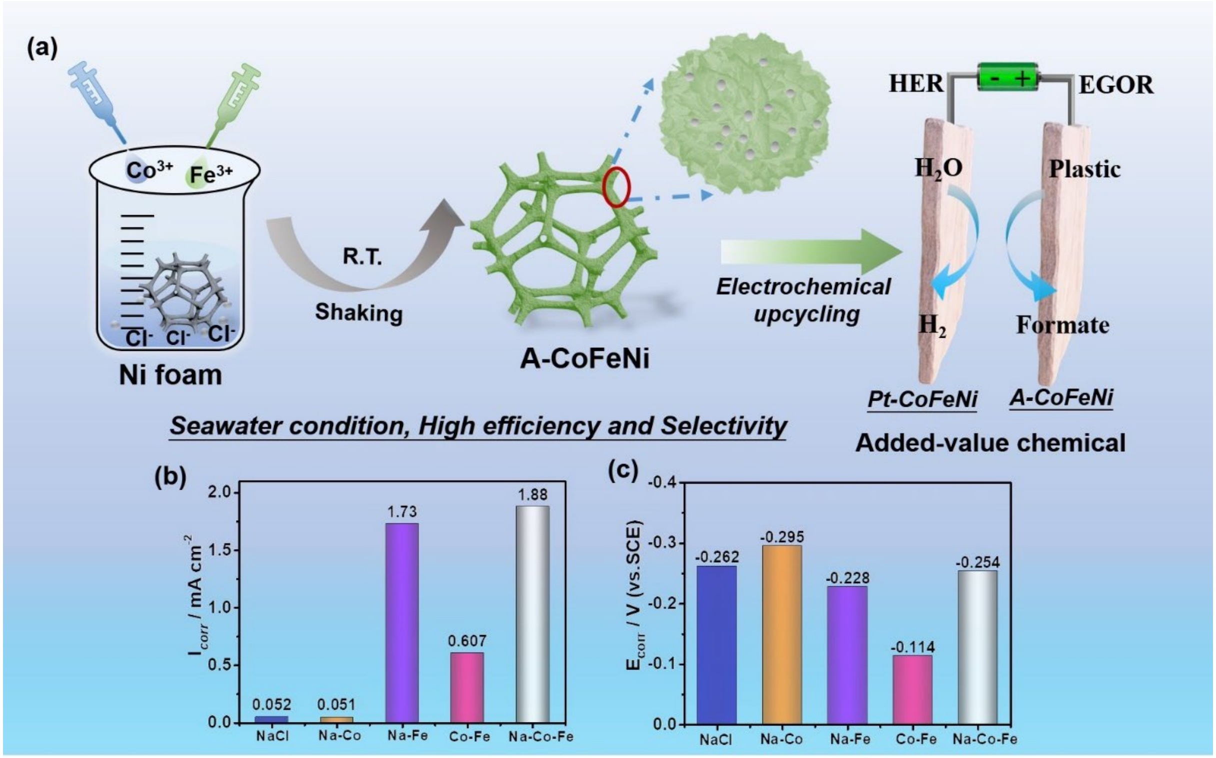

Figure V.1. (**a**) Schematic illustration of the synthesis of A-CoFeNi catalyst *via* seawater corrosion technology. (**b**) Comparison of self-corrosion potentials (E_{corr}) and (**c**) self-corrosion current densities (I_{corr}).

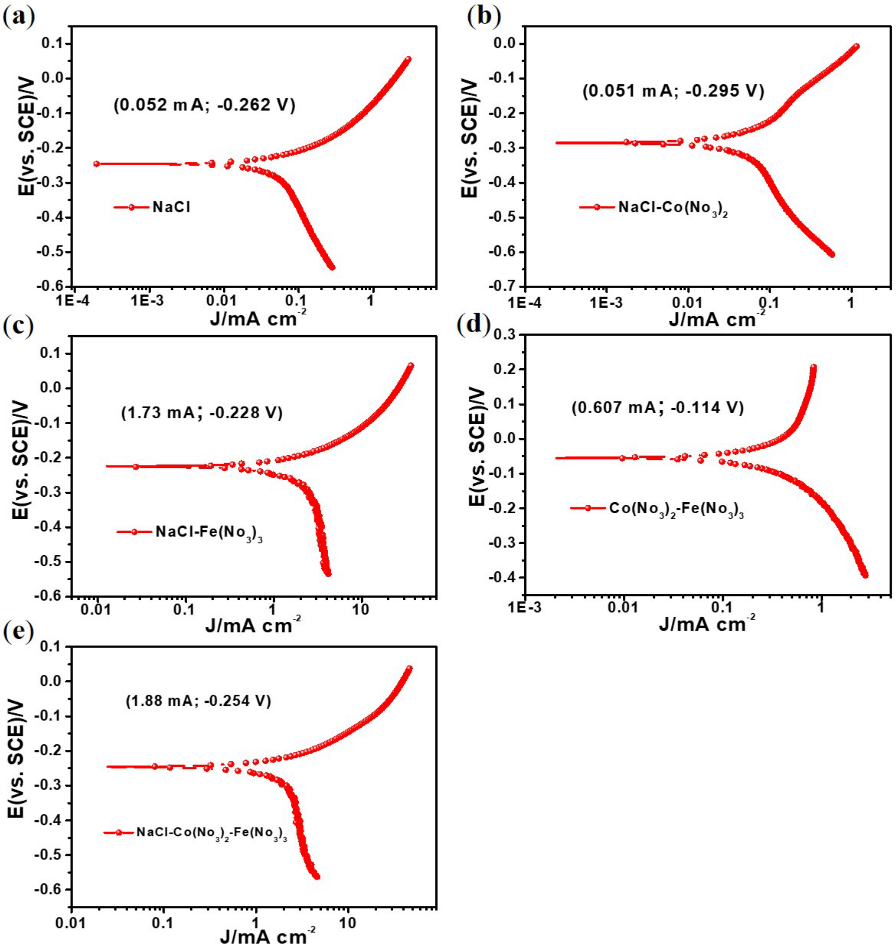

Figure V.2. Corrosion polarization curves of nickel foam (NF) in (a) 0.5 M NaCl, (b) 0.5 M NaCl+20 mM $Co(NO_3)_3$, (**c**) 0.5 M NaCl+2.5 mM $Fe(NO_3)_3$, (**d**) 20 mM $Co(NO_3)_3$+2.5 mM $Fe(NO_3)_3$, (**e**) 0.5 M NaCl+20 mM $Co(NO_3)_3$+2.5 mM $Fe(NO_3)_3$ aqueous solutions.

Sample	Concentration	pH-1	pH-2	pH-3	Average
$Co(NO_3)_2\cdot 6H_2O$	20 mM	4.64	4.64	4.66	4.65
$Fe(NO_3)_3\cdot 9H_2O$	2.5 mM	2.86	2.86	2.88	2.87
$Co(NO_3)_2\cdot 6H_2O$ + $Fe(NO_3)_3\cdot 9H_2O$	20 mM + 2.5 mM	2.82	2.84	2.85	2.84
$Co(NO_3)_2\cdot 6H_2O$ + $Fe(NO_3)_3\cdot 9H_2O$ + H_2PtCl_6	20 mM + 2.5 mM + 0.1 mM	2.68	2.70	2.70	2.69

Table 1. pH values of (1) Co(NO3)2·6H2O, (2) Fe(NO3)3·9H2O, (3) Co(NO3)2·6H2O+ Fe(NO3)3·9H2O, (4) Co(NO3)2·6H2O+ Fe(NO3)3·9H2O+ H2PtCl6 in 0.5M NaCl solutions.

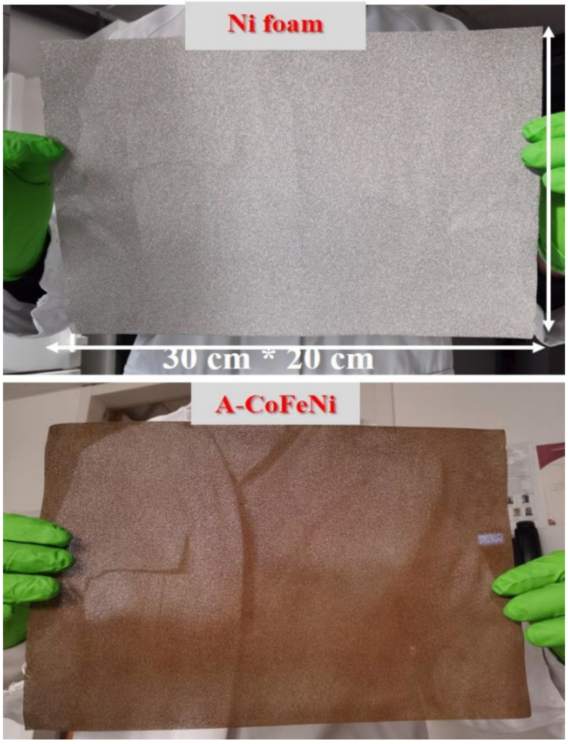

Figure V.3. Display diagram of large-scale preparation of A-CoFeNi sample.

V.3.2 Morphology and Structural Characterization

To investigate the morphological variation of different samples (0.5 M NaCl+20 mM $Co(NO_3)_2$, 0.5 M NaCl+2.5 mM $Fe(NO_3)_3$ and 0.5 M NaCl+20 mM $Co(NO_3)_2$ + 2.5 mM $Fe\ (NO_3)_3$ systems), scanning electron microscopy (SEM) was firstly performed (**Figure V.4-5**). For Co/Ni or Fe/Ni system, the surface morphology gradually becomes rougher with obvious growth of irregular particles after 12 h corrosion and ion exchange reaction. Interestingly, the morphology of A-CoFeNi foam exhibited unique layered array structure with apparent nanoflowers in the size of several micrometers (0.6~1.2 μm) and a thickness of dozens of nanometers. Furthermore, transmission electron microscopy (TEM) revealed the typical porous flower-like interconnected nanosheets, which exhibited a large surface area with numerous active sites. The high-resolution TEM (HR-TEM) showed no lattice fringes, confirming the amorphous nature of the A-CoFeNi electrode material (**Figure V.4 d,e**). No diffraction peaks were obvious in the X-ray diffraction (XRD) pattern, except the two typical nickel foam peaks at 44.4° and 51.8°, further indicating that the catalyst structure was amorphous. The three-metallic system owns new Co/Fe sites, coupled with Ni corrosion and spalling, resulting in disordered structure and amorphous morphology. Energy dispersive X-ray spectroscopy (EDS) analysis was performed to acquire the elemental chemical composition and distribution. As shown in **Figure V.4g** and **Table 2**, the presence of Co (4.5 at. %), Fe (6.7 at. %), Ni (23.2 at. %), and O (63.1 at. %) atoms is completely consistent with the chemical composition of the A-CoFeNi catalyst.

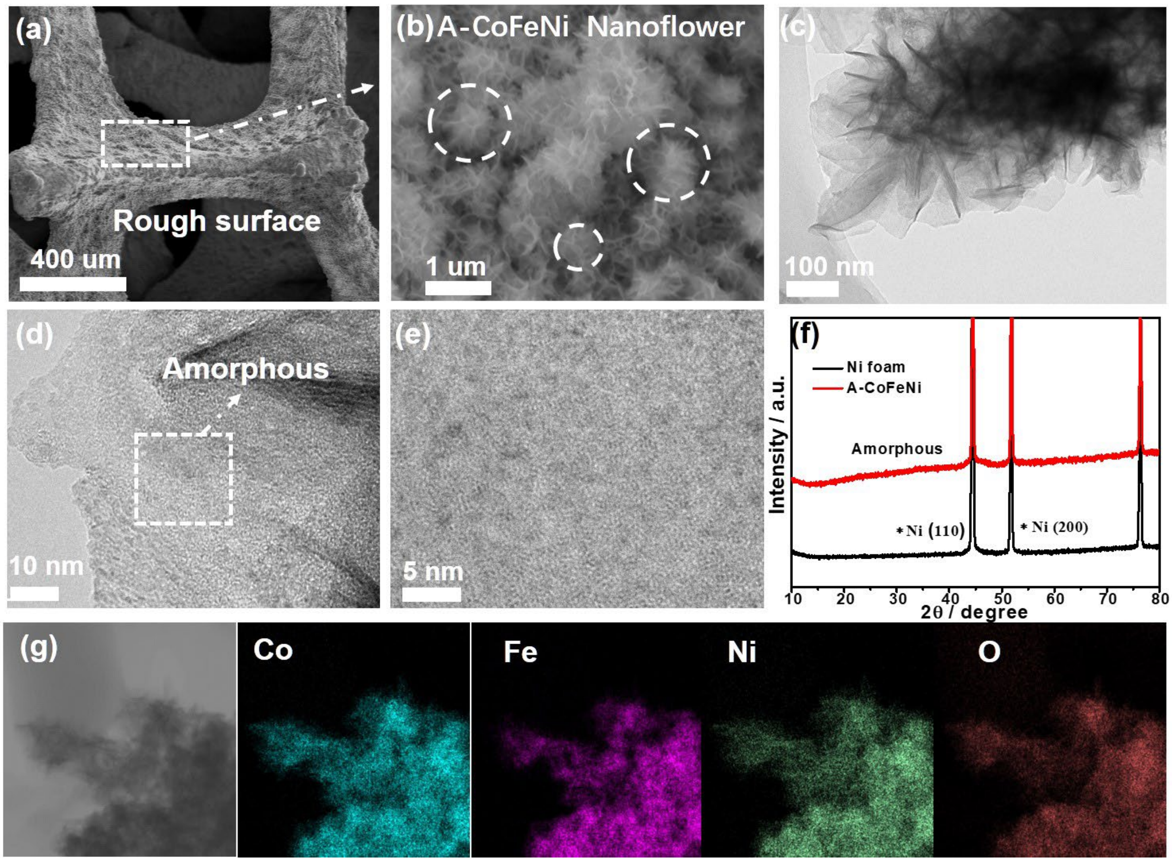

Figure V.4. (**a-b**) SEM, (**c**) TEM, (**d–e**) HRTEM images, (**f**) XRD patterns, and (**g**) TEM image and EDX elemental mapping (Co, Fe, Ni, O) of the A-CoFeNi trimetallic sample prepared using 0.5 M NaCl + 20 mM $Co(NO_3)_2·6H_2O$ + 2.5 mM $Fe(NO_3)_3·9H_2O$.

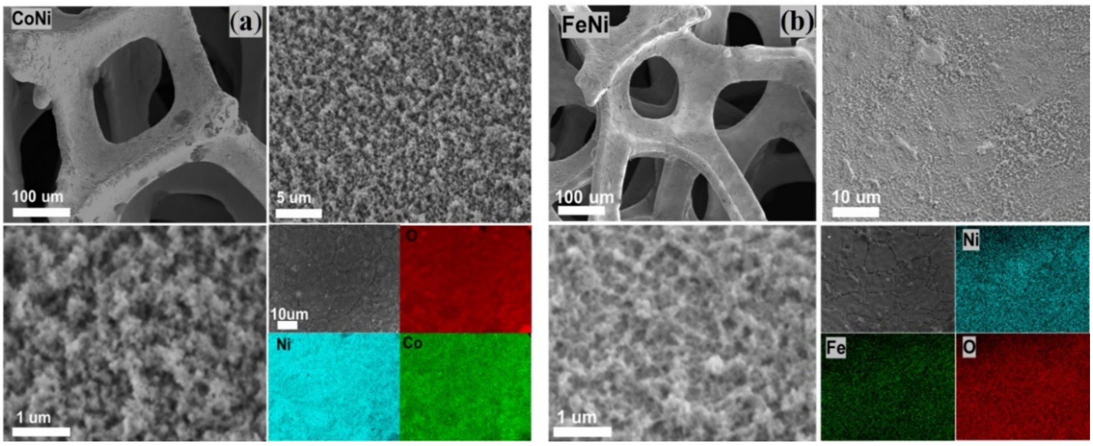

Figure V.5. SEM images of (**a**) CoNi sample and (**b**) FeNi sample at different magnifications, and its elemental mapping images.

No	Sample	Co (at.%)	Fe (at.%)	Ni (at.%)	O (at.%)	Cl (at.%)
1	A-CoFeNi	4.5	6.7	23.2	63.1	1.5
2	A-CoFeNi after EGOR	7.3	6.6	27.1	56.6	0.1
3	A-CoFeNi after OER	4.3	5.7	40	44.4	1.6

Table 2. EDX analysis of Co, Fe, Ni, O and Cl elements before and after EGOR/OER stability tests.

X-ray photoelectron spectroscopy (XPS) revealed the chemical composition and valence states of different elements [8, 9]. The XPS full plot of A-CoFeNi showed Co (11.36 at. %), Fe (3.5 at. %), Ni (20.4 at. %), and O (44.46 at. %), which is in agreement with the SEM/EDS elemental content trend results. Specifically, the high-resolution XPS plots of the chosen elements are displayed in **Figure V.6**. The Co 2p and Fe 2p spectra of A-CoNiFe sample displayed small peaks indicative of Co^{0} and Fe^{0} at 777.7 eV and 706 eV, respectively, indicating the presence of metal structure. This phenomenon can be attributed to the redox reaction that occurs during the self-corrosion process of building an amorphous CoFeNi structure, causing the Co/Fe element to assume multiple type valence states. In addition, the Co 2p spectrum of A-CoNiFe is curve-fitted with two typical peaks due to Co 2p1/2 of Co^{3+} (780.45 eV) and Co^{2+} (782.15 eV), while the deconvoluted region of Co 2p3/2 is separated into two peaks at 795.95 eV (Co^{3+})

and 797.6 eV (Co^{2+}). In addition, 786.05 eV and 802.1 eV belong to the typical satellite peaks of Co^{2+}, and 790.0 eV and 805.0 eV correspond to the typical satellite peaks of Co^{3+} [10, 11]. The Ni 2p spectrum of A-CoNiFe exhibits a peak at 873.8 eV corresponding to the Ni 2p1/2 state and a peak at 855.9 eV corresponding to the Ni 2p3/2 state, which are attributed to the binding energies of oxidized Ni species[12]. Interestingly, the higher ratio of Co^{2+}/Co^{3+} peaks and Ni^{2+}/Ni^{3+} demonstrated that Ni and Co elements possessed with higher valence (II) state and lower valence (III) state. Moreover, the weak peaks at 711.05 and 724.0 eV could be ascribed to Fe^{2+}, whereas the other major peaks at 713.9 and 726.6 eV are assigned to Fe^{3+}, along with the satellite peaks at 719.1 and 734.7 eV[13]. Actually, a lot of work has proved that transition metal oxides are precursor catalysts for small organic molecule oxidation reaction or four electron oxygen evolution reaction [14]. Specifically, Co, Ni and Fe are in the bivalent and trivalent states (M−O or M−OH), which are more favorable to reconstruct metal-based oxy(hydroxide) [15]. Furthermore, the O 1s spectrum can be deconvoluted into three distinct peaks. The O1 peak at 530.0 eV corresponds to the metal-oxygen bond, the O2 band at 531.6 eV is associated with defect sites that have low oxygen coordination, and the component at 533.1 eV is attributed to adsorbed molecular water (O3)[16, 17]. The A-CoFeNi sample exhibited higher O2 content, suggesting the presence of several defect sites that could enhance catalytic reaction efficiency. It could be inferred that chloride ions consistently erode metal surfaces and introduce defect sites during the synthesis process. Therefore, this system catalyst possesses active high valence, defect sites and is of low crystallinity. These features are expected to be more conducive to high catalytic performance.

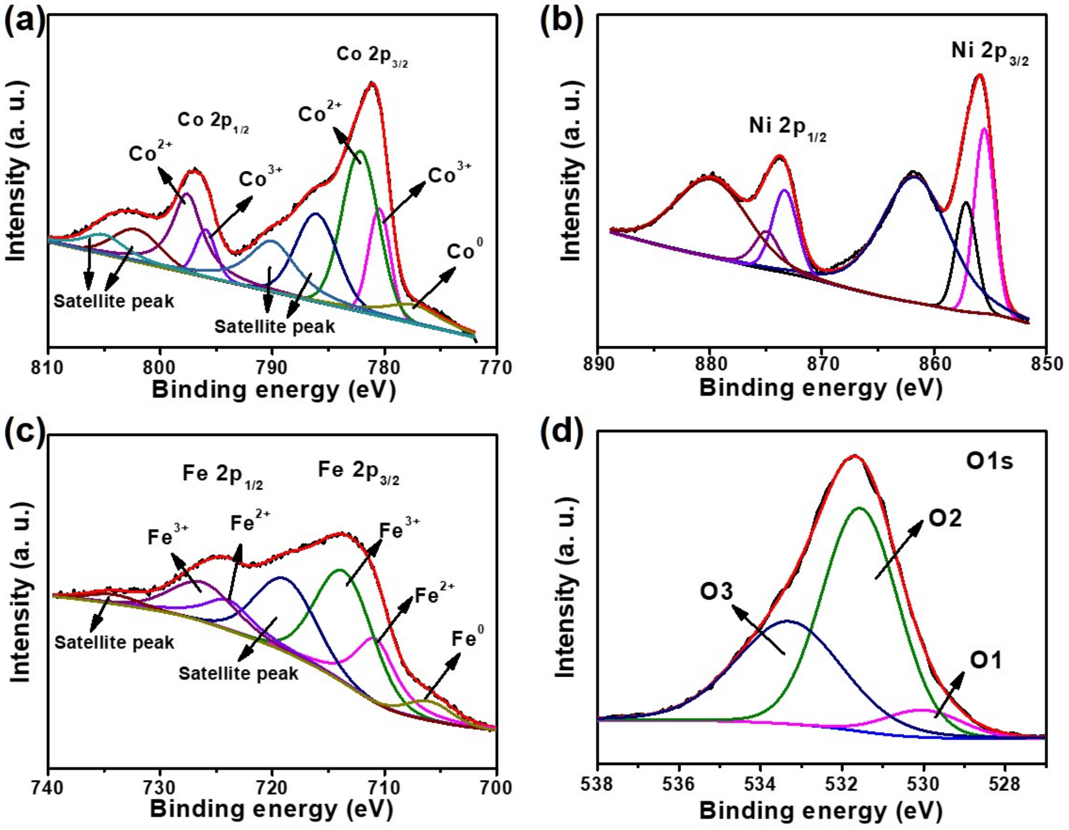

Figure V.6. High-resolution XPS plots of (**a**) Co 2p, (**b**) Ni 2p, (**c**) Fe 2p, (**d**) O 1s of A-CoFeNi.

V.3.3. Electrochemical OER Performance Evaluation

The prepared tri-mental A-CoFeNi sample, possessing a modulated electronic structure and abundant oxygen vacancies, is regarded as a good electrocatalyst for the oxygen evolution reaction (OER) even in an alkaline seawater solution.

In order to optimize the sample performance, we first explored the OER of the Co/Ni system and Fe/Ni systems prepared at different Co and Fe concentrations. As shown in **Figure V.7**, for Co/Ni system, the OER performance was obviously enhance after immersion of Ni foam in low concentrations of $Co(NO_3)_2$ (1, 5, 10 mM) compared with bare Ni foam, However, upon immersion in a high-concentration of Co salt (20, 30, 50 mM), the OER performance decreased because a large amount of Co particles covers the Ni active sites, resulting in a decrease of charge transfer ability and OER performance. For Fe/Ni system, it was demonstrated similar excellent OER performance such as lower resistance of charge transfer and overpotential (Rct~1.5 Ω, η~300 mV for 30 mM Fe sample) compared to Co/Ni system (Rct~43.9 Ω, η~430 mV for 30 mM Co sample), indicating Fe element plays a vital role in the OER process. However, the Fe/Ni system did not greatly improve the activity of the EGOR, while Co element presented good effect, so we used the Co/Fe/Ni ternary system for EG oxidation reaction. As shown in **Figure V.8**, excessive high or low ratio of Fe/Co concentration is detrimental to the formation of catalyst surface structure and reaction efficiency.

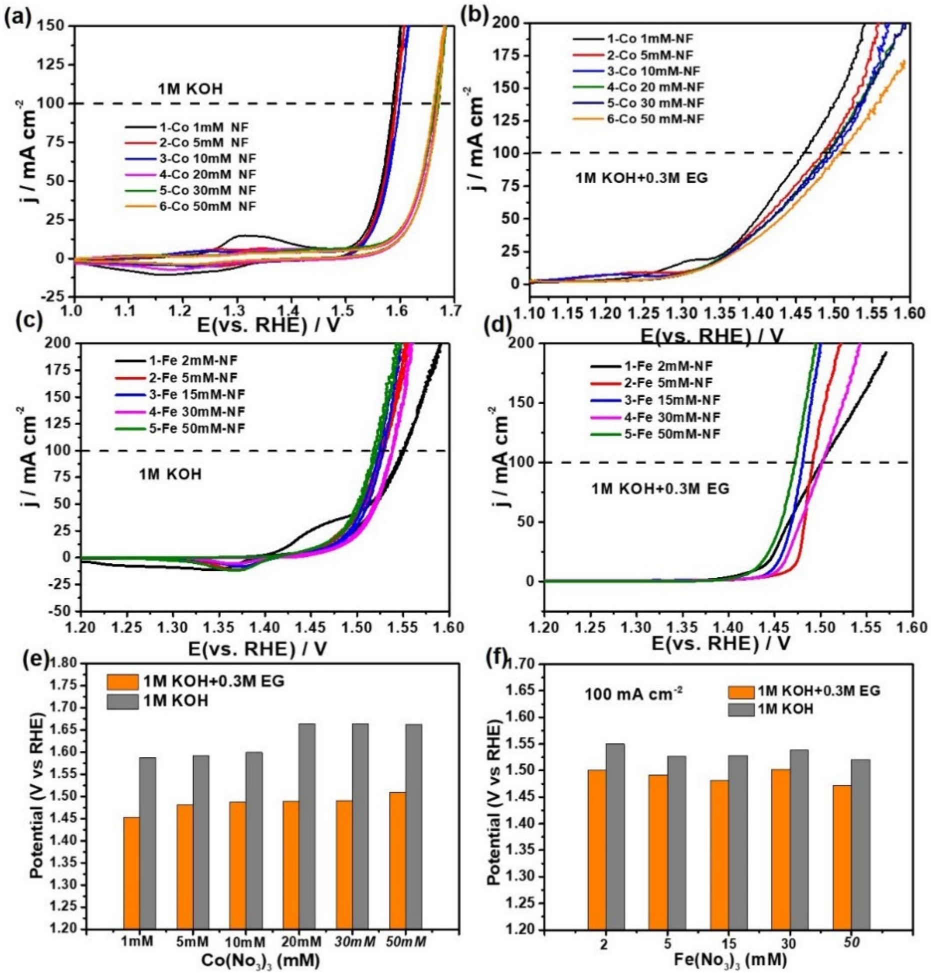

Figure V.7. LSV and CV polarization curves of CoNi and FeNi samples prepared using various concentrations of Co salt for catalyzing (**a, c**) OER and (**b, d**) EGOR at a scan rate of 5 mV s^{-1}. (**c**) Nyquist plots of CoNi samples in 1 M KOH at 1.5V *vs.* RHE. (**e, f**) Comparison of their overpotential values at a current density of 100 mA cm^{-2}.

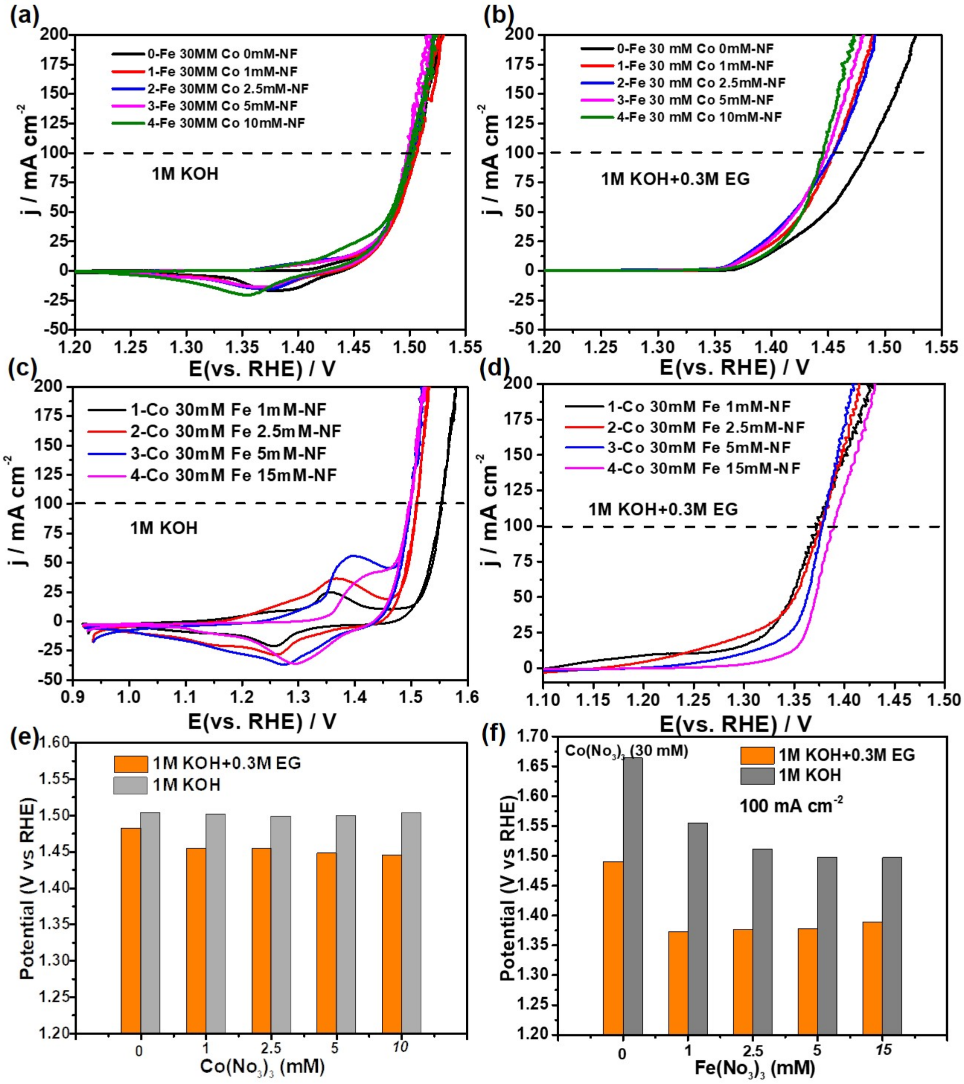

Figure V.8. LSV polarization curves of A-FeNiCo samples prepared using various concentrations of Fe/Co salts for catalyzing (**a**, **c**) OER and (**b**, **d**) EGOR at a scan rate of 5 mV s^{-1}. (**e**, **f**) Comparison of their overpotential values at a current density 100 mA cm^{-2}.

Therefore, the optimal catalytic performance was achieved using 2.5 mM $Fe(NO_3)_3$, 20 mM $Co(NO_3)_2$ and 0.5 M NaCl mixed solution. Significantly, the obvious peaks in the CV curves between 1.2 and 1.5 V *vs.* reversible hydrogen electrode (RHE) could be attributed to the oxidation of M^{2+} to M^{3+} (M=Co, Fe) (**Figure V.9a**). The as-formed A-CoFeNi exhibited the lowest overpotential value of 270 mV at 100 mA cm^{-2} in 1 M KOH freshwater, which is lower than those of A-NiCo (370 mV) and RuO_2/Ni foam (390 mV) at 100 mA cm^{-2}. Additionally, the A-CoFeNi electrode recorded the smallest Tafel slope of 32.8 mV dec^{-1} compared to A-CoNi (55.9 mV dec^{-1}), RuO_2/Ni foam (88.7 mV dec^{-1}), and Ni foam (94.1 mV dec^{-1}), inferring the fast OER kinetics (**Figure V.9b**). In order to provide additional evidence for the enhanced OER activity of A-CoFeNi, we also assessed the electrochemically active surface area by measuring the double-layer capacitance (C_{dl}) obtained from **Figure V.10**. The A-CoFeNi material displayed the highest C_{dl} value of 2.52 mF cm^{-2}, as compared to 2.17 mF cm^{-2} for A-CoNi and 0.37 mF cm^{-2} for Ni foam, indicating larger electrochemically active surface area and more exposed active sites on its nanoflower sheets. Despite the incorporation of Fe elements did not obviously increase the number of active sites, it notably enhanced the efficiency of charge transfer, as shown in **Figure V.9c**. Electrochemical impedance spectroscopy (EIS) is an effective method to investigate the reaction kinetics of catalysts at the electrode/electrolyte interface [18, 19]. A-CoNi sample exhibited higher charge transfer resistance (R_{ct}~5.1Ω) even larger than that of RuO_2/Ni foam (R_{ct}~2.4Ω) at 1.5 V (*vs.* RHE), indicating poor electron transfer ability between catalyst surface and interface. After Fe incorporation, the A-CoFeNi achieved the smallest value (R_{ct}~0.8 Ω), indicating Fe ion promotes charge transfer and enhances OER kinetics (**Figure V.9c**).The above excellent electrochemical performance of A-CoFeNi could be ascribed to appealing 3D flower-like nanosheets supplying abundant accessible active sites, faster ion diffusion, and excellent electron transfer ability, which is more relevant to application in complex seawater conditions (**Figure V.9d**). A-CoFeNi exhibited an overpotential of 320 mV at a current density of 100 mA cm^{-2} in 1 M KOH seawater, as compared to 280 mV in 1 M KOH+0.5 M NaCl and 270 mV in KOH freshwater. The A-CoFeNi catalyst displayed decreased activity, owing to the presence of pollutants in natural seawater, such as bacteria, microorganisms, and tiny particles, all of which can cause electrode poisoning [20]. In addition, the precipitate deposition on the electrode surface might lead to covering active sites and affect the mass transfer and ion diffusion during the OER process. Notably, the overpotential is below 490 mV (chloride oxidation potential), which features development prospects for large-scale seawater electrolysis. Furthermore, the OER stability performance was assessed using long-term chronoamperometry tests (**Figure V.9e**). The results clearly evidenced the excellent stability for a duration of 105 h at a voltage of 1.5 V in 1 M KOH, 1 M KOH+0.5 M NaCl, or 1 M KOH seawater. **Figure V.9f** demonstrated that the CV curve after 1000 scans showed no obvious decrease. Interestingly, there was an obviously positive shift in the redox peak (1.38→1.45V) because the transition metal (Fe/Ni/Co) transformation into oxides/hydroxides during the CV cycle, which is beneficial for OER[21, 22]. The SEM image of A-CoFeNi after the CV scans revealed that the porous nanoflower structure of the electrode remained intact in the seawater alkaline condition (**Figure V.11**). Overall, the A-CoFeNi catalyst demonstrated enhanced OER performance in both alkaline simulated and real saltwater electrolytes. Nevertheless, the initiation potential of CER was almost 490 mV higher than OER, which may cause a competition at higher current densities. Therefore, it is imperative to explore a new strategy, such as EG oxidation reaction. EG, as an organic alcohol molecule, could be obtained from waste PET and could prevent the occurrence of CER due to the preferential thermodynamics in the electrolysis process [23, 24].

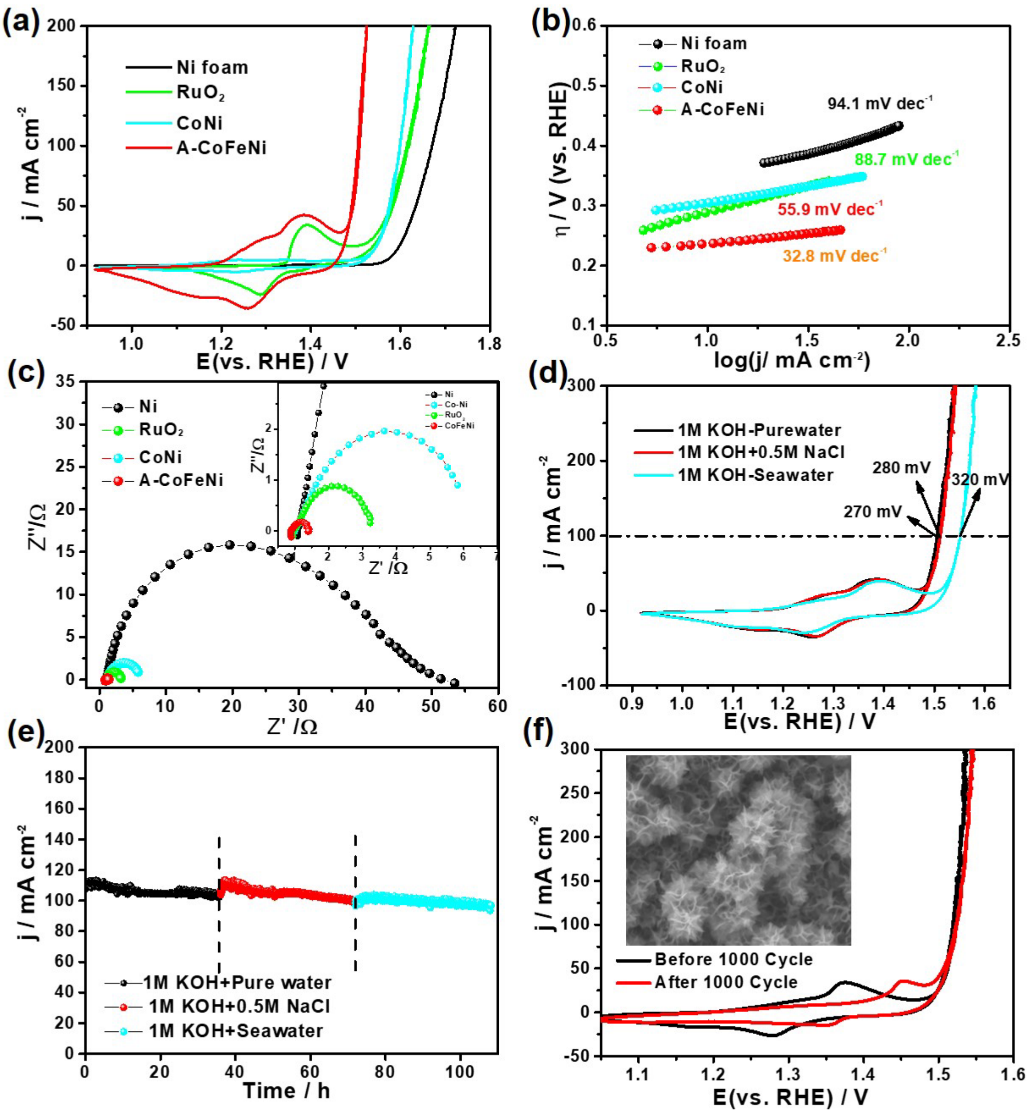

Figure V.9. A comparison of OER performance of the different catalysts in 1M KOH solution at a scan rate of 5 mV s^{-1}. (**a**) Polarization CV curves, (**b**) Tafel plots, (**c**) Nyquist plots at 1.5 V *vs.* RHE, (**d**) LSV polarization curves of A-CoFeNi sample in 1 M KOH, 1 M KOH+0.5 M NaCl, and 1 M KOH seawater electrolyte. (**e**) Durability tests at a constant potential for 105 h in different electrolytes; (**f**) LSV curves of A-CoFeNi before and after 1000 CV cycles in 1 M KOH seawater solution (insets: SEM image of the post-OER sample).

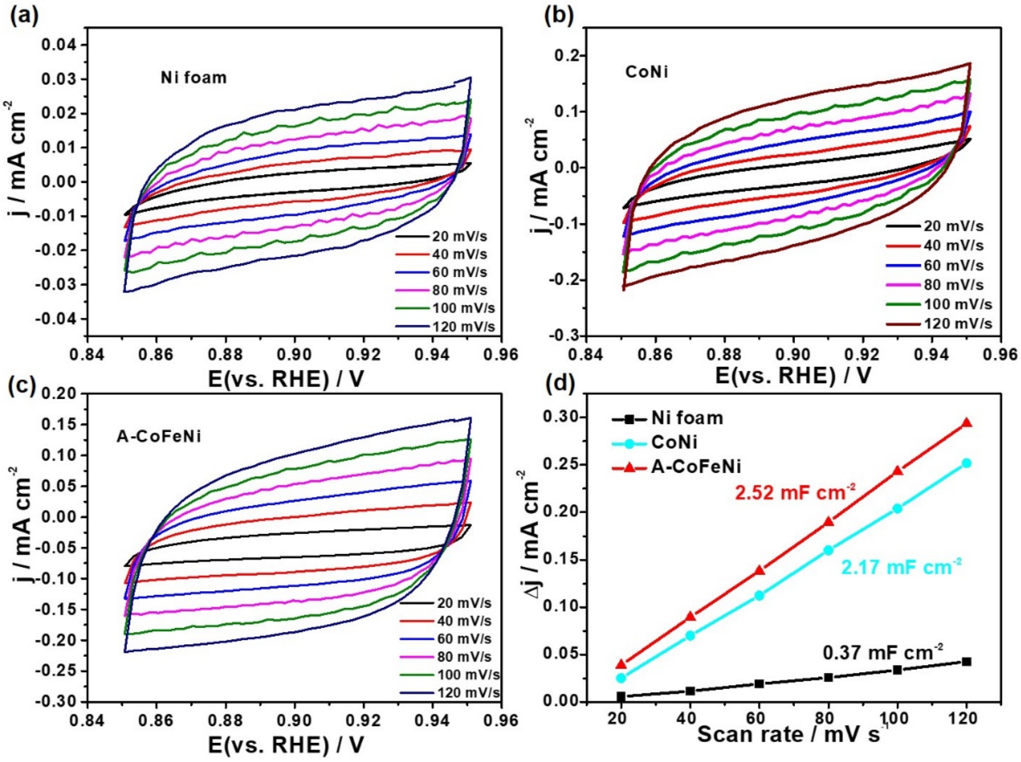

Figure V.10. CV curves in the potential range from 0.85 to 0.95 V at various scan rates in 1M KOH solution of (**a**) Ni foam, (**b**) CoNi and (**c**) A-CoFeNi. (**d**) Electrochemical double-layer capacitance as a function of scan rate.

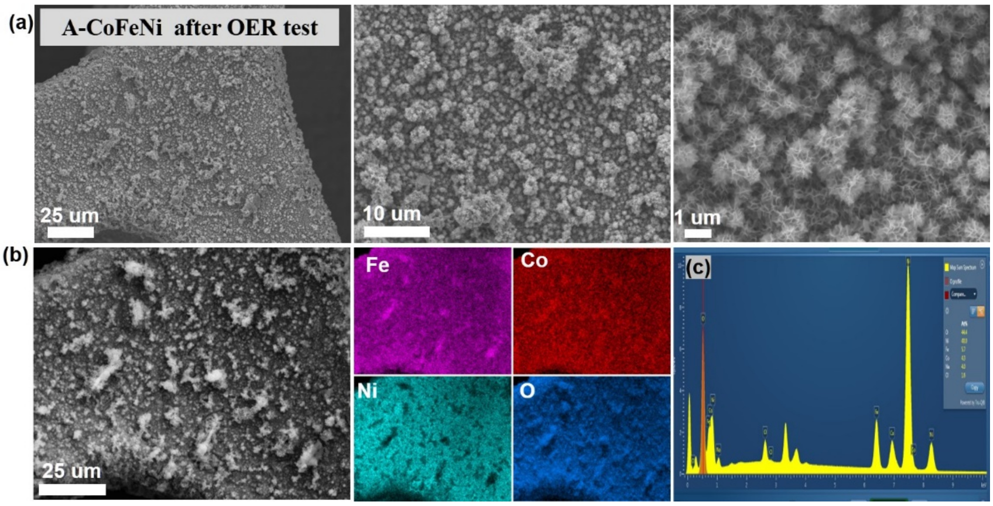

Figure V.11. (**a**) SEM images of A-CoFeNi sample at different magnifications after OER test, (**b**) the corresponding elemental mapping images of Fe, Co, Ni and O, (**c**) EDX spectrum and elemental composition.

V.3.4. Electrochemical EGOR Performance Evaluation

The electrochemical performance of A-CoFeNi was examined *via* a standard three-electrode configuration to assess its suitability for PET hydrolysate upcycling to high value products at the anode. Prior to the oxidation of PET hydrolysate, the OER and ethylene glycol oxidation reaction (EGOR) performances were initially tested to examine the electro-oxidation activity of EG, as shown in **Figure V.13**. The LSV results demonstrated that the A-NiCoFe catalyst featured excellent EGOR performance and achieved an overpotential of 1.38 V *vs.* RHE at 100 mA cm^{-2} in 1 M KOH+0.3 M EG freshwater and 1.39 V vs. RHE (100 mA cm^{-2}) in seawater condition (**Figure V.12)**. Furthermore, the open-circuit potential (OCP) was measured to discern changes in organic adsorbent content within the inner Helmholtz layer [25, 26]. Upon introducing 0.3 M EG, a significant decrease in the OCP for A-CoFeNi was observed (a decrease of $\Delta = 512$ mV), which exceeded the reduction observed for CoNi ($\Delta = 20$ mV), Ni foam ($\Delta = 150$ mV), and FeNi ($\Delta = 387$ mV) as depicted in **Figure V.13b**. This suggests a higher quantity of EG molecules being adsorbed within the inner Helmholtz layer, emphasizing the enhanced efficiency of EG adsorption on A-CoFeNi. The figure further illustrates that the inclusion of Fe resulted in a more rapid decline in OCP, indicating that the presence of Fe enhances the dynamic adsorption process of EG. Simultaneously, the *in-situ* EIS measurements were performed to explore the relationship between potential and interfacial reactions (**Figure V.13)**. The high-frequency region (10^1-10^5 Hz) corresponds to the internal oxidation of the electrode, a phenomenon observed within this frequency range. Conversely, the low-frequency region (10^{-2}-10^1 Hz) is linked to non-uniform charge distribution, specifically the presence of oxidized electrolyte at the electrode interface [27]. Firstly, the Bode phase plots provided additional evidence and clarification in various frequency ranges. A-NiCoFe consistently displayed a lower phase angle in the high-frequency range during the progress of OER or EGOR in the 1.0-1.5 V detection range. This suggests good electron conduction within the catalyst's inner layer. Noteworthy, the EGOR process exhibited a faster phase angle downtrend in the low frequency compared to OER processes, indicating charge transfer and kinetics are more efficient [28, 29]. To further explore the relationship between the internal and the interfacial reaction of the electrode, the EIS data were fitted with typical model shown in **Figure V.14-15,** which Nyquist plots recorded R_p and R_{ct}. R_p represents the resistance of electrode internal while R_{ct} reveals resistance of catalyst interfacial redox[25]. For A-CoNiFe, Rp initially decreases at the potential between 1.1~1.2 V *vs.* RHE, indicating the evolution of the catalyst structure. The significant decrease of R_{ct} at the potential between 1.2~1.3 V *vs.* RHE, indicates the beginning of EGOR reaction region (**Figure V.13g-f**). In addition, for the OER process, the Nyquist plot presents vertical lines and high R_{ct} values in the range of 1.0~1.4 V, indicating that there is no charge transfer on the catalyst surface and OER is difficult to occur. By increasing the applied voltage to 1.45 V, a semicircle with a practical value of R_{ct} appeared, demonstrating the initial OER potential after reaching 1.45 V *vs.* RHE. Comparatively, the EGOR process displayed a significant downtrend of R_{ct} between 1.2-1.3V *vs.* RHE, indicating its enhanced charge transfer rate even at lower potential conditions. A comparison the R_p and R_{ct} value with Ni foam, CoNi and FeNi catalysts, A-CoFeNi revealed a faster decrease trend at different potential conditiond, indicating a faster rate of internal oxidation and EGOR process. Above results both proved that A-CoFeNi possessed the best activity and higher adsorption capacity for OH^- and EG molecules, consequently facilitating EGOR even at lower potential conditions (**Figure V.13h**).

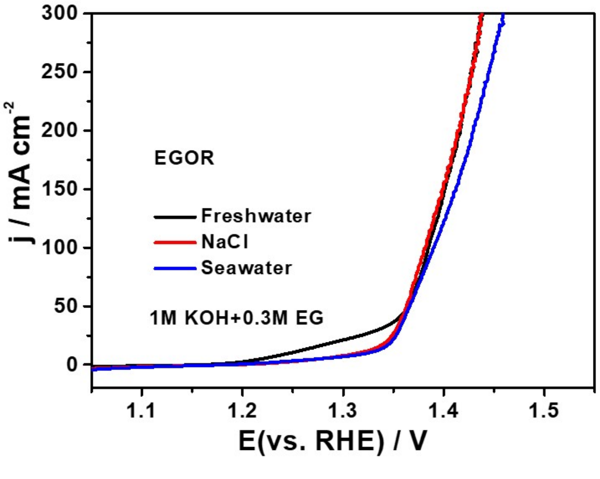

Figure V.12. LSV polarization curves of A-CoFeNi sample in different electrolytic solutions for catalyzing EGOR at a scan rate of 5 mV s^{-1}

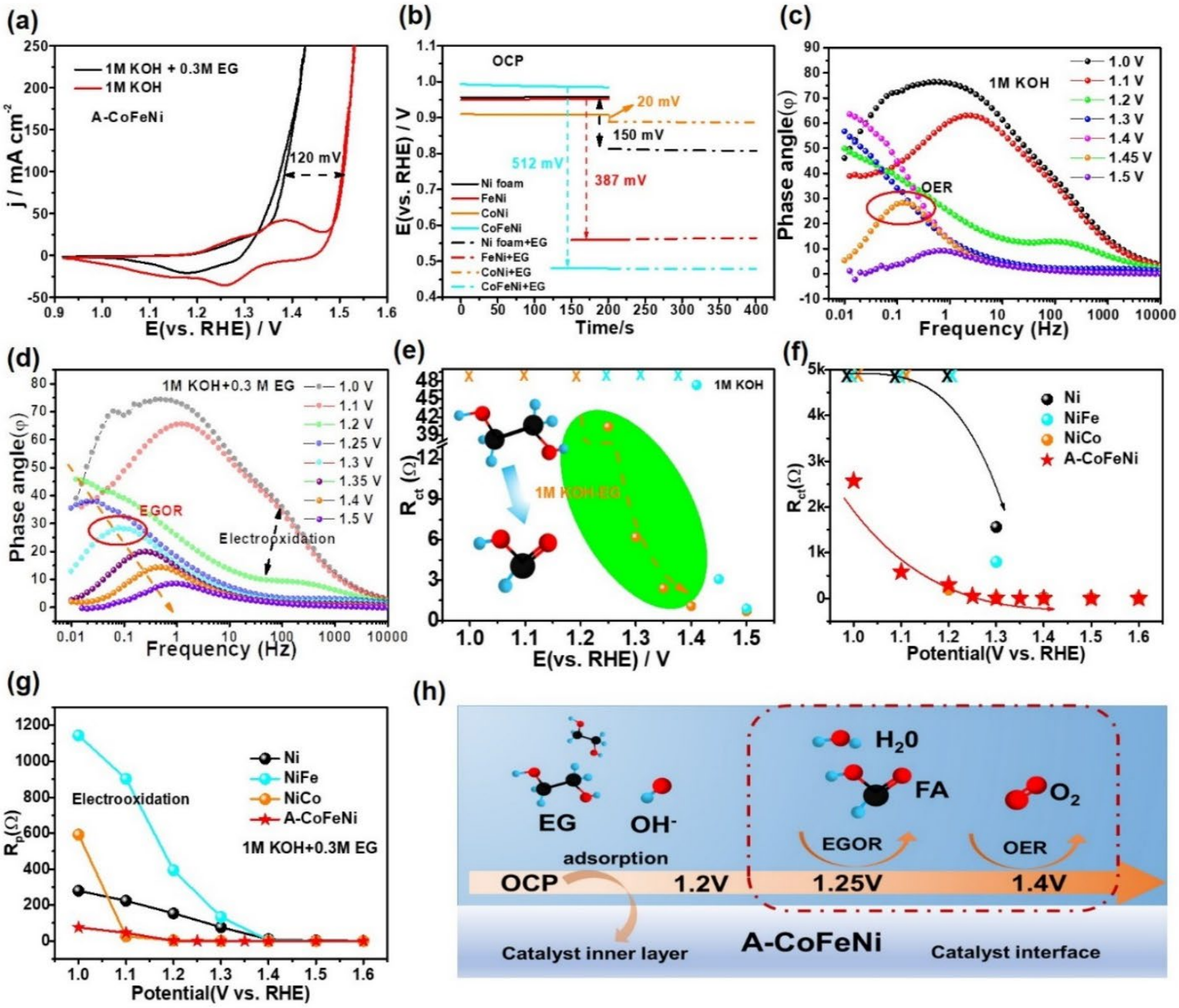

Figure V.13. EGOR performance mechanism insight. (**a**) CV curves in 1 M KOH with and without 0.3 M EG, (**b**) Open circuit potential (OCP) curves of Ni foam (black), FeNi (red), CoNi (orange) and A-CoFeNi (blue) in 1 M KOH and 1 M+0.3 M EG, (**c-d**) Bode and phase plots of A-CoFeNi sample at different potentials (*vs.* RHE), (**e**) the corresponding R_{ct} values of the different prepared samples at 1.0–1.5 V. (**f-g**) The comparison of charge transfer resistance (R_{ct}) and electrode inner oxidation resistance (R_p) of Ni foam, FeNi, CoNi and A-CoFeNi at different potentials in 1 M KOH + 0.3 M EG. (**h**) Schematic diagram of the EGOR process under different potential conditions. Schematic diagram of the EGOR process under different potential conditions.

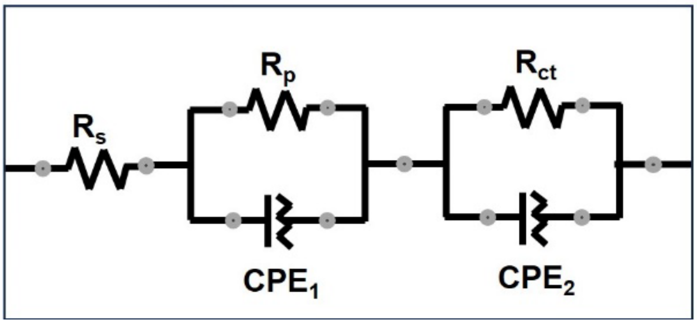

Figure V.14. Equivalent circuit simulation diagram.

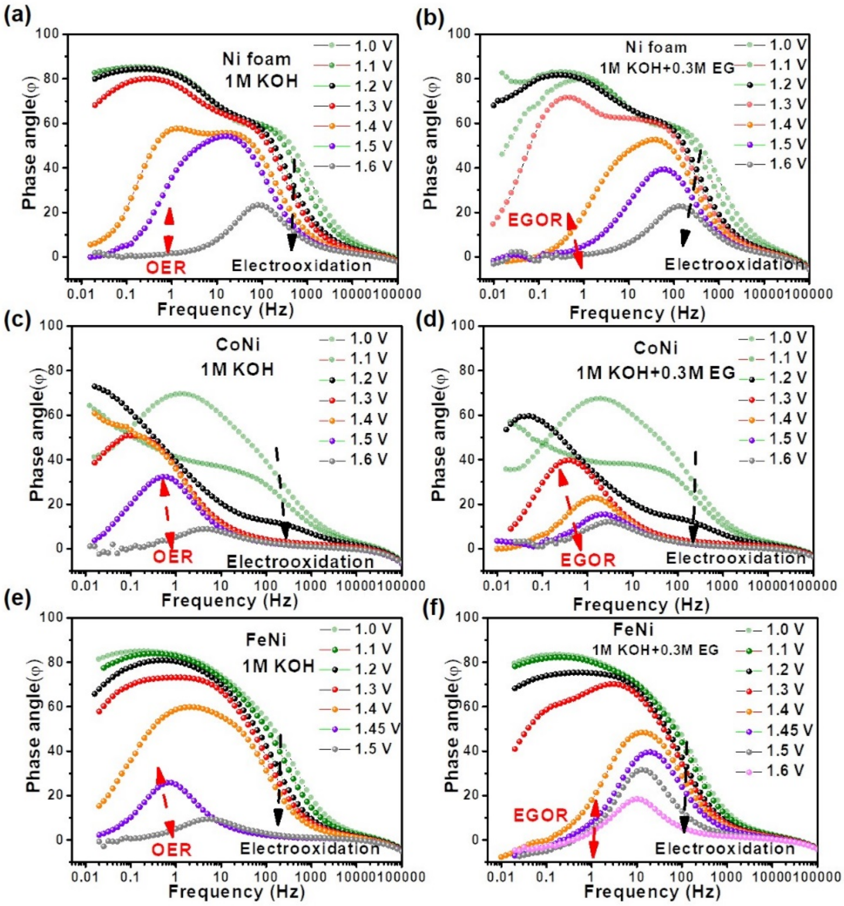

Figure V.15. Bode plots of (**a-b**) Ni foam, (**c-d**) CoNi and (**e-f**) FeNi sample in 1M KOH and 1M KOH+0.3M EG recorded at different potentials *vs.* RHE.

Subsequently, ^{1}H and ^{13}C NMR spectra were employed to qualitatively and quantitatively examine the EG electro-reformed products. **Figure V.16a** describes the ^{1}H NMR spectra of EGOR before and post performed by chronoamperometry at an applied potential of 1.5 V for 12 h. As expected, the peak of EG (~3.5 ppm) gradually decreased while the peak of formate at 8.35 ppm increased, proving the successful transformation of EG to formate. As shown in

Figure V.16b, A-CoFeNi both possessed a high faradaic efficiency to produce formate under a varied potential from 1.4 to 1.9 V, and displayed the highest FE of 94.8% with a productivity of 2.37 mmol cm^{-2} h^{-1} at 1.6 V. More importantly, A-CoFeNi also displayed good FE performance (83.1~92.6%) to produce formate even in seawater (**Figure V.17**). Formate productivity showed a linear growth trend (from 0.63 to 5.21 mmol cm^{-2} h^{-1}) with increasing applied potential in both seawater and freshwater (**Figure V.16c**).

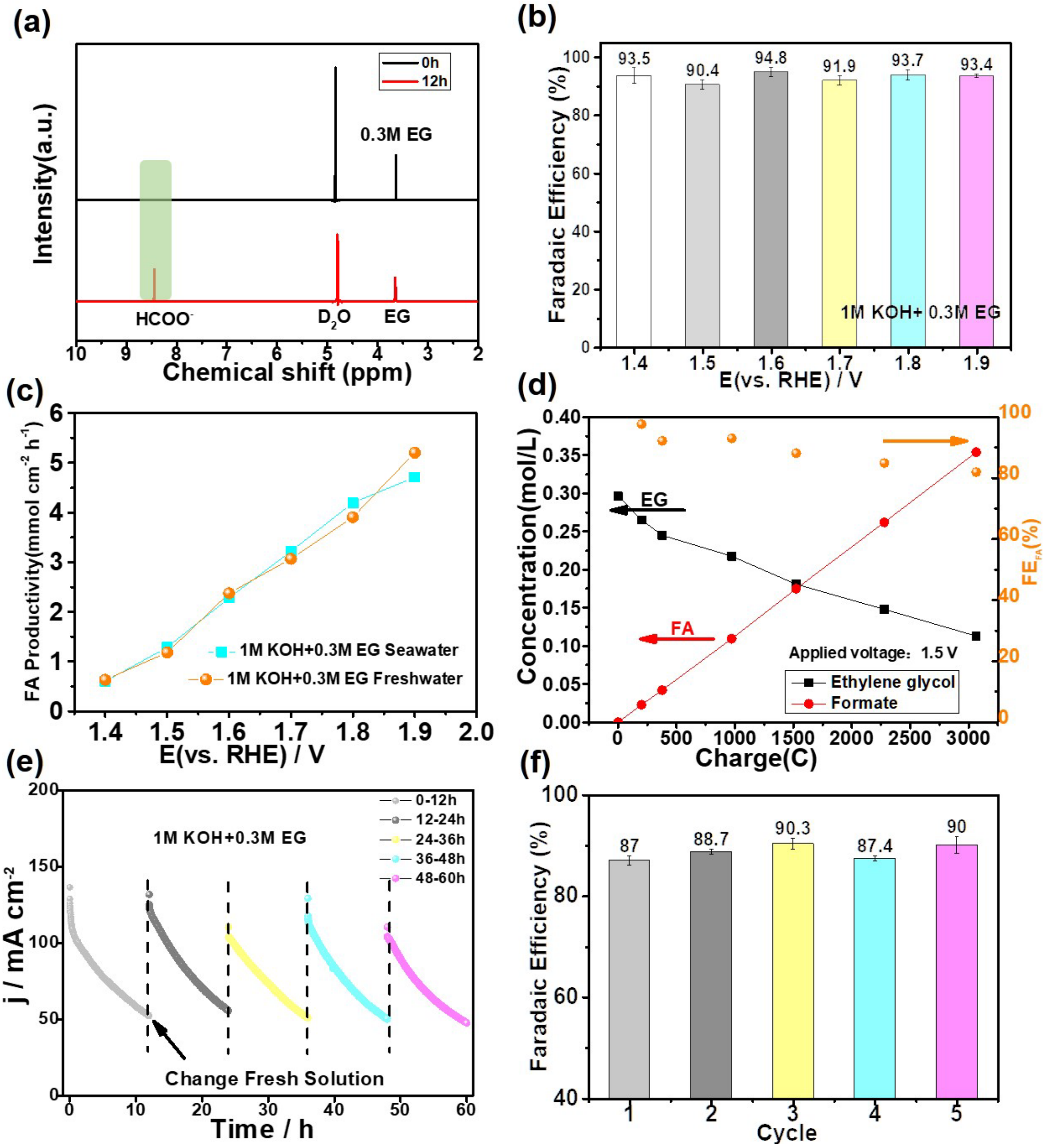

Figure V.16. EGOR performance in 1 M KOH with and without 0.3 M EG. (**a**) ^{1}H NMR spectra of products before and after electrolysis, (**b**) Faradaic efficiency of A-CoFeNi for formate production at various voltages, (**c**) Formate productivity of A-CoFeNi at various potentials in seawater and freshwater, (**d**) the concentrations of reactants EG and FA, and FE during electrolysis at different charges at 1.5 V *vs.* RHE. (**e**) Durability test at a constant potential for 12 h-5 cycles, (**e**) Faradaic efficiency after EGOR durability test for 5 cycles.

Furthermore, stability is a vital factor in assessing the electrochemical performance of catalysts. ^{1}H NMR analysis was conducted to assess the formate formation at different time intervals; the results revealed a consistent increase of the formate concentration throughout enhancing charge (**Figure V.16d**). In addition, the chronoamperometry (*I-t*) curve was employed for a 12-h duration test in a solution containing 1 M KOH+0.3 M EG, whose current intensity revealed a consistently decreasing trend owing to the consumption of EG (**Figure V.16e** and **Figure V.18**). A-CoFeNi could recover its original current density after exchanging fresh solution six times in 1 M KOH+0.3 M EG freshwater or seawater, exhibiting long-term electrochemical stability. In addition, the FE of formate varied only slightly from 97.0 to 90.3% following six consecutive cycles, as shown in **Figure V.16f**. Furthermore, SEM imaging performed (**Figure V.19**) after the stability test clearly showed that the nanoflower-like structure of the A-CoFeNi catalyst was highly stable and well-preserved, which facilitates the efficient release and transfer of mass products. As shown in **Table 3** and **Figure V.20**, XPS analysis recorded the element variation in 1 M KOH+0.3 M EG freshwater and seawater such as Co (11.36→8.96→ 4.90 at. %), Fe (3.50→2.65→3.29 at. %), Ni (20.40→16.38→20.00 at. %). The Co elements content had a continuous noticeable decrease, indirectly proving that cobalt was crucial in the EG oxidation reaction. The XRD pattern analysis conducted after the long-term reaction revealed no significant variation in the crystal structure of the catalyst, as depicted in **Figure V.21**. Therefore, the effective active species of the A-CoFeNi catalyst in the OER process is the collaboration between Ni and Fe elements, whereas it is attributed to the cooperation between Co/Ni and Fe in the EGOR process, enhancing electron transfer upon Fe addition. The aforementioned electrochemical studies confirmed that the A-CoFeNi catalyst exhibited good activity and stability for OER/EGOR in both freshwater and seawater electrolytes. The excellent performance could be ascribed to the following factors: (1) The porous nanoflower layer construction not only provided a large surface area and a high density of active sites for the catalytic reaction, but also achieved the hydrophilic transformation from Ni foam (CA=103°) to A-CoFeNi (CA=0°), as shown in **Figure V.22**, promoting the effective diffusion of electrolyte and the rapid release of gas bubbles. (2) The amorphous A-CoFeNi material possessed large defect sites and oxygen vacancies, facilitating the catalytic process. (3) Seawater directly etches the commercial Ni foam into an amorphous A-CoFeNi layer, ensuring strong adhesion between the active material and the substrate, reducing contact resistance and improving mechanical stability.

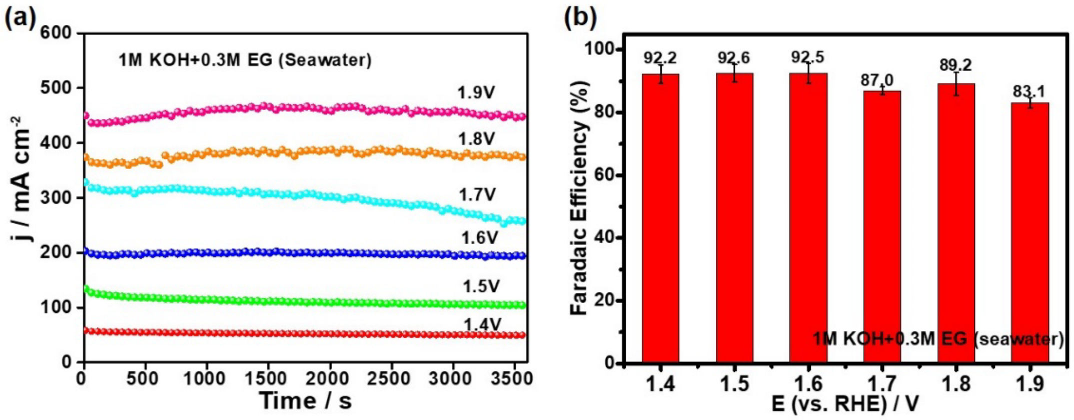

Figure V.17. (a) Multistep chronoamperometric curves at various applied overpotentials in 1M KOH+0.3M EG (seawater). **(b)** Faradaic efficiencies of formate production at various potentials.

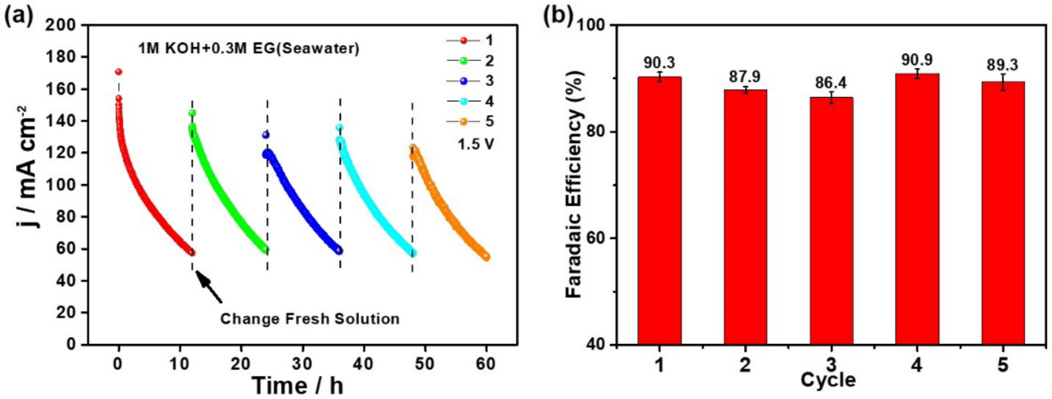

Figure V.18. (a) Multi-cycle chronoamperometric curves at a constant potential of 1.5 V in 1M KOH+0.3M EG (seawater). **(b)** Faradaic efficiencies of formate production for consecutive 5 cycles.

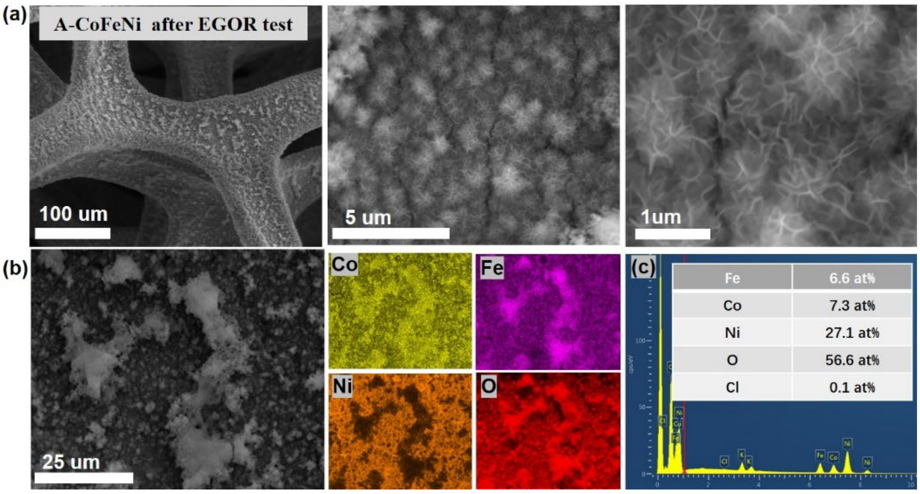

Fe	6.6 at%
Co	7.3 at%
Ni	27.1 at%
O	56.6 at%
Cl	0.1 at%

Figure V.19. (**a**) SEM images of A-CoFeNi sample at different magnifications after EGOR test, (**b**) the corresponding elemental mapping images of Co, Fe, Ni and O. (**c**) EDX spectrum and elemental composition.

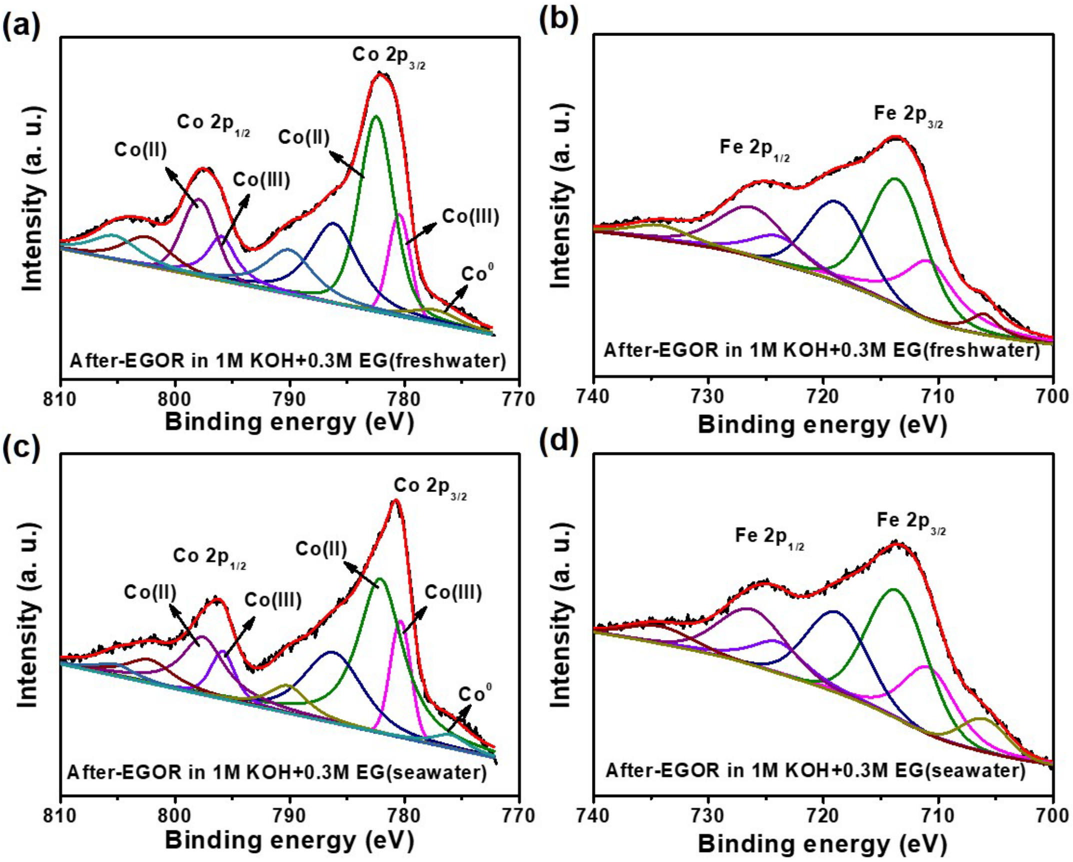

Figure V.20. (**a-b**) Co 2p, (**c-d**) Fe 2p XPS high-resolution spectra of A-CoFeNi after 1000 CV cycles EGOR in freshwater and seawater, respectively.

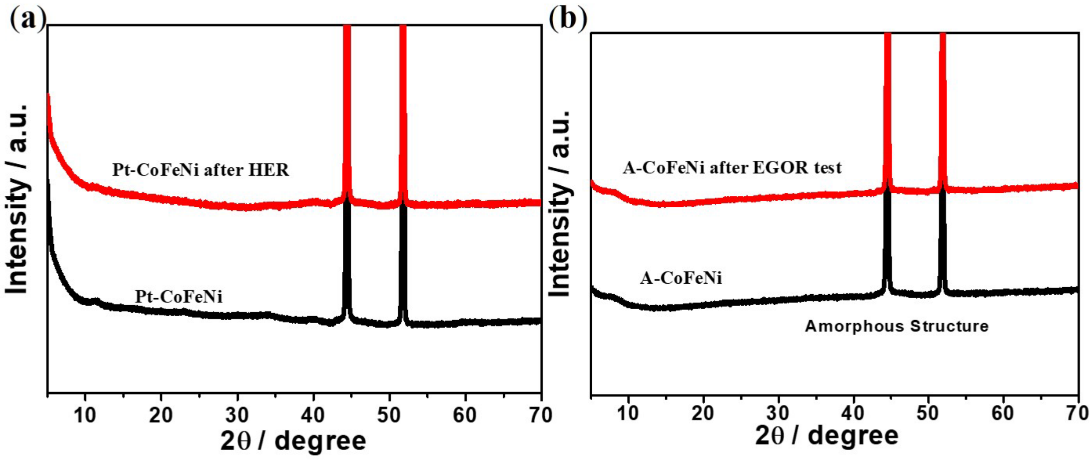

Figure V.21. XRD patterns of **(a)** Pt-CoFeNi and **(b)** A-CoFeNi before and after HER/EGOR 1000 CV cycles.

No	Sample	Co (at.%)	Fe (at.%)	Ni (at.%)	O (at.%)	C (at.%)	Cl (at.%)
1	A-CoFeNi	11.36	3.50	20.4	44.46	17.75	2.52
2	After EOR freshwater	8.96	2.65	16.38	49.38	22.23	0.41
3	After EOR seawater	4.90	3.29	20.00	46.44	23.20	1.05

Table 3. XPS analysis of Co, Fe, Ni, O and Cl elements before and after EGOR stability tests.

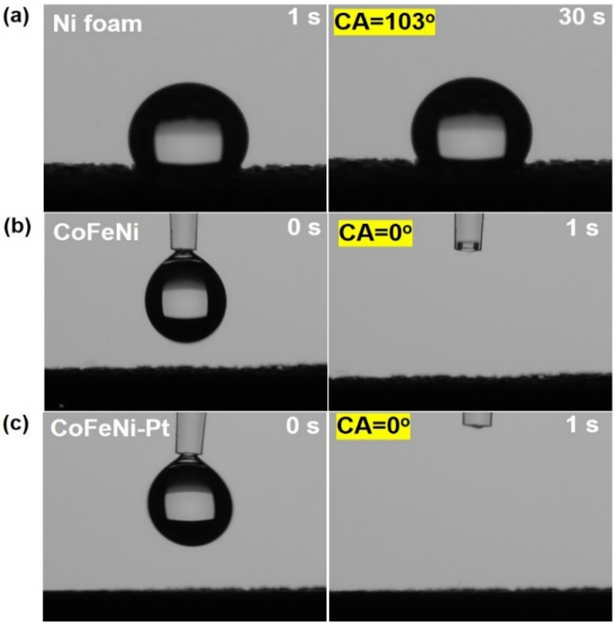

Figure V.22. Contact angle (CA) measurements of (**a**) Ni foam, (**b**) A-CoFeNi and (**c**) CoFeNi-Pt using 10 μL water droplet.

V.3.5. Overall Seawater-EG Splitting Performance

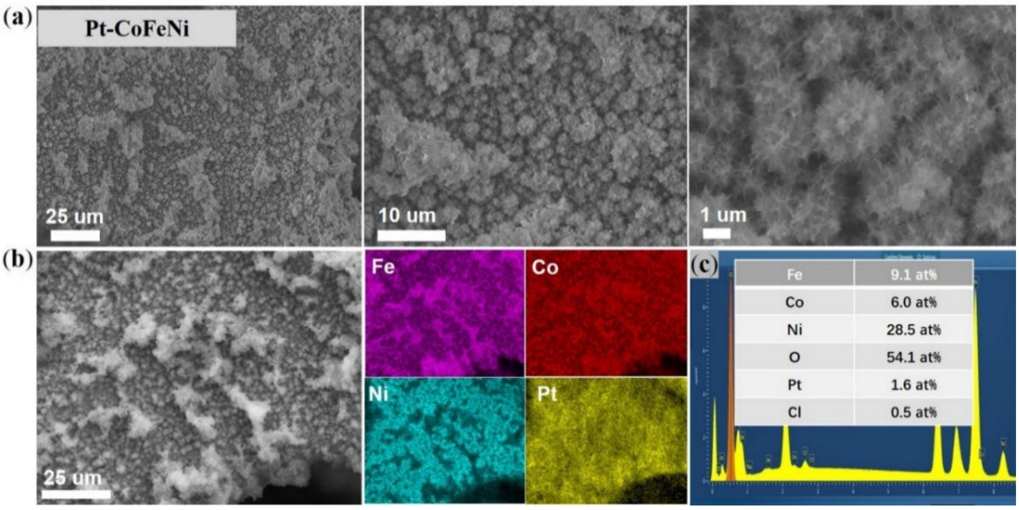

Figure V.23. (**a**) SEM images at different magnifications, (**b**) the corresponding elemental mapping images of Fe, Co, Ni and Pt, (**c**) EDX spectrum and elemental composition of Pt-CoFeNi sample.

Considering the good EGOR performance of A-CoFeNi, a further test was applied to demonstrate the energy-saving hydrogen production by overall seawater-EG splitting. Firstly, the catalytic HER performance of A-CoFeNi was assessed, and the LSV analysis demonstrated unsatisfactory activity with η_{10} = 220 mV, which is much higher than commercial Pt/C catalyst with η_{10} = 49 mV and η_{100} = 139.8 mV. The Co-Fe-Ni system without precious metal loading, it has good OER/EGOR performance at the anode region, but its HER performance is poor due to its intrinsic metal-H bonding energy and electronic structure. Therefore, we choose an ultra-low noble metal loading strategy to improve the HER performance. Co/Fe/Ni trimetallic samples were prepared by NaCl corrosion method, and try to loading different type precious metal (such as Pt, Au, Ru, Rh and Pd et). More importantly, the Pt-Co/Fe/Ni catalyst showed good electronic structure and durability after tests. Therefore, we prepared a Pt-CoFeNi catalyst using trace amounts of Pt loading strategy. SEM and EDX spectra featured similar 3D porous nanoflower layer morphology and uniform dispersion of Fe (9.1 %), Co (6.0 %), Ni (28.5 %), O (54.1 %) and Pt (1.6 %) (**Figure V.23**). As expected, Pt-CoFeNi showed excellent HER activity with η_{10} = 49 mV and η_{100} = 91.1 mV, outperforming state-of-the-art and commercial catalysts (**Figure V.24**). Additionally, the Pt-CoFeNi electrode exhibited a small Tafel slope of

44.7 mV dec^{-1} compared to Ni foam (154.2 mV dec^{-1}), Pt/C-Ni foam (53.7 mV dec^{-1}), and A-CoFeNi (106.4 mV dec^{-1}), suggesting its favorable HER kinetics. As shown in **Figure V.24 d-f**, the electrocatalytic experiments were further conducted in two electrolytes: 1 M KOH+0.5 M NaCl (simulated seawater) and 1 M KOH natural seawater(collected from Calais seawater, France). The results revealed that the measured overpotential was 122.1 mV (100 mA cm^{-2}) in 1 M KOH seawater and 105.3 mV in 1 M KOH+0.5 M NaCl, indicating its potential for large-scale seawater decomposition. Significantly, the electrochemical activity of Pt-CoFeNi showed no discernible decrease in performance over 1000 CV cycles or 45 h of chronopotentiometry operation. Furthermore, the SEM imaging (**Figure V.25**) demonstrated that the 3D flower-shaped nanosheet morphology of Pt-CoFeNi remained intact after the durability test, indicating its structural stability even at high current density or under corrosive seawater conditions.

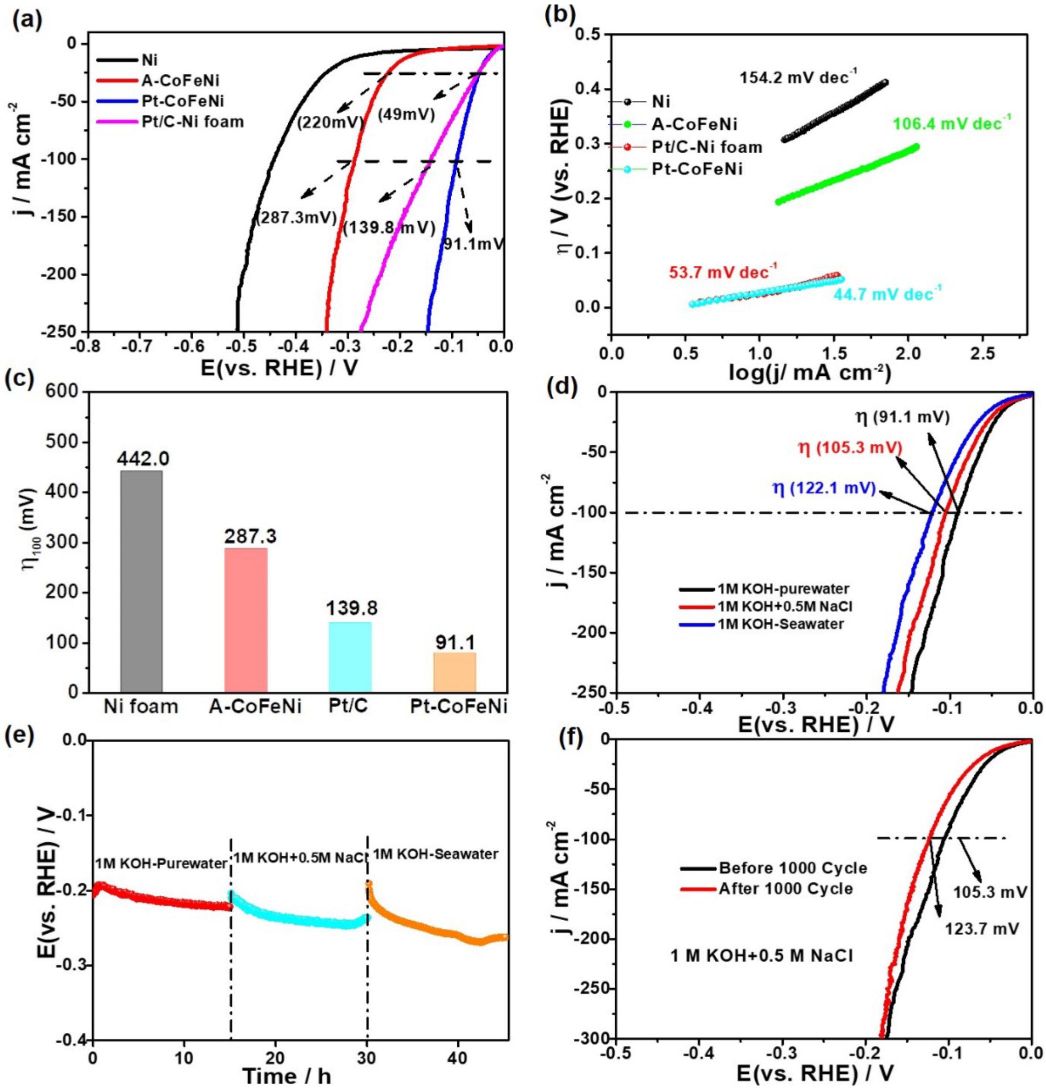

Figure V.24. The electrochemical HER behavior of Ni foam, Pt/C-NF, A-CoFeNi and Pt-CoFeNi in 1M KOH aqueous solution. (**a**) LSV polarization curves, (**b**) The corresponding Tafel plots, (**c**) Graphic of overpotential comparison acquired at 100 mA cm^{-2}, (**d**) Comparison of Pt-CoFeNi polarization curves in 1M KOH, 1M KOH+0.5M NaCl, and 1M KOH seawater solution, (**e**) Durability tests at a constant potential for 15 h in different electrolytes; (**f**) LSV curves of Pt-CoFeNi before (black) and after (red) 1000 CV cycles in 1M KOH+0.5M NaCl solution.

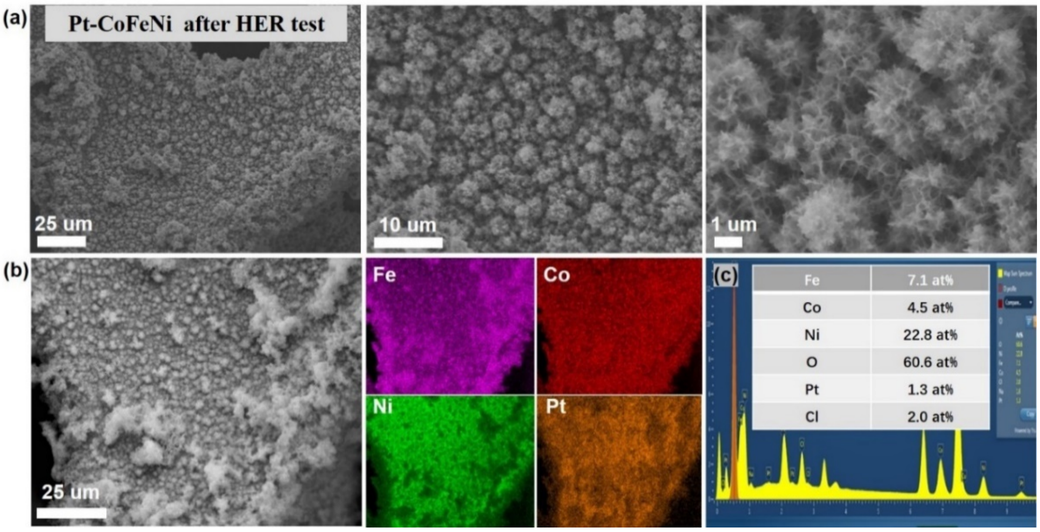

Fe	7.1 at%
Co	4.5 at%
Ni	22.8 at%
O	60.6 at%
Pt	1.3 at%
Cl	2.0 at%

Figure V.25. (**a**) SEM images of Pt-CoFeNi sample at different magnifications after HER test, (**b**) the corresponding elemental mapping images Fe, Co, Ni and Pt, (**c**) EDX spectrum and elemental composition.

Remarkably, we set up a two-electrode electrolyzer for overall seawater splitting assisted with EG in different simulated and natural seawater electrolytes (**Figure V.26a**), in which the A-CoFeNi electrode (anode) was coupled with HER catalyst (Pt-CoFeNi, cathode). Firstly, the A-CoFeNi//Pt-CoFeNi recorded a low voltage of 1.52 V at 100 mA cm^{-2} in 1 M KOH + 0.3 M EG, which is even lower than that for the coupled benchmark RuO_2@Pt/C (1.71 V). Besides, a potential difference of 110 mV at 100 mA cm^{-2} in 1 M KOH with and without 0.3 M EG was acquired. The activity slightly decreased in the alkaline natural seawater electrolyte (1 M KOH + 0.3 M EG seawater). However, it was still effective (**Figure V.26b**) and achieved 1.38 and 1.56 V at current densities of 10 and 100 mA cm^{-2}, respectively, suggesting that the EG molecule played a positive role and enhanced the efficiency of H_2 generation in natural seawater. As shown in **Figure V.26c-d**, we applied the chronoamperometry (*I-t*) durability test at 1.8 V without IR compensation; the catalyst maintained a high current density for six consecutive cycles and disclosed an interesting phenomenon. Along with the EGOR reaction, the concentration of EG molecules gradually diminished, while the concentration of FA increased, leading to a steady decrease in current density. This is a normal phenomenon in which FA was continuously generated to cover the catalyst active sites, and the OER reaction will compete with the EGOR reaction as the EG concentration dramatically decreases, resulting in a decrease in current density. After changing the fresh 1 M KOH+0.3 M EG seawater solution, the current density was recovered and almost approached the original value. Moreover, the value-added formate production with higher FE could be continuously achieved from 90.2-80.3%, indicating the catalyst's excellent durability. As illustrated in **Figure V.26e, g**, Faradaic efficiency for hydrogen generation was determined in a solution containing 1 M KOH +0.3 M EG by comparing the experimentally collected amount of gas with the theoretically calculated volume of gas [22]. The V_{H2} value obtained was in full agreement with the theoretically-calculated values, suggesting that the electrolysis process produced H_2 with nearly 100% Faradaic efficiency for overall seawater-EG splitting process. By comparing the electricity cost in seawater electrolyzers, it is evident that the utilization of A-CoFeNi//Pt-CoFeNi as electrocatalyst resulted in lower expense of 3.75 kWh m^{-2} H_2 at 100 mA cm^{-2}. This demonstrates superior energy efficiency for hydrogen production when compared to numerous recently published works (**Figure V.26f** and **Table 4**). In addition, no hypochlorite was formed during the seawater electrocatalytic process (**Figure V.27**), which infers considerable advantages in energy-saving hydrogen production. Furthermore, the A-CoFeNi//Pt-CoFeNi, powered by solar panels, offered an exciting approach for overall seawater-EG splitting. This process utilized abundant natural seawater and waste PET hydrolysate as an electrolyte and solar energy as a source of electricity generation, which could produce H_2 and achieve waste plastic upcycling, enabling efficient conversion of solar energy, electricity and hydrogen energy.

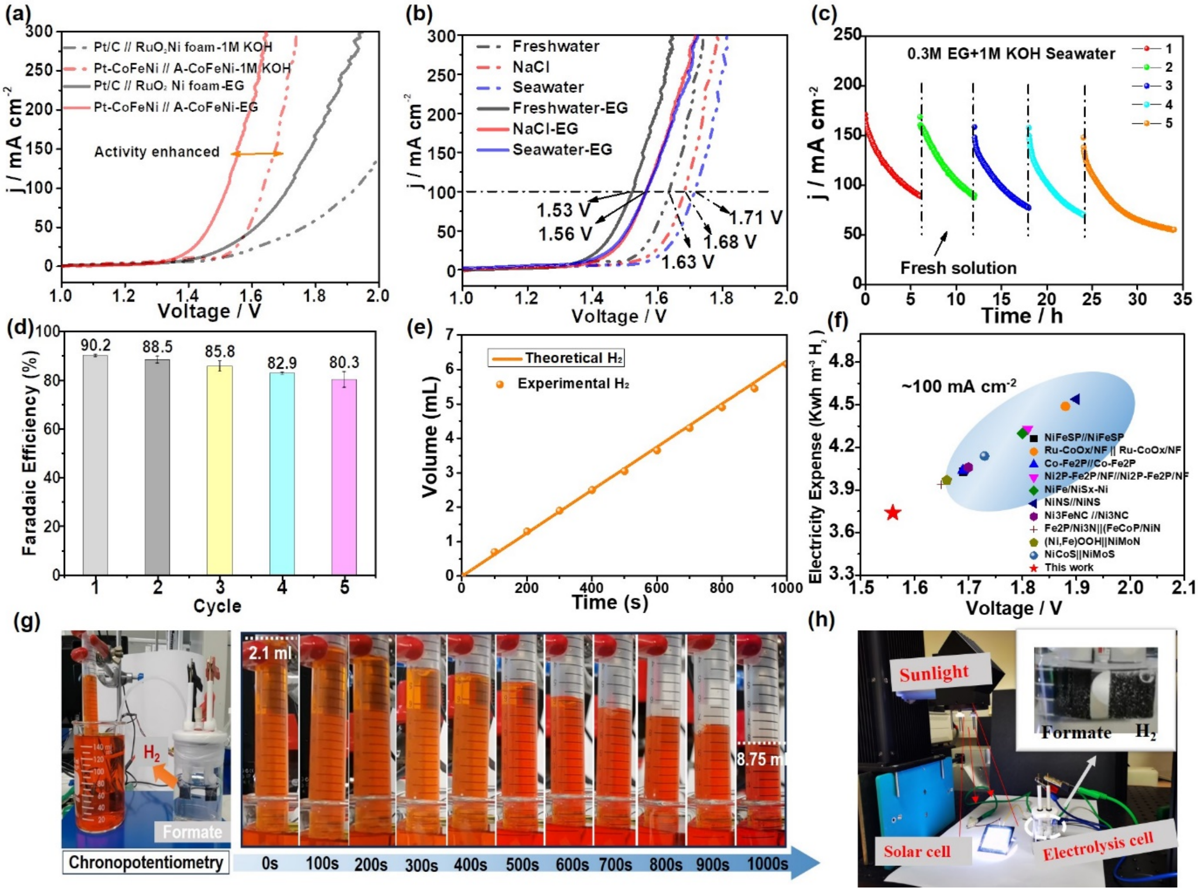

Figure V.26. Overall seawater splitting and EG oxidation of A-CoFeNi//Pt-CoFeNi. (**a**) The comparison of the polarization curves with or without 0.3 M EG. (**b**) the LSV polarization curves in 1 M KOH freshwater, 0.5 M NaCl and seawater. (**c-d**) Faradaic efficiencies to produce formate *via* consecutive six cycles at 1.8 V without IR compensation. (**e**) The volume of the H_2 gas determined experimentally and theoretically. **(f)** Comparison of potential and electricity expense at 100 mA cm^{-2} between this work and other published works. (**g**) Photo of the cell for the determination of the Faradaic efficiency of the device and gas collected at different times. (**h**) Digital photograph of the solar-to-hydrogen energy conversion system through a commercial solar cell (2 V) and this work catalyst device in 1 M KOH+0.3 M EG seawater.

Table 4. Comparison of the two-electrode system potential and basic electricity expense of the developed catalyst and reported catalysts at 100 mA cm^{-2}.

Catalyst	Electrolyte	Current density (mA cm^{-2})	Cell Voltage (V)	BEE (kWh m^{-3} H_2)	Reference
NiFeSP//NiFeSP	1.0 m KOH + 0.5 M NaCl + 0.5 M urea	100	1.69	4.03	[30]
Ru-CoO_x/NF || Ru-CoO_x/NF	1M KOH	100	1.59	3.80	[22]
	1M KOH seawater	100	1.88	4.49	
Co-Fe_2P//Co-Fe_2P	1M KOH seawater	100	1.69	4.04	[31]
Ni2P-Fe_2P/NF//Ni_2P-Fe_2P/NF	1M KOH	100	1.68	4.02	[32]
	1M KOH seawater	100	1.81	4.33	
NiFe/NiS_x-Ni	1M KOH seawater	100	1.8	4.30	[33]
NiNS//NiNS	1M KOH	100	1.9	4.54	[34]
FeNiMoN//FeMoNiO	1M KOH seawater	100	1.58	3.78	[35]
Ni_3FeNC //Ni_3NC	1M KOH seawater	100	1.70	4.06	[36]
Fe_2P/Ni_3N||(FeCoP/NiN	1M KOH seawater	100	1.65	3.94	[37]
(Ni,Fe)OOH||NiMoN	1M KOH seawater	100	1.66	3.97	[20]
NiCoS(+)||NiMoS(−)	1M KOH seawater	100	1.73	4.14	[38]
A-CoFeNi//Pt-CoFeNi	1M KOH+0.3M EG	100	1.52	3.63	**This work**
	1M KOH +0.3M EG seawater	100	1.56	3.74	

BEE: Basic electricity expense

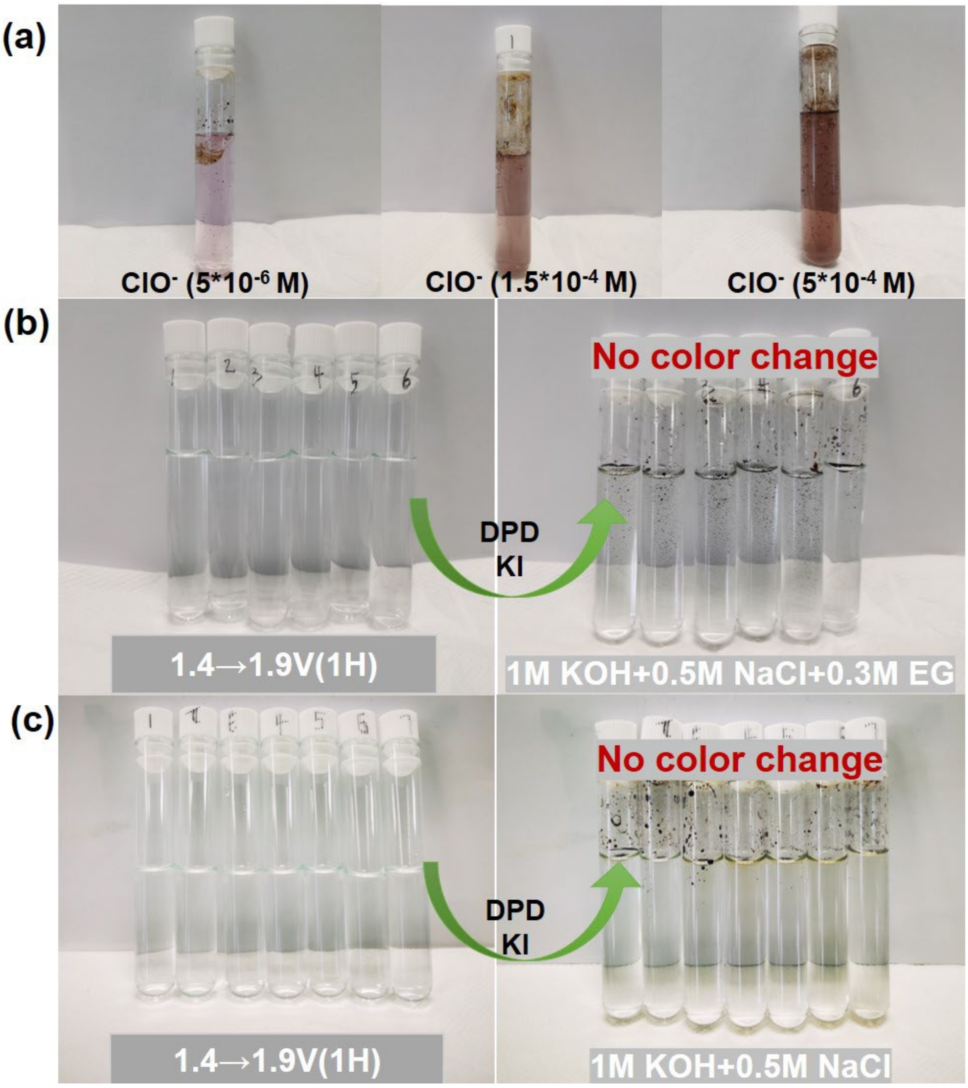

Figure V.27. Testing results for ClO^- formation in (**a**) standard ClO^- solution, (**b**) 1 M KOH seawater electrolytes and (**c**) 1 M KOH+0.3M EG seawater electrolytes after the corresponding OER and EGOR stability tests.

NOTE: Under alkaline conditions, the thermodynamically favorable EGOR could effectively avoid the anodic chlorine evolution reaction (ClER). To further verify whether hypochlorite is formed during overall seawater-EG splitting electrocatalysis, we performed a 1-h chronoamperometry measurement. Following the stability tests, the seawater electrolyte used was subsequently examined using *N, N*-diethyl-p-phenylenediamine (DPD) and KI reagent to determine whether any hypochlorite was formed. There was no color change in the reagent, indicating that no hypochlorite was formed during overall seawater-EG splitting.

V.3.6. Real Plastic Electro-Upcycling Process

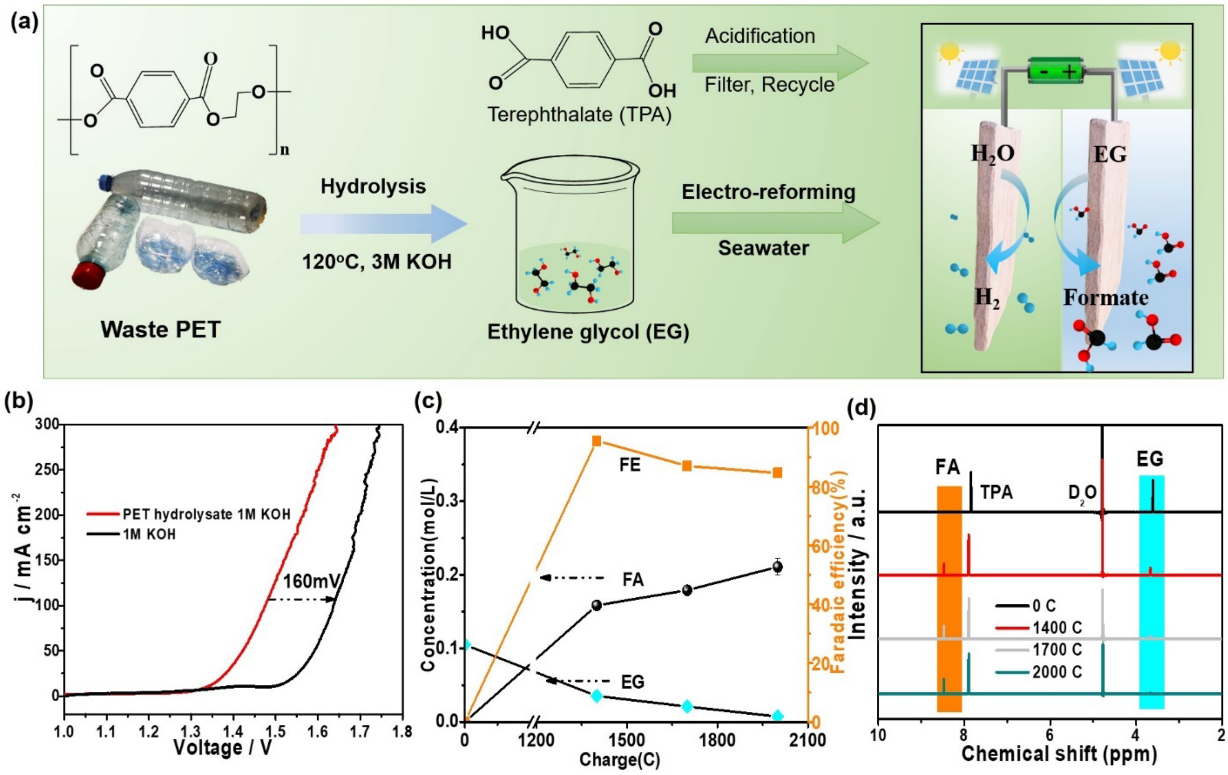

Figure V.28. (a) Schematic illustration of the PET electro-reforming process. **(b)** LSV curves of the PET hydrolysate and water electrolysis. (**c**) Comparison of anode product concentration and FE for PET hydrolysate at different charges, and (**d**) the corresponding ^{1}H NMR spectra.

A typical schematic illustration of PET upcycling is depicted in **Figure V.28a**. Firstly, the waste PET plastic bottle was hydrolyzed under alkaline conditions (3 M KOH) to generate EG and terephthalic acid (PTA) molecules. Secondly, the collected hydrolysate was separated by acidification and filtration to obtain the desired PTA product. On the other hand, the small EG molecules were further electro-reformed into a more valuable product by two key steps. The first process of catalytic oxidation of EG to glycolaldehyde occurs, which is cleaved through a rapid C-C oxidation to produce formate. In addition, a small portion of glycolaldehyde is oxidized to glycolic acid and then undergoes a delayed C-C cleavage process to produce formate [39, 40]. The A-CoFeNi // Pt-CoFeNi exhibited the lower voltage 1.48V at 100 mA cm^{-2} in 1 M KOH PET hydrolysate, lower by 160 mV in 1 M KOH seawater. The catalyst displayed good activity even in low-concentration PET hydrolysate solution, owing to its large surface area and good electronic transfer ability. The chronopotentiometry and ^{1}H NMR test was employed to detect electro-reforming ability in low-concentration PET hydrolysate solution (**Figure V.28c-d**). As expected, the catalyst recorded higher FE (95.6%) at 1400 C, while it depicted a decreasing trend of FE to 87.0% and 84.6% at respectively 1700 C and 2000 C, owing to competition with OER at the ultralow EG concentration (5 or 20 mM). In the meantime, the formate yield gradually increased from 76.1% (1400 C),83.8% (1700 C) to 95.6% (2000 C). Overall, the A-CoFeNi // Pt-CoFeNi catalyst was prepared via a low-cost and easy scale-up seawater corrosion process, implying a promising application perspective. Furthermore, utilizing waste plastic hydrolysate as an anolyte and cost-free saltwater as an elecrolyte could efficiently achieve waste utilization and decrease the expenses associated with hydrogen generation.

V.4 Conclusion

In summary, this work offers a cost-effective and industrially compatible seawater corrosion engineering to turn commercial Ni foam into robust OER/EGOR catalysts for high-performance seawater electrolysis and PET electro-upcycling. Benefiting from the advantages of a large surface area with abundant active sites and oxygen defects, a hydrophilic feature for electrolyte diffusion, and good charge-transfer ability, the synthesized A-CoFeNi catalyst displayed overpotential values as low as 1.55 and 1.39 V to deliver 100 mA cm^{-2} for OER and EGOR in alkaline natural seawater electrolyte, respectively. Furthermore, benefiting from modulated electronic configurations and optimized nanoflower shape morphology, A-CoFeNi//Pt-CoFeNi required a cell voltage of 1.56 V at 100 mA cm^{-2} to drive the coupled two-electrode system, which is 150 mV lower than that of the seawater splitting and is superior to commercial catalysts, e.g., Pt/C and RuO_2, testifying that EG plays a key role in decreasing overpotential and energy consumption. Simultaneously, the electrolyzer also recorded high FE for the generation of H_2 (almost 100%) and high value-added formate (95.6%). The present work explores a coordinative strategy for green hydrogen production, PET waste plastic upcycling and cost-free seawater utilization by the design and construction of cost-effective and high-efficient electrocatalysts, achieving efficient conversion of solar energy, electricity and hydrogen energy.

References

[1] S. Hao, L. Chen, C. Yu, B. Yang, Z. Li, Y. Hou, L. Lei, X. Zhang, NiCoMo Hydroxide Nanosheet Arrays Synthesized via Chloride Corrosion for Overall Water Splitting, ACS Energy Lett. 4(4) (2019) 952-959. https://doi.org/10.1021/acsenergylett.9b00333.

[2] Y. Wang, W. Yu, B. Zhou, W. Xiao, J. Wang, X. Wang, G. Xu, B. Li, Z. Li, Z. Wu, L. Wang, Corrosive engineering assisted in situ construction of an Fe–Ni-based compound for industrial overall water-splitting under large-current density in alkaline freshwater and seawater media, J. Mater. Chem. A 11(4) (2023) 1886-1893. https://doi.org/10.1039/d2ta07586e.

[3] Z.-H. Zhang, Z.-R. Yu, Y. Zhang, A. Barras, A. Addad, P. Roussel, L.-C. Tang, M. Naushad, S. Szunerits, R. Boukherroub, Construction of desert rose flower-shaped NiFe LDH-Ni_3S_2 heterostructures via seawater corrosion engineering for efficient water-urea splitting and seawater utilization, J. Mater. Chem. A 11(36) (2023) 19578-19590. https://doi.org/10.1039/d3ta02770h.

[4] Z.-H. Zhang, Y. Zhang, A. Barras, A. Addad, P. Roussel, L.-C. Tang, M.A. Amin, S. Szunerits, R. Boukherroub, Preparation of Flower-Shaped Co-Fe Layer Double Hydroxide Nanosheets Loaded with Pt Nanoparticles by Corrosion Engineering for Efficient Electrocatalytic Water Splitting, ACS Appl. Energy Mater. 5(12) (2022) 15269-15281. https://doi.org/10.1021/acsaem.2c02905.

[5] S.K. Kilaparthi, A. Addad, A. Barras, S. Szunerits, R. Boukherroub, Simultaneous upcycling of PET plastic waste and CO_2 reduction through Co-electrolysis: a novel approach for integrating CO_2 reduction and PET hydrolysate oxidation, J. Mater. Chem. A 11(47) (2023) 26075-26085. https://doi.org/10.1039/d3ta05726g.

[6] Y. Zhao, Y. Gao, Z. Chen, Z. Li, T. Ma, Z. Wu, L. Wang, Trifle Pt coupled with NiFe hydroxide synthesized via corrosion engineering to boost the cleavage of water molecule for alkaline water-splitting, Appl. Catal., B 297 (2021) 120395. https://doi.org/10.1016/j.apcatb.2021.120395.

[7] X. Liu, M. Gong, D. Xiao, S. Deng, J. Liang, T. Zhao, Y. Lu, T. Shen, J. Zhang, D. Wang, Turning Waste into Treasure: Regulating the Oxygen Corrosion on Fe Foam for Efficient Electrocatalysis, Small 16(24) (2020) 2000663. https://doi.org/10.1002/smll.202000663.

[8] M. Wei, L. Huang, L. Li, F. Ai, J. Su, J. Wang, Coordinatively Unsaturated PtCo Flowers Assembled with Ultrathin Nanosheets for Enhanced Oxygen Reduction, ACS Catal. 12(11) (2022) 6478-6485. https://doi.org/10.1021/acscatal.1c05153.

[9] S. Huang, Q. Zhang, P. Xin, J. Zhang, Q. Chen, J. Fu, Z. Jin, Q. Wang, Z. Hu, Construction of Fe-doped NiS-NiS_2 Heterostructured Microspheres Via Etching Prussian Blue Analogues for Efficient Water-Urea Splitting, Small 18(14) (2022) 2106841. https://doi.org/10.1002/smll.202106841.

[10] Y. Lin, H. Wang, C.K. Peng, L. Bu, C.L. Chiang, K. Tian, Y. Zhao, J. Zhao, Y.G. Lin, J.M. Lee, L. Gao, Co-Induced Electronic Optimization of Hierarchical NiFe LDH for Oxygen

Evolution, Small 16(38) (2020) e2002426. https://doi.org/10.1002/smll.202002426.

[11] L. Ge, W. Lai, Y. Deng, J. Bao, B. Ouyang, H. Li, Spontaneous Dissolution of Oxometalates Boosting the Surface Reconstruction of CoMO(x) (M = Mo, V) to Achieve Efficient Overall Water Splitting in Alkaline Media, Inorg. Chem. 61(5) (2022) 2619-2627. https://doi.org/10.1021/acs.inorgchem.1c03677.

[12] Z. Gu, Y. Zhang, X. Wei, Z. Duan, L. Ren, J. Ji, X. Zhang, Y. Zhang, Q. Gong, H. Wu, K. Luo, Unveiling the Accelerated Water Electrolysis Kinetics of Heterostructural Iron-Cobalt-Nickel Sulfides by Probing into Crystalline/Amorphous Interfaces in Stepwise Catalytic Reactions, Adv. Sci. 9(30) (2022) e2201903. https://doi.org/10.1002/advs.202201903.

[13] D. Zheng, Z. Jing, Q. Zhao, Y. Kim, P. Li, H. Xu, Z. Li, J. Lin, Efficient Co-doped pyrrhotite $Fe_{0.95}S_{1.05}$ nanoplates for electrochemical water splitting, Chem. Eng. J. 402 (2020) 125069. https://doi.org/10.1016/j.cej.2020.125069.

[14] Z. Pu, T. Liu, I.S. Amiinu, R. Cheng, P. Wang, C. Zhang, P. Ji, W. Hu, J. Liu, S. Mu, Transition-Metal Phosphides: Activity Origin, Energy-Related Electrocatalysis Applications, and Synthetic Strategies, Adv. Funct. Mater. 30(45) (2020) 2004009. https://doi.org/10.1002/adfm.202004009.

[15] J.S. Kim, B. Kim, H. Kim, K. Kang, Recent Progress on Multimetal Oxide Catalysts for the Oxygen Evolution Reaction, Adv. Energy Mater. 8(11) (2018) 1702774. https://doi.org/10.1002/aenm.201702774.

[16] L. Zhuang, L. Ge, Y. Yang, M. Li, Y. Jia, X. Yao, Z. Zhu, Ultrathin Iron-Cobalt Oxide Nanosheets with Abundant Oxygen Vacancies for the Oxygen Evolution Reaction, Adv. Mater. 29(17) (2017) 1606793. https://doi.org/10.1002/adma.201606793.

[17] Q. Wen, K. Yang, D. Huang, G. Cheng, X. Ai, Y. Liu, J. Fang, H. Li, L. Yu, T. Zhai, Schottky Heterojunction Nanosheet Array Achieving High-Current-Density Oxygen Evolution for Industrial Water Splitting Electrolyzers, Adv. Energy Mater. 11(46) (2021) 2102353. https://doi.org/10.1002/aenm.202102353.

[18] V.M. Nikolic, S.L. Maslovara, G.S. Tasic, T.P. Brdaric, P.Z. Lausevic, B.B. Radak, M.P. Marceta Kaninski, Kinetics of Hydrogen Evolution Reaction In Alkaline Electrolysis On a Ni Cathode In the Presence Of Ni–Co–Mo Based Ionic Activators, Appl. Catal., B 179 (2015) 88-94. https://doi.org/10.1016/j.apcatb.2015.05.012.

[19] W. Chen, B. Wu, Y. Wang, W. Zhou, Y. Li, T. Liu, C. Xie, L. Xu, S. Du, M. Song, D. Wang, Y. liu, Y. Li, J. Liu, Y. Zou, R. Chen, C. Chen, J. Zheng, Y. Li, J. Chen, S. Wang, Deciphering the alternating synergy between interlayer Pt single-atom and NiFe layered double hydroxide for overall water splitting, Energy Environ. Sci. 14(12) (2021) 6428-6440. https://doi.org/10.1039/d1ee01395e.

[20] L. Yu, L. Wu, B. McElhenny, S. Song, D. Luo, F. Zhang, Y. Yu, S. Chen, Z. Ren, Ultrafast Room-Temperature Synthesis of Porous S-Doped Ni/Fe (Oxy)Hydroxide Electrodes For Oxygen Evolution Catalysis in Seawater Splitting, Energy Environ. Sci. 13(10) (2020) 3439-3446. https://doi.org/10.1039/d0ee00921k.

[21] F. Ma, Z. Li, R. Hu, Z. Wang, J. Wang, J. Li, Y. Nie, Z. Zheng, X. Jiang, Electrocatalytic Waste-Treating-Waste Strategy for Concurrently Upgrading of Polyethylene Terephthalate Plastic and CO_2 into Value-Added Formic Acid, ACS Catal. 13(21) (2023) 14163-14172.

https://doi.org/10.1021/acscatal.3c03428.

[22] D. Wu, D. Chen, J. Zhu, S. Mu, Ultralow Ru Incorporated Amorphous Cobalt-Based Oxides for High-Current-Density Overall Water Splitting in Alkaline and Seawater Media, Small 17(39) (2021) e2102777. https://doi.org/10.1002/smll.202102777.

[23] M. Du, Y. Zhang, S. Kang, C. Xu, Y. Ma, L. Cai, Y. Zhu, Y. Chai, B. Qiu, Electrochemical Production of Glycolate Fuelled By Polyethylene Terephthalate Plastics with Improved Techno-Economics, Small 19(39) (2023) e2303693. https://doi.org/10.1002/smll.202303693.

[24] Z. Chen, R. Zheng, T. Bao, T. Ma, W. Wei, Y. Shen, B.J. Ni, Dual-Doped Nickel Sulfide for Electro-Upgrading Polyethylene Terephthalate into Valuable Chemicals and Hydrogen Fuel, Nano-Micro Lett. 15(1) (2023) 210. https://doi.org/10.1007/s40820-023-01181-8.

[25] Z. Li, Z. Yang, S. Wang, H. Luo, Z. Xue, Z. Liu, T. Mu, Medium entropy metal oxide induced *OH species targeted transfer strategy for efficient polyethylene terephthalate plastic recycling, Chem. Eng. J. 479 (2024) 147611. https://doi.org/10.1016/j.cej.2023.147611.

[26] F. Liu, X. Gao, R. Shi, Z. Guo, E.C.M. Tse, Y. Chen, Concerted and Selective Electrooxidation of Polyethylene-Terephthalate-Derived Alcohol to Glycolic Acid at an Industry-Level Current Density over a Pd-Ni(OH)($_2$) Catalyst, Angew. Chem. Int. Ed. 62(11) (2023) e202300094. https://doi.org/10.1002/anie.202300094.

[27] W. Chen, L. Xu, X. Zhu, Y.C. Huang, W. Zhou, D. Wang, Y. Zhou, S. Du, Q. Li, C. Xie, L. Tao, C.L. Dong, J. Liu, Y. Wang, R. Chen, H. Su, C. Chen, Y. Zou, Y. Li, Q. Liu, S. Wang, Unveiling the Electrooxidation of Urea: Intramolecular Coupling of the N-N Bond, Angew. Chem. Int. Ed. 60(13) (2021) 7297-7307. https://doi.org/10.1002/anie.202015773.

[28] X. Chen, Q. Wang, Y. Cheng, H. Xing, J. Li, X. Zhu, L. Ma, Y. Li, D. Liu, S-Doping Triggers Redox Reactivities of Both Iron and Lattice Oxygen in FeOOH for Low-Cost and High-Performance Water Oxidation, Adv. Funct. Mater. 32(26) (2022) 2112674. https://doi.org/10.1002/adfm.202112674.

[29] R. Chen, S.F. Hung, D. Zhou, J. Gao, C. Yang, H. Tao, H.B. Yang, L. Zhang, L. Zhang, Q. Xiong, H.M. Chen, B. Liu, Layered Structure Causes Bulk NiFe Layered Double Hydroxide Unstable in Alkaline Oxygen Evolution Reaction, Adv. Mater. 31(41) (2019) e1903909. https://doi.org/10.1002/adma.201903909.

[30] Z. Yu, Y. Li, V. Martin-Diaconescu, L. Simonelli, J. Ruiz Esquius, I. Amorim, A. Araujo, L. Meng, J.L. Faria, L. Liu, Highly Efficient and Stable Saline Water Electrolysis Enabled by Self-Supported Nickel-Iron Phosphosulfide Nanotubes With Heterointerfaces and Under-Coordinated Metal Active Sites, Adv. Funct. Mater. 32(38) (2022) 2206138. https://doi.org/10.1002/adfm.202206138.

[31] S. Wang, P. Yang, X. Sun, H. Xing, J. Hu, P. Chen, Z. Cui, W. Zhu, Z. Ma, Synthesis of 3D heterostructure Co-doped Fe_2P electrocatalyst for overall seawater electrolysis, Appl. Catal., B 297 (2021) 120386. https://doi.org/10.1016/j.apcatb.2021.120386.

[32] L. Wu, L. Yu, F. Zhang, B. McElhenny, D. Luo, A. Karim, S. Chen, Z. Ren, Heterogeneous Bimetallic Phosphide Ni_2P-Fe_2P as an Efficient Bifunctional Catalyst for Water/Seawater Splitting, Adv. Funct. Mater. 31(1) (2020) 2006484. https://doi.org/10.1002/adfm.202006484.

[33] Y. Kuang, M.J. Kenney, Y. Meng, W.H. Hung, Y. Liu, J.E. Huang, R. Prasanna, P. Li, Y. Li, L. Wang, M.C. Lin, M.D. McGehee, X. Sun, H. Dai, Solar-driven, highly sustained splitting of

seawater into hydrogen and oxygen fuels, Proc Natl Acad Sci U S A 116(14) (2019) 6624-6629. https://doi.org/10.1073/pnas.1900556116.

[34] Y. Zhao, B. Jin, A. Vasileff, Y. Jiao, S.-Z. Qiao, Interfacial nickel nitride/sulfide as a bifunctional electrode for highly efficient overall water/seawater electrolysis, J. Mater. Chem. A 7(14) (2019) 8117-8121. https://doi.org/10.1039/c9ta01903k.

[35] M. Ning, F. Zhang, L. Wu, X. Xing, D. Wang, S. Song, Q. Zhou, L. Yu, J. Bao, S. Chen, Z. Ren, Boosting efficient alkaline fresh water and seawater electrolysis via electrochemical reconstruction, Energy Environ. Sci. 15(9) (2022) 3945-3957. https://doi.org/10.1039/d2ee01094a.

[36] B. Wang, M. Lu, D. Chen, Q. Zhang, W. Wang, Y. Kang, Z. Fang, G. Pang, S. Feng, NixFeyN@C microsheet arrays on Ni foam as an efficient and durable electrocatalyst for electrolytic splitting of alkaline seawater, J. Mater. Chem. A 9(23) (2021) 13562-13569. https://doi.org/10.1039/d1ta01292d.

[37] W. Ma, D. Li, L. Liao, H. Zhou, F. Zhang, X. Zhou, Y. Mo, F. Yu, High-Performance Bifunctional Porous Iron-Rich Phosphide/Nickel Nitride Heterostructures for Alkaline Seawater Splitting, Small 19(19) (2023) e2207082. https://doi.org/10.1002/smll.202207082.

[38] C. Wang, M. Zhu, Z. Cao, P. Zhu, Y. Cao, X. Xu, C. Xu, Z. Yin, Heterogeneous bimetallic sulfides based seawater electrolysis towards stable industrial-level large current density, Appl. Catal., B 291 (2021) 120071. https://doi.org/10.1016/j.apcatb.2021.120071.

[39] J. Wang, X. Li, T. Zhang, Y. Chen, T. Wang, Y. Zhao, Electro-Reforming Polyethylene Terephthalate Plastic to Co-Produce Valued Chemicals and Green Hydrogen, J. Phys. Chem. Lett. 13(2) (2022) 622-627. https://doi.org/10.1021/acs.jpclett.1c03658.

[40] F. Liu, X. Gao, R. Shi, E.C.M. Tse, Y. Chen, A general electrochemical strategy for upcycling polyester plastics into added-value chemicals by a $CuCo_2O_4$ catalyst, Green Chem. 24(17) (2022) 6571-6577. https://doi.org/10.1039/d2gc02049a.

Chapter VI. Conclusions and perspectives

VI.1 Conclusions

Electrocatalytic high-throughput seawater electrolysis for hydrogen production is a promising green energy technology that offers environmental and energy sustainability possibilities. However, the large-scale application is limited by the complex composition of seawater, high concentration of Cl^- leading to competing reactions, and severe corrosion of electrode materials. This thesis presents the seawater splitting process's electrode reactions and basic parameters. It summarizes the types and selection principles of transition metal catalysts with a critical analysis of the design principles for seawater electrocatalysts. Furthermore, utilizing the potential energy of seawater corrosion, a low-cost catalyst synthesis process that can be manufactured on a large scale was proposed. Interestingly, water splitting assisted by the oxidation of small molecules strategy was proposed for the highly efficient electrochemical production of hydrogen, which not only effectively reduces overpotential, avoiding CER reaction competition at the anode, but also successfully converts waste into high value-added products. From a safety perspective, it effectively impedes the production of the explosive H_2 / O_2 mixture and reactive oxygen species.

Specifically, for the first project, a bifunctional electrode with flower-like heterostructure consisting of Fe/Co LDH loaded with small Pt nanoparticles was successfully synthesized through a facile oxygen corrosion method and applied for efficient overall water splitting. The Pt-Co/Fe LDH electrode exhibited an outstanding HER, OER, and overall water splitting activities in an alkaline medium, which are superior to noble metal-based catalysts e.g., Pt/C and RuO_2. The Pt-Co/Fe LDH electrode recorded overpotential values as low as 126 and 285 mV to deliver 100 mA cm^{-2} for HER and OER, respectively. In this work, the facile and scalable strategy and extremely low content of the precious metal Pt in conjunction with a transition metal catalyst provide great industrial production potential.

For the second project, a NiFe LDH-Ni_3S_2 bifunctional electrode with a desert rose flower-shaped heterostructure was successfully synthesized *via* seawater corrosion and ion exchange.

The NiFe LDH-Ni_3S_2 electrode displayed overpotential values as low as 257 and 280 mV to deliver 100 mA cm^{-2} for HER and OER in 1 M KOH seawater, respectively. In addition, benefiting from the modulated electronic configuration and optimized free-energy of oxygen-containing intermediates adsorption and desorption, NiFe LDH-Ni_3S_2 electrode featured outstanding urea oxidation reaction and overall seawater-urea splitting activities in 1 M KOH+0.33 M urea, which are superior to commercial catalysts, e.g., Pt/C and RuO_2. Noteworthy, an electrolyzer comprising NiFe LDH-Ni_3S_2 as both anode and cathode exhibited a small cell voltage of 1.63 V to reach 100 mA cm^{-2}, demonstrating that urea plays an important role in reducing overpotential and prevent chlorine evolution reaction competition. The facile and scalable seawater corrosion synthesis strategy to prepare nanoflower heterostructure of metal hydroxides coupled with Ni_3S_2 can be utilized to explore other bifunctional electrocatalysts in the field of energy, achieving efficient conversion of solar energy, electricity and hydrogen.

For the third project, a cost-effective and industrially compatible seawater corrosion engineering was proposed to turn commercial Ni foam into robust OER/EGOR catalysts for high-performance seawater electrolysis and plastic PET upcycling. The synthesized A-CoFeNi catalyst displayed overpotential values as low as 1.55 and 1.39 V to deliver 100 mA cm^{-2} for OER and EGOR in alkaline natural seawater electrolyte, respectively. Furthermore, benefiting from modulated electronic configurations and optimized nanoflower shape morphology, A-CoFeNi//Pt-CoFeNi required a cell voltage of 1.56 V at 100 mA cm^{-2} to drive the coupled two-electrode system, which is 150 mV lower than that of the seawater splitting and is superior to commercial catalysts, e.g., Pt/C and RuO_2, testifying that EG plays a key role in decreasing overpotential and energy consumption. Simultaneously, the electrolyzer also recorded high FE for the generation of H_2 (almost 100%) and high value-added formate (95.6%). The present work explores a coordinative strategy for green hydrogen production, PET waste plastic upcycling and cost-free seawater utilization by the design and construction of cost-effective and high-efficient electrocatalysts, achieving efficient conversion of solar energy, electricity and hydrogen energy.

VI.2 Perspectives

Despite the noticeable progress made in the highly efficient seawater splitting assisted by organic molecule oxidation, there is a long way to go before industrial applications could be achieved. In order to further develop high performance catalysts for hydrogen production, our perspectives for future studies are outlined below.

From catalyst design and mechanistic investigation perspective: Currently, most of the catalyst explanation mechanisms are for traditional water electrolysis, and there is a need for a targeted catalyst design for small molecule oxidation reactions. Therefore, it is necessary to have an in-depth understanding of the relevant catalytic reaction mechanisms and to achieve a targeted design for each small molecule oxidation reaction, such as EG, urea, glycerol, 5-hydroxymethylfurfural and formaldehyde, etc. It is imperative to apply advanced *in-situ* characterization techniques (*in-situ* XPS, Raman, FTIR etc.) to analyze key intermediates and actual catalytic species in real time. In addition, it is better to combine with density functional theory field to explain the catalytic mechanisms of the resultant electrocatalysts.

From the industry application perspective: Firstly, achieving high selectivity and Faradaic efficiency via proper catalysts for producing H_2 by seawater electrolysis at a high current density condition is a considerable challenge. We will further optimize the seawater corrosive fabrication processes and combine them with another traditional method for the preparation of N/S/P doping materials to improve catalytic activity and durable performance. Secondly, a flow-electrolyzer assembly enhances reactant mass transport and product removal from the catalyst, optimizing contact between reactants and active sites to achieve high current density at low voltages. Therefore, it is imperative to prepare larger electrodes close to the needs of the industry and assemble them into a full cell (such as AEM, PEM SOEC, etc.) to serve the industrial production of directly seawater electrolysis in the future. Thirdly, the organic molecule oxidation reaction effectively decreases energy consumption and produces highly-added value products. However, separating and purifying valuable anodic products are critical points for industrial applications. We will develop feasible methods to efficiently separate target products, such as finding the proper selectivity of ion-exchange membranes, exploring novel organic molecules that can be easily separated, etc.

Publications

1.**Zhao-Hui Zhang**, Zhi-Ran Yu, Yi Zhang, Alexandre Barras, Ahmed Addad, Pascal Roussel, Long-Cheng Tang, Sabine Szunerits, Rabah Boukherroub. Construction of desert rose flower-shaped NiFe LDH-Ni_3S_2 heterostructures via seawater corrosion engineering for efficient water-urea splitting and seawater utilization. **J. Mater. Chem. A** 11(36) (2023) 19578-19590.

2. **Zhao-Hui Zhang**, Yi Zhang, Alexandre Barras, Ahmed Addad, Pascal Roussel, Mohammed A. Amin, Long-Cheng Tang, Sabine Szunerits, Rabah Boukherroub. Preparation of Flower-Shaped Co-Fe Layer Double Hydroxide Nanosheets Loaded with Pt Nanoparticles by Corrosion Engineering for Efficient Electrocatalytic Water Splitting, **ACS Appl. Energy Mater.** 5(12) (2022) 15269-15281.

3. **Zhao-Hui Zhang**, Zhi-Ran Yu, Yi Zhang, Alexandre Barras, Ahmed Addad, Pascal Roussel, Long-Cheng Tang, Sabine Szunerits, Rabah Boukherroub. Seawater Corrosive Engineering Assisted in-situ Room-Temperature Synthesis of Ni/Co/Fe Trimetallic Composition to Achieve Polyester Plastics Upgrading and Green Hydrogen Production. **Manuscript in preparation.**

4. Yi Zhang, **Zhao-Hui Zhang**, Qi Wang, Alexandre Barras, Ahmed Addad, Mohammed A. Amin,Pascal Roussel, Sabine Szunerits, Rabah Boukherroub. 0D/2D Co_3O_4/Ti_3C_2 MXene Composite: A Dual-Functional Electrocatalyst for Energy-Saving Hydrogen Production and Urea Oxidation, ACS Appl. Energy Mater. 5(12) (2022) 15471-15482.

5. Yi Zhang, **Zhao-Hui Zhang**, Zhi-Ran Yu, Qi Wang, Alexandre Barras, Ahmed Addad, Mohammed A. Amin, Pascal Roussel, Sabine Szunerits, Rabah Boukherroub. Ruthenium Oxide Nanoparticles Immobilized on Ti_3C_2 MXene Nanosheets for Boosting Seawater Electrolysis. ACS Appl. Mater. Interfaces 15(50) (2023) 58345-5835